A Three Dimensional Gaussian Beam Diffraction Approach to Analysis of Quasi-optical Networks.

Xu, Liang

A Three Dimensional Gaussian Beam Diffraction Approach to Analysis of Quasi-optical Networks

A thesis submitted to the University of London for partial fulfilment of the requirements for the degree of Doctor of Philosophy

By
Liang Xu

Supervisors: Prof. Xiaodong Chen and Dr. Robert.S.Donnan

School of Electronic Engineering and Computer Science
Queen Mary University of London
24 November 2015

I, Liang Xu, confirm that the research included within this thesis is my own work or that where it has been carried out in collaboration with, or supported by others, that this is duly acknowledged below and my contribution indicated. Previously published material is also acknowledged below.

I attest that I have exercised reasonable care to ensure that the work is original, and does not to the best of my knowledge break any UK law, infringe any third party's copyright or other Intellectual Property Right, or contain any confidential material.

I accept that the College has the right to use plagiarism detection software to check the electronic version of the thesis.

I confirm that this thesis has not been previously submitted for the award of a degree by this or any other university.

Signature: Liang Xu

Date: 24 November 2015

Details of collaboration and publications:

Please refer to section "List of collaboration and publications" on page 201-202

Abstract

Millimetre and sub-millimetre wave systems have been applied in many areas, such as radio astronomy, remote sensing of the atmosphere, plasma diagnostics, material exploration. A Quasi-optical Network (QoN) is the most efficient approach to transport signals within such systems.

The Gaussian beam summation method has proven to be a useful ray-tracing-based solution in designing the complex configurations of QoNs. An efficient approach, diffracted Gaussian beam analysis (DGBA) has been developed at Queen Mary, University of London. However, this version of DGBA can be only used for a 2.5-D analysis, for the following reasons: (1) the input Gaussian beams (GBs) should be stigmatic (circular); (2) all incident beams are approximated as normally incident, unable to treat oblique polar angles of incidence. So in this regard, there is a need to develop a 3D treatment of diffraction in DGBA.

In this thesis, a 3D diffracted GB approach (3D-DGBA) to the analysis of multi-reflector QoNs is presented. This new approach expands the input beam/field into a set of elementary GBs by using windowed Fourier transforms (WFT). The ensuing GBs propagate to the reflector. Reflected and diffracted beams are respectively handled by a phase-matching method and a 3D GB diffraction method. In addition, it is modular and suitable for analysis of large, multi-element, QoNs.

A specific design procedure of multi-path, multi-reflector, QoNs is presented and two different kinds of dual-path QoNs are built and assessed. By analysing one of these QoNs, the new 3D-DGBA approach is verified experimentally, as well as compared to the original DGBA and GRASP predictions. It is observed that 3D-DGBA is more accurate than the original DGBA. For example, in one of the simulated cases, the far-field deviation between 3D-DGBA and GRASP within 20˚ stays in the range of ±8.0 dB in comparison with ±23.0 dB of the original DGBA.

Acknowledgements

I would like hereby to express my deep and sincere gratitude to my supervisors Prof. Xiaodong Chen and Dr. Robert. S. Donnan for their guidance. I would have never come to this point without their professional and rigorous work, which will continuously benefit my future career. I want especially to thank Prof. Chen, who taught me from my first day as a post-graduate until the last day finishing my PhD study - ten years; his precious personalities and serious research attitude not only influenced my time of study, but will continue to do so throughout my life.

I am also greatly indebted to Dr. C. Rieckmann. My research is based mainly on his prior development of the subject. During my post-graduate study, he came to China and discussed the work with me, which was of great help.

Special thanks go to my colleague Dr. Xiaoming Liu. We studied and worked together for nine years. His support in my research and friendship in life is very generous.

I also want to thanks Prof. Junsheng Yu and all the students in the two labs, *BUPT-QMUL EM Theory & Applications International Research Lab* in *Beijing University of Posts and Telecommunications*, and *Antennas & Electromagnetics Lab* of *Queen Mary, University of London*. I did many experiments, and undertook much research and discussion with them; their kind encouragement and helpful sharing contributed much to my research. Particular thanks go to Dr. Zejian Lu and Mr. Hai Wang. They were involved in the simulation experiments using GRASP in Chapter 3-5.

I want to thanks Melissa, the PhD student administrator at Queen Mary University of London. She always passed important messages to me on time. Thanks also to my colleagues Mr. Xiang Li, Mr. Yang Zheng and Mr. Li Cheng. They helped me a lot.

Last but not least, I want to express my deep thanks for my grandparents who are already now in heaven; to my parents, who not only raised me but also support me in pursuing my research dream; to my sister who is my moral support and listener; and to

my dear wife who always encourages me and takes care of me. All your love and support means so much to me.

Table of Contents

Abstract **3**
Acknowledgements **4**
Table of Contents **6**
List of Figures **9**
List of Tables **22**
Abbreviations and Glossary **23**
Symbols and Units **24**
Chapter 1 Introduction **25**
1.1 Overview of Quasi-optical techniques 25
1.2 Overview of analysis methods for QoN 28
1.2.1 Brief introduction to diffraction integrals 29
1.2.2 Brief introduction to geometrical optics 30
1.2.3 Brief introduction to physical optics 31
1.2.4 Overview of Gaussian beam summation method 33
1.3 Introduction of QoN analysis software 35
1.4 Research motivation 38
1.5 Summary and thesis outlines 39
References 40
Chapter 2 Gaussian Beams and their Propagation **45**
2.1 Overview 45
2.2 The circular Gaussian beam in cylindrical coordinates 45
2.3 The elliptical astigmatic Gaussian beam 48
2.4 Spectral representation of 3D incident Gaussian beams 52
2.5 Gaussian beams propagation 56
2.5.1 Circular Gaussian beam propagation 56
2.5.2 Propagation of a general astigmatic Gaussian beam 57
2.6 Numerical examples of Gaussian beams 57
2.6.1 Circular stigmatic Gaussian beam 57
2.6.2 Elliptical astigmatic Gaussian beam 59
2.7 Summary 62
References 62
Chapter 3 Gaussian Beam Reflection on a Curved Surface **64**
3.1 Overview 64
3.2 Gaussian beam reflection using physical optics 64
3.3 Gaussian beam reflection using geometrical optics 66
3.4 Gaussian beam reflection using the phase matching method 69
3.4.1 General case 69
3.4.2 Extended phase-matching method 73
3.5 Numerical verification 76

3.5.1. Experiments with a circular incident Gaussian beam 76
3.5.2. Experiments with general astigmatic incident Gaussian beams 78
3.6 Summary 83
References 84
Chapter 4 2D Gaussian Beam Diffraction on a Half-Plane 85
4.1 Overview 85
4.2 Boundary diffraction wave theory in 2D-DGBA 85
4.2.1 Principles of BDW theory in 2D-DGBA 85
4.2.2 Limitations and approximations of the BDW method in 2D-DGBA 89
4.2.2.1 Circular incident beams limitation 89
4.2.2.2 Circular emergent beams approximation 90
4.2.2.3 Normal polar incidence approximation 91
4.2.2.4 Oblique azimuth angle incidence error 92
4.3 Gaussian beam summation method in half plane diffraction 93
4.4 Numerical verification 99
4.5 Summary 101
References 102
Chapter 5 3D Gaussian Beam Diffraction on a Half-Plane 103
5.1 Overview 103
5.2 Spectral representations of the scattered field 104
5.3 GB summation representation of a 3D diffraction 105
5.3.1. Total field representations in the forward-scattering region 105
5.3.2. Representation of spectral function Φ 106
5.3.3. GBS representation 115
5.3.3.1 Problem description and WFT Expansion 115
5.3.3.2 Expansion Coefficients Expression 119
5.3.3.3 GBS Representation 125
5.4 Field representations in the backward-scattering region 127
5.5 Numerical verification 132
5.6 Summary 140
References 141
Chapter 6 Implementation of a Modular 3D Gaussian Beam Diffraction Approach 142
6.1 Overview 142
6.2 Applying the Gaussian beam expansion method 142
6.3 Incorporating the phase matching reflection method 146
6.4 Incorporating 3D GBS diffraction analysis 150
6.4.1 Models adaptation 150
6.4.2 Selection of parameters 155
6.4.3 Methods of accelerating analysis 156
6.5 Modularity 159
6.6 Flow chart of 3D-DGBA 160
6.7 Summary 163
References 163

Chapter 7 Experimental Verification of 3D-DGBA Analysis 164
7.1 Overview 164
7.2 System requirement and QoN configuration 164
7.3 Ellipsoidal reflectors design 166
7.4 Single path design 172
7.5 Dual path QoN design 174
7.6 Another dual path QoN 176
7.7 Simulation and experimental verification 178
7.8 Summary 195
References 196
Chapter 8 Summary and Future Work 197
8.1 Conclusions 197
8.2 Key contributions 198
8.3 Future work 199
List of collaboration and publications 201
Appendix I Approximated PO Reflection Method 203
References 205
Appendix II Phase Matching Analysis Method in GO 206
References 209
Appendix III Details of Proof that Equation (5.5) is Equivalent to (5.1) 210
Appendix IV Calculations of $\widetilde{\eta}_i$ and$\widetilde{q}_i$ 212

List of Figures

Figure 1.1 A perspective view of the Advanced Microwave Sounding Unit-B (AMSU-B). A dual-reflector main-antenna is followed by a quasi-optical network (QoN). In this QoN, the train of plain and ellipsoidal reflectors steers the signal beams through the demultiplexing dichroic plates DCP1, DCP2, into receiver feedhorns H1, H2, H3 covering three bands: H1 for 175-191 GHz, H2 for 148-152 GHz and H3 for 86-92 GHz. This Figure is reproduced from Martin *et al*, [12]. 26

Figure 1.2 Image and design graphics of SPIRE photometer. They depict the quasi-optical network layout. In this QoN, the train of seven ellipsoidal, flat, toric and spherical reflectors (M3-M9) steers the signal beams through the two demultiplexing dichroic plates into three detectors, covering the 200-300 μm, 300-400 μm and 400-670 μm bands. 28

Figure 1.3 Schematic diagram showing the relationship between some diffraction analysis methods, reproduced from O'Sullivan *et al*, [18]. 29

Figure 1.4 An example of flux tube. The sides of such ray tubes are formed by the trajectories of the adjacent rays, the power flow through any cross section of a given ray tube is the same insofar as no power flows across the sides of the tube. In geometrical optics, it gives $\left|E_0(s)\right|^2 dS = \left|E_0(0)\right|^2 dS_0$, which is a statement of power conservation along the flux tube, [26]. 30

Figure 1.5 An example of shadow boundary in geometrical theory of diffraction (GTD): Plane wave illuminates a semi-infinite wedge. ISB is the shadow boundary of the incident field and RSB is the shadow boundary of the reflected field. GTD is not valid in the transition region... 31

Figure 1.6 (a) Uniform components of the field at points P_1 and P_2 on the scattering object are those on the infinite tangential planes shown by blue dotted lines. (b) Non-uniform components of the surface field induced by the incident wave near the edge E is asymptotic to those are the tangential wedges with infinite faces shown by green dotted lines. 32

Figure 2.1 A Gaussian beam (the arrow in the figure) impinges on a half plane $(y = 0, x \geq 0)$ at $\mathbf{x}_i = (x_i, z_i)$ in the direction of (φ_i, θ_i). $(\vec{x}, \vec{y}, \vec{z})$ is the original global coordinate. Two beam based coordinate systems are constructed: coordinate $(\vec{\sigma}, \vec{\eta}_1, \vec{\eta}_2)$ with the beam direction $\vec{\sigma}$ and coordinate $(\bar{\bar{\mathbf{x}}}, \vec{y}, \vec{z})$ with $\mathbf{x} = \bar{\mathbf{x}} + \mathbf{x}_i$. 52

Figure 2.2 Amplitude profile and the trace of a Gaussian beam. The beam waist of the beam is located at z=0 plane. The amplitude profile distribution is of a Gaussian type. The size of the beam waist is w_0 which is defined as the radius where the field amplitude decays to e^{-1} of its on-axis value. The Gaussian beam propagates along the z-axis with a divergent angle θ. Propagating Gaussian beam indicates increase in the radius of wave surface and the relative beam width, and diminution of peak amplitudes as distance from the waist increases. Both of them can be traced at arbitrary locations on the axis, i.e. z_1 and z_2. 56

Figure 2.3 The side view of total field $|B_i(r)|$ of a circular stigmatic GB with $q(0) = -500i$, $\delta_{12} = \delta_{21} = 0$, and $\delta_{11} = \delta_{22} = 1$. 58
Figure 2.4 The plan view of total field $|B_i(r)|$ of a circular stigmatic GB with $q(0) = -500i$, $\delta_{12} = \delta_{21} = 0$, and $\delta_{11} = \delta_{22} = 1$. 59
Figure 2.5 The side view of total field of an elliptical astigmatic GB with $q(0) = -500i$, $\delta_{12} = \delta_{21} = 0$, $\delta_{11} = 4\delta_{22}$ and $\delta_{22} = 1$ 60
Figure 2.6 The plan view of total field of an elliptical astigmatic GB with $q(0) = -500i$, $\delta_{12} = \delta_{21} = 0$, $\delta_{11} = 4\delta_{22}$ and $\delta_{22} = 1$ 60
Figure 2.7 the side view of total field of an elliptical astigmatic GB with $q(0) = -500i$, $\delta_{11} = 1.5\delta_{22}$, $\delta_{22} = 1$ and $\delta_{12} = \delta_{21}$=1 61
Figure 2.8 the plan view of total field of an elliptical astigmatic GB with $q(0) = -500i$, $\delta_{11} = 1.5\delta_{22}$, $\delta_{22} = 1$ and $\delta_{12} = \delta_{21}$=1 62
Figure 3.1 Geometry of PO method: 3D Gaussian beam reflection at a curved surface. $(\hat{x}, \hat{y}, \hat{z})$ is the surface coordinate at the intersection point. z_i and z_r are the propagation directions of the incident and reflected beams. θ_i is the incident angle; θ_r, the reflected angle; and d_i, the distance from the incident beam waist to the intersection point. 65
Figure 3.2 Geometry of GO method: reflection of a Gaussian beam at a curved surface. A circular incident GB impinges on a curved surface with an incident angle θ_i. $(\hat{\xi}, \hat{\eta}, \hat{n})$ is the surface coordinate at the intersection point; $(\hat{\xi}^i, \hat{\eta}^i, \hat{s}^i)$, the incident GB based coordinate system; and $(\hat{\xi}^r, \hat{\eta}^r, \hat{s}^r)$, reflected GB based coordinate system. 67
Figure 3.3 Geometry of Phase Matching method: 3D Gaussian beam reflection at a curved surface with incident beam along the principal direction. $(\hat{x}, \hat{y}, \hat{z})$ is the surface coordinate at the intersection point. $(\hat{x}_i, \hat{y}_i, \hat{z}_i)$ is the incident coordinate with $\hat{z}_i$, the propagation directions of the incident beam. θ_i is the incident angle; and d_i, the distance from the incident beam waist to the intersection point. $(\hat{x}_r, \hat{y}_r, \hat{z}_r)$ is the reflected coordinate with $\hat{z}_r$, the propagation directions of the reflected beam. θ_i is the reflected angle; and d_r, the distance from the reflected beam waist to the intersection point. 70
Figure 3.4 Geometry of extended Phase Matching method: 3D Gaussian beam reflection at a curved surface with arbitrary incident direction. The direction of projection of the incident beam onto the surface is $\hat{\xi}$ rather than $\hat{x}$. A coordinate system $(\hat{\xi}, \hat{\eta}, \hat{n})$ is constructed with $\hat{n}$, the normal direction of the curved surface around the intersection point P. The angle between $\hat{\xi}$ and $\hat{x}$ is φ. All other symbols have the same meanings as in Figure 3.3. 75
Figure 3.5 Simulation results of circular Gaussian beam reflection from a concave surface by PO, GO and Phase Matching methods with incident beam and surface parameters $w_i = 3\lambda$, $d_i = 20\lambda$, $\theta_i = 0^\circ$, $R_1 = -80\lambda$, $R_2 = -60\lambda$ 77

Figure 3.6 Simulation results of circular Gaussian beam reflection from a concave surface by PO, GO and Phase Matching methods with incident beam and surface parameters $w_i = 3\lambda$, $d_i = 20\lambda$, $\theta_i = 30^\circ$, $R_1 = -80\lambda$, $R_2 = -60\lambda$. 77
Figure 3.7 Simulation results of circular Gaussian beam reflection from a convex surface by PO, GO and Phase Matching methods with incident beam and surface parameters $w_i = 3\lambda$, $d_i = 20\lambda$, $\theta_i = 0^\circ$, $R_1 = 60\lambda$, $R_2 = 80\lambda$ 77
Figure 3.8 Simulation results of circular Gaussian beam reflection from a convex surface by PO, GO and Phase Matching methods with incident beam and surface parameters $w_i = 3\lambda$, $d_i = 20\lambda$, $\theta_i = 15^\circ$, $R_1 = 60\lambda$, $R_2 = 80\lambda$ 78
Figure 3.9 Simulation results of circular Gaussian beam reflection from a convex surface by PO, GO and Phase Matching methods. Incident beam and surface parameters $w_i = 8\lambda, d_i = 100\lambda$, $\theta_i = 0^\circ$, $R_1 = -20\lambda$, $R_2 = -10\lambda$. 78
Figure 3.10 Simulation results of general astigmatic Gaussian beam reflection from a concave surface by PO, GO and Phase Matching methods with incident beam and surface parameters $w_{i1} = 3\lambda$, $w_{i2} = 1.5\lambda$, $d_{i1} = d_{i2} = 20\lambda$, $\theta_i = 0^\circ$, $R_1 = -80\lambda$, $R_2 = -60\lambda$. 79
Figure 3.11 Simulation results of general astigmatic Gaussian beam reflection from a concave surface by PO, GO and Phase Matching methods with incident beam and surface parameters $w_{i1} = 3\lambda$, $w_{i2} = 1.5\lambda$, $d_{i1} = 20\lambda$, $d_{i2} = 30\lambda$, $\theta_i = 0^\circ$, $R_1 = -80\lambda$, $R_2 = -60\lambda$. 80
Figure 3.12 Simulation results of general astigmatic Gaussian beam reflection from a concave surface by PO, GO and Phase Matching methods with incident beam and surface parameters $w_{i1} = 3\lambda$, $w_{i2} = 1.5\lambda$, $d_{i1} = 20\lambda$, $d_{i2} = 30\lambda$, $\theta_i = 30^\circ$, $R_1 = -80\lambda$, $R_2 = -60\lambda$. 80
Figure 3.13 Simulation results of general astigmatic Gaussian beam reflection from a concave surface by PO, GO and Phase Matching methods with incident beam and surface parameters $w_{i1} = 3\lambda$, $w_{i2} = 1.5\lambda$, $d_{i1} = d_{i2} = 20\lambda$, $\theta_i = 0^\circ$, $R_1 = 60\lambda$, $R_2 = 80\lambda$. 81
Figure 3.14 Simulation results of general astigmatic Gaussian beam reflection from a concave surface by PO, GO and Phase Matching methods with incident beam and surface parameters $w_{i1} = 3\lambda$, $w_{i2} = 1.5\lambda$, $d_{i1} = 20\lambda$, $d_{i2} = 15\lambda$, $\theta_i = 0^\circ$, $R_1 = 60\lambda$, $R_2 = 80\lambda$. 81
Figure 3.15 Simulation results of general astigmatic Gaussian beam reflection from a concave surface by PO, GO and Phase Matching methods with incident beam and surface parameters $w_{i1} = 3\lambda$, $w_{i2} = 1.5\lambda$, $d_{i1} = 20\lambda$, $d_{i2} = 15\lambda$, $\theta_i = 15^\circ$, $R_1 = 60\lambda$, $R_2 = 80\lambda$ 82
Figure 3.16 Simulation results of general astigmatic Gaussian beam reflection from a concave surface by PO, GO and Phase Matching methods with incident beam and surface parameters $w_{i1} = 8\lambda$, $w_{i2} = 6\lambda$, $d_{i1} = 20\lambda$, $d_{i2} = 15\lambda$, $\theta_i = 15^\circ$, $R_1 = 20\lambda$, $R_2 = 10\lambda$ 82
Figure 3.17 Simulation results of circular Gaussian beam reflection from a concave surface by PO, GO and Phase Matching methods with incident beam and surface parameters $w_{i1} = 3\lambda$, $w_{i2} = 1.5\lambda$, $d_{i1} = 20\lambda$, $d_{i2} = 15\lambda$, $\theta_i = 0^\circ$, $\varphi_i = 15^\circ$, $R_1 = -80\lambda$, $R_2 = -60\lambda$. 83
Figure 4.1 Geometry of boundary diffraction wave (forward-scattering region). An incident Gaussian beam with beam waist w_0 at $z = -z_0$ normally impinges upon a half-screen $(x > a, z = 0)$. The Gaussian beam is propagating along the z-axis. $Q(x_0, y_0, z_0)$ is a source-

point of boundary-diffraction located on the boundary of the half-screen and $P(x,y,z)$ represents the observation point. [1] 86
Figure 4.2 Equivalent geometry for determining the diffracted field in the backward-scattering region at oblique incidence. An incident Gaussian beam with beam waist w_0 at $z_t = -z_0$ obliquely impinges upon a half-screen $(z > z_e, x = 0)$. The incident Gaussian beam is propagating along the z_t-axis with reflected beam along z_r-axis. Three coordinate systems are constructed: the transmitted beam related coordinate system (x_t, y_t, z_t), the reflected beam related coordinate system (x_r, y_r, z_r), and the half-screen based coordinate system (x,y,z). The incidence angle is ϕ_0 and the observation point is described in the half-screen-based cylindrical (ρ,ϕ,y) coordinate system. The diffracted field in the backward-scattering region is characterised by an image beam with same magnitude but opposite in sign to the incident beam at the opposite side of the half-screen. [4] 89
Figure 4.3 Simulated backscattered field with Boundary diffraction wave theory (BDT) in 2D-DGBA and PO for a normally incident elliptical Gaussian beam. The two principal radii of curvature at the diffracting edge are 200λ and 500λ, respectively. The beam half width is 8λ. The diffracted field is simulated at a distance of 300λ for various angles α characterising the principal directions. [4] 90
Figure 4.4 A Gaussian beam (the arrow in the figure) impinges on a half-plane $(y = 0, x \geq 0)$ in an arbitrary direction of (φ_i, θ_i). However, in 2D-DGBA, all the incident beams are approximated by the beams that normally impinge the half plane ($\theta_i = \pi/2$). 91
Figure 4.5 Simulated backscattered field with BDT in 2D-DGBA and PO for various azimuth angle φ_i of the incident beam, with polar angle normal incidence ($\theta_i = 90°$). The field are calculated for a nearfield cut with the coordinates ($y = 0; z = -300\lambda$), based on the modelled scenario of Fig. 4.1. The parameter a is chosen to be zero and the half beam width w_0 is 8λ. [3] 92
Figure 4.6 Geometry for determining the problem of 2D Gaussian beam summation method. A Gaussian beam impinges upon a half-plane at an angle φ_0. σ_0 is the distance of the edge from the beam waist, and η_0 is that from the beam axis which describes the incident beam displacement from the edge. The scattered field is described as a sum of Gaussian beam emerging from the edge in all directions with the spectral discretization $\delta\alpha$. The observation point is $\mathbf{r} = (r,\phi)$, [2]. 94
Figure 4.7 For $\alpha \in (0, 2\pi)$, the result of spectral function $\left|\breve{\Phi}\right|$ with a stigmatic incident Gaussian beam ($\delta_{11} = \delta_{22} = 1$, $\delta_{12} = \delta_{21} = 0$, $w_0 = 8\lambda$) intersecting the half plane at $(\sigma_0 = 100\lambda, \eta_0 = 8\lambda)$ in the direction of $\phi_0 = \pi/2$ 96
Figure 4.8 For $\alpha \in (0, 2\pi)$, the result of spectral function $\left|\breve{\Phi}\right|$ with a stigmatic incident Gaussian beam ($\delta_{11} = \delta_{22} = 1$, $\delta_{12} = \delta_{21} = 0$, $w_0 = 8\lambda$) intersects the half plane at $(\sigma_0 = 100\lambda, \eta_0 = 8\lambda)$ in the direction of $\phi_0 = \pi/4$ 97

Figure 4.9 For $\alpha \in (0, 2\pi)$, the result of spectral function $\left|\breve{\Phi}\right|$ with a stigmatic incident Gaussian beam ($\delta_{11} = \delta_{22} = 1$, $\delta_{12} = \delta_{21} = 0$, $w_0 = 8\lambda$) intersecting the half plane at $(\sigma_0 = 100\lambda, \eta_0 = -8\lambda)$ in the direction of $\phi_0 = \pi / 2$ 97

Figure 4.10 For $\alpha \in (0, 2\pi)$, the result of spectral function $\left|\breve{\Phi}\right|$ with a stigmatic incident Gaussian beam ($\delta_{11} = \delta_{22} = 1$, $\delta_{12} = \delta_{21} = 0$, $w_0 = 8\lambda$) intersecting the half plane in the direction of $\phi_0 = \pi / 2$. The blue line represents the result with the intersection-point located at $(\sigma_0 = 100\lambda, \eta_0 = 8\lambda)$, and the black line is that with the intersection-point at $(\sigma_0 = 100\lambda, \eta_0 = -8\lambda)$ 98

Figure 4.11 Comparison of the backward scattered field at $(y = 300\lambda)$ with physical optics and 2D Kirchhoff half-screen BDT with a stigmatic incident Gaussian beam ($w_0 = 8\lambda$) impinging on the half plane at $(\sigma_0 = 100\lambda, \eta_0 = 8\lambda)$ in the direction of $\phi_0 = \pi / 2$ 99

Figure 4.12 Comparison of the backward scattered field at $(y = 300\lambda)$ with physical optics and 2D Kirchhoff half-screen BDT with a stigmatic incident Gaussian beam ($w_0 = 8\lambda$) impinging on half plane out of the edge at $(\sigma_0 = 100\lambda, \eta_0 = -8\lambda)$ in the direction of $\phi_0 = \pi / 2$. 100

Figure 4.13 Comparison of the backward scattered field (600λ away from the half-plane along the principal optical axis of the reflected beam) with physical optics and 2D Kirchhoff half-screen BDT. The stigmatic oblique incident Gaussian beam ($w_0 = 8\lambda$) impinges on half plane at $(\sigma_0 = 100\lambda + w_0 \cos\phi_0, \eta_0 = w_0 \sin\phi_0)$ in the direction of $\phi_0 = \pi / 4$ 101

Figure 5.1 For $\alpha \in (0, \pi)$, the side view of the result of spectral function $\Phi(\alpha, \zeta)$ with a stigmatic incident Gaussian beam ($\delta_{11} = \delta_{22} = 1$, $\delta_{12} = \delta_{21} = 0$, $q(0) = -500i$) impinging upon the half plane at $(x_i = 2, z_i = 0)$ in the direction of $(\theta_i, \pi + \varphi_i) = (\pi / 2, \pi + \pi / 2)$ 110

Figure 5.2 For $\alpha \in (0, \pi)$, the plan view of the result of spectral function $\Phi(\alpha, \zeta)$ with a stigmatic incident Gaussian beam ($\delta_{11} = \delta_{22} = 1, \delta_{12} = \delta_{21} = 0, q(0) = -500i$) impinging upon the half plane at $(x_i = 2, z_i = 0)$ in the direction of $(\theta_i, \pi + \varphi_i) = (\pi / 2, \pi + \pi / 2)$ 111

Figure 5.3 For $\alpha \in (\pi, 2\pi)$, the side view of the result of spectral function $\Phi(\alpha, \zeta)$ with a stigmatic incident Gaussian beam ($\delta_{11} = \delta_{22} = 1$, $\delta_{12} = \delta_{21} = 0$, $q(0) = -500i$) impinging upon the half plane at $(x_i = 2, z_i = 0)$ in the direction of $(\theta_i, \pi + \varphi_i) = (\pi / 2, \pi + \pi / 2)$ 111

Figure 5.4 For $\alpha \in (\pi, 2\pi)$, the plan view of the result of spectral function $\Phi(\alpha, \zeta)$ with a stigmatic incident Gaussian beam ($\delta_{11} = \delta_{22} = 1$, $\delta_{12} = \delta_{21} = 0$, $q(0) = -500i$) impinging upon the half plane at $(x_i = 2, z_i = 0)$ in the direction of $(\theta_i, \pi + \varphi_i) = (\pi / 2, \pi + \pi / 2)$ 112

Figure 5.5 For $\alpha \in (0, 2\pi)$, the side view of the result of spectral function $\Phi(\alpha, \zeta)$ with a stigmatic incident Gaussian beam ($\delta_{11} = \delta_{22} = 1$, $\delta_{12} = \delta_{21} = 0$, $q(0) = -500i$) impinging upon the half plane at $(x_i = 2, z_i = 0)$ in the direction of $(\theta_i, \pi + \varphi_i) = (\pi / 2, \pi + \pi / 2)$ 112

Figure 5.6 For $\alpha \in (0, 2\pi)$, the plan view of the result of spectral function $\Phi(\alpha, \zeta)$ with a stigmatic incident Gaussian beam ($\delta_{11} = \delta_{22} = 1$, $\delta_{12} = \delta_{21} = 0$, $q(0) = -500i$) impinging upon the half plane at $(x_i = 2, z_i = 0)$ in the direction of $(\theta_i, \pi + \varphi_i) = (\pi / 2, \pi + \pi / 2)$ 113
Figure 5.7 For $\alpha \in (0, 2\pi)$, the side view of the result of spectral function $\Phi(\alpha, \zeta)$ with an elliptical astigmatic incident Gaussian beam ($\delta_{12} = \delta_{21} = 0$, $\delta_{11} = 1 / q(0) = 4\delta_{22}$, $q(0) = -500i$) impinging upon the half plane at $(x_i = 2, z_i = 0)$ in the direction of $(\theta_i, \pi + \varphi_i) = (\pi / 4, \pi + \pi / 3)$. 114
Figure 5.8 For $\alpha \in (0, 2\pi)$, the plan view of the result of spectral function $\Phi(\alpha, \zeta)$ with an elliptical astigmatic incident Gaussian beam ($\delta_{12} = \delta_{21} = 0$, $\delta_{11} = 1 / q(0) = 4\delta_{22}$, $q(0) = -500i$) impinging upon the half plane at $(x_i = 2, z_i = 0)$ in the direction of $(\theta_i, \pi + \varphi_i) = (\pi / 4, \pi + \pi / 3)$. 114
Figure 5.9 Physical configuration: A general Gaussian beam, marked by a heavy arrow, impinges on a half-plane (wedge angle $\Psi = 2\pi$ at direction (φ_i, θ_i). It intersects the $y = 0$ plane at an arbitrary point $X_i = (x_i, z_i)$, where x_i can be positive or negative. The beam expansion of the scattered field (dashed arrows) involves a phase-space beam expansion along the edge, and an azimuthal spectrum of beams around the edge. The beams emerge from the points z_m, m = 0, ±1, ... , along the edge with conical angle $\theta_n = \cos^{-1} \zeta_n$, n = 0, ±1, ... , and azimuthal angles α_j , j = 0, 1, ..., reprint from [1].....116
Figure 5.10 The side view of absolute value of $a_{\boldsymbol{\mu}}(\alpha)$ in the (z_m, ζ_n) plane with $\alpha_i = \pi / 2$, $b_z = 12000$ and . It is calculated for a stigmatic incident Gaussian beam ($\delta_{11} = \delta_{22} = 1$, $\delta_{12} = \delta_{21} = 0$, $q(0) = -500i$) impinging upon the half plane at $(x_i = 2, z_i = 0)$ in the direction of $(\theta_i, \pi + \varphi_i) = (\pi / 2, \pi + \pi / 2)$, corresponding to the case of Fig. 5.5 and Fig. 5.6. 120
Figure 5.11 The plan view of absolute value of $a_{\boldsymbol{\mu}}(\alpha)$ in the (z_m, ζ_n) plane with $\alpha_i = \pi / 2$, $b_z = 12000$ and $v = 1 / 4$. It is calculated for a stigmatic incident Gaussian beam ($\delta_{11} = \delta_{22} = 1$, $\delta_{12} = \delta_{21} = 0$, $q(0) = -500i$) impinging upon the half plane at $(x_i = 2, z_i = 0)$ in the direction of $(\theta_i, \pi + \varphi_i) = (\pi / 2, \pi + \pi / 2)$, corresponding to the case of Fig. 5.5 and Fig. 5.6. 121
Figure 5.12 The side view of absolute value of $a_{\boldsymbol{\mu}}(\alpha)$ in the (α_j, ζ_n) plane with $z_m = 0$, $b_z = 12000$ and $v = 1 / 4$. It is calculated for a stigmatic incident Gaussian beam ($\delta_{11} = \delta_{22} = 1$, $\delta_{12} = \delta_{21} = 0$, $q(0) = -500i$) impinging upon the half plane at $(x_i = 2, z_i = 0)$ in the direction of $(\theta_i, \pi + \varphi_i) = (\pi / 2, \pi + \pi / 2)$, corresponding to the case of Fig. 5.5 and Fig. 5.6. 121
Figure 5.13 The plan view of absolute value of $a_{\boldsymbol{\mu}}(\alpha)$ in the (α_j, ζ_n) plane with $z_m = 0$, $b_z = 12000$ and $v = 1 / 4$. It is calculated for a stigmatic incident Gaussian beam ($\delta_{11} = \delta_{22} = 1$, $\delta_{12} = \delta_{21} = 0$, $q(0) = -500i$) impinging upon the half plane at $(x_i = 2, z_i = 0)$ in the direction of $(\theta_i, \pi + \varphi_i) = (\pi / 2, \pi + \pi / 2)$, corresponding to the case of Fig. 5.5 and Fig. 5.6. 122

Figure 5.14 The side view of absolute value of $a_{\boldsymbol{\mu}}(\alpha)$ in the (z_m, ζ_n) plane with $\alpha_j = 2\pi/3$, $b_z = 12000$, and $v = 1/4$. It is calculated for an elliptical astigmatic incident Gaussian beam ($\delta_{12} = \delta_{21} = 0$, $\delta_{11} = 1/q(0) = 4\delta_{22}$, $q(0) = -500i$) impinging upon the half plane at $(x_i = 2, z_i = 0)$ in the direction of $(\theta_i, \pi + \varphi_i) = (\pi/4, \pi + \pi/3)$, corresponding to the case of Fig. 5.7 and Fig. 5.8. 122
Figure 5.15 The plan view of absolute value of $a_{\boldsymbol{\mu}}(\alpha)$ in the (z_m, ζ_n) plane with $\alpha_j = 2\pi/3$, $b_z = 12000$, and $v = 1/4$. It is calculated for an elliptical astigmatic incident Gaussian beam ($\delta_{12} = \delta_{21} = 0$, $\delta_{11} = 1/q(0) = 4\delta_{22}$, $q(0) = -500i$) impinging upon the half plane at $(x_i = 2, z_i = 0)$ in the direction of $(\theta_i, \pi + \varphi_i) = (\pi/4, \pi + \pi/3)$, corresponding to the case of Fig. 5.7 and Fig. 5.8. 123
Figure 5.16 The side view of absolute value of $a_{\boldsymbol{\mu}}(\alpha)$ in the (α_j, ζ_n) plane with $z_m = 0$, $b_z = 12000$, and $v = 1/4$. It is calculated for an elliptical astigmatic incident Gaussian beam ($\delta_{12} = \delta_{21} = 0$, $\delta_{11} = 1/q(0) = 4\delta_{22}$, $q(0) = -500i$) impinging upon the half plane at $(x_i = 2, z_i = 0)$ in the direction of $(\theta_i, \pi + \varphi_i) = (\pi/4, \pi + \pi/3)$, corresponding to the case of Fig. 5.7 and Fig. 5.8. 123
Figure 5.17 The plan view of absolute value of $a_{\boldsymbol{\mu}}(\alpha)$ in the (α_j, ζ_n) plane with $z_m = 0$, $b_z = 12000$, and $v = 1/4$. It is calculated for an elliptical astigmatic incident Gaussian beam ($\delta_{12} = \delta_{21} = 0$, $\delta_{11} = 1/q(0) = 4\delta_{22}$, $q(0) = -500i$) impinging upon the half plane at $(x_i = 2, z_i = 0)$ in the direction of $(\theta_i, \pi + \varphi_i) = (\pi/4, \pi + \pi/3)$, corresponding to the case of Fig. 5.7 and Fig. 5.8. 124
Figure 5.18 The side view of spectral function $\breve{\Phi}(\alpha, \zeta)$ with a stigmatic incident Gaussian beam ($\delta_{12} = \delta_{21} = 0$, $\delta_{11} = \delta_{22} = 1$, $q(0) = -500i$) impinging upon the half plane at $(x_i = 2, z_i = 0)$ in the direction of $(\theta_i, \pi + \varphi_i) = (\pi/3, \pi + \pi/4)$ with $k = 1$. 129
Figure 5.19 The side view of absolute value of $\breve{a}_{\boldsymbol{\mu}}(\alpha)$ in the (z_m, ζ_n) plane with $a_j = 3\pi/4$. It is calculated for a stigmatic incident Gaussian beam ($\delta_{12} = \delta_{21} = 0$, $\delta_{11} = \delta_{22} = 1$, $q(0) = -500i$) impinging upon the half plane at $(x_i = 2, z_i = 0)$ in the direction of $(\theta_i, \pi + \varphi_i) = (\pi/3, \pi + \pi/4)$ with $k = 1$ 130
Figure 5.20 The side view of absolute value of $\breve{a}_{\boldsymbol{\mu}}(\alpha)$ in the (α_j, ζ_n) plane with $z_m = 0$. It is calculated for a stigmatic incident Gaussian beam ($\delta_{12} = \delta_{21} = 0$, $\delta_{11} = \delta_{22} = 1$, $q(0) = -500i$) impinging upon the half plane at $(x_i = 2, z_i = 0)$ in the direction of $(\theta_i, \pi + \varphi_i) = (\pi/3, \pi + \pi/4)$ with $k = 1$ 130
Figure 5.21 The side view of absolute value of the field u with $\rho = 3500$. It is the total field for a stigmatic incident Gaussian beam ($\delta_{12} = \delta_{21} = 0$, $\delta_{11} = \delta_{22} = 1$, $q(0) = -500i$) impinging

upon the half plane at $(x_i = 2, z_i = 0)$ in the direction of $(\theta_i, \pi + \varphi_i) = (\pi/3, \pi + \pi/4)$ with $k = 1$ 131
Figure 5.22 The plan view of absolute value of total field u with $\rho = 3500$. It is the total field for a stigmatic incident Gaussian beam ($\delta_{12} = \delta_{21} = 0$, $\delta_{11} = \delta_{22} = 1$, $q(0) = -500i$) impinging upon the half plane at $(x_i = 2, z_i = 0)$ in the direction of $(\theta_i, \pi + \varphi_i) = (\pi/3, \pi + \pi/4)$ with $k = 1$ 131
Figure 5.23 The basic model of 3D half plane diffraction. A Gaussian beam (the arrow in the figure) impinges on a half plane $(y = 0, x \geq 0)$, in the direction of (φ_i, θ_i) 132
Figure 5.24 The first scenario modelled in GRASP where a circular Gaussian beam ($w_0 = 8\lambda$) impinges on the half plane at $\mathbf{X}_i = (w_0, 0)$ in the direction of $(\varphi_i = \pi + \pi/2, \theta_i = \pi/2)$ 133
Figure 5.25 Comparison of the backward scattered field with PO and Kirchhoff half-screen BDT with the parameters $w_0 = 8\lambda$, $\mathbf{X}_i = (w_0, 0)$ and $(\varphi_i = \pi + \pi/2, \theta_i = \pi/2)$, based on the modelled scenario of Fig. 5.24. 133
Figure 5.26 The model built in GRASP for the second case with a circular Gaussian beam ($w_0 = 8\lambda$) impinges on the half plane at $\mathbf{X}_i = (-w_0, 0)$ in the direction of $(\varphi_i = \pi + \pi/2, \theta_i = \pi/2)$ 134
Figure 5.27 Comparison of the backward scattered field with PO and Kirchhoff half-screen BDT with the parameters $w_0 = 8\lambda$, $\mathbf{X}_i = (-w_0, 0)$ and $(\varphi_i = \pi + \pi/2, \theta_i = \pi/2)$, based on the modelled scenario of Fig. 5.26. 135
Figure 5.28 The model built in GRASP for the third case with a circular Gaussian beam ($w_0 = 8\lambda$) impinges on the half plane at $\mathbf{X}_i = (w_0, 0)$ in the direction of $(\varphi_i = \pi + \pi/4, \theta_i = \pi/2)$ 136
Figure 5.29 Comparison of the backward scattered field with PO and Kirchhoff half-screen BDT with the parameters $w_0 = 8\lambda$, $\mathbf{X}_i = (w_0, 0)$ and $(\varphi_i = \pi + \pi/4, \theta_i = \pi/2)$, based on the model in Fig. 5.28. 136
Figure 5.30 The model built in GRASP for the fourth case with a circular Gaussian beam ($w_0 = 8\lambda$) impinges on the half plane at $\mathbf{X}_i = (w_0, 0)$ in the direction of $(\varphi_i = \pi + \pi/2, \theta_i = \pi/4)$ 137
Figure 5.31 Comparison of the backward scattered field with PO and Kirchhoff half-screen BDT with the parameters $w_0 = 8\lambda$, $\mathbf{X}_i = (w_0, 0)$ and $(\varphi_i = \pi + \pi/2, \theta_i = \pi/4)$ 137
Figure 5.32 The model built in GRASP for the fifth case with a circular Gaussian beam ($w_0 = 8\lambda$) impinges on the half plane at $\mathbf{X}_i = (w_0, 0)$ in the direction of $(\varphi_i = \pi + \pi/4, \theta_i = \pi/4)$ 138
Figure 5.33 Comparison of the backward scattered field with PO and Kirchhoff half-screen BDT with the parameters $w_0 = 8\lambda$, $\mathbf{X}_i = (w_0, 0)$ and $(\varphi_i = \pi + \pi/4, \theta_i = \pi/4)$, for the scenario modelled in Fig. 5.32 139

Figure 5.34 3D GBS simulation analysis result of the backward scattered field of an elliptical, normally-incident GB with waist parameters $\delta_{11} = 4\delta_{22}$, $\delta_{22} = 1$ from a half plane. The intersection point is $\mathbf{X}_i = (w_0, 0)$ 140
Figure 6.1 Interpretation of Gaussian beam expansion used in DGBA. An electromagnetic field on the aperture plane $z = 0$ is expanded into a set of elementary Gaussian beams with Windowed Fourier Transform (WFT) method, with m and μ are indices of spatial-shift at an interval of L_0 ; and, n and v denote the spectral shift at an interval of Ω_0 . Each of the expanded Gaussian beam are propagate along the direction of $\hat{z}_t$, and P is denoted as an observation point.....144
Figure 6.2 Schematic diagram of comparison between the fields with and without expansion. In the lower part of the figure, a Gaussian beam (GB) propagates along $z+$ from beam waist plane z=0 to plane z=0.1. In the upper part, the field produced by the same GB on z=0.05 plane is expanded by Windowed Fourier Transform (WFT) method. The expanded sub GBs also propagates to the z=0.1 plane.....145
Figure 6.3 Comparison of field descriptions in terms of 1) constituent Gaussian beams and 2) with the original Gaussian Beam field expression (blue-line). 146
Figure 6.4 Schematic diagram: A normally incident Gaussian beam impinges on a half-plane with an intersection-point P. Only about 0.006% of the beam power is out of the rim when P is $2w$ away from the edge. 147
Figure 6.5 Geometry of the reflection on an ellipsoidal reflector. A Gaussian beam (GB) is first expanded on the expansion plane, and the produced sub GBs hit a reflector. The reflected field is calculated.....148
Figure 6.6 Geometry of single reflector taken as the portion of the surface from an ellipsoid centred at point P having distance R_1 and R_2 to the foci of the ellipse at F_1 and F_2 respectively. w is the beam width of the incident Gaussian beam and $4w$ is the diameter of the cylinder used to cut the surface.....148
Figure 6.7 Reflected field 0.2m behind the ellipsoidal reflector (co-polar, offside plane), based on the modelled scenario of Fig. 6.5.....149
Figure 6.8 Reflected field 0.2m behind the ellipsoidal reflector (co-polar, symmetric plane), based on the modelled scenario of Fig. 6.5.....150
Figure 6.9 Two incident Gaussian beams with the same incident angle $(\pi/2 - \varphi)$ impinge on the left and right side of a reflector/half-plane at intersection-points P. R denote the nearest points on the rim of the reflector. The local coordinate system $(\hat{x}_s, \hat{y}, \hat{n}_s)$ and reflected beam related coordinate system $(\hat{x}_r, \hat{y}, \hat{z}_r)$ with are constructed with $\hat{s}_i$ is the propagating direction of the incident beam, and $\hat{z}_r$, that of the reflected beam. R' are the symmetric points of R with respect to point P along the line x_s , and $\vec{z}_e$ denotes a vector from rim R to the intersection point P. A and $ZOFFS$ are the projected lengths of $\vec{z}_e$ on the $\hat{x}_r$ and the $\hat{z}_r$. The conclusion is when $A > 0$ and $ZOFFS < 0$, the intersection point P is on the surface of the reflector/half-plane with azimuth angle $0 < \varphi_i < \pi/2$ 152

Figure 6.10 When $A > 0$ and $ZOFFS > 0$, the intersection-point P is on the surface of the reflector/half plane with azimuth angle $\pi/2 < \varphi_i < \pi$. All other annotations are as for Fig. 6.9. 152
Figure 6.11 When $A < 0$ and $ZOFFS > 0$, the intersection-point P is out of the surface of the reflector/half plane with azimuth angle $0 < \varphi_i < \pi/2$. All other annotations are as for Fig. 6.9. 153
Figure 6.12 When $A < 0$ and $ZOFFS < 0$, the intersection-point P is out of the surface of the reflector/half plane with azimuth angle $\pi/2 < \varphi_i < \pi$. All other annotations are as for Fig. 6.9. 153
Figure 6.13 Geometry of a Gaussian beam imping on a reflector in the direction of $\hat{s}_i$ with an incident spherical angle (φ_i, θ_i). The intersection point is P, and the closest point on the rim of the reflector to P is denoted as e'. $\hat{n}_s$ is along the normal direction of the surface of the reflector at intersection point P, and a local coordinate system $(\hat{x}_s, \hat{n}_s, \hat{z}_s)$ is constructed with $\hat{z}_s$ tangent to the rim. The distance between P and e' is $z_{e'}$ Point e is denoted as the projected point of e' on vector $\hat{x}_s$. 154
Figure 6.14 Near field difference between optimised and without optimised 3D-DGBA on the offset plane (co-polar). Parameters of without optimised 3D-DGBA: $-1 \le \zeta \le 1$, $0 \le \alpha \le 2\pi$ and m = 0, ±1, ..., ±8. Parameters of optimised 3D-DGBA: $\max(-1, \zeta_i - 2\sin\theta_0) \le \zeta \le \min(1, \zeta_i + 2\sin\theta_0)$, $0 \le \alpha \le \pi$ and m = 0, ±1. 158
Figure 6.15 Near field difference between optimised and without optimised 3D-DGBA on the symmetric plane (co-polar and cross-polar). Parameters of without optimised 3D-DGBA: $-1 \le \zeta \le 1$, $0 \le \alpha \le 2\pi$ and m = 0, ±1, ..., ±8. Parameters of optimised 3D-DGBA: $\max(-1, \zeta_i - 2\sin\theta_0) \le \zeta \le \min(1, \zeta_i + 2\sin\theta_0)$, $0 \le \alpha \le \pi$ and m = 0, ±1. 158
Figure 6.16 Illustration of a single step of the 3D-DGBA in a multi-reflector analysis: 3D-DGBA applies a WFT on the input field to produce elementary Gaussian beams. Those Gaussian beams subsequently reflected are treated by Phase Matching analysis and so reflected Gaussian beams are produced. Those beams that meet the reflector at less than 3.5 beam widths away from the rim are analysed 3D GBS, producing a set of scattered GBs. The reflected and scattered fields are superposed in the output plane. By repeating these steps, the cascaded reflectors can be analysed, which make 3D-DGBA highly modularised. 160
Figure 6.17 Files relationship in 3D-DGBA. The arrows represent the input and output files to the three "f90" programs. "gaubeam.f90" is the main program of 3D-DGBA. 161
Figure 6.18 Flow chart of 3D-DGBA. Reflected beam analysis and diffracted beam analysis are two of the most important nodes. 162
Figure 7.1 Layout of the dual-path Quasi-Optical Network. The 54 GHz (blue lines) is the transmission path; the 89 GHz (red lines) is the reflection path. H-54 and H-89 are the corrugated horns for 54 GHz path and 89 GHz path respectively; M1-54 and M1-89 are the first ellipsoidal mirrors for 54 GHz path 89 GHz path respectively; M2 is the second ellipsoidal mirror for both paths; D stands for the dichroic. 165
Figure 7.2 Fabricated Quasi-Optical Network according to the schematic of Figure 7.1. Annotation is as for Fig. 7.1 165

Figure 7.3 Quasi-optical network design procedure, reprint from [4] 166
Figure 7.4 Geometry of single reflector taken as the portion of the surface from an ellipsoid centred at point P having distance R1 and R2 to the foci of the ellipse at F1 and F2respectively. The angle between incident and emergent beam is θ. w is the beam width of the incident Gaussian beam and 4w will be the diameter of the cylinder used to cut the surface. 168
Figure 7.5 Gaussian beam transformation by a quasi-optical system. The input Gaussian beam waist is w_{0in} at a distance d_{in} from the input reference plane and the output waist is w_{0out} at a distance d_{out} from the output reference plane. [4].....168
Figure 7.6 Focal length required for modal matching in terms of confocal distance. With a specific value of system magnification M=0.25, 0.5, 1.0, 2.0 and 5.0, the relationship between the input distance d_{in} and the focal length f is shown. For $M>1$, there is a minimum value for d_{in}/z_c, which means the input distance has to be chosen large enough for a specific system magnification $M>1$, [4]. 171
Figure 7.7 Fundamental Mode Gaussian beam and edge taper. If the reflector radius $r_e=2w$, the corresponding $T_e=-34.74dB$ and about 99.97% of the input power is intercepted. 171
Figure 7.8 Illustration of transmission path: an afocal phase-error cancellation mirror train separated by the sum of mirror focal distances. M1 and M2 are reflector mirrors in sequence. w_{0in} is the beam waist of incident Gaussian beam produced by a horn. $w_{0\mathrm{int}er}$ is the beam waist between the two reflectors and w_{0out} is the beam output beam waist of M2. 174
Figure 7.9 The dichroic with rectangular slots and square lattice, (a) Photograph and (b) diagram. The dichroic is a round metal plate (100 mm in diameter) perforated with rectangular shaped holes: being 2.8 mm × 0.2 mm, and the separations between holes being 0.4 mm in horizontal and 2.2 mm in vertical. The thickness of the each plate is 0.2 mm. The separation of the two layers is 1.2 mm. 175
Figure 7.10 A comparison between measured (dotted curves) and simulated (solid curves) transmission and reflection coefficients of the dichroic over a range of frequencies. 176
Figure 7.11 Dual channel QO system: (a) Diagram and (b) photograph.M1–54 stands for the first mirror of 54 GHz channel; M1–89 stands for the first mirror of 89 GHz channel; M2 stands for the second mirror; H-54 stands for the horn of 54 GHz channel; H-89 stands for the horn of 89 GHz channel. The diagram is not to the scale. 177
Figure 7.12 Dual Perforated plate of circular unit cell and equal lateral lattice: (a) Diagram and (b) photograph. The diameter of the unit circular hole is 2.16 mm, the distance between the centres of two neighbouring unit circular hole is 2.46 mm. The thickness is 2.25 mm. 177
Figure 7.13 Comparison of the measured and simulated results of the perforated plate. T denotes the transmission coefficient; R, the reflection coefficient; f1 is the first resonant frequency point. Simulation results are produced by the periodic method of moments. 178
Figure 7.14 The near field distribution of 54GHz M1 in offset plane ($\varphi=0^\circ$). The scan plane is 199.8 mm (~ 36λ) from the optical centre of reflector M1-54. 180
Figure 7.15 The near field distribution of 54GHz M1 in the symmetric plane ($\varphi=90^\circ$). The scan plane is 199.8 mm (~ 36λ) from the optical centre of reflector M1-54. 180
Figure 7.16 The far field distribution of 54 GHz M1 in the offset plane ($\varphi=0^\circ$). 181

Figure 7.17 The far field distribution of 54GHz M1 in symmetric plane ($\varphi = 90^\circ$).....181
Figure 7.18 The near field distribution of M2 at 54 GHz in offset plane ($\varphi = 0^\circ$) without the dichroic present. The scan plane is 184.8 mm (~ 33λ) from the optical centre of reflector M2. 183
Figure 7.19 The near field distribution of M2 at 54 GHz in symmetric plane ($\varphi = 90^\circ$) with the dichroic in place. The scan plane is 184.8 mm (~ 33λ) from the optical centre of reflector M2. 183
Figure 7.20 The near field distribution of M2 at 54GHz in offset plane ($\varphi = 0^\circ$) without the dichroic. The scan plane is 184.8 mm (~ 33λ) from the optical centre of reflector M2. 184
Figure 7.21 The near field distribution of M2 at 54 GHz in symmetric plane ($\varphi = 90^\circ$) with the dichroic in place. The scan plane is 184.8 mm (~ 33λ) from the optical centre of reflector M2. 184
Figure 7.22 The far field distribution of 54 GHz M2 in the offset plane ($\varphi = 0^\circ$) without the dichroic. 185
Figure 7.23 Field difference of far field distributions of 54 GHz M2 in the offset plane ($\varphi = 0^\circ$) without the dichroic. GRASP analysis provides the baseline reference standard.....186
Figure 7.24 The far field distribution of 54 GHz M2 in the offset plane ($\varphi = 0^\circ$) with the dichroic in place.....186
Figure 7.25 The far field distribution of 54 GHz M2 in the symmetric plane ($\varphi = 90^\circ$) without the dichroic. 187
Figure 7.26 Field difference of far field distributions of 54 GHz M2 in the symmetric plane ($\varphi = 90^\circ$) without the dichroic. GRASP analysis provides the baseline reference standard. ...187
Figure 7.27 The far field distribution of 54 GHz M2 in the symmetric plane ($\varphi = 90^\circ$) with the dichroic in place.....188
Figure 7.28 The near field distribution of 89 GHz M1 in the offset plane ($\varphi=0^\circ$). The scan plane is 330 mm (~ 98λ), from the optical centre of reflector M1-89. 188
Figure 7.29 The near field distribution of 89 GHz M1 in the symmetric plane ($\varphi=90^\circ$). The scan plane is 330 mm (~ 98λ) from the optical centre of reflector M1-89. 189
Figure 7.30 The far field distribution of 89 GHz M1 in the offset plane ($\varphi=0^\circ$).....189
Figure 7.31 The far field distribution of 89 GHz M1 in the symmetric plane ($\varphi=90^\circ$).....190
Figure 7.32 The near field distribution of M2 at 89 GHz in the offset plane ($\varphi=0^\circ$) without the dichroic present. The scan plane is 170 mm (~ 50λ) from the optical centre of reflector M2-89. 190
Figure 7.33 The near field distribution of M2 at 89 GHz in the offset plane ($\varphi=0^\circ$) with the dichroic in place. The scan plane is 170 mm (~ 50λ) from the optical centre of reflector M2-89. 191
Figure 7.34 The near field distribution of M2 at 89 GHz in the symmetric plane ($\varphi=90^\circ$) without the dichroic present. The scan plane is 170 mm (~ 50λ) from the optical centre of reflector M2. 191

Figure 7.35 The near field distribution of M2 at 89 GHz in the symmetric plane (φ=90°) with the dichroic in place. The scan plane is 170 mm (~ 50λ) from the optical centre of reflector M2. 192
Figure 7.36 The far field distribution of 89 GHz M2 in the offset plane (φ=0°) without the dichroic 192
Figure 7.37 Field difference of far fields distribution of 89 GHz M2 in the offset plane (φ=0°) without the dichroic. GRASP analysis provides the baseline reference standard.....193
Figure 7.38 The far field distribution of 89 GHz M2 in the offset plane (φ=0°) with the dichroic in place.....193
Figure 7.39 The far field distribution of 89 GHz M2 in the symmetric plane (φ=90°) without the dichroic. 194
Figure 7.40 Field difference of far fields distribution of 89 GHz M2 in the symmetric plane (φ=90°) without the dichroic. GRASP analysis serves as the standard for reference. 194
Figure 7.41 The far field distribution of 89 GHz M2 in the symmetric plane (φ=90°) with the dichroic in place.....195

List of Tables

Table 1.1 Comparisons between GRASP and DGBA 37
Table 1.2 Comparisons between GRASP and DGBA (cont.)..... 38
Table 2.1 Gaussian beam and its fraction of power..... 48
Table 5.1 Expressions and their spectral counterparts in WFT frame expansion 124
Table 6.1 Parameters of the ellipsoidal reflector 149
Table 6.2 Efficiency of 3D DGBA with and without speeding up methods.....158
Table 7.1 Parameters of the ellipsoidal reflectors (mm) 178
Table 7.2 Parameters of the horns.....179

Abbreviations and Glossary

QO	Quasi-optical
QoN	Quasi-optical Network
AMSU-B	Advanced Microwave Sounding Unit-B
NOAA	American National Oceanographic and Atmospheric Administration
SPIRE	Spectral and Photometric Imaging Receiver
PO	Physical Optics
GO	Geometrical Optics
TEM	Transverse Electromagnetic
GTD	Geometrical Theory of Diffraction
UTD	Uniform Theory of Diffraction
PTD	Physical Theory of diffraction
GB	Gaussian beam
GBS	Gaussian beam summation
FD	Frequency domain
TD	Time domain
UWB	Ultra-wide-band
ID-GBs	Iso-diffracting Gaussian beams
DGBA	Diffracted Gaussian Beam Analysis
MoM	Method of Moments
PMM	Periodic Method of Moments
FSS	frequency-selective surface
BDW	boundary diffraction wave
BDT	boundary diffraction wave theory
WFT	Windowed Fourier transform

Symbols and Units

$\boldsymbol{M}$	Magnetisation	A/m
$\boldsymbol{H}$	Magnetic field strength	A/m
$\boldsymbol{B}$	Magnetic flux density	Wb/m^2
μ	Absolute permeability	H/m
μ_0	Permeability of free space	H/m
$\boldsymbol{P}$	Electric polarisation	C/m^2
$\boldsymbol{E}$	Electric field strength	V/m
$\boldsymbol{D}$	Electric flux density	C/m^2
ε	Absolute permittivity	F/m
ε_r	Relative permittivity	
ε_0	Permittivity of free space	F/m
χ	Electric susceptibility	
I	Current	A
t	Time	S
Z	Impedance	Ω
ρ	Mass density	kg/m^3
λ	Wavelength	M
f	Frequency	Hz

Chapter 1 Introduction

1.1 Overview of Quasi-optical techniques

Millimetre wave and sub-millimetre wave systems have found wide applications in remote sensing [1], radio astronomy [2], and air-borne radiometers [3]. In a millimetre wave system, quasi-optical (QO) techniques are frequently used. These systems are consequently referred to as QO systems. A typical QO system consists of beam-forming mirrors, spatial and spectral frequency filters, polarizers, etc.

In the millimetre wave band, waveguide and microstrip-line suffer significant power loss due to their ohmic and/or dielectric losses. A quasi-optical network, however, uses reflectors (or sometimes), lenses, to focus and re-focus diffractive spreading of a beam, and so forming a beam waveguide, operating with considerably reduced losses and superior transmission efficiency. In addition, a QO network has the ability to transport multiple beams at different frequencies and polarisations. Additionally, QO networks have the advantage of being wideband and possessing good resistance to electromagnetic interference. In summary, a QO network has several advantages: (1) low loss; (2) an ability to support multiple beams; (3) wideband operation, and (4), good power handling capacity [4].

QO technology has many attractive properties and has been receiving increasing interest over recent decades and a great number of QO systems have been constructed [5-11]. For instance, in 1996, QMUL developed a QO Network (QoN) for the Advanced Microwave Sounding Unit-B (AMSU-B), as shown in Figure 1.1 [12]. AMSU-B is a millimetre wave radiometer system carried by a NOAA (the American National Oceanographic and Atmospheric Administration) satellite, launched in 1996 into a sun-synchronous polar orbit. The purpose of the AMSU-B instrument was to measure radiation from a number of different layers of the atmosphere in order to obtain global

data on humidity profiles. In AMSU-B, a dual-reflector main-antenna is followed by a QO demultiplexing network. In this QoN, the train of plain and ellipsoidal reflectors steers the signal beams through the demultiplexing dichroic plates DCP1, DCP2, into receiver feed horns H1, H2, H3 covering three bands, H1 for 175-191 GHz, H2 for 148-152 GHz, and H3 for 86-92 GHz.

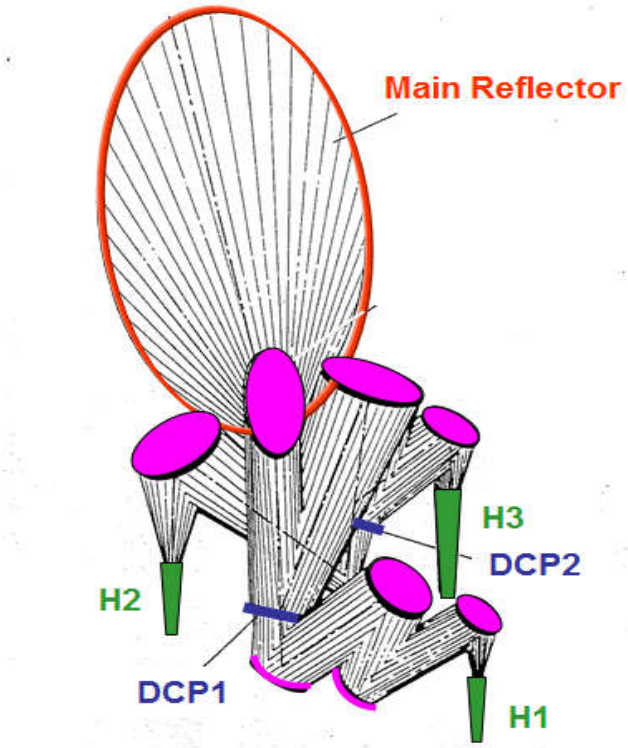

Figure 1.1 A perspective view of the Advanced Microwave Sounding Unit-B (AMSU-B). A dual-reflector main-antenna is followed by a quasi-optical network (QoN). In this QoN, the train of plain and ellipsoidal reflectors steers the signal beams through the demultiplexing dichroic plates DCP1, DCP2, into receiver feedhorns H1, H2, H3 covering three bands: H1 for 175-191 GHz, H2 for 148-152 GHz and H3 for 86-92 GHz. This Figure is reproduced from Martin *et al*, [12].

In 2009, the European Space Agency launched the Herschel and Planck Space Telescopes in the domain of sub-millimetre wave space astronomy [13-16]. The Herschel Space Observatory is a common user facility with a 3.5 m aperture. It adopts a Cassegrain telescope configuration. Herschel performs spot-target observations of astrophysical objects and phenomena in the frequency domain spanning 448 GHz to 5.3 THz. One of the instruments loaded on Herschel is SPIRE, the Spectral and Photometric Imaging Receiver. It is a combined submillimetre wave camera and spectrometer. It comprises a three-band imaging photometer operating at 250, 350 and 500 μm, and an imaging Fourier Transform Spectrometer. Figure 1.2 shows the layout of the

photometer with a QoN of mirrors, dichroics, and detector arrays [15]. It is all-reflective except for the dichroics used to direct the three bands onto the bolometer arrays. Input mirror M3, an offset ellipsoidal mirror, lying below the telescope focus, receives the f/8.7 telescope beam and forms an image at the flat, beam-steering mirror, M4. Toric M5 mirror converts the focal ratio to f/5 and provides an intermediate focus at M6 (toric), which re-images the M4 pupil to a cold stop. Three spherical mirrors, M7 (concave), M8 (convex) and M9 (concave) form a one-to-one optical relay to bring the M6 focal-plane to the detectors. The 1.7K box contains the three detector arrays, covering the short (200-300 μm), medium (300-400 μm) and long (400-670 μm) wavelength bands. The two dichroics direct the same field-of-view onto the arrays so that it can be observed simultaneously in the three bands.

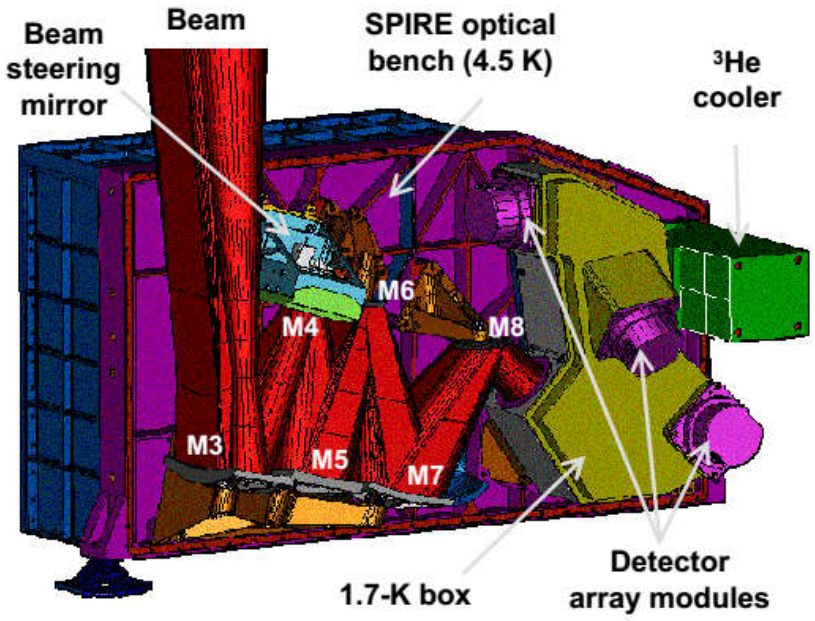

(a) Image of the SPIRE photometer layout, reproduced from Griffin *et al*, [14].

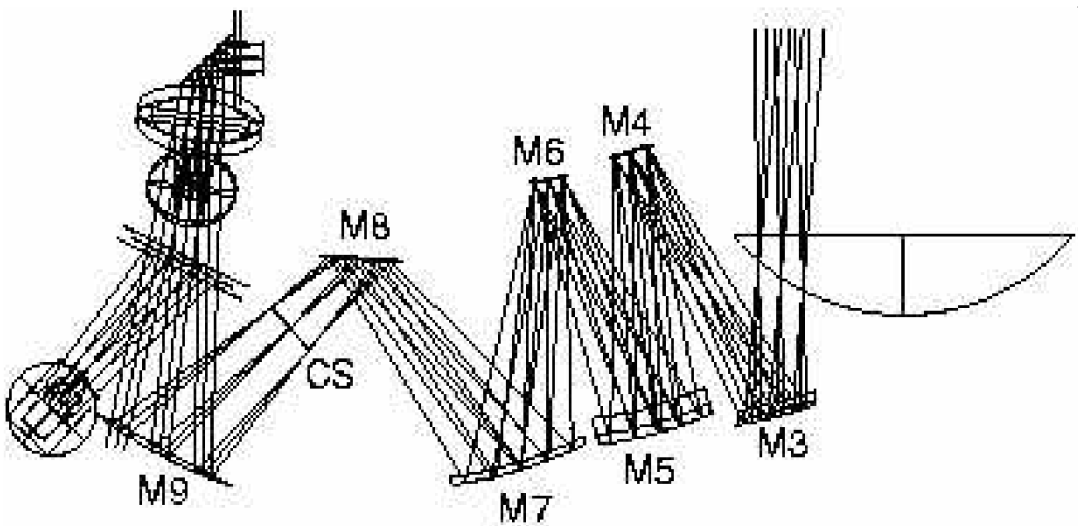

(b) Design graphics of the QoN in SPIRE photometer, reproduced from Dohlen *et al*, [15].

Figure 1.2 Image and design graphics of SPIRE photometer. They depict the quasi-optical network layout. In this QoN, the train of seven ellipsoidal, flat, toric and spherical reflectors (M3-M9) steers the signal beams through the two demultiplexing dichroic plates into three detectors, covering the 200-300 μm, 300-400 μm and 400-670 μm bands.

In these examples, it can be seen that QoNs are used to transfer signals from the reflector antenna to its receivers. Reflection, frequency and spatial-frequency filtering, multiplexing, isolation, calibration and other signal conditioning are conducted in the QoN. The QoN is therefore a major determinant of the system's antenna pattern [17].

1.2 Overview of analysis methods for QoN

With the development of QO technology, efficient analysis methods for QoNs are highly desired. However, in engineering practice, there are only limited methods for the design and optimisation of a QoN. Solving an electromagnetic field over a reflector surface in a QoN is a fundamental requirement, which usually involves accounting for beam diffraction at the edge of the reflector. A full theoretical solution is usually extremely difficult to find and in practice various approximation methods have been developed. In reference [18], different theoretical methods that can be used to analyse diffraction are introduced and compared, as shown in Figure 1.3. The approximation methods for analysing QoNs mainly included Diffraction Integrals, Physical Optics (PO) method, Geometrical Optics (GO), and Modal analysis.

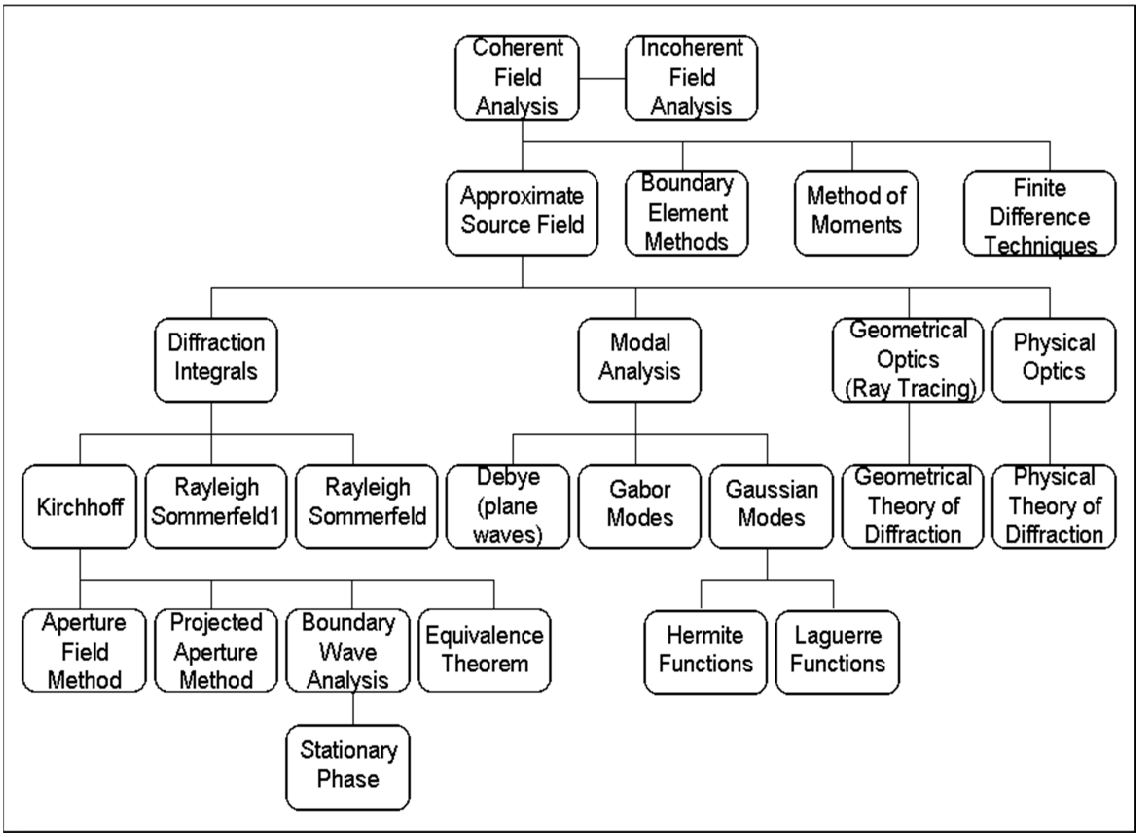

Figure 1.3 Schematic diagram showing the relationship between some diffraction analysis methods, reproduced from O'Sullivan *et al*, [18].

1.2.1 Brief introduction to diffraction integrals

The diffraction problem is the most difficult in QoNs. Huygens–Fresnel principle is the basic method in solving it. It is proposed that every point of a wave-front may be considered as a centre of a secondary source which gives rise to spherical wavelets, and the wave-front at any later instant may be regarded as the envelop of these wavelets [19, 20]. In 1882, the Huygens–Fresnel principle was given a sound mathematical basis by Kirchhoff. He showed that the principle can be expressed in the approximate form of a certain integral theorem, (now called Kirchhoff's integral theorem). As late as 1896, Rayleigh and Sommerfeld gave a rigorous solution of the wave equation, known as Rayleigh-Sommerfield diffraction theory, when either the scalar quantity (Dirichlet solution) or its normal derivative (Neumann solution) is under consideration [18-21]. The boundary diffraction wave (BDW) theory was first proposed by Thomas Young, in which the diffraction field is simply expressed as the superposition of the diffracted boundary wave and the incident wave [22, 23]. In 1981, Takashi Takensaka published

an asymptotic method of BDW for a 3D Gaussian beam incident upon a Kirchhoff half-screen, by introducing the geometrical theory of diffraction (GTD) [24]. More details on this method will be given in Chapter 4.

1.2.2 Brief introduction to geometrical optics

Geometrical optics (GO), or ray optics, describes wave propagation in terms of rays. The ray in geometric optics is an abstraction, or instrument, useful in approximating the paths along which a wave propagates in certain circumstances [25, 26]. The basic postulates of GO are:

- Wave-fronts are locally plane and waves are TEM
- Wave direction is specified by the normal to the equiphase-planes
- Rays travel in rectilinear paths in a homogeneous medium
- Power in a flux tube is conserved, illuminated in Figure 1.4.
- Polarization is constant along a ray in an isotropic medium
- Reflection and refraction obey their respective Snell's law
- The reflected field is linearly related to the incident field at the reflection point by a reflection coefficient

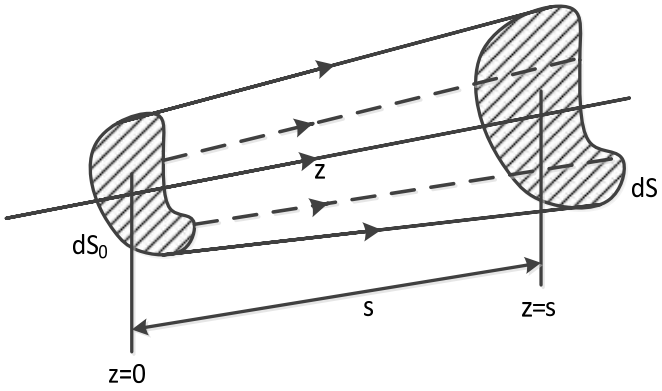

Figure 1.4 An example of flux tube. The sides of such ray tubes are formed by the trajectories of the adjacent rays, the power flow through any cross section of a given ray tube is the same insofar as no power flows across the sides of the tube. In geometrical optics, it gives $|E_0(s)|^2 dS = |E_0(0)|^2 dS_0$, which is a statement of power conservation along the flux tube, [26].

GO has the relative advantage of simplicity and can be used for analysing the propagating incident and emerging beam fields. However, GO does not account for the

effects of edge diffraction. The geometrical theory of diffraction (GTD) is an extension to GO which includes diffraction effects. In GTD the total field at an observation point is decomposed into GO and diffracted components. Two postulates hold in GTD: 1) the diffracted field strength is inversely proportional to the cross-sectional area of the flux tube; 2) the diffracted field is linearly related to the incident field at the diffraction point by a diffraction coefficient. GTD still has the advantage of simplicity but fails at shadow boundaries because field expressions here have singularities [25, 26], shown in Figure 1.5. The Uniform Theory of Diffraction (UTD) resolves such deficiencies in GTD, but cannot be easily employed for multi-reflector systems because of its nature of non-modularity [27-30].

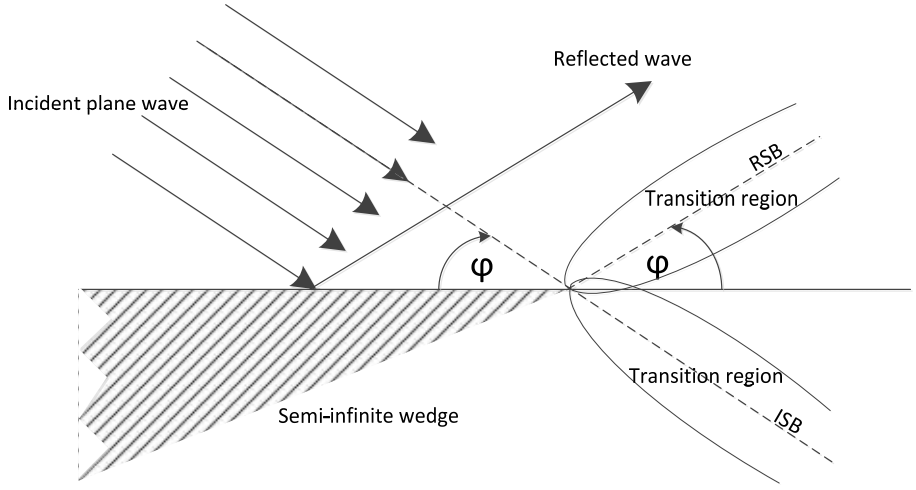

Figure 1.5 An example of shadow boundary in geometrical theory of diffraction (GTD): Plane wave illuminates a semi-infinite wedge. ISB is the shadow boundary of the incident field and RSB is the shadow boundary of the reflected field. GTD is not valid in the transition region.

1.2.3 Brief introduction to physical optics

Physical Optics (PO) is an approximate method for the determination of the field scattered by an object through an assumption about the specific form of the field distribution on the surface. Taking a reflector as an example, the field radiated by the reflector can be calculated by using an approximated surface current distribution determined from the incident magnetic field at each point on the geometrically-illuminated side of the reflector. A basic assumption of the PO method is that the field on the part of the reflector not directly illuminated by the incoming field is zero. The

method is appropriate where the diameter of curvature of the reflector is electrically larger than wavelength, e.g. $D > 20\lambda$ [18, 32]. More details on PO will be given in Chapter 3.

The Physical theory of diffraction (PTD) is an extension to PO to deal with the problem of diffraction. The diffracted-field in PTD is considered as the radiation generated by the scattering sources (currents) induced on the objects. The so-called uniform and non-uniform scattering sources are introduced in PTD. Uniform sources are defined as the sources induced on the infinite plane tangent to the object at a source point. In the case of the incident plane wave, this field is uniformly distributed over the tangent plane, as shown in Figure 1.6 (a). Non-uniform sources are caused by any deviation of the scattering surface from the tangent plane. They are the diffraction part of the surface field, illustrated in Figure 1.6 (b). For large convex objects with sharp edges, the basic contributions to the scattered field are produced by the uniform sources and by those non-uniform sources that concentrate near edges (often called fringe sources) [33, 34].

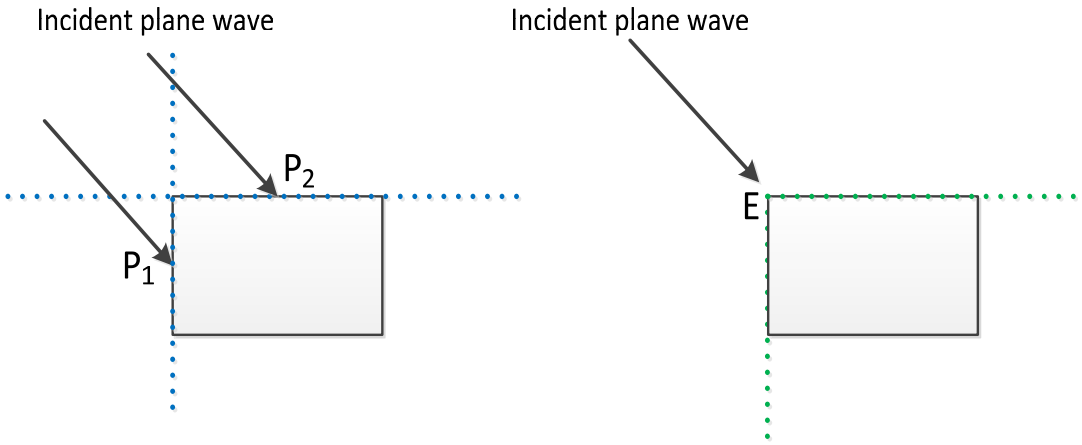

(a) uniform components **(b) non-uniform components**

Figure 1.6 (a) Uniform components of the field at points P_1 and P_2 on the scattering object are those on the infinite tangential planes shown by blue dotted lines. (b) Non-uniform components of the surface field induced by the incident wave near the edge E is asymptotic to those are the tangential wedges with infinite faces shown by green dotted lines.

PO and PTD methods are accurate, but are demanding in terms of computation time and storage for electrically large system. Furthermore, in a QON system with signal pre-conditioning components, such as polarisers and dichroics, these two methods are not suitable due to the prohibitive requirements on computing resources [35].

1.2.4 Overview of Gaussian beam summation method

The Gaussian beam method, particularly, Gaussian beam summation (GBS) is proven to be a successful scheme for analysing complex configurations. This method expands the field into a cluster of collimated beam-propagators that emit from the source. They are then traced and analysed locally in the medium, and their contributions can be summed (i.e. super-posed), at an observation plane.

The Gaussian beam analysis method has been under development for decades and has been more and more widely adopted in wave theories. In 1976, Felsen published his research work on using complex-source-point solutions of field equations to deal with Gaussian beam scattering problems [36]. Three years later, Felsen and colleagues, described shadow boundaries by approximating an exact integral representation for the total field. They then derived the expression of the field-near the shadow-boundary when a Gaussian beam was shadowed by an edge [37]. In 1980, Bastiaans showed how an optical signal can be expanded in Gaussian beams. He expanded a signal into a discrete set of properly shifted and modulated Gaussian elementary signals. Essentially, Bastiaans used the Gabor transform but with a set of functions which are bi-orthonormal to the set of Gaussian elementary signals [38]. In 1982, Červený and his colleagues found an asymptotic procedure to the computation of wave fields in two-dimensional, laterally-inhomogeneous, media. This procedure is based on the simulation of the wave field by Gaussian beams [39].

Methods of Gaussian beam expansion for point source configurations then involved beams that emerge from a source in all directions. In 1982, Popov proposed a Gaussian beam summation method to compute wave fields in the high-frequency approximation [40]. In 1985, Červený discussed numerical modelling of high-frequency seismic wave fields in complex, laterally-varying, layered structures, by expanding the field into dynamic Gaussian beams [41]. In 1986, Norris used Gaussian beam summation methods to derive an exact representation of a complex point-source. The representation can be used to consider the propagation of point disturbances through inhomogeneous media and across interfaces [42]. In 1987, Suedan and Jull described the far-field of a two-dimensional beam resulting from an electric line source at a complex position and found a solution of beam diffraction by a wide slit [43]. In 1989, they showed uniform

and asymptotic solutions of beam diffraction by a half-plane and wedges [44]. It was a development of Felsen's work in 1979. In the same year, Klimes proposed a method of computing seismic wave fields by expansion of Gaussian packets, which is very similar to Gaussian beam expansion [45]. Also in 1989, Heyman introduced a new spectral representation for transient radiation in terms of a continuum of pulsed, beam-fields, emanating radially from a source in all directions, which was the time-domain analogue of the Gaussian beam summation method [46].

From 1990s to the 2000s, the Gaussian beam method had been further developed by introducing new methods for representing distributed (or aperture) sources involving beams emerging from a set of phase-space points and directions in the aperture and the improved representations for point sources. In 1990, Maciel and Felsen published two papers on Gaussian beam analysis of propagation from an extended, plane-aperture distribution, through plane and curved dielectric layers [47, 48]. In 1991, Burkholder and Pathak proposed an approximate Gaussian beam shooting method to analyse the electromagnetic-coupling into, and scattering by, electrically-large, perfectly-conducting, open-ended, non-uniform waveguide cavities, with slowly varying wall curvature [49]. In the same year, Steinberg, Heyman, and Felsen presented an alternative parameterisation, in a configuration-wave-number phase-space, of the radiation of high-frequency fields from extended, plane-aperture sources based on the Gaussian beam method and Gaussian windows [50]. Also in 1991 Suedan and Jull proposed a method to evaluate the three-dimensional scalar beam (point-source) diffraction by a half-plane which gave numerical evaluation of the diffraction integrals. In their method, the Fresnel integrals with complex arguments are converted to complementary error functions with complex arguments to reduce calculating time [51]. In 1993, Anastassiu and Pathak used superposition of Gaussian beams to express electromagnetic field distributions and gave an analysis of Gaussian beam scattered by a parabolic surface and its edge [52]. In 1994 and 1995, Ianconescu and Heyman published two papers about pulsed beam diffraction by a perfectly conducting wedge [53, 54]. In 1998 Goldsmith published a book about Gaussian beam QoNs' design and applications, where the fundamental Gaussian mode was widely used. [4]

From 1997 to 2004, Chou and his colleagues published three important papers. These papers proposed some fast and novel Gaussian beam methods to analyse shaped,

electrically-large reflector antennas. In the paper published in 1997, they presented a closed-form solution for the reflection and diffraction of a Gaussian beam, impinging on an electrically-large, smooth, slowly-varying curved and perfectly-conducting reflector. This closed-form solution is obtained via an asymptotic evaluation of the radiation integral for the fields scattered from the reflector with the physical optics approximations [55-57].

In recent years, Heyman and his colleagues continued their work on the Gaussian beam method and published many interesting papers. In 2001, Heyman and Felsen presented the result for their examination of the Gaussian beam concept from a broad perspective in the frequency domain (FD) and the short-pulse time domain (TD) and within, as well as arbitrarily beyond, the paraxial constraint [58]. In 2004, Shlivinski and Heyman proposed a method for the ultrawide-band (UWB) beam summation representation. Windowed Fourier transform (WFT) frames and iso-diffracting Gaussian beams (ID-GBs) are respectively used to construct the beam-lattice and make the results frequency-independent [59]. In 2005, Gordon and Heyman published two papers introducing a Gaussian beam summation (GBS) representation for scattering by rough surfaces [60, 61]. From 2007 to 2008, Katsav and Heyman published five papers to explain their new achievements. It concerned a 2D formulation, and a full 3D formulation of Gaussian beam summation for half-plan diffraction [62-66]. The details of their work will be presented in Chapter 4 and 5.

1.3 Introduction of QoN analysis software

Currently, the most popular simulation software for analysing QoNs is GRASP, originally based on PO, was, and continues to be developed, by the Danish Company, TICRA. The latest version, V10, can calculate the electromagnetic radiation from QoNs consisting of multiple reflectors with several feeds and feed arrays, and even the interaction between antenna systems. It not only accommodates all the standard geometrical surfaces, but also user-defined shapes, which means that it can handle all asymmetrical and numerically-defined reflectors. It can also simulate the scattering effects from supporting struts. [65]

In fact, GRASP has more algorithms other than PO. With the evolution of the GRASP, quite a few functionalities and numerical methods were added. GTD, multi-GTD, Method of Moments (MoM), and PDT have been employed in the latest version. Simultaneously, acceleration mechanisms such as making the best use of the hardware and parallel algorithms are also utilised to reduce the calculation time. The details of all these add-on functionalities and improvements can be found in Technical description of GRASP10.3 [65].

In the 1990s，a faster method in comparison with PO, namely diffracted Gaussian beam analysis (DGBA) was proposed at Queen Mary, University of London [33]. It is based on the Gaussian beam method and has been verified as fast, efficient and accurate analysis software for electrically-large, QO systems. Some attributes of the DGBA are summarised as follows:

1) Computational Efficiency

When running DGBA, the input field is expanded into a series of Gaussian beams. The computation time of DGBA comes primarily from the Gaussian beam expansion. The emerging Gaussian beam field has a size comparable to that of mirrors it illuminates. The computation time is consequently of the same order as for the current integral, which is the major computation in PO. So, for electrically intermediate-sized QoNs, DGBA gives no advantage in terms of computation time. But for electrically-large systems, the computational time of DGBA sharply drops.

2) Approximation Method

All the incident Gaussian beams are classified into two groups: reflected beams and diffracted beams. Those beams that intersect the reflector at less than two beam-widths away from the rim are reflected beams. This is a good approximation for an electrically-large reflector. However, the computationally accuracy will be degraded if the size of the reflector is reduced.

3) Modularity

The field over the output plane consists of the diffracted field and the reflected field. The output plane serves as the input plane for the treatment of the next reflector. This gives DGBA a high degree of modularity. The modularity of DGBA enables it to

interface easily with other numerical methods such as the Periodic Method of Moments (PMM).

It is worth of comparing DGBA with the latest version of GRASP, as shown in Table 1.1 and Table 1.2. This comparison can give us a better understanding of where DGBA stands and what improvements are needed.

Table 1.1 Comparisons between GRASP and DGBA

Tools / Items	DGBA	GRASP	Comments
Computation Time	-For electrically large systems (+) -For medium-sized systems (Still good but no advantage)	-For electrically large System (-) -For medium-sized system (Time greatly reduced)	1. For electrically medium-sized (10λ-20λ) system, DGBA has the computation time of the same order of GRASP. 2. The computation time is reduced by an acceleration mechanism employed in the current version of GRASP.
Accuracy	-For medium-sized systems (good in the main-beam) -For electrically large systems (good accuracy) -For electrically small systems (bad). (+)	-For medium-sized system (good, but accuracy decreases with reduced size); -For electrically large system (+) accuracy. -For electrically small systems (bad). (+)(+)	1. The accuracy of DGBA is good for electrically large systems, and decreases with decreasing size. 2. The accuracy of GRASP will also decrease if the system-size decreases. However, GRASP has an add-on functionality of MoM to calculate small-sized components. PO is not suggested for these electrically small-sized components.
Modelling of signal conditioning components in QoN	(+)	(-)	1. The modelling of a signal conditioning component is greatly time-consuming in GRASP. And it is not intuitive. 2. DGBA gives an easier way than that of GRASP.
Modularity	(++)	(+)	1. The latest version of GRASP has a tool called “Frame Design” for better modularity, but sometimes is not easy to operate. 2. The modularity of DGBA is excellent.
Interfaces	-Current version operative only for selected frequency-selective surface (FSSs) (-) -Easy to use (+)	-A lot of interfaces for all kinds of components and other numerical methods (+) -Easy to use (-)	1. GRASP has a lot of interfaces but is not so easy to use. 2. More interfaces are under development in DGBA.

Table 1.2 Comparisons between GRASP and DGBA (cont.)

Items \ Tools	DGBA	GRASP	Comments
Applicable system/phase	-Current version only for symmetrical structures (-) -At least medium-sized systems (we suggest > 10λ)(-) -Potentially all-phase (+)	-For any kind of structures (+) - > 20λ best for PO -< 1λ not recommended to use PO. MoM better instead. - all-phase (+)	1. Current version of DGBA is only for symmetrical 2D QoN, extension is anticipated. And the 3D DGBA will be capable of analysing asymmetrical QoN systems. 2. GRASP employs MoM or other methods for those structures where PO fails.
Feed types	Only Gaussian beam mode horns for current version (-) Only Circular beamwaist 'footprint' for incident GB (-)	Any feeds used in reflector antenna systems (+) Elliptical GB (+)	1. DGBA is based on a symmetrical structure and a symmetrical feed.
Adaptability for more complicated structures	Current version (-)	asymmetric and numerically defined reflectors, supporting struts (+)	1. GRASP is suitable for more complicated structures; A model for more complex structures may be difficult.
For Numerical defined reflector	Capable (+)	Capable (+)	
Improvements-including other algorithms	- Not difficult to work with other numerical methods (+) - interfaces with other algorithms (+)	PO+PTD+GO+GTD+MoM+ Ray-optical methods	1. The task for compound-numerical methods is not difficult in DGBA;

1.4 Research motivation

There are several limitations with the current version of DGBA, which is only valid under certain approximations, including:

1) All the incident Gaussian beams for reflection and diffraction analysis have to be circular;

2) When dealing with diffraction, the reflected elliptical Gaussian beams have to be approximated as circular;
3) In diffraction analysis, all the incident beams have to be approximated normal to the half-screen.

Therefore, this version of DGBA is referred to as "two dimensional DGBA (2D-DGBA)". It is desirable to improve the applicability of DGBA.

To this end, there is need to develop a 3D treatment of diffraction in the pursuit of DGBA. The aim of this thesis is to develop a 3D Gaussian Beam (GB) diffraction analysis approach for the study of electrically-large reflector antenna systems.

This thesis proposes a 3D-DGBA scheme consisting of the following stages: (1) beam expansion; (2) beam reflection treated in a GO manner suitable for general astigmatic GBs; (3) beam diffraction treated with a 3D DGBA; (4) beam superposition of all reflected and diffracted GBs.

In addition, the thesis includes relevant QoN design techniques and experimental verification of the proposed 3D-DGBA method.

1.5 Summary and thesis outlines

This thesis develops a 3D-DGBA method for multi-reflector antenna analysis. The test benches of QoNs are designed, fabricated and measured to verify the 3D-DGBA tool.

An introduction to QO techniques is given in Chapter 1.Pertinent diffraction integrals, GO, PO, GBS and DGBA methods are also briefly discussed. The QoN design software, GRASP, is compared with 2D DGBA.

Chapter 2 prepares formulation of circular Gaussian beams and elliptical astigmatic Gaussian beams including their spectral representation.

Chapter 3 studies Gaussian beam reflection analysis methods. PO, GO and phase-matching reflection methods are investigated and compared. Extended phase-matching expressions are developed to examine the canonical problem where the incident beam is not coincident with one of the two principal directions of the surface.

In Chapter 4, two kinds of 2D Gaussian beam half-plane diffraction theory are treated; canonical Gaussian beam (Kirchhoff) boundary diffraction wave (BDW) theory and, 2D Gaussian beam summation (GBS). Limitations and approximations of BDW theory used in 2D-DGBA are also discussed.

In Chapter 5, the principle of the 3D GBS half plane diffraction method is presented. Numerical verification is then undertaken to compare the 3D method with PO and also the BDW method used in 2D-DGBA.

In Chapter 6, a 3D Gaussian Beam (GB) diffraction approach for reflector analysis is developed. In this method, the reflected beams are treated in an extended Phase Matching manner and the diffracted beams are treated with the 3D Gaussian beam diffraction method. Ways to incorporate reflection and diffraction (such as model adaption and acceleration methods) are also presented and discussed.

In Chapter 7, a specific design procedure of a dual-path QoN is presented. Two different kinds of QoN are designed and manufactured. 3D-DGBA is utilised to analyse one of these QoNs and compared to GRASP, 2D-DGBA and measured results.

Finally, a conclusion of the overall research is performed and avenues for future work are presented in Chapter 8.

References

[1] Vasić, Vladimir, et al. "An airborne radiometer for stratospheric water vapor measurements at 183 GHz. [J]" Geoscience and Remote Sensing, IEEE Transactions on 43.7 (2005): 1563-1570.

[2] Blundell, Raymond, and Cheuk-yu Edward Tong. "Submillimeter receivers for radio astronomy. [J]" Proceedings of the IEEE 80.11 (1992): 1702-1720.

[3] Hewison, Tim J., and Stephen J. English. "Airborne retrievals of snow and ice surface emissivity at millimeter wavelengths. [J]" Geoscience and Remote Sensing, IEEE Transactions on 37.4 (1999): 1871-1879.

[4] Goldsmith, Paul F., "Quasioptical systems: Gaussian beam quasioptical propagation and applications [M].” Institute of Electrical and Electronics Engineers, and Microwave Theory and Techniques Society. New York: IEEE press, 1998.

[5] Jones, Douglas Emron., "The Mariner II Microwave Radiometer Experiment [J] ". NATIONAL AERONAUTICS AND SPACE ADMINISTRATION. Technical Report No. 32-722 (1996).

[6] Goodwin, F. E., M. S. Hersman, and J. C. Shiue. "A Four Band Millimeter Wave Radiometer Design for Atmospheric Remote Sensing. [C]" In 1978 IEEE-MTT-S International Microwave Symposium Digest, pp. 245-247. 1978.
[7] Moore, E. L. "A 10-183 GHz common aperture antenna with a quasioptical frequency multiplexer. [C]" In Combined Optical-Microwave Earth and Atmosphere Sensing, 1995. Conference Proceedings, Second Topical Symposium on, pp. 220-222. IEEE, 1995.
[8] Hewison, Timothy J., and Roger Saunders. "Measurements of the AMSU-B antenna pattern." IEEE Transactions on Geoscience and Remote Sensing, vol 34, no. 2 (1996): 405-412.
[9] Mo, Tsan. "Prelaunch calibration of the advanced microwave sounding unit-A for NOAA-K. [J]" Microwave Theory and Techniques, IEEE Transactions on 44, no. 8 (1996): 1460-1469.
[10] Foster, P. R., Peter AR Ade, R. Donnan, J. Dupuy, and J. McNiff. "Validation of Design Techniques on a Quasi-Optics Test Bench. [J]" International Journal of Infrared and Millimeter Waves 28, no. 7 (2007): 521-529.
[11] Oldfield, Matthew, Brian P. Moyna, Elie Allouis, Robert Brunt, Ugo Cortesi, Brian N. Ellison, John Eskell et al. "MARSCHALS: Development of an airborne millimeter-wave limb sounder.[C]" In International Symposium on Remote Sensing, pp. 221-228. International Society for Optics and Photonics, 2001.
[12] Martin, R. J., and D. H. Martin. "Quasi-optical antennas for radiometric remote-sensing. [J]" Electronics & communication engineering journal 8, no. 1 (1996): 37-48.
[13] Dominic Doyle, Go ¨ran Pilbratt, and Jan Tauber. “The Herschel and Planck Space Telescopes [J].” Vol. 97, No. 8, August 2009 | Proceedings of the IEEE 1403
[14] Griffin M, Abergel A, Ade P, et al. “Herschel-SPIRE: design, performance, and scientific capabilities [J].” Proc Spie, 2006, 6265:62650A-62650A-12.
[15] Dohlen K, Origne A, Pouliquen D, et al. “Optical design of the SPIRE instrument for FIRST [C].” Astronomical Telescopes and Instrumentation. International Society for Optics and Photonics, 2000:119-128.
[16] Griffin M J, Abergel A, Abreu A, et al. “The Herschel-SPIRE instrument and its in-flight performance [J].” Astronomy & Astrophysics, 2010, 518: L3.
[17] Donnan R S, Martin D H, Wylde R J, et al. Aberration-free quasi-optical systems. [C] Twelfth International Conference on Antennas and Propagation (ICAP 2003), 2003 p. 546 – 549
[18] O'Sullivan C, Atad-Ettedgui E, Duncan W, et al. “Far-Infrared Optics Design & Verification [J].” International Journal of Infrared & Millimeter Waves, 2002, 23(7):1029-1045.
[19] Born M. E. Wolf. “Principles of optics [J].” Pergamon Press, 1980, 6: 188-189.
[20] Born M, Wolf E. “Principles of optics: electromagnetic theory of propagation, interference and diffraction of light [M].” Cambridge university press, 1999.
[21] Heurtley J C. “Scalar Rayleigh-Sommerfeld and Kirchhoff diffraction integrals: A comparison of exact evaluations for axial points [J].” Journal of the Optical Society of America (1917-1983), 1973, 63(8):1003-1008.
[22] Miyamoto, Kenro, and Emil Wolf. "Generalization of the Maggi-Rubinowicz theory of the boundary diffraction wave—Part I." JOSA 52.6 (1962): 615-622.
[23] Miyamoto, Kenro, and Emil Wolf. "Generalization of the Maggi-Rubinowicz theory of the boundary diffraction wave—Part II." JOSA 52.6 (1962): 626-636.

[24] Takenaka, Takashi, and Otozo Fukumitsu. "Asymptotic representation of the boundary-diffraction wave for a three-dimensional Gaussian beam incident upon a Kirchhoff half-screen." JOSA 72.3 (1982): 331-336.
[25] Keller, Joseph B. "Geometrical theory of diffraction. [J]" JOSA 52.2 (1962): 116-130.
[26] Mcnamara D A, Pistorius C W I, Malherbe J A G. “Introduction to the Uniform Geometrical Theory of Diffraction [M].” Artech House, 1994, (1944).
[27] Kouyoumjian R G, Pathak P H. “A uniform geometrical theory of diffraction for an edge in a perfectly conducting surface [J].” Proceedings of the IEEE, 1974, 62(11): 1448-1461.
[28] Lee S W, Deschamps G A. “A uniform asymptotic theory of electromagnetic diffraction by a curved wedge [J].” Antennas and Propagation, IEEE Transactions on, 1976, 24(1): 25-34.
[29] Ahluwalia D S, Lewis R M, Boersma J. “Uniform asymptotic theory of diffraction by a plane screen [J].” SIAM Journal on applied mathematics, 1968, 16(4): 783-807.
[30] Ludwig D. “Uniform asymptotic expansions at a caustic [J].” Communications on Pure and Applied Mathematics, 1966, 19(2): 215-250.
[31] Pelosi, Giuseppe, Yahya Rahmat-Samii, and John L. Volakis. "High-Frequency Techniques in Diffraction Theory: 50 Years of Achievements in GTD, PTD, and Related Approaches (Second Part)." Antennas and Propagation Magazine, IEEE 55.4 (2013): 17-19.
[32] Bowman J J, Senior T B, Uslenghi P L. “Electromagnetic and acoustic scattering by simple shapes[R].” MICHIGAN UNIV ANN ARBOR RADIATION LAB, 1970.
[33] Ufimtsev P Y. “Method of edge waves in the physical theory of diffraction[R].” FOREIGN TECHNOLOGY DIV WRIGHT-PATTERSONAFB OH, 1971.
[34] Ufimtsev P Y.” Fundamentals of the physical theory of diffraction [M].” John Wiley & Sons, 2007.
[35] C. Rieckmann, M. R. Rayner, C. G. Parini, D. H.Martin and R.S.Donnan, “Novel modular approach based on Gaussian beam diffraction for analyzing quasi-optical multi-reflector antennas”, IEE Proc.-Microw. Antennas Propag. 149, No. 3, June 2002.
[36] L. B. Felsen, “Complex-source-point solutions of the field Equations and their relation to the propagation and scattering of Gaussian beams,” in Symposia Matematica, Istituto Nazionale di Alta Matematica, London, 1976, vol. XVIII, pp. 40-56, Academic Press.
[37] A. Green, H. Bertoni, and L. Felsen, “Properties of the shadow cast by a half-screen when illuminated by a Gaussian beam,” J. Opt. Soc. Am., vol. 69, pp. 1503-1508, 1979.
[38] M. J. Bastiaans, “The expansion of an optical signal into a discrete set of Gaussian beams,” Optik, vol. 57, pp. 95-102, 1980.
[39] V. Červený, M. M. Popov, I. Pšenčík, “Computation of wave fields in inhomogeneous media — Gaussian beam approach,” Geophysical Journal of the Royal Astronomical Society Vol. 70, Issue 1, pp. 109–128, 1982
[40] M. Popov, “A new method of computation of wave fields using Gaussian beams,” Wave Motion, vol. 4, pp. 85-97, 1982.
[41] V. Červený, “Gaussian beam synthetic seismogram,” J. Geophys., vol.58, pp. 44-72, 1985.

[42] A. N. Norris, "Complex point-source representation of real sources and the Gaussian beam summation method," J. Opt. Soc. Am. A, vol. 3, pp.2005-2010, 1986.
[43] G. A. Suedan and E. V. Jull, "Two-dimensional beam diffraction by a half-plane and wide slit," IEEE Trans. Antennas Propagat., vol. 35, pp.1077-1083, 1987.
[44] G. Suedan and E. Jull, "Beam Diffraction by a half-plane and wedges: Uniform and asymptotic solutions," J. Electromagnetic Waves Applicat., vol. 3, pp. 17-26, 1989.
[45] L. Klimes, "Gaussian packets in the computation of seismic wavefields," Geophys. J. Int., vol. 99, pp. 421-433, 1989.
[46] E. Heyman, "Complex source pulsed beam expansion of transient radiation," Wave Motion, vol. 11, pp. 337-349, 1989.
[47] J.J.Maciel, L.B.Felsen, "Gaussian beam analysis of propagation from an extended plane aperture distribution through dielectric layers. I. Plane layer," IEEE Trans. Antennas Propagat., vol. 38, pp. 1607-1617, Oct. 1990.
[48] J.J.Maciel, L.B.Felsen, "Gaussian beam analysis of propagation from an extended plane aperture distribution through dielectric layers. II. Circular cylindrical layer," IEEE Trans. Antennas Propagat., vol. 38, pp. 1618-1624, Oct. 1990.
[49] R. J. Burkholder and P. H. Pathak, "Analysis of EM penetration into and scattering by electrically large open waveguide cavities using Gaussian beam shooting," Proc. IEEE, vol. 79, pp. 1401-1412, Oct. 1991.
[50] B. Z. Steinberg, E. Heyman, and L. B. Felsen, "Phase-space beam summation for time-harmonic radiation from large apertures," J. Opt. Soc. Am. A, vol. 8, pp. 41-59, 1991.
[51] G. A. Suedan and E. V. Jull, "3-dimensional scalar beam diffraction by a half plane," Comput. Phys. Commun., vol. 68, pp. 346-352, 1991.
[52] H. T. Anastassiu and P. H. Pathak, "High frequency analysis of Gaussian beam scattering by a parabolic surface containing an edge," Antennas and Propagation Society International Symposium, vol. 3, pp. 1718-1721, 1993.
[53] R. Ianconescu and E. Heyman, "Pulsed beam diffraction by a perfectly conducting wedge. Part I: Exact solution," IEEE Trans. Antennas Propag., vol. 42, pp. 1377-1385, 1994.
[54] R. Ianconescu and E. Heyman, "Pulsed beam diffraction by a perfectly conducting wedge. Part II: Local scattering models," IEEE Trans. Antennas Propag., vol. 43, pp. 519-528, 1995.
[55] H.-T. Chou and P. H. Pathak, "Uniform asymptotic solution for electromagnetic reflection and diffraction of an arbitrary Gaussian beam by a smooth surface with an edge," Radio Sci., vol. 32, pp. 1319-1336, 1997.
[56] H.-T. Chou, P. H. Pathak, and R. J. Burkholder, "Novel Gaussian beam method for the rapid analysis of large reflector antennas," IEEE Trans. Antennas Propag., vol. 49, pp. 880-893, 2001.
[57] H.-T. Chou and P. H. Pathak, "Fast Gaussian beam based synthesis of shaped reflector antennas for contoured beam applications," IEE Proc. Microw. Antennas Propag. vol. 151, pp. 13-20, 2004.
[58] E. Heyman and L. B. Felsen, "Gaussian beam and pulsed beam dynamics: Complex source and spectrum formulations within and beyond paraxial asymptotics," J. Opt. Soc. Am. A, vol. 18, pp. 1588-1610, 2001.

[59] A. Shlivinski, E. Heyman, A. Boag, and C. Letrou, "A phase-space beam summation formulation for ultra wideband radiation," IEEE Trans. Antennas Propag., vol. 52, pp. 2042-2056, 2004.
[60] G. Gordon, E. Heyman, and R. Mazar, "A phase-space Gaussian beam summation representation of rough surface scattering," J. Acoust. Soc. Am., vol. 117, pp. 1911-1921, 2005.
[61] G. Gordon, E. Heyman, and R. Mazar, "Phase space beam summation analysis of rough surface waveguide," J. Acoustical Soc. Am., vol. 117, pp. 1922-1932, 2005.
[62] M. Katsav and E. Heyman, "Phase space beam summation analysis of half plane diffraction," IEEE Trans. Antennas Propag., vol. 55, pp. 1535-1545, 2007.
[63] Katsav M, Heyman E. "Gaussian Beam Summation Representation of a Two-Dimensional Gaussian Beam Diffraction by a Half Plane [J]". Antennas & Propagation IEEE Transactions on, 2007, 55(8):2247-2257.
[64] M. Katsav, "Gaussian beam expansion representation of edge diffracted fields," Ph.D. dissertation, Tel Aviv Univ., Tel Aviv, Israel, May 2008.
[65] M. Katsav and E. Heyman, "A beam summation representation for 3D radiation from a line source distribution," IEEE Trans. Antennas Propag., vol. 56, pp. 601-605, 2008.
[66] Katsav M, Heyman E. Gaussian beams summation representation of half plane diffraction: A full 3-D formulation [J]. Antennas and Propagation, IEEE Transactions on, 2009, 57(4): 1081-1094.
[67] C. Rieckmann, M. R. Rayner, C. G. Parini,"Diffracted Gaussian beam analysis of quasi-optical multi-reflector systems",IEE-ELECTRONICS LETTERS.,vol. 36, No.19, pp 1600-1601,2000.
[68] C. Rieckmann, "SOFTWARE USER'S MANUAL FOR THE DIFFRACTED GAUSSIAN BEAM ANALYSIS (DGBA) TOOL FOR A SINGLE REFLECTOR" [R], Queen Mary and Westfield College, 1999.
[69] C. Rieckmann, "UPDATE OF THE SOFTWARE USER'S MANUAL FOR THE DIFFRACTED GAUSSIAN BEAM ANALYSIS (DGBA) TOOL" [R], Queen Mary College, University of London, 2007.

Chapter 2 Gaussian Beams and their Propagation

2.1 Overview

The Gaussian beam and its propagation is the foundation of this research project. A circular-spot illumination of a surface by a Gaussian beam has been extensively used in Gaussian beam related analyses. However, an elliptical-spot, astigmatic, Gaussian beam, needs to be considered for the more general cases. This chapter covers: firstly, the derivation of formulas concerning circular case, followed by the elliptical, astigmatic case, including its spectral representation; secondly, interpretations of their propagation; and finally, some numerical examples. It needs to be noted that the formulation of elliptical astigmatic Gaussian beam will be used in later 3D reflection and diffraction investigations.

2.2 The circular Gaussian beam in cylindrical coordinates

The formulation of the circular Gaussian beam is usually described in cylindrical coordinates, due to the fact that its cross-section is circularly-symmetric about the axis of propagation. The formula for the fundamental circular Gaussian beam mode can be derived from the solution of the paraxial wave equation. In a uniform isotropic medium, electromagnetic waves propagate according to the Helmholtz equation [1]

$$(\nabla^2 + k^2)\vec{E} = 0 \tag{2.1}$$

where k is the wavenumber of the medium, i.e.

$$k = \frac{2\pi}{\lambda} \tag{2.2}$$

Assuming the direction of propagation is in the $+z$ direction, the distribution of any component of electric field can be written in cylindrical coordinates with suppressing the time-dependence,

$$E = u(r, \varphi, z) \cdot \exp(-jkz) \tag{2.3}$$

where u is a complex scalar function that defines the non-plane wave part of the beam. Using equation (2.3) in (2.1) yields

$$\nabla^2 u + \frac{\partial^2 u}{\partial z^2} - 2jk\frac{\partial u}{\partial z} = 0\,. \tag{2.4}$$

$\nabla^2 = \frac{\partial^2}{\partial r^2} + \frac{1}{r}\frac{\partial}{\partial r} + \frac{1}{r^2}\frac{\partial^2}{\partial \varphi^2}$. Making a paraxial approximation, i.e. assuming the variation along the direction of propagation of the amplitude is a distance smaller comparable to the wavelength, it is found that $\frac{\partial^2 u}{\partial z^2}$ is negligible compared to $k\frac{\partial u}{\partial z}$. Therefore, the paraxial wave equation can be written as

$$\frac{\partial^2 u}{\partial r^2} + \frac{1}{r}\frac{\partial u}{\partial r} + \frac{1}{r^2}\frac{\partial^2 u}{\partial \varphi^2} - 2jk\frac{\partial u}{\partial z} = 0 \tag{2.5}$$

where, u is independent of φ since circularly symmetry is assumed. The axially-symmetric paraxial wave equation is then

$$\frac{\partial^2 u}{\partial r^2} + \frac{1}{r}\frac{\partial u}{\partial r} - 2jk\frac{\partial u}{\partial z} = 0\,. \tag{2.6}$$

Solving (2.6) by guessing the solution to have a Gaussian distribution, yields

$$u(r, z) = A(z)\exp\left(\frac{-jkr^2}{2q(z)}\right)\,. \tag{2.7}$$

Using (2.7) together with (2.6), gives

$$u(r,z)=\frac{q(0)}{q(z)}\exp\{-jk[\mathrm{z}+\frac{r^2}{2q(z)}]+j\phi_0\} \tag{2.8}$$

where,

$$q(z)=\frac{j\pi w_0^2}{\lambda}+z=[\frac{1}{R}-\frac{j\lambda}{\pi w^2}]^{-1}\ . \tag{2.9}$$

The function $q(z)$ is referred to as the complex beam parameter. Finally, the well-known normalised fundamental Gaussian beam mode for the circular symmetric Gaussian beam (Cylindrical Coordinates) is given by [1]

$$E(r,z)=(\frac{2}{\pi w^2})^{\frac{1}{2}}\exp(\frac{-r^2}{w^2}-jkz-\frac{j\pi r^2}{\lambda R}+j\phi_0)\,. \tag{2.10}$$

Note that throughout the above equations the time-dependence factor e^{jwt} that has been suppressed. In Equation (2.10),

$$R=z+\frac{1}{z}(\frac{\pi w_0^2}{\lambda})^2\ ; \tag{2.11}$$

$$w=w_0[1+(\frac{\lambda z}{\pi w_0^2})^2]^{\frac{1}{2}}\ ; \tag{2.12}$$

$$\text{and}\quad \tan\phi_0=\frac{\lambda z}{\pi w_0^2}\ . \tag{2.13}$$

R is the radius of curvature; w, the beam radius; and ϕ_0, the Gaussian beam phase shift. The beam waist w_0 is defined as the radius where the field amplitude decays to e^{-1} of its on-axis value.

The intensity of the Gaussian beam is

$$I(\mathrm{r})=\left|\hat{u}(\mathbf{r},z)\right|^2=\frac{2}{\pi w^2}\exp(\frac{-2r^2}{w^2})\,. \tag{2.14}$$

The fraction of power subtended within a circle with radius a, centred on the beam axis, is defined by [1]

$$F = \frac{P_a}{P_\infty} = \frac{\int_0^a \int_0^{2\pi} I(r) 2\pi dr d\theta}{\int_0^\infty \int_0^{2\pi} I(r) 2\pi dr d\theta} = 1 - \exp(\frac{-2a^2}{w^2}). \tag{2.15}$$

It is found that more than 99.8% of the energy of a Gaussian beam is contained within the bound $a = 1.5w$. Several typical ratios are shown in Table 2.1.

Table 2.1 Gaussian beam and its fraction of power

Aperture(a)	0.5w	1w	1.5w	2w
F (%)	39.3469	86.4665	98.8891	99.9665

2.3 The elliptical astigmatic Gaussian beam

The formulation of a general astigmatic Gaussian beam in Cartesian coordinates is to be derived in this section. Again, starting from the Helmholtz scalar wave equation

$$(\nabla^2 + k^2) u(x, y, z) = 0 \tag{2.16}$$

where $\nabla^2 = \frac{\partial^2}{\partial x^2} + \frac{\partial^2}{\partial y^2} + \frac{\partial^2}{\partial z^2}$. The Fourier transform pair that satisfies (2.16) is [2]

$$u(x, y, z) = \int_{-\infty}^{\infty} \int_{-\infty}^{\infty} \tilde{u}(k_x, k_y, z) e^{-jk_x x} e^{-jk_y y} dk_x dk_y \tag{2.17}$$

$$\tilde{u}(k_x, k_y, z) = \frac{1}{2\pi} \int_{-\infty}^{\infty} \int_{-\infty}^{\infty} u(x, y, z) e^{jk_x x} e^{jk_y y} dx dy \tag{2.18}$$

Substituting (2.17) to u of (2.16), yields

$$(\frac{d^2}{dz^2} + k_z^2) \tilde{u}(k_x, k_y, z) = 0 \tag{2.19}$$

where $k_z^2 = k^2 - (k_x^2 + k_y^2)$. If $z > 0$, a possible solution under radiation conditions is given by

$$\tilde{u}(k_x, k_y, z) = A(k_x, k_y) \cdot \exp(-jk_z \, z) \tag{2.20}$$

where $\mathrm{Im}\{k_z\} < 0$. Equations (2.20) and (2.17) together are used to find the spectral integral form of the scalar field u, which is presented as a superposition of plane waves with spectral weights $A(k_x, k_y)$

$$u(x, y, z) = \int_{-\infty}^{\infty} \int_{-\infty}^{\infty} A(k_x, k_y) e^{-jk_x x} e^{-jk_y y} e^{-jk_z z} dk_x dk_y \, . \tag{2.21}$$

$$A(k_x, k_y) = \tilde{u}(x, y, z = 0) = \frac{1}{2\pi} \int_{-\infty}^{\infty} \int_{-\infty}^{\infty} u(x, y, z = 0) e^{jk_x x} e^{jk_y y} dxdy \, . \tag{2.22}$$

In the x-y plane, the aperture distribution of a Gaussian beam can be expressed as

$$u(x, y, z = 0) = u_0 \cdot e^{-j\frac{k}{2}\left[\Gamma_{11} x^2 + \Gamma_{22} y^2 + 2\Gamma_{12} xy\right]} \tag{2.23}$$

where $\mathbf{\Gamma} = \begin{bmatrix} \Gamma_{11} & \Gamma_{12} \\ \Gamma_{12} & \Gamma_{22} \end{bmatrix}$ with $\Gamma_{12} = \Gamma_{21}$. $\mathbf{\Gamma}$ is a complex symmetric matrix with Γ_{11} and Γ_{22} are complex in general, but Γ_{12} is real.

Substituting (2.23) into (2.22), the spectral amplitude is

$$A(k_x, k_y) = \frac{u_0}{2\pi} \int_{-\infty}^{\infty} \int_{-\infty}^{\infty} e^{-j\frac{k}{2}\Gamma_{11} x^2 + jk_x x} e^{-j\frac{k}{2}\Gamma_{22} y^2 + jk_y y} e^{-jk\Gamma_{12} xy} dxdy \, . \tag{2.24}$$

Since [2]

$$\int_{-\infty}^{\infty} \int_{-\infty}^{\infty} e^{-a_0 x^2 + b_0 x - a_1 y^2 + b_1 y - 2cxy} dxdy = \frac{\pi}{\sqrt{a_0 a_1 + c^2}} e^{\frac{a_1 b_0^2 + a_0 b_1^2 - 2b_0 b_1 c}{4\left[a_0 a_1 - c^2\right]}} \tag{2.25}$$

$$\text{when } \mathrm{Re}\{a_0, a_1\} > 0$$

the spectral amplitude is simplified to

$$A(k_x, k_y) = \frac{u_0}{jk\sqrt{\Gamma_{11}\Gamma_{22} - \Gamma_{12}^2}} e^{\frac{-j}{2k}\left[\frac{\Gamma_{22} k_x^2 + \Gamma_{11} k_y^2 - 2\Gamma_{12} k_x k_y}{\Gamma_{11}\Gamma_{22} - \Gamma_{12}^2}\right]} . \tag{2.26}$$

Taking $\Lambda_{1,2}$ as the eigenvalues of $\mathbf{\Gamma}$, one has

$$\Lambda_{1,2} = (1/2)\{tr\mathbf{\Gamma} \pm \sqrt{(tr\mathbf{\Gamma})^2 - 4\det(\mathbf{\Gamma})}\} \tag{2.27}$$

$$\delta_{1,2} = 1/\Lambda_{1,2} \tag{2.28}$$

and $A(k_x, k_y)$ can be rewritten as

$$A(k_x, k_y) = \frac{u_0}{jk}\sqrt{\delta_1\delta_2}\, e^{\frac{-j}{2k}\delta_1\delta_2(\Gamma_{22}k_x^2 + \Gamma_{11}k_y^2 - 2\Gamma_{12}k_xk_y)} \quad . \tag{2.29}$$

In the paraxial region, the following approximation holds

$$k_z = \sqrt{k^2 - (k_x^2 + k_y^2)} \approx k - \frac{k_x^2 + k_y^2}{2k} \tag{2.30}$$

and (2.21) can be rewritten as

$$u(x, y, z) \approx e^{-jkz} \int_{-\infty}^{\infty}\int_{-\infty}^{\infty} A(k_x, k_y) e^{-jk_x x} e^{-jk_y y} e^{jz(\frac{k_x^2 + k_y^2}{2k})} dk_x dk_y \tag{2.31}$$

Substituting (2.29) into (2.31), and applying (2.25), the astigmatic Gaussian field is given by

$$u(x, y, z) = u_0\sqrt{\frac{\delta_1\delta_2}{(z+\delta_1)(z+\delta_2)}}\, e^{-jk_z z} \cdot e^{-\frac{j}{2k}\left[\frac{x^2(z+\delta_1\delta_2\Gamma_{11}) + y^2(z+\delta_1\delta_2\Gamma_{22}) + 2xy\delta_1\delta_2\Gamma_{12}}{(z+\delta_1)(z+\delta_2)}\right]} \quad . \tag{2.32}$$

Assuming $\bar{X} = [x, y]^T$, where superscript T means transposition. The phase of Expression (2.32) can be reorganised as

$$S = z + \frac{1}{2}\bar{X}^T \cdot \Gamma(z) \cdot \bar{X} \, . \tag{2.33}$$

The divergence factor can be also written in matrix form, thus

$$\sqrt{\frac{\delta_1\delta_2}{(z+\delta_1)(z+\delta_2)}} = \sqrt{\frac{\det\mathbf{\Gamma}(\sigma)}{\det\mathbf{\Gamma}(0)}} \quad . \tag{2.34}$$

The matrix form of (2.32) is therefore given by

$$u(x,y,z) = u_0 \sqrt{\frac{\det \mathbf{\Gamma}(z)}{\det \mathbf{\Gamma}(0)}} e^{jk[z+\frac{1}{2}\bar{\mathbf{X}}'\mathbf{\Gamma}(z)\bar{\mathbf{X}}]}. \tag{2.35}$$

In cylindrical coordinates, the astigmatic Gaussian beam can be described in general form as [3]

$$B(\mathbf{r}) = A_i \sqrt{\frac{\det \mathbf{\Gamma}(\sigma)}{\det \mathbf{\Gamma}(0)}} e^{jk[\sigma+\frac{1}{2}\boldsymbol{\eta}'\Gamma(\sigma)\boldsymbol{\eta}]}, \operatorname{Im}\sqrt{\det \mathbf{\Gamma}(\sigma)} > 0 \tag{2.36}$$

where $\boldsymbol{\eta}^{\mathbf{t}}$ is the transpose of $\boldsymbol{\eta}$ and $\boldsymbol{\eta} = (\eta_1, \eta_2)$. $\Gamma(\sigma)$ is a 2 by 2 complex symmetric matrix which is determined from its value at $\sigma = 0$, so

$$\mathbf{\Gamma}(\sigma) = [\mathbf{\Gamma}_0^{-1} + \sigma \mathbf{I}]^{-1}, \mathbf{\Gamma}_i = \mathbf{\Gamma}(0) \ . \tag{2.37}$$

$\mathbf{\Gamma}(0)$ is complex symmetric with $\operatorname{Im}\mathbf{\Gamma}(0)$ positive definite. $\operatorname{Im}\mathbf{\Gamma}(0)$ is symmetric for all σ and also positive definite. Under these conditions, the quadratic term in the exponential of the equation $\boldsymbol{\eta}^{\mathbf{t}}\mathbf{\Gamma}\boldsymbol{\eta} = \sum \eta_i \eta_j \Gamma_{ij} = \eta_1^2\Gamma_{11} + 2\eta_1\eta_2\Gamma_{12} + \eta_2^2\Gamma_{22}$ has a positive imaginary part that increases quadratically with distance from the σ axis, thus describing the Gaussian shape of the beam. Here, $\operatorname{Re}(\mathbf{\Gamma})$ is defined as the phase-front-curvature matrix, whereas $\operatorname{Im}(\mathbf{\Gamma})$ controls the beam amplitude. In general, both the wave-front curvature, and the beam amplitude, are astigmatic and their principal axes are not co-aligned. In a special case that matrix $\Gamma(0) = \delta_{ij} / q(0)$, where $\delta_{ij} = 0, i \neq j$ and $\delta_{ii} = 1$, the general beam degenerates into an axially symmetric Gaussian beam [4].

The beam waist w_0 of a circular Gaussian beam is defined as the contour where the field amplitude decays to e^{-1} from its on-axis value. However, beam widths of an astigmatic Gaussian beam are usually described by using two orthogonal beam widths aligned to the two principal axes. The beam widths $W_{1,2}$ are given by [3]

$$W_{i1,2} = 1/\sqrt{k\lambda_{1,2}} \tag{2.38}$$

where $\lambda_{1,2}$ are the eigenvalues of $\operatorname{Im}\mathbf{\Gamma}$. But $W_{i1,2}$ are different for the circular case and are defined as the field amplitudes drop to $e^{-1/2}$ of their axial values.

2.4 Spectral representation of 3D incident Gaussian beams

In reference [3], to Figure 2.1, it is assumed that a general, astigmatic, Gaussian beam, impinges on a perfectly-conducting half-plane in a 3-D coordinate frame supporting $\mathbf{r} = (x, y, z)$.

The beam-axis is, in general, displaced from the edge, intersecting the y = 0 plane at $\mathbf{x}_i = (x_i, z_i)$. The arc length along the beam-axis is denoted by σ where, without loss of generality, we set $\sigma = 0$ at the intersection point $\mathbf{x}_i$. The beam direction $\vec{\sigma}$ is given by [3]

$$\vec{\boldsymbol{\sigma}} = -\bar{\mathbf{x}} \sin\theta_i \cos\varphi_i - \bar{\mathbf{y}} \sin\theta_i \sin\varphi_i + \bar{\mathbf{z}} \cos\theta_i = \bar{\mathbf{x}}\xi_i - \bar{\mathbf{y}}\gamma_i + \bar{\mathbf{z}}\zeta_i \tag{2.39}$$

in which the over-arrows denote unit-vectors. $(\xi_i, \gamma_i, \zeta_i)$ are the wave vectors of the incident beam. Without loss of generality, it is assumed that $\theta_i \in [0, \pi/2]$ and $\varphi_i \in [0, \pi]$, which means $\zeta_i > 0, \gamma_i > 0$.

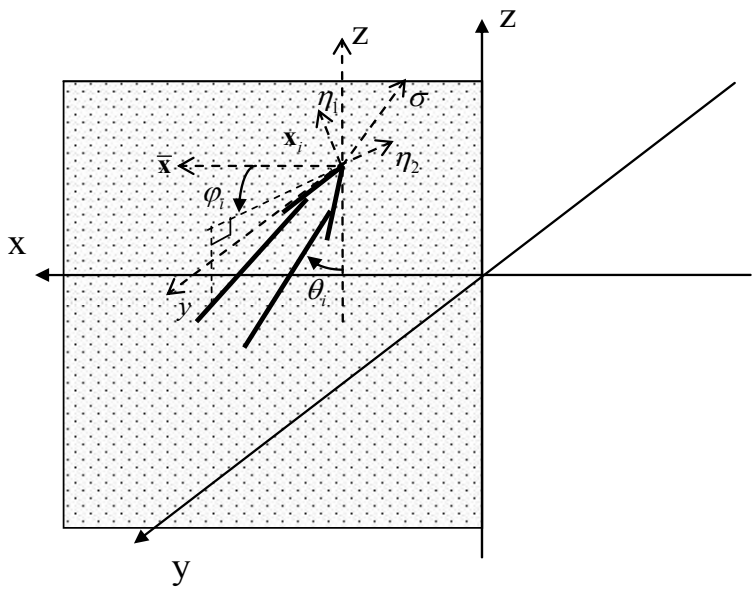

Figure 2.1 A Gaussian beam (the arrow in the figure) impinges on a half plane $(y = 0, x \geq 0)$ at $\mathbf{x}_i = (x_i, z_i)$ in the direction of (φ_i, θ_i). $(\bar{x}, \bar{y}, \bar{z})$ is the original global coordinate. Two beam based coordinate systems are constructed: coordinate $(\vec{\sigma}, \vec{\eta}_1, \vec{\eta}_2)$ with the beam direction $\vec{\sigma}$ and coordinate $(\bar{\bar{\mathbf{x}}}, \bar{y}, \bar{z})$ with $\mathbf{x} = \bar{\mathbf{x}} + \mathbf{x}_i$.

Rather than calculating the Gaussian beam form of equation (2.36), it is simpler to work with the plane wave spectrum in the plane $y = 0$ [3] so that

$$B_i(\mathbf{r}) = (\frac{k}{2\pi})^2 \int_{-\infty}^{\infty} d\zeta \int_{-\infty}^{\infty} d\xi \tilde{B}_i(\boldsymbol{\kappa}) e^{ik(\boldsymbol{\kappa}^T \mathbf{x} - y\gamma)} \text{ and} \tag{2.40}$$

$$\tilde{B}_i(\boldsymbol{\kappa}) = \int_{-\infty}^{\infty} dx \int_{-\infty}^{\infty} dz\, B_i(\mathbf{r})\big|_{y=0}\, e^{-ik\boldsymbol{\kappa}^T \mathbf{x}} , \tag{2.41}$$

where, points in the $y = 0$ plane are denoted as $\mathbf{x} = (x, z)^T$ and also $\boldsymbol{\kappa} = (\xi, \zeta)^T$. The superscript T denotes the transpose of a vector. $\gamma = \sqrt{1 - \boldsymbol{\kappa} \cdot \boldsymbol{\kappa}}$ with $\text{Im}\,\gamma > 0$ being the normalized spectral wavenumber in the $-y$ direction.

To find the explicit expression of $\tilde{B}_i(\boldsymbol{\kappa})$, it is expressed in the $y = 0$ plane in terms of the $\mathbf{x}$ coordinates rather than the $(\sigma, \boldsymbol{\eta})$ coordinates as used in (2.36). Here, a new coordinate system $(\bar{\mathbf{x}}, y)$ is introduced and is centred about the $\mathbf{x}_i$ in the $y = 0$ plane, i.e., $\mathbf{x} = \bar{\mathbf{x}} + \mathbf{x}_i$. Without loss of generality, the transverse coordinate system is chosen to make $\vec{\boldsymbol{\eta}}_1$ lie in the plane-of-incidence ($(\vec{\boldsymbol{\sigma}}, \vec{\mathbf{y}})$, while $\vec{\boldsymbol{\eta}}_2$ is perpendicular to this plane

$$\vec{\boldsymbol{\eta}}_2 = \frac{\vec{\boldsymbol{\sigma}} \times \vec{\mathbf{y}}}{\left|\vec{\boldsymbol{\sigma}} \times \vec{\mathbf{y}}\right|}, \vec{\boldsymbol{\eta}}_1 = \vec{\boldsymbol{\eta}}_2 \times \vec{\boldsymbol{\sigma}} . \tag{2.42}$$

Under these conditions,

$$\vec{\boldsymbol{\sigma}} \times \vec{\mathbf{y}} = (\vec{\mathbf{x}}\xi_i - \vec{\mathbf{y}}\gamma_i + \vec{\mathbf{z}}\zeta_i) \times \vec{\mathbf{y}} = -\zeta_i \vec{\mathbf{x}} + \xi_i \vec{\mathbf{z}} \quad \text{and} \tag{2.43}$$

$$\left|\vec{\boldsymbol{\sigma}} \times \vec{\mathbf{y}}\right| = \left|-\zeta_i \vec{\mathbf{x}} + \xi_i \vec{\mathbf{z}}\right| = \sqrt{\xi_i^2 + \zeta_i^2} = \left|\boldsymbol{\kappa}_i\right| = \kappa_i , \tag{2.44}$$

therefore

$$\vec{\boldsymbol{\eta}}_2 = \frac{\vec{\boldsymbol{\sigma}} \times \vec{\mathbf{y}}}{\left|\vec{\boldsymbol{\sigma}} \times \vec{\mathbf{y}}\right|} = \frac{-\zeta_i \vec{\mathbf{x}} + \xi_i \vec{\mathbf{z}}}{\kappa_i} \quad \text{and} \tag{2.45}$$

$$\vec{\boldsymbol{\eta}}_1 = \vec{\boldsymbol{\eta}}_2 \times \vec{\boldsymbol{\sigma}} = \frac{-\zeta_i \vec{\mathbf{x}} + \xi_i \vec{\mathbf{z}}}{\kappa_i} \times (\vec{\mathbf{x}}\xi_i - \vec{\mathbf{y}}\gamma_i + \vec{\mathbf{z}}\zeta_i) = \frac{\gamma_i \xi_i \vec{\mathbf{x}} + (\xi_i^2 + \zeta_i^2)\vec{\mathbf{y}} + \gamma_i \zeta_i \vec{\mathbf{z}}}{\kappa_i} . \tag{2.46}$$

In the $y = 0$ plane, (2.46) is simplified to

$$\eta_1 = \frac{\gamma_i \xi_i x + \gamma_i \zeta_i z}{\kappa_i}, y = 0 \ . \tag{2.47}$$

Consequently, the relationship between $\boldsymbol{\eta}$ and $\mathbf{r} = (x, y, z)$ is given by,

$$\boldsymbol{\eta} = (\eta_1, \eta_2)^t = \kappa_i^{-1} \begin{pmatrix} \gamma_i \xi_i x + (\xi_i^2 + \zeta_i^2) y + \gamma_i \zeta_i z \\ -\zeta_i z + \xi_i z \end{pmatrix} . \tag{2.48}$$

For simplicity, $\mathbf{T} = \kappa_i^{-1} \begin{pmatrix} \gamma_i \xi_i & \gamma_i \zeta_i \\ -\zeta_i & \xi_i \end{pmatrix}$ and $\mathbf{v} = (\kappa_i, 0)^t$ are defined. Thus, (2.48) becomes $\boldsymbol{\eta} = \mathbf{T}\bar{\mathbf{x}} + \mathbf{v}y$.

From equation (2.39), the relationship between σ and $\mathbf{r} = (x, y, z)$ can be written as,

$$\sigma = x\xi_i - y\gamma_i + z\zeta_i = \xi_i x + \zeta_i z - \gamma_i y = \boldsymbol{\kappa}_i \bar{\mathbf{x}} - \gamma_i y \, . \tag{2.49}$$

To sum up, in the v$(\sigma, \boldsymbol{\eta})$ coordinate system, one has

$$\begin{pmatrix} \boldsymbol{\eta} \\ \sigma \end{pmatrix} = \begin{pmatrix} \mathbf{T} & \mathbf{v} \\ \boldsymbol{\kappa}_\mathbf{i} & -\gamma_i \end{pmatrix} \begin{pmatrix} \bar{\mathbf{x}} \\ y \end{pmatrix} . \tag{2.50}$$

Substituting (2.50) into (2.36), B_i in the $y = 0$ plane can be expressed in terms of the $\bar{\mathbf{x}}$ coordinate.

First, from (2.37), it is seen that $\boldsymbol{\Gamma}(\sigma) = [\boldsymbol{\Gamma}_i^{-1} + \sigma \mathbf{I}]^{-1}$, therefore

$$\boldsymbol{\eta}^t \boldsymbol{\Gamma}(\sigma) \boldsymbol{\eta} = (\mathbf{T}\bar{\mathbf{x}} + \mathbf{v}y)^t [\boldsymbol{\Gamma}_i^{-1} + \sigma \mathbf{I}]^{-1} (\mathbf{T}\bar{\mathbf{x}} + \mathbf{v}y) \ , \tag{2.51}$$

and in the $y = 0$ plane, it simplifies as

$$\boldsymbol{\eta}^t \boldsymbol{\Gamma}(\sigma) \boldsymbol{\eta} \Big|_{y=0} = (\mathbf{T}\bar{\mathbf{x}})^t [\boldsymbol{\Gamma}_i^{-1} + \boldsymbol{\kappa}_i \bar{\mathbf{x}}]^{-1} (\mathbf{T}\bar{\mathbf{x}}) \, . \tag{2.52}$$

For further simplicity, let $\boldsymbol{\eta}^t \boldsymbol{\Gamma}(\sigma) \boldsymbol{\eta} \Big|_{y=0} = \mathbf{F}$. The inverse of the matrix $\mathbf{F}$ is

$$\begin{aligned}\mathbf{F}^{-1} &= ((\mathbf{T}\overline{\mathbf{x}})^t[\boldsymbol{\Gamma}_i^{-1}+\boldsymbol{\kappa}_i\overline{\mathbf{x}}]^{-1}(\mathbf{T}\overline{\mathbf{x}}))^{-1} \\ &= (\mathbf{T}\overline{\mathbf{x}})^{-1}[\boldsymbol{\Gamma}_i^{-1}+\boldsymbol{\kappa}_i\overline{\mathbf{x}}]((\mathbf{T}\overline{\mathbf{x}})^t)^{-1} \\ &= \overline{\mathbf{x}}^{-1}\mathbf{T}^{-1}[\boldsymbol{\Gamma}_i^{-1}+\boldsymbol{\kappa}_i\overline{\mathbf{x}}](\mathbf{T}^t)^{-1}(\overline{\mathbf{x}}^t)^{-1} \\ &= \overline{\mathbf{x}}^{-1}\mathbf{T}^{-1}\boldsymbol{\Gamma}_i^{-1}(\mathbf{T}^t)^{-1}(\overline{\mathbf{x}}^t)^{-1}+\overline{\mathbf{x}}^{-1}\mathbf{T}^{-1}\boldsymbol{\kappa}_i\overline{\mathbf{x}}(\mathbf{T}^t)^{-1}(\overline{\mathbf{x}}^t)^{-1} \\ &\approx \overline{\mathbf{x}}^{-1}\mathbf{T}^{-1}\boldsymbol{\Gamma}_i^{-1}(\mathbf{T}^t)^{-1}(\overline{\mathbf{x}}^t)^{-1}\end{aligned}, \tag{2.53}$$

which means,

$$\mathbf{F} = (\overline{\mathbf{x}}^t)(\mathbf{T}^t)\boldsymbol{\Gamma}_i\mathbf{T}\overline{\mathbf{x}} \ . \tag{2.54}$$

Further, letting $\overline{\boldsymbol{\Gamma}}_i = \mathbf{T}^t\Gamma_i\mathbf{T}$,

$$\boldsymbol{\eta}^t\boldsymbol{\Gamma}(\sigma)\boldsymbol{\eta} = \overline{\mathbf{x}}^t\overline{\Gamma}_i\overline{\mathbf{x}} \ . \tag{2.55}$$

From equation (2.49), one has $\sigma\big|_{y=0} = \boldsymbol{\kappa}_i\overline{\mathbf{x}}$ in the $y=0$ plane. Subsequently,

$$\sigma+\frac{1}{2}\boldsymbol{\eta}^t\boldsymbol{\Gamma}(\sigma)\boldsymbol{\eta}\bigg|_{y=0} = \boldsymbol{\kappa}_i\cdot\overline{\mathbf{x}}+\frac{1}{2}\overline{\mathbf{x}}^t\overline{\Gamma}_i\overline{\mathbf{x}} \ . \tag{2.56}$$

Substituting equation (2.56) into equation (2.36), yields

$$B_i(\mathbf{r})\big|_{y=0} = A_i e^{jk[\boldsymbol{\kappa}_i\cdot\overline{\mathbf{x}}+\frac{1}{2}\overline{\mathbf{x}}^t\overline{\Gamma}_i\overline{\mathbf{x}}]} \ . \tag{2.57}$$

Further substituting (2.57) and $\mathbf{x} = \overline{\mathbf{x}}+\mathbf{x}_i$ into equation (2.41),

$$\tilde{B}_i(\boldsymbol{\kappa}) \simeq \int_{-\infty}^{\infty} d\overline{\mathbf{x}}^2 A_i e^{jk[(\boldsymbol{\kappa}_i-\boldsymbol{\kappa})\cdot\overline{\mathbf{x}}+\frac{1}{2}\overline{\mathbf{x}}^t\overline{\Gamma}_i\overline{\mathbf{x}}-\boldsymbol{\kappa}\cdot\mathbf{x}_i]} \ . \tag{2.58}$$

Finally, this integral can be evaluated in closed form, to give [5]

$$\tilde{B}_i(\boldsymbol{\kappa}) = A_i\frac{2\pi i}{k\sqrt{\det\overline{\boldsymbol{\Gamma}}_i}}e^{-jk[\frac{1}{2}(\boldsymbol{\kappa}_i-\boldsymbol{\kappa})^t\overline{\Gamma}_i(\boldsymbol{\kappa}_i-\boldsymbol{\kappa})\cdot\overline{\mathbf{x}}+\mathbf{x}_i\cdot\boldsymbol{\kappa}]} \ . \tag{2.59}$$

It is noted that $\det\mathbf{T} = \gamma_i$ and $\det\overline{\boldsymbol{\Gamma}}_i = (\det\mathbf{T})^2\det\boldsymbol{\Gamma}_i$, so that the final expression is given by,

$$\tilde{B}_i(\boldsymbol{\kappa}) = \frac{2\pi i A_i}{k\gamma_i \sqrt{\det \boldsymbol{\Gamma}_i}} e^{jk\psi} \quad \text{and} \tag{2.60}$$

$$\Psi(\alpha', \zeta) = \frac{1}{2}(\boldsymbol{\kappa} - \boldsymbol{\kappa}_i)^t \bar{\boldsymbol{\Gamma}}_i^{-1}(\boldsymbol{\kappa} - \boldsymbol{\kappa}_i) + \boldsymbol{\kappa}^t \mathbf{x}_i \quad . \tag{2.61}$$

Once the plane wave spectrum is calculated, the field of the incident beam can be obtained by equation (2.40).

2.5 Gaussian beams propagation

2.5.1 Circular Gaussian beam propagation

The field distribution of a circular Gaussian beam is described by equation (2.10). Assuming the Gaussian beam propagates along the z-axis, the amplitude profile in the plane $(x, y, z = 0)$, and the trace of the Gaussian beam, are as shown in Figure 2.2.

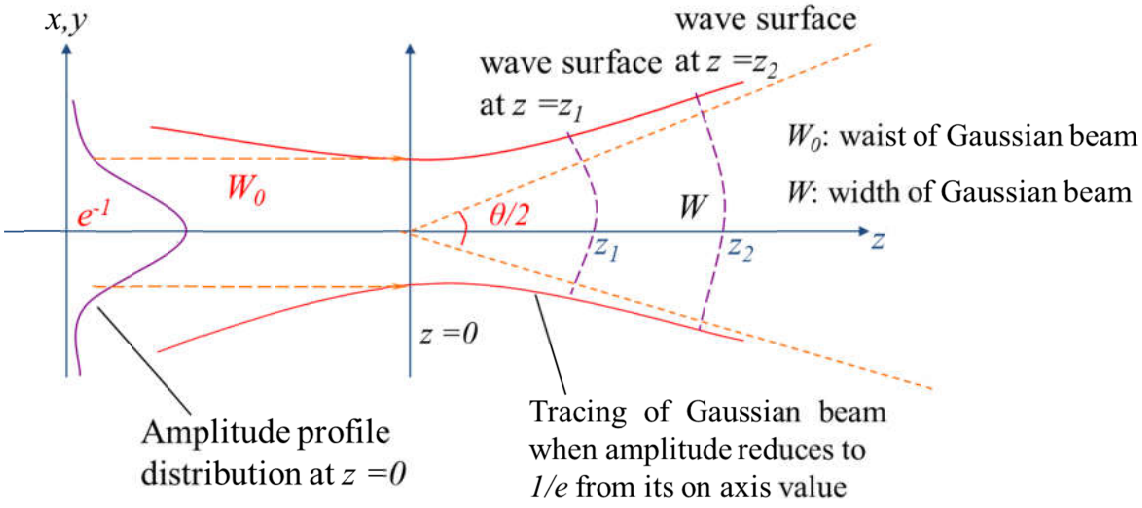

Figure 2.2 Amplitude profile and the trace of a Gaussian beam. The beam waist of the beam is located at z=0 plane. The amplitude profile distribution is of a Gaussian type. The size of the beam waist is w_0 which is defined as the radius where the field amplitude decays to e^{-1} of its on-axis value. The Gaussian beam propagates along the z-axis with a divergent angle θ. Propagating Gaussian beam indicates increase in the radius of wave surface and the relative beam width, and diminution of peak amplitudes as distance from the waist increases. Both of them can be traced at arbitrary locations on the axis, i.e. z_1 and z_2.

2.5.2 Propagation of a general astigmatic Gaussian beam

To understand the propagation of a general astigmatic Gaussian beam, the expression of equation (2.32) is rewritten to be

$$u(x,y,z)=u_0\sqrt{\frac{q_1q_2}{(z+q_1)(z+q_2)}}e^{-jk_zz}\cdot e^{\frac{j}{2k}\left[\frac{x^2}{z+q_1}+\frac{y^2}{z+q_2}\right]} \quad , \tag{2.62}$$

where

$$q_1=-j\pi\frac{w_{01}^2}{\lambda}+l_1 \qquad \text{and} \tag{2.63}$$

$$q_2=-j\pi\frac{w_{02}^2}{\lambda}+l_2 \quad . \tag{2.64}$$

l_1 and l_2 are the z coordinates of the location of the beam waists in the x and y directions, respectively. After obtaining the location and size of the beam waists in the two orthogonal axes x and y, the propagation of a 3D, general, astigmatic, Gaussian beam, can be independently handled in these two orthogonal directions as a normal Gaussian beam. For example, the equations (2.11, 2.12) of a 3D general astigmatic Gaussian beam become

$$R_{1,2}=z+l_{1,2}+\frac{1}{z+l_{1,2}}(\frac{\pi w_{01,02}^2}{\lambda})^2 \text{ and} \tag{2.65}$$

$$w_{1,2}=w_{01,02}[1+(\frac{\lambda(z+l_{1,2})}{\pi w_{01,02}^2})^2]^{\frac{1}{2}} \quad . \tag{2.66}$$

2.6 Numerical examples of Gaussian beams

2.6.1 Circular stigmatic Gaussian beam

Firstly, let us choose $\delta_{11}=\delta_{22}=1$, $\delta_{12}=\delta_{21}=0$ and let $q(0)=-500i$ in equation (2.36). As discussed above, under these conditions, the general beam degenerates into an

axially-symmetric Gaussian beam. We assume the beam conventionally propagates along the z-axis. The side-view of the normalized total field $|B_i(\mathbf{r})|$ on the plane $(x, y, z = 0)$ is shown in Figure 2.3, and the plan-view of the field is shown in Figure 2.4, with the beam width referring to e^{-1} level; $w_0 = w_{01} = w_{02} = 0.94m$ and the beam widths are $e^{-1/2}$, $W_i = W_{i1} = W_{i2} = 0.6649m$.

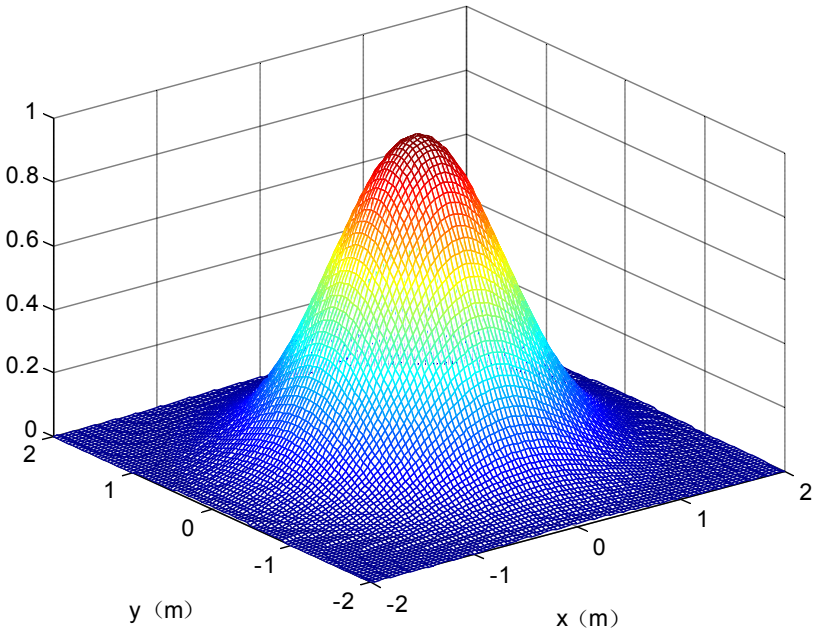

Figure 2.3 The side view of total field $|B_i(r)|$ of a circular stigmatic GB with $q(0) = -500i$, $\delta_{12} = \delta_{21} = 0$, and $\delta_{11} = \delta_{22} = 1$.

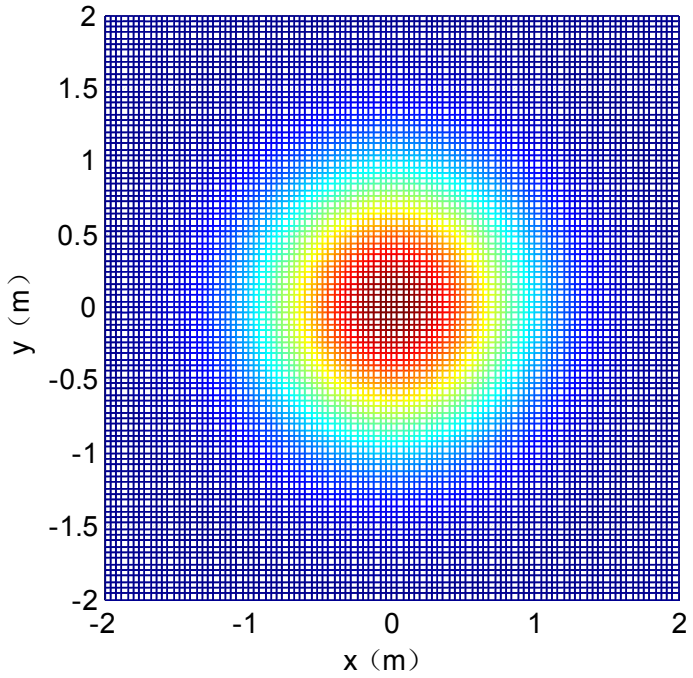

Figure 2.4 The plan view of total field $|B_i(r)|$ of a circular stigmatic GB with $q(0) = -500i$, $\delta_{12} = \delta_{21} = 0$, and $\delta_{11} = \delta_{22} = 1$.

2.6.2 Elliptical astigmatic Gaussian beam

With the choice $\delta_{12} = \delta_{21} = 0$, $q(0) = -500i$, with $\delta_{11} = 4\delta_{22}, \delta_{22} = 1$ a general elliptical beam rather than a symmetric circular Gaussian beam, is obtained. As with the previous case, the beam propagates along the z axis. The side-view in Figure 2.5 shows the normalized total field $|B_i(\mathbf{r})|$ on the plane $(x, y, z = 0)$. The plan-view of Figure 2.6, show the beam widths ($e^{-1/2}$) $W_{i1} = 0.6649m$ and $W_{i2} = 0.3325m$.

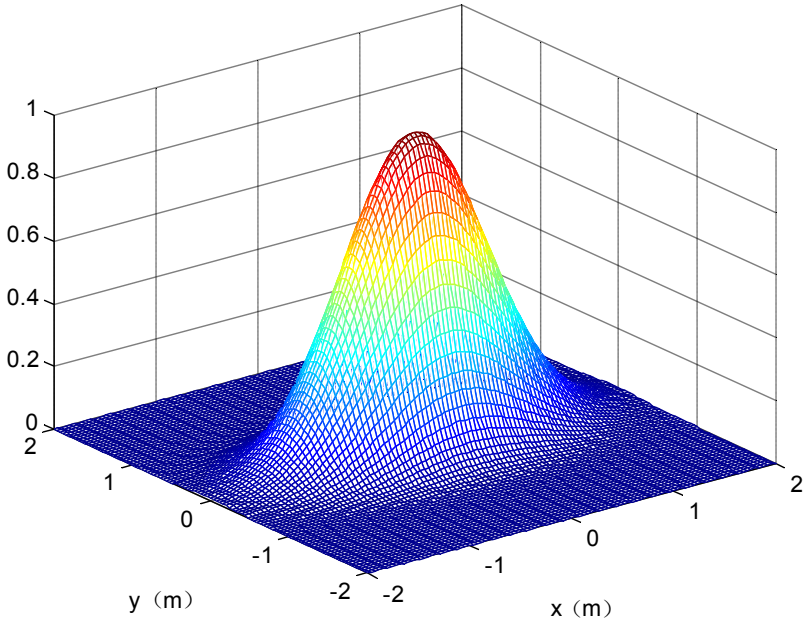

Figure 2.5 The side view of total field of an elliptical astigmatic GB with $q(0) = -500i$, $\delta_{12} = \delta_{21} = 0$, $\delta_{11} = 4\delta_{22}$ **and** $\delta_{22} = 1$.

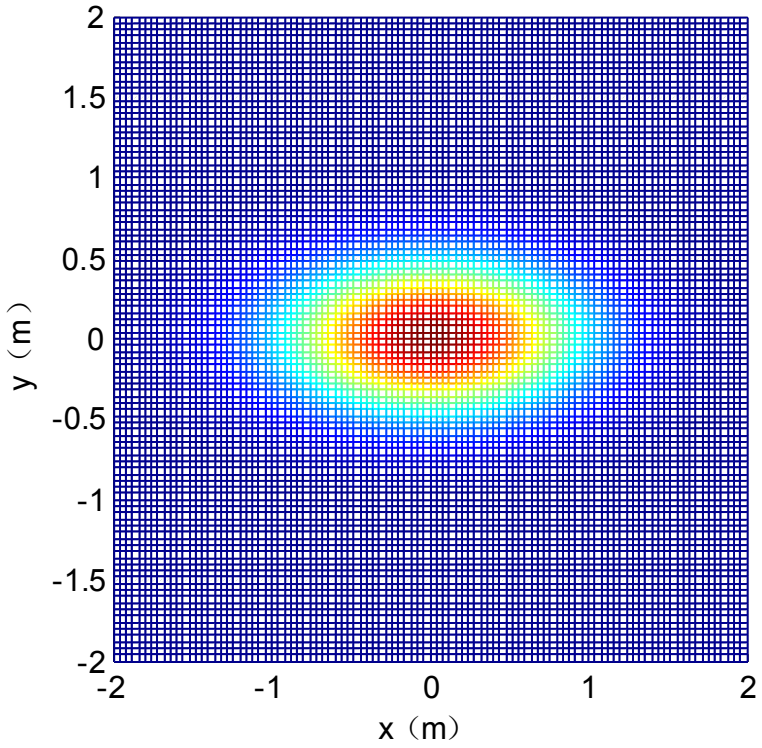

Figure 2.6 The plan view of total field of an elliptical astigmatic GB with $q(0) = -500i$, $\delta_{12} = \delta_{21} = 0$, $\delta_{11} = 4\delta_{22}$ **and** $\delta_{22} = 1$

Usually, the complex symmetric matrix $\mathbf{\Gamma}$ of a 3D, general, astigmatic, Gaussian beam, is a diagonal matrix with $\delta_{12}=\delta_{21}=0$, and this form is commonly used in most circumstances. If $\delta_{12}=\delta_{21}\neq 0$, a "rotated" Gaussian beam is obtained. With $q(0)=-500i$, $\delta_{11}=1.5\delta_{22}$, $\delta_{22}=1$ and $\delta_{12}=\delta_{21}$=1, Figure 2.7 depicts the side-view of the total field $\left|B_i(\mathbf{r})\right|$ for this rotated Gaussian beam in the plane $(x,y,z=0)$. A plan view of the same is shown in Figure 2.8.

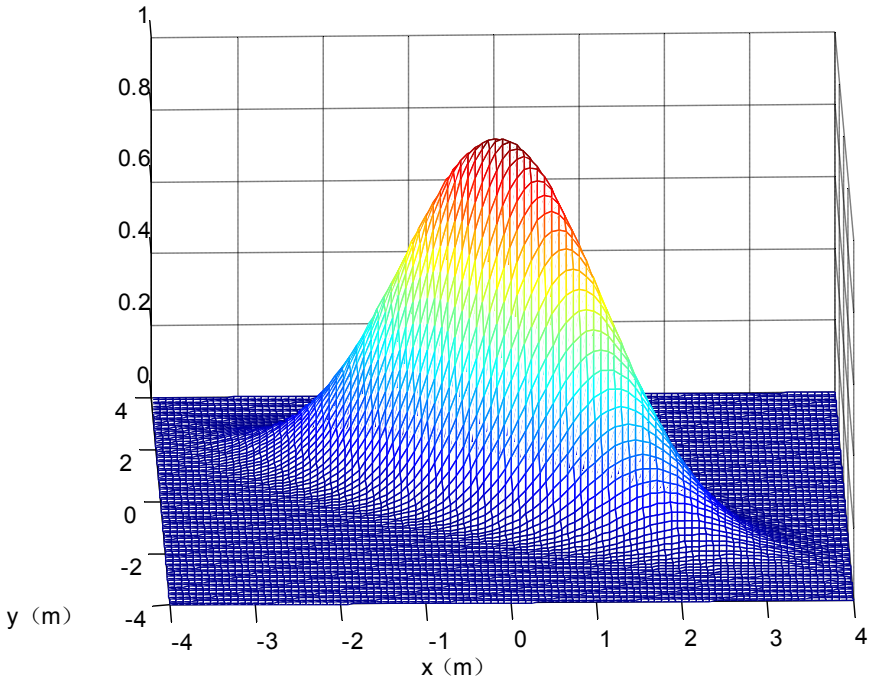

Figure 2.7 the side view of total field of an elliptical astigmatic GB with $q(0)=-500i$, $\delta_{11}=1.5\delta_{22}$, $\delta_{22}=1$ and $\delta_{12}=\delta_{21}$=1

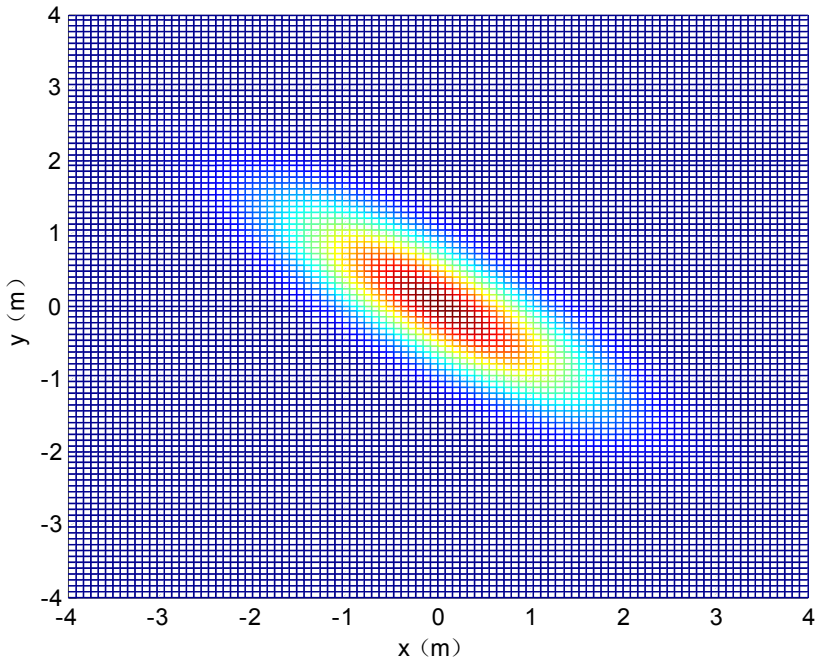

Figure 2.8 the plan view of total field of an elliptical astigmatic GB with $q(0) = -500i$ **,** $\delta_{11} = 1.5\delta_{22}$ **,** $\delta_{22} = 1$ **and** $\delta_{12} = \delta_{21}$=1

2.7 Summary

The formulation of a circular Gaussian beam and an elliptical, astigmatic, Gaussian beam, and their propagation has been introduced. The elliptic, astigmatic, Gaussian beam, and its spatial-spectral representation will be used to investigate the reflection and diffraction of general Gaussian beams in later chapters.

References

[1] P.F.Goldsmith, “Quasioptical Systems: Gaussian Beam Quasioptical Propagation and Applications,” IEEE Press, 1998

[2] G. C. Zogbi, “Reflection and diffraction of general astigmatic Gaussian beam from curved surfaces and edges,” Ph.D. dissertation, The Ohio State University, Columbus, OH, USA, Jun. 1994.

[3] Katsav M, Heyman E. Gaussian beams summation representation of half plane diffraction: A full 3-D formulation [J]. Antennas and Propagation, IEEE Transactions on, 2009, 57(4): 1081-1094.

[4] E. Heyman and L. B. Felsen, “Gaussian beam and pulsed beam dynamics: Complex source and spectrum formulations within and beyond paraxial asymptotics,” J. Opt. Soc. Am. A, vol. 18, pp. 1588-1610, 2001.

[5] G. Gordon, E. Heyman, and R. Mazar, “Phase space beam summation analysis of rough surface waveguide,” J. Acoustical Soc. Am., vol. 117, pp. 1922-1932, 200.

Chapter 3 Gaussian Beam Reflection on a Curved Surface

3.1 Overview

In this chapter, three different kinds of methods for analysing Gaussian beam reflection are introduced and compared. The PO method has the advantage of accuracy; however, the form of the result can only be presented by "reflected field" rather than "reflected Gaussian beam". The GO method and the Phase Matching method both describe the reflected field in the form of a Gaussian beam. Because the GO method in original DGBA is not suitable for elliptical astigmatic incidence, the Phase Matching method is introduced for a broader range of applications. The Phase Matching method is also extended to examine the situation of the incident beam not coinciding with one of the two principal directions of the surface.

3.2 Gaussian beam reflection using physical optics

The PO method has been verified as a very popular method for analysing electrically large systems. In many cases, the spot size of the incident beam is assumed to be reasonably smaller in comparison with the surface radii of curvature. The surface can be considered as electrically large and the PO approach applied.

The treatment of Gaussian beam reflection using the PO method is presented below. The geometry of the Gaussian beam reflection is shown in Figure 3.1. The reflected field of a Gaussian beam is obtained by integrating the surface currents derived from the incident field over the reflecting surface. Here, it is assumed that the reflecting surface is locally approximated by a local parabola at the intersection point, thus

$$z = -\frac{1}{2}\left(\frac{x^2}{R_1} + \frac{y^2}{R_2}\right) . \tag{3.1}$$

R_1 and R_2 are the surface curvatures in the x and y direction. Positive radius of curvature defines a convex surface and negative radius of curvature, a concave surface.

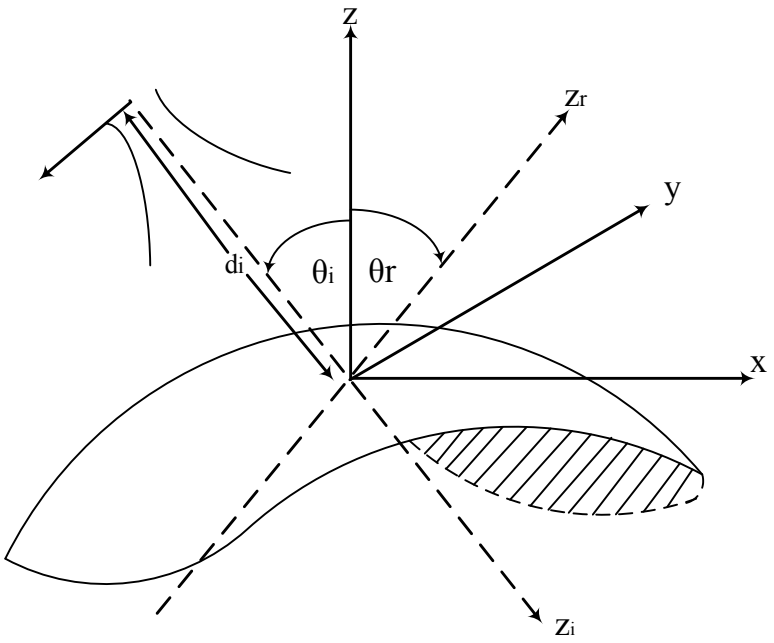

Figure 3.1 Geometry of PO method: 3D Gaussian beam reflection at a curved surface. $(\hat{x}, \hat{y}, \hat{z})$ **is the surface coordinate at the intersection point.** z_i **and** z_r **are the propagation directions of the incident and reflected beams.** θ_i **is the incident angle;** θ_r **, the reflected angle; and** d_i **, the distance from the incident beam waist to the intersection point.**

The incident beam is assumed to be a general astigmatic Gaussian beam and it is easy to write the incident beam in the form of (2.36),

$$H_i(x_i, y_i, z_i) = H_{0i}\sqrt{\frac{\det(\boldsymbol{\Gamma}(z_i))}{\det(\boldsymbol{\Gamma}(0))}}\, e^{jk[z_r + \frac{1}{2}\bar{\mathbf{x}}_i^t \boldsymbol{\Gamma}(z_i)\bar{\mathbf{x}}_i]} . \tag{3.2}$$

The magnetic vector potential used to describe the reflected field is

$$\bar{A}^e(x, y, z) = \frac{1}{4\pi}\int_{-\infty}^{\infty}\int_{-\infty}^{\infty} \bar{J}^e(s')\frac{e^{-jkR}}{R} ds' \tag{3.3}$$

where

$$R = \sqrt{(x-x')^2 + (y-y')^2 + (z-z')^2} \quad . \tag{3.4}$$

The integral (3.3) is over the whole reflecting surface and R in (3.4) is the distance from the source point on the curved surface to the observation point. The differential area is given by

$$ds' = \sqrt{1 + (\frac{x'}{R_1})^2 + (\frac{y'}{R_2})^2}\, dx'dy' \quad . \tag{3.5}$$

Therefore, the equivalent current in J^e is the surface current density and is evaluated as

$$\bar{J}^e(s') = 2\hat{n} \times \bar{H}_i(s') \, . \tag{3.6}$$

Consequently, the reflected field is given by

$$\bar{E}^r = -j\omega(\bar{A}^e + \frac{1}{k^2}\nabla(\nabla \cdot \bar{A}^e)) \quad . \tag{3.7}$$

Following the approach of Zogbi [1], an approximated reflected magnetic field, with a closed form, is given by

$$\bar{H}^r(x,y,z) = -\frac{jk}{2\pi}\frac{e^{-jkr}}{r}\sum_{n=0}^{3}\sum_{m=0}^{3}\bar{W}_{nm}I_{nm} \, . \tag{3.8}$$

The expression of terms W_{nm} and I_{nm} can be found in ***Appendix-I***. Equation (3.8) is in excellent agreement with the original form of PO.

3.3 Gaussian beam reflection using geometrical optics

The 2D-DGBA uses GO to determine reflection at a curved reflector surface. The key issue is to find how the complex beam parameter q changes when a Gaussian beam impinges. At this reflection point, the spot size of the beam stays the same while the beam curvature changes according to the local curvature of the reflecting surface. In other words, this GO method assumes that the beam width w does not change when

dealing with reflection. Since the complex beam parameter q of the incident beam is known, it is required to find the reflected complex beam parameter in equation (2.9).

It is clear that if the beam width w stays the same, one only needs to find out how the radius of curvature R changes. GO characterizes the field in terms of differential rays around the axes of the incident and the reflected beams. Figure 3.2 shows the geometry of the reflection. The details on this GO treatment can be found in reference [2-4].

Firstly, the surface about the point $\vec{r}_0$ can be described by the bi-parabolic expansion

$$\vec{r}(u,v) = \vec{r}_0 + u\hat{\tau}_1 + v\hat{\tau}_2 - \frac{1}{2}\left(\frac{u^2}{R_1} + \frac{v^2}{R_2}\right)\hat{n}, \tag{3.9}$$

where: $\hat{n}$ is the surface normal; and, $\hat{\tau}_1$ and $\hat{\tau}_2$ denote the two principal directions of curvature of the surface. R_1 and R_2 are the two principal radii of curvature.

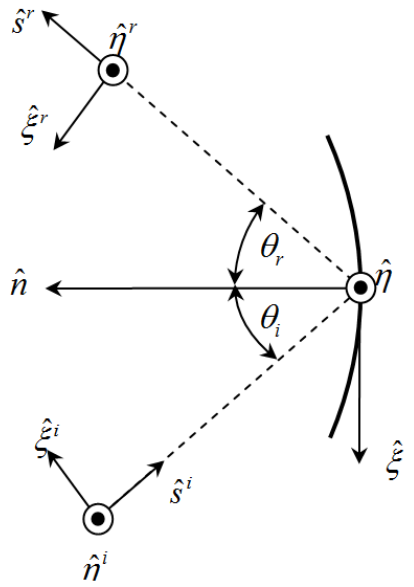

Figure 3.2 Geometry of GO method: reflection of a Gaussian beam at a curved surface. A circular incident GB impinges on a curved surface with an incident angle θ_i. $(\hat{\xi},\hat{\eta},\hat{n})$ is the surface coordinate at the intersection point; $(\hat{\xi}^i,\hat{\eta}^i,\hat{s}^i)$, the incident GB based coordinate system; and $(\hat{\xi}^r,\hat{\eta}^r,\hat{s}^r)$, reflected GB based coordinate system.

The relationship of $(\hat{u},\hat{v})$ in (3.9) and $(\hat{\xi},\hat{\eta})$ is given by

$$\begin{pmatrix} u^{i,c,r} \\ v^{i,c,r} \end{pmatrix} = \begin{bmatrix} \cos(\alpha_{i,c,r}) & \sin(\alpha_{i,c,r}) \\ -\sin(\alpha_{i,c,r}) & \cos(\alpha_{i,c,r}) \end{bmatrix} \begin{pmatrix} \xi^{i,c,r} \\ \eta^{i,c,r} \end{pmatrix} . \tag{3.10}$$

$\alpha_{i,c,r}$ is the counter clockwise rotation angle from $\hat{\xi}^{i,c,r}$ to $u^{i,c,r}$ with respect to $\hat{n}$.

Matching the phase between the incident and the reflected wave fronts on the surface of the reflector and, dropping all third and higher order terms, result in an matrix equation for the curvature of the reflected beam this:

$$\begin{aligned} \begin{pmatrix} T_1 \\ T_2 \\ T_3 \end{pmatrix} &= \begin{pmatrix} \Sigma_r \\ \cos(2\alpha_r)\Delta_r \\ \sin(2\alpha_r)\Delta_r \end{pmatrix} \\ &= \begin{pmatrix} \Sigma_i \\ \cos(2\alpha_i)\Delta_i \\ -\sin(2\alpha_i)\Delta_i \end{pmatrix} \\ &+ \begin{bmatrix} 1/\cos\theta + \cos\theta & 1/\cos\theta - \cos\theta & 0 \\ 1/\cos\theta - \cos\theta & 1/\cos\theta + \cos\theta & 0 \\ 0 & 0 & 2 \end{bmatrix}, \\ &\times \begin{pmatrix} \Sigma_c \\ \cos(2\alpha_c)\Delta_c \\ \sin(2\alpha_c)\Delta_c \end{pmatrix} \end{aligned} \tag{3.11}$$

with $\sum_{i,c,r} = \dfrac{1/R_2^{i,c,r} + 1/R_1^{i,c,r}}{2}$ and $\Delta_{i,c,r} = \dfrac{1/R_2^{i,c,r} - 1/R_1^{i,c,r}}{2}$.

In (3.11), $R_1^{i,c,r}$ and $R_2^{i,c,r}$ are respectively the principal radius of curvature of the incident Gaussian beam at the curved surface and, the reflected Gaussian beam at the intersection point. From (3.11), one has

$$\alpha_r = 0.5\tan^{-1}(T_3/T_2), \tag{3.12}$$

$$R_1^r = 0.5\tan^{-1}(T_3/T_2)\begin{cases} \dfrac{1}{T_1 - T_3/\sin(2\alpha_r)}, \alpha_r = \pm\dfrac{\pi}{4} \\ \dfrac{1}{T_1 - T_2/\cos(2\alpha_r)}, \alpha_r \neq \pm\dfrac{\pi}{4} \end{cases} \quad \text{and} \tag{3.13}$$

$$R_2^r = 0.5\tan^{-1}(T_3/T_2)\begin{cases}\dfrac{1}{T_1+T_3/\sin(2\alpha_r)}, \alpha_r = \pm\dfrac{\pi}{4} \\ \dfrac{1}{T_1+T_2/\cos(2\alpha_r)}, \alpha_r \neq \pm\dfrac{\pi}{4}\end{cases}. \tag{3.14}$$

In 2D-DGBA practice, because the entire incident beam is from Gaussian beam expansion over an input plane, they are formed into circular Gaussian beams. That is $R_1^i = R_2^i$ and $\alpha_i = 0$. By substituting (3.12) and (3.13) into (2.9), one has the complex beam parameters q_1^r and q_2^r; the electric field of the reflection field is given by

$$E^r = E_0\sqrt{\frac{q_1^r q_2^r}{(z_r+q_1^r)(z_r+q_2^r)}}e^{-jk_z z}\cdot e^{\frac{j}{2k}\left[\frac{x_r^2}{z_r+q_1^r}+\frac{y_r^2}{z_r+q_2^r}\right]}. \tag{3.15}$$

However, when dealing with diffraction, the 2D-DGBA cannot handle an elliptic, astigmatic, Gaussian beam. Therefore, in the treatment of diffraction in 2D-DGBA, the reflected beam is approximated by a circular beam with a complex beam parameter

$$\frac{1}{q} = \frac{1}{\sqrt{R_1^r R_2^r}} + j\frac{\lambda}{\pi w^2}. \tag{3.16}$$

3.4 Gaussian beam reflection using the phase matching method

3.4.1 General case

This section covers the Phase Matching method, which is a branch of GO. In order to distinguish one from the other, we refer to the method in section 3.2 as the "GO" method and that of this section as the "Phase Matching" method. In the Phase Matching approach, the reflected field is given as a Gaussian beam. It is assumed that the reflected field has a quadratic phase and its relative reflected beam parameters are found by phase matching the incident and reflected fields on the doubly-curved paraboloidal surface. It will be shown later that this Phase Matching approach yields the reflected Gaussian beam in the form of a general, astigmatic, Gaussian beam, as described by (2.36). It is a better solution and can be used easily for 3D diffraction treatment in chapter 5.

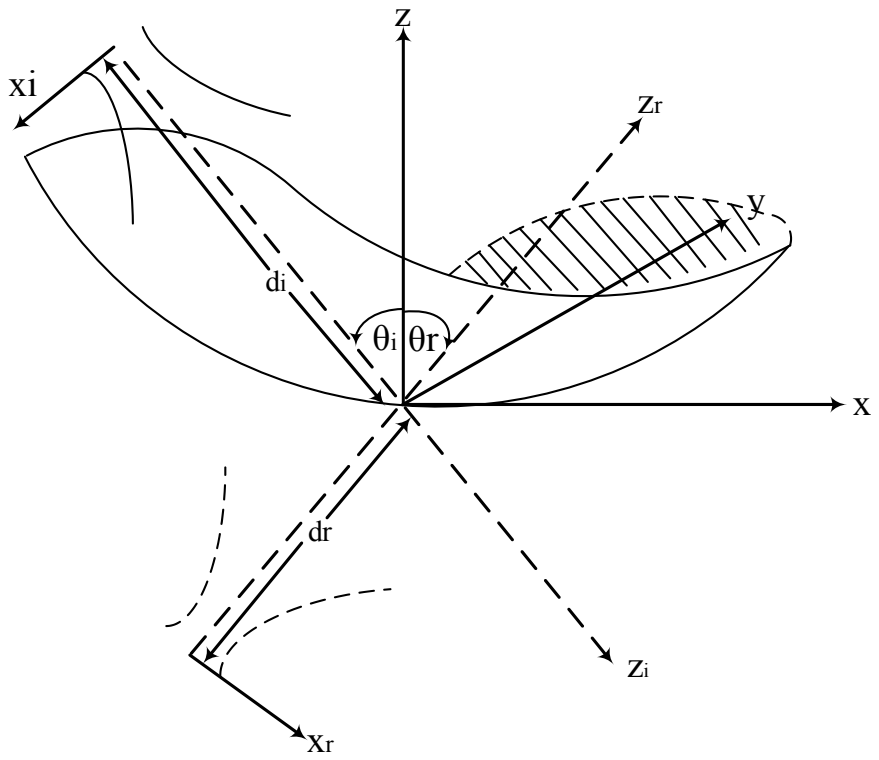

Figure 3.3 Geometry of Phase Matching method: 3D Gaussian beam reflection at a curved surface with incident beam along the principal direction. $(\hat{x}, \hat{y}, \hat{z})$ **is the surface coordinate at the intersection point.** $(\hat{x}_i, \hat{y}_i, \hat{z}_i)$ **is the incident coordinate with** $\hat{z}_i$**, the propagation directions of the incident beam.** θ_i **is the incident angle; and** d_i**, the distance from the incident beam waist to the intersection point.** $(\hat{x}_r, \hat{y}_r, \hat{z}_r)$ **is the reflected coordinate with** $\hat{z}_r$**, the propagation directions of the reflected beam.** θ_i **is the reflected angle; and** d_r**, the distance from the reflected beam waist to the intersection point.**

The geometry for the problem is shown in Figure 3.3. The incident coordinate system (x_i, y_i, z_i) is defined by the principal axis of the incident beam z_i. The origin of the surface coordinate system (x, y, z) coincides with the beam-reflection intersection-point. The incident angle is θ_i. The original of the reflected coordinate system is also at the intersection point and defined as (x_r, y_r, z_r). The reflected angle is θ_r.

The expression of the surface using the surface coordinates is given just as for (3.1)

$$z = -\frac{1}{2}\left(\frac{x^2}{R_1} + \frac{y^2}{R_2}\right). \tag{3.17}$$

The Rayleigh range is defined by the beam-width coinciding with the beam-waist, thus

$$b = z_R = \frac{\pi w_0^2}{\lambda} \ . \tag{3.18}$$

With the aid of this definition, the incident 3D general, astigmatic, Gaussian beam, has the form

$$B_i(x_i, y_i, z_i) = A_{0i}\sqrt{\frac{-jb_1^i + d_1^i}{z_i - jb_1^i + d_1^i}}\sqrt{\frac{-jb_2^i + d_2^i}{z_i - jb_2^i + d_2^i}}e^{jk_z z_i} \cdot e^{\frac{j}{2k}\left[\frac{x_i^2}{z_i - jb_1^i + d_1^i} + \frac{y_i^2}{z_i - jb_2^i + d_2^i}\right]} \ . \tag{3.19}$$

The incident beam can be rewritten in the form of (2.36) to be

$$B_i(x_i, y_i, z_i) = A_{0i}\sqrt{\frac{\det(\boldsymbol{\Gamma}(z_i))}{\det(\boldsymbol{\Gamma}(0))}}e^{jk[z_r + \frac{1}{2}\bar{\mathbf{x}}_i^t \boldsymbol{\Gamma}(z_i)\bar{\mathbf{x}}_i]} \tag{3.20}$$

where

$$\bar{X}_i = [x_i, y_i]^t \quad \text{and} \tag{3.21}$$

$$\boldsymbol{\Gamma}(z_i) = \begin{bmatrix} \dfrac{1}{z_i - jb_1^i + d_1^i} & 0 \\ 0 & \dfrac{1}{z_i - jb_2^i + d_2^i} \end{bmatrix} . \tag{3.22}$$

If $z_i = 0$, $\boldsymbol{\Gamma}(0)$ becomes

$$\boldsymbol{\Gamma}(0) = \begin{bmatrix} \dfrac{1}{-jb_1^i + d_1^i} & 0 \\ 0 & \dfrac{1}{-jb_2^i + d_2^i} \end{bmatrix} . \tag{3.23}$$

Assuming the reflected beam has the similar form, then

$$B_r(x_r, y_r, z_r) = A_{0i}\sqrt{\frac{\det(\boldsymbol{\Gamma}(z_r))}{\det(\boldsymbol{\Gamma}(0))}}e^{jk[z_r + \frac{1}{2}\bar{\mathbf{x}}_r^t \boldsymbol{\Gamma}(z_r)\bar{\mathbf{x}}_r]} \ . \tag{3.24}$$

In the Phase Matching method [1], suppose that the phase of the incident beam is equal to that of the reflected beam at the point of intersection. Details for this situation can be

found in ***Appendix-II*** and the curvature-matrix of the reflected wave front at the intersection-point is

$$\mathbf{\Gamma}^r(0) = \mathbf{\Gamma}^i(0) - 2\cos\theta_i(\Theta^{-1})^t Q\Theta^{-1} \tag{3.25}$$

where Θ is the projection operator, and Q is the curvature matrix for the surface

$$Q = \begin{bmatrix} \dfrac{1}{R_1} & 0 \\ 0 & \dfrac{1}{R_2} \end{bmatrix}. \tag{3.26}$$

The transformation between the reflected-beam coordinate system and the surface coordinate system is

$$\begin{bmatrix} x_r \\ y_r \\ z_r \end{bmatrix} = \begin{bmatrix} p_{11} & p_{12} & p_{13} \\ p_{21} & p_{22} & p_{23} \\ p_{31} & p_{32} & p_{33} \end{bmatrix} \begin{bmatrix} x \\ y \\ z \end{bmatrix} \tag{3.27}$$

where

$$\begin{gathered} P_{11}^2 + P_{12}^2 + P_{13}^2 = P_{21}^2 + P_{22}^2 + P_{23}^2 = P_{31}^2 + P_{32}^2 + P_{33}^2 = 1 \\ P_{11}^2 + P_{21}^2 + P_{31}^2 = P_{12}^2 + P_{22}^2 + P_{32}^2 = P_{13}^2 + P_{23}^2 + P_{33}^2 = 1 \\ P_{11}P_{22} - P_{12}P_{21} = P_{33} \\ P_{12}P_{31} - P_{11}P_{32} = P_{23} \\ P_{21}P_{32} - P_{22}P_{31} = P_{13} \\ P_{11}P_{31} + P_{12}P_{32} = -P_{13}P_{33} \\ P_{31}P_{21} + P_{32}P_{22} = -P_{33}P_{23} \\ P_{11}P_{21} + P_{12}P_{22} = -P_{13}P_{23} \\ P_{11}^2P_{22}^2 + P_{21}^2P_{12}^2 - 2P_{11}P_{22}P_{12}P_{21} = P_{33}^2 \\ P_{33} = \hat{z}_r \cdot \hat{z} = \cos\theta_i \end{gathered} \tag{3.28}$$

The projection operator can be written as

$$\Theta = \begin{bmatrix} p_{11} & p_{12} \\ p_{21} & p_{22} \end{bmatrix}. \tag{3.29}$$

By substituting (3.26 – 29) into (3.25), the reflected-curvature matrix at the intersection point is

$$\mathbf{\Gamma}^r(0)=\begin{bmatrix}\Gamma_{11}^r & \Gamma_{12}^r\\ \Gamma_{21}^r & \Gamma_{22}^r\end{bmatrix} \tag{3.30}$$

where

$$\mathbf{\Gamma}_{11}^r=\frac{1}{-jb_1^i+d_1^i}+\frac{2}{\cos\theta_i}\left[\frac{p_{22}^2}{R_1}+\frac{p_{21}^2}{R_2}\right], \tag{3.31}$$

$$\mathbf{\Gamma}_{12}^r=-\frac{2}{\cos\theta_i}\left[\frac{p_{12}p_{22}}{R_1}+\frac{p_{21}p_{11}}{R_2}\right], \tag{3.32}$$

$$\mathbf{\Gamma}_{21}^r=\mathbf{\Gamma}_{12}^r \text{ and} \tag{3.33}$$

$$\mathbf{\Gamma}_{11}^r=\frac{1}{-jb_1^i+d_1^i}+\frac{2}{\cos\theta_i}\left[\frac{p_{12}^2}{R_1}+\frac{p_{11}^2}{R_2}\right]. \tag{3.34}$$

The reflected field can be ultimately calculated by (3.24).

3.4.2 Extended phase-matching method

In the previous discussion, the direction of projection of the incident beam onto the surface was coincident with one of the two principal directions. Also, the observation coordinate system was the same as the surface coordinate system. Now we try to extend this method to give an expression containing the two different principal curvature directions of the surface according to the direction of projection of the incident beam.

Figure 3.4 shows the geometry of this scenario. The intersection point of the incident beam and the curved surface is denoted as P. Around the point P, we can find a surface that is formed by using the lines of curvature of the surface. This curved surface has a normal $\hat{n}$. By making P the origin, and setting $\hat{\xi}$ and $\hat{\eta}$ to be the two orthogonal principal directions of curvature through P and tangent to curved surface, a coordinate

system $(\hat{\xi},\hat{\eta},\hat{n})$, can be constructed. The curved surface matrix can be represented using curvature matrix Q

$$n = X^t Q X \tag{3.35}$$

where

$$X = \begin{bmatrix} \xi \\ \eta \end{bmatrix} \text{ and} \tag{3.36}$$

$$Q = \begin{bmatrix} Q_{11} & Q_{12} \\ Q_{21} & Q_{22} \end{bmatrix}. \tag{3.37}$$

We assume that the principal radii of curvature of the surface at point P are R_1 and R_2, which are also the principal radii of curvature of the curved surface in equation (3.17). $\hat{x}$ and $\hat{y}$ are the two orthogonal directions passing through P and tangent to the curved surface. The angle φ in Figure 3.4 is the angle that rotates counter clockwise $\hat{x}$ to $\hat{\xi}$ on the plane $(x, y, z = 0)$ with respect to $\hat{n}$.

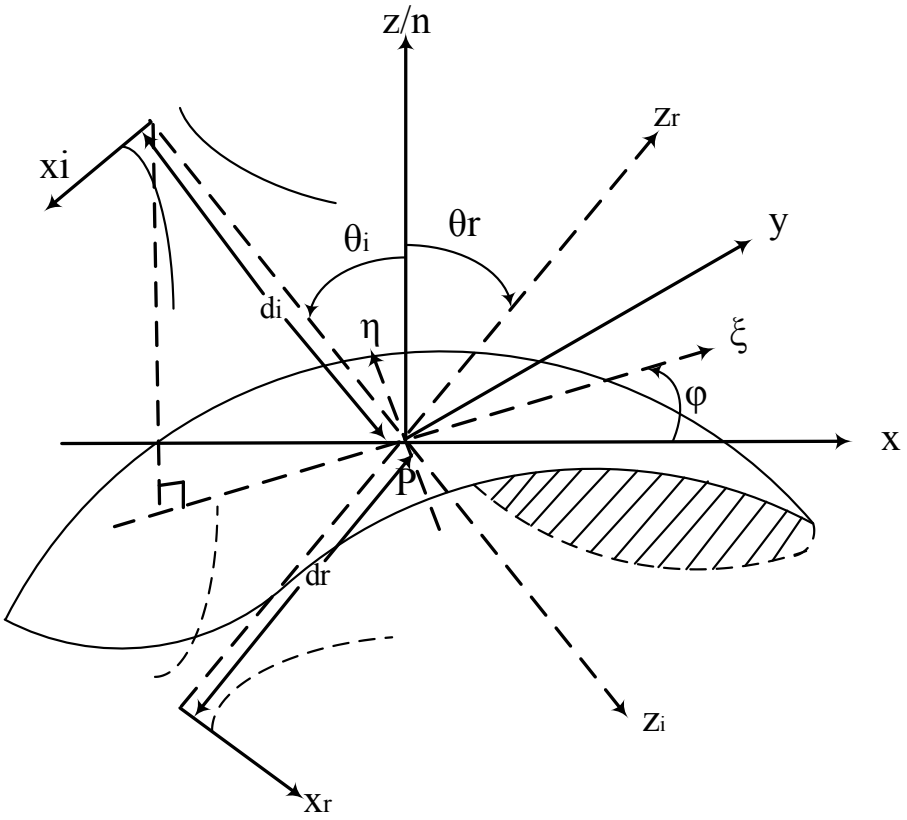

Figure 3.4 Geometry of extended Phase Matching method: 3D Gaussian beam reflection at a curved surface with arbitrary incident direction. The direction of projection of the incident beam onto the surface is $\hat{\xi}$ rather than $\hat{x}$. A coordinate system $(\hat{\xi},\hat{\eta},\hat{n})$ is constructed with $\hat{n}$, the normal direction of the curved surface around the intersection point P. The angle between $\hat{\xi}$ and $\hat{x}$ is φ. All other symbols have the same meanings as in Figure 3.3.

Q in the $(\hat{x},\hat{y},\hat{z})$ coordinate system is rewritten as

$$Q = J^t Q_0 J \tag{3.38}$$

where

$$Q_0 = \begin{bmatrix} \frac{1}{R_1} & 0 \\ 0 & \frac{1}{R_2} \end{bmatrix} \tag{3.39}$$

and

$$J = \begin{bmatrix} \cos(\varphi) & \sin(\varphi) \\ -\sin(\varphi) & \cos(\varphi) \end{bmatrix}. \tag{3.40}$$

By substituting this new curvature matrix Q into (3.25) and then substituting $\mathbf{\Gamma}^r(0)$ into (3.24), the reflected field can be evaluated with arbitrary directions.

3.5 Numerical verification

In this section, several numerical experiments are conducted. Through comparison with the PO, the accuracy of GO and the Phase Matching methods are assessed.

3.5.1. Experiments with a circular incident Gaussian beam

Assume all the directions of projection of the incident beams onto the surface are in directions of principal curvature. The geometry of the problem is similar to what has been shown in Figure 3.3. For simplicity, we assume directions of projection of the incident beam are along the $+x$ direction. In this section, all cases are simulated with PO as outlined in section 3.1; GO method of section 3.2 and, the Phase Matching method of section 3.3. The simulated reflected fields in this section are near fields, 300 λ from the point of intersection with $y = 0$.

The circular incident Gaussian beams used in the 2D-DGBA are tested with both convex and concave surfaces. In addition, different incident angles with $\theta_i = 0^\circ$, $\theta_i = 15^\circ$ and $\theta_i = 30^\circ$ are also considered.

Figure 3.5-8 illustrate the reflected beam profiles generated by the GO and Phase Matching methods, in comparison with the PO. It is shown that when the spot-sizes of the incident beam are very small, (i.e. < 1/20), compared with the principal curvatures of the surface (concave or convex), all three methods present agreements with only a ± 0.35 dB field amplitude deviation can be observed within ± 50λ range when the incident angle is $\theta_i = 0^\circ$. This deviation increases with increase of the incident angle. A ± 0.8 dB field deviation occurs when the incident angle increases to 30°.

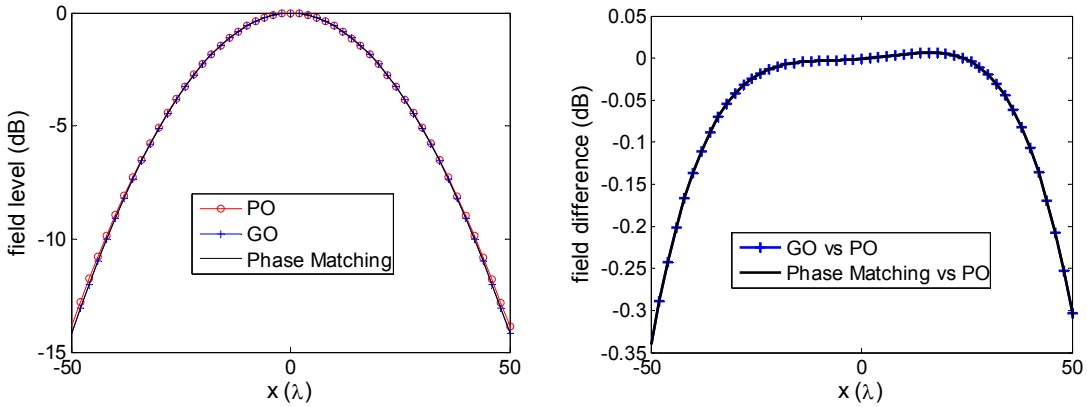

Figure 3.5 Simulation results of circular Gaussian beam reflection from a concave surface by PO, GO and Phase Matching methods with incident beam and surface parameters $w_i = 3\lambda, d_i = 20\lambda$, $\theta_i = 0^\circ$, $R_1 = -80\lambda, R_2 = -60\lambda$.

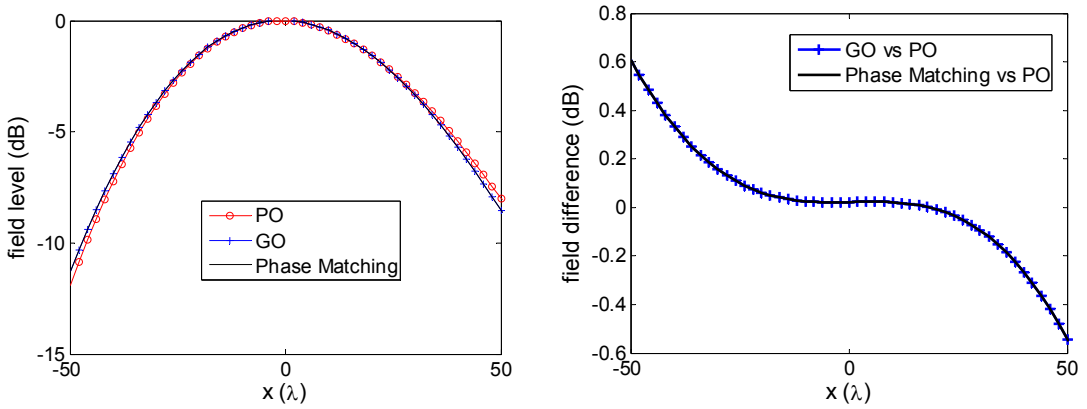

Figure 3.6 Simulation results of circular Gaussian beam reflection from a concave surface by PO, GO and Phase Matching methods with incident beam and surface parameters $w_i = 3\lambda, d_i = 20\lambda$, $\theta_i = 30^\circ$, $R_1 = -80\lambda, R_2 = -60\lambda$.

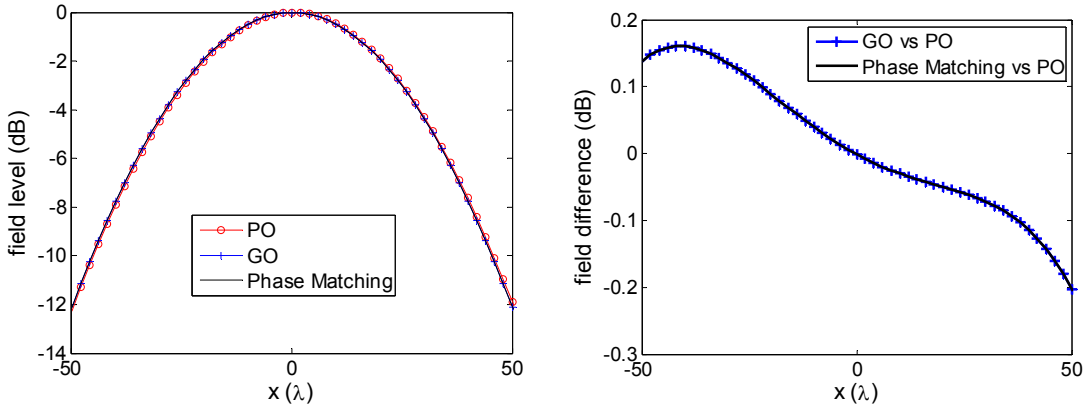

Figure 3.7 Simulation results of circular Gaussian beam reflection from a convex surface by PO, GO and Phase Matching methods with incident beam and surface parameters $w_i = 3\lambda, d_i = 20\lambda$, $\theta_i = 0^\circ$, $R_1 = 60\lambda, R_2 = 80\lambda$.

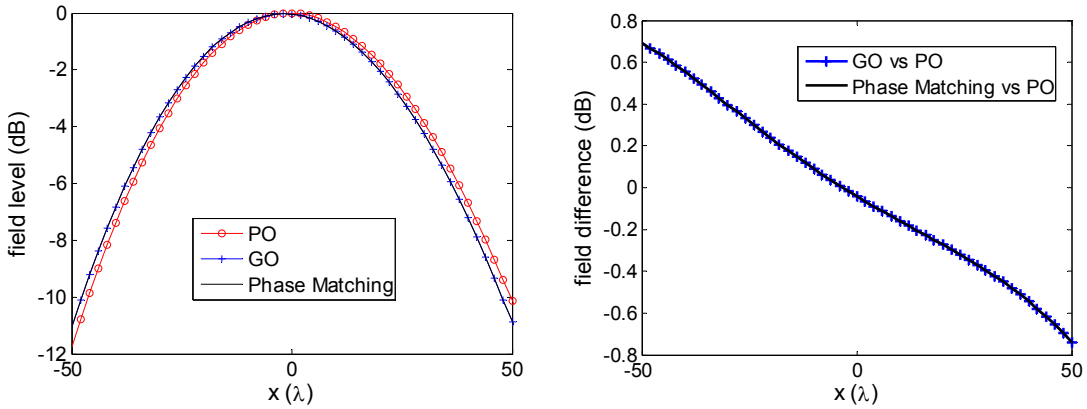

Figure 3.8 Simulation results of circular Gaussian beam reflection from a convex surface by PO, GO and Phase Matching methods with incident beam and surface parameters $w_i = 3\lambda, d_i = 20\lambda$, $\theta_i = 15^\circ$, $R_1 = 60\lambda, R_2 = 80\lambda$.

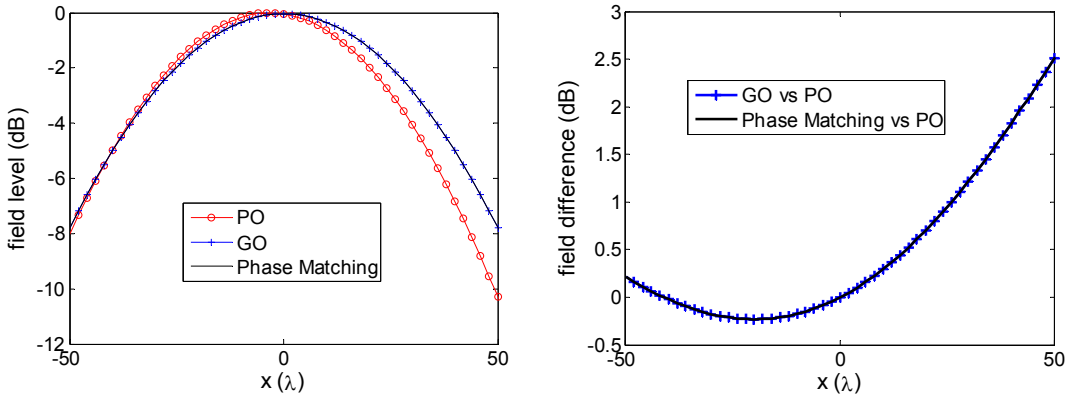

Figure 3.9 Simulation results of circular Gaussian beam reflection from a convex surface by PO, GO and Phase Matching methods. Incident beam and surface parameters $w_i = 8\lambda, d_i = 100\lambda$, $\theta_i = 0^\circ$, $R_1 = -20\lambda, R_2 = -10\lambda$.

However, as shown in Figure 3.9, the field amplitude deviation increases to ± 2.5 dB in the case of a beam spot-size comparable to the principal curvature of the surface. It seems that both GO and Phase Matching methods have lost their accuracy. So, for GO or Phase Matching methods, the incident beam widths on the surface should be much smaller (i.e. < 1/20) than the principal radii of curvature. Also, GO and Phase Matching methods generate exactly the same results for circular incident Gaussian beams.

3.5.2. Experiments with general astigmatic incident Gaussian beams

In this section, circular incident Gaussian beams are replaced by general, astigmatic, incident Gaussian beams. We assume the projecting directions of these incident beams are still coincident with the directions of principal curvature for the curved surface. In

some cases the beam waists w_{i1} and w_{i2} of these general, astigmatic, incident, Gaussian beams, not only have different sizes but also have different locations, meaning different beam waists d_{i1} and d_{i2} are used. The simulation results of PO, GO and Phase Matching are shown below.

Figure 3.10-15 illustrate the comparison of the Phase Matching method with PO. In all these figures, it can be observed that the GO method loses its accuracy, with field amplitude deviation running to tens of dB. That is because the equations of the GO Method in section 3.2 are not designed for general, astigmatic, Gaussian beams. Also, it is to be emphasised that it does not mean the entire GO method is unsuitable for handling astigmatic Gaussian beams; it only refers to the equations of section 3.2. Contrariwise, the Phasing Matching reflection method is suitable for general, astigmatic, incident Gaussian beams, and the field deviation remains at ± 2.5 dB within a $\pm\ 50\lambda$ range, even when the incident angle is $\theta_i = 30^\circ$.

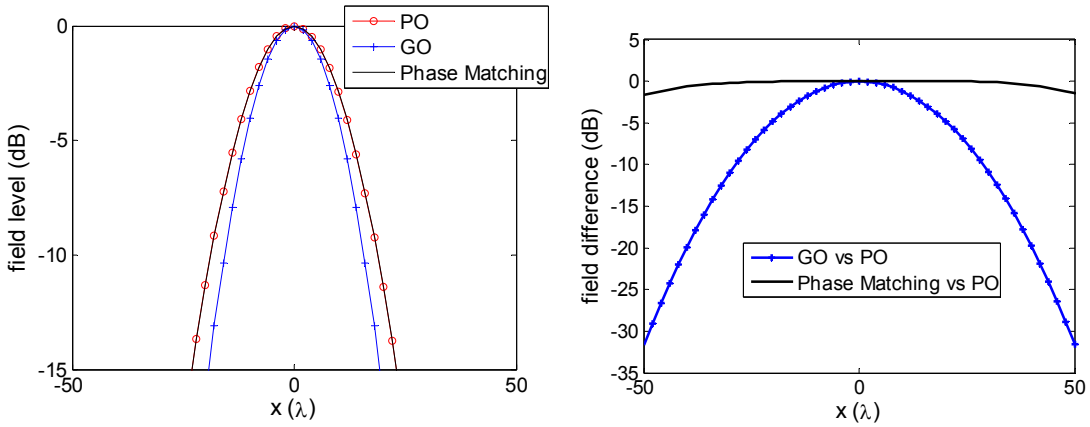

Figure 3.10 Simulation results of general astigmatic Gaussian beam reflection from a concave surface by PO, GO and Phase Matching methods with incident beam and surface parameters $w_{i1} = 3\lambda$ **,** $w_{i2} = 1.5\lambda$ **,** $d_{i1} = d_{i2} = 20\lambda$ **,** $\theta_i = 0^\circ$ **,** $R_1 = -80\lambda$ **,** $R_2 = -60\lambda$ **.**

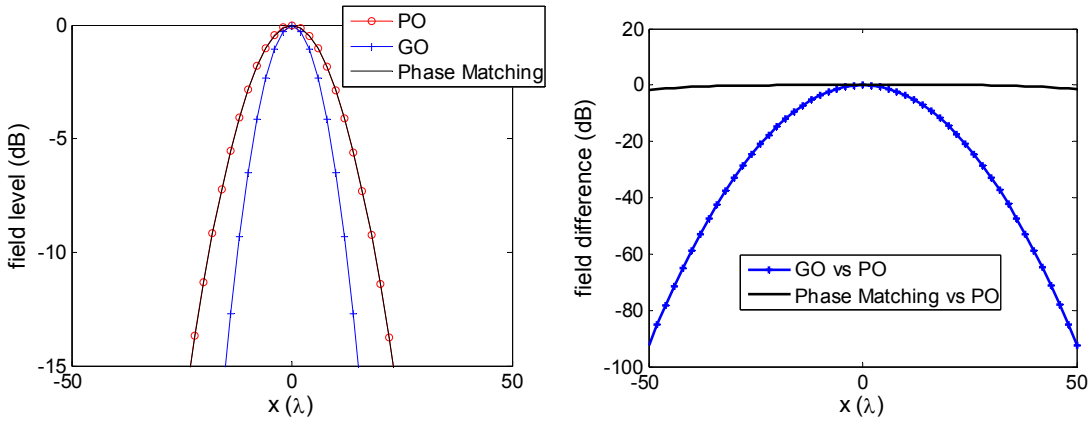

Figure 3.11 Simulation results of general astigmatic Gaussian beam reflection from a concave surface by PO, GO and Phase Matching methods with incident beam and surface parameters $w_{i1}=3\lambda$, $w_{i2}=1.5\lambda$, $d_{i1}=20\lambda$, $d_{i2}=30\lambda$, $\theta_i=0^\circ$, $R_1=-80\lambda$, $R_2=-60\lambda$.

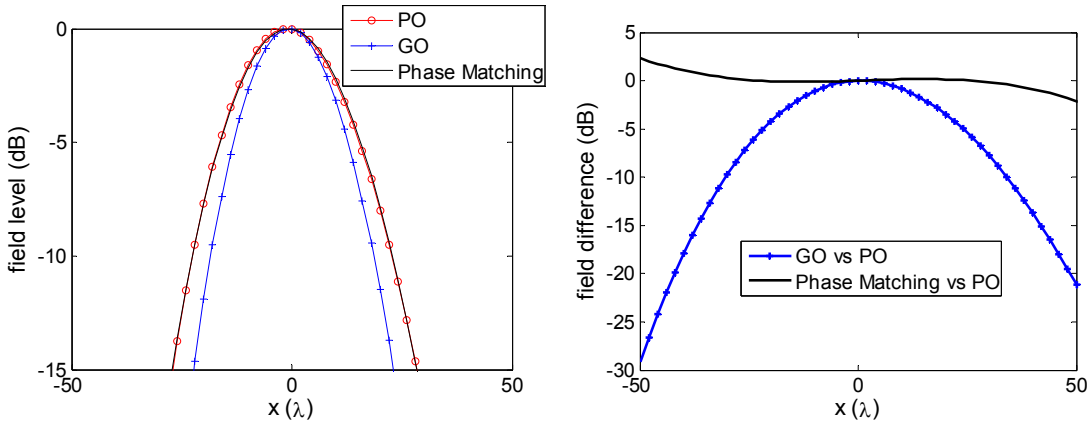

Figure 3.12 Simulation results of general astigmatic Gaussian beam reflection from a concave surface by PO, GO and Phase Matching methods with incident beam and surface parameters $w_{i1}=3\lambda$, $w_{i2}=1.5\lambda$, $d_{i1}=20\lambda$, $d_{i2}=30\lambda$, $\theta_i=30^\circ$, $R_1=-80\lambda$, $R_2=-60\lambda$.

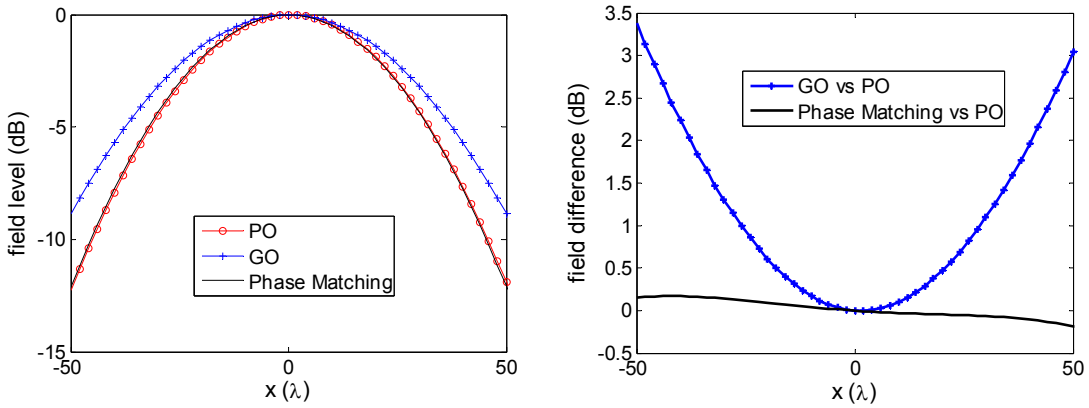

Figure 3.13 Simulation results of general astigmatic Gaussian beam reflection from a concave surface by PO, GO and Phase Matching methods with incident beam and surface parameters $w_{i1}=3\lambda$, $w_{i2}=1.5\lambda$, $d_{i1}=d_{i2}=20\lambda$, $\theta_i=0^\circ$, $R_1=60\lambda$, $R_2=80\lambda$.

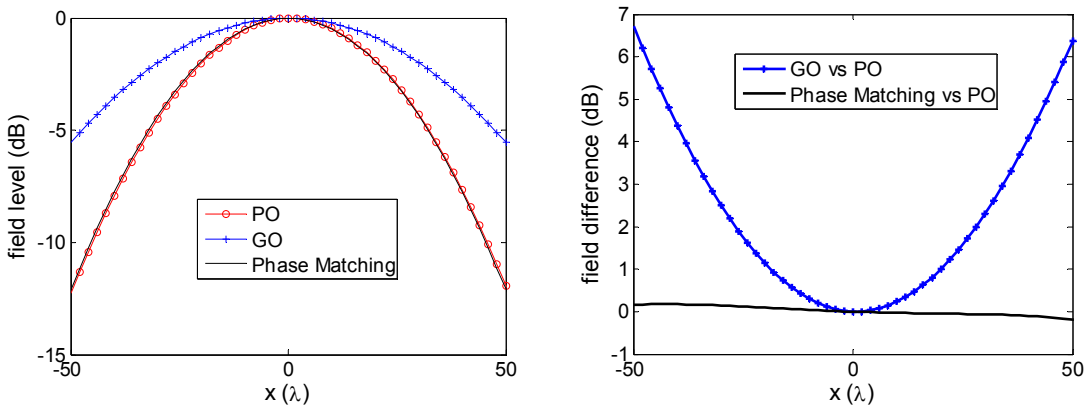

Figure 3.14 Simulation results of general astigmatic Gaussian beam reflection from a concave surface by PO, GO and Phase Matching methods with incident beam and surface parameters $w_{i1}=3\lambda$, $w_{i2}=1.5\lambda$, $d_{i1}=20\lambda$, $d_{i2}=15\lambda$, $\theta_i=0^\circ$, $R_1=60\lambda$, $R_2=80\lambda$.

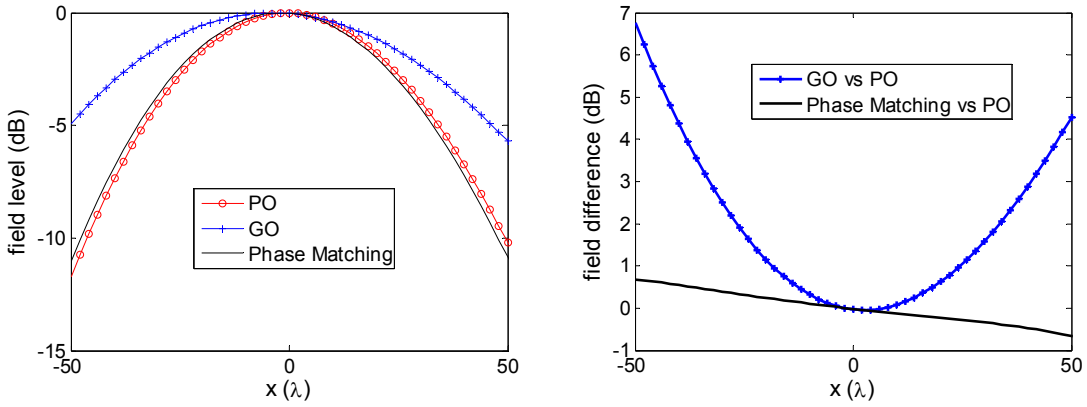

Figure 3.15 Simulation results of general astigmatic Gaussian beam reflection from a concave surface by PO, GO and Phase Matching methods with incident beam and surface parameters $w_{i1}=3\lambda$, $w_{i2}=1.5\lambda$, $d_{i1}=20\lambda$, $d_{i2}=15\lambda$, $\theta_i=15^\circ$, $R_1=60\lambda$, $R_2=80\lambda$.

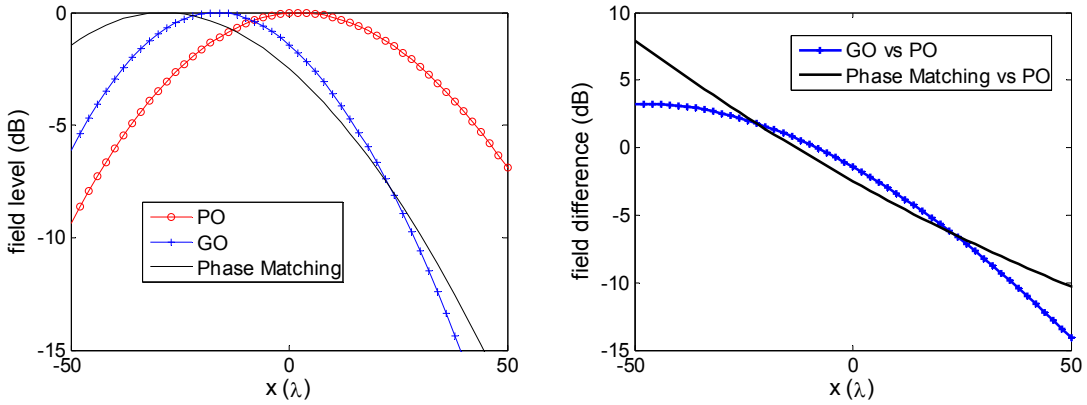

Figure 3.16 Simulation results of general astigmatic Gaussian beam reflection from a concave surface by PO, GO and Phase Matching methods with incident beam and surface parameters $w_{i1}=8\lambda$, $w_{i2}=6\lambda$, $d_{i1}=20\lambda$, $d_{i2}=15\lambda$, $\theta_i=15^\circ$, $R_1=20\lambda$, $R_2=10\lambda$.

As for circular Gaussian beams, in Figure 3.16, the spot-size of the incident general astigmatic Gaussian beam is comparable to the principal curvatures of the surface in the Phase Math method showing an obvious deviation that is more than ±10 dB.

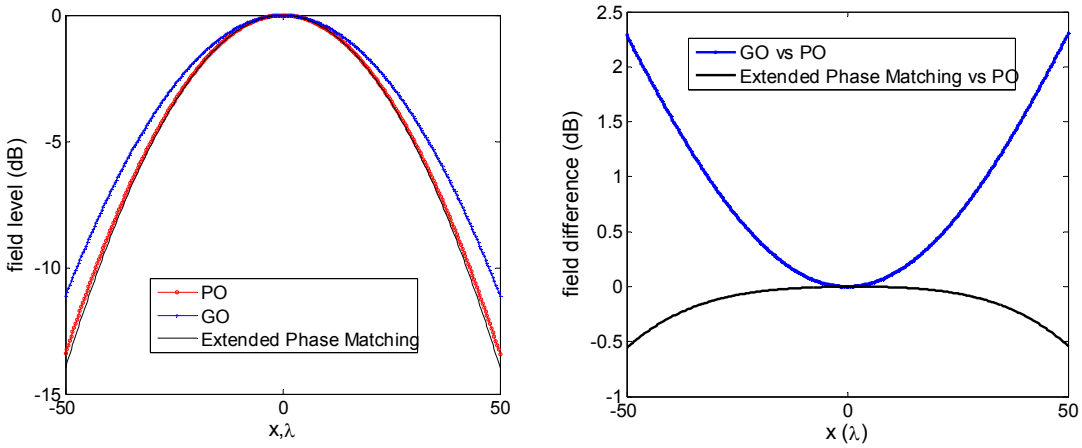

Figure 3.17 Simulation results of circular Gaussian beam reflection from a concave surface by PO, GO and Phase Matching methods with incident beam and surface parameters $w_{i1}=3\lambda$, $w_{i2}=1.5\lambda$, $d_{i1}=20\lambda$, $d_{i2}=15\lambda$, $\theta_i=0^\circ$, $\varphi_i=15^\circ$, $R_1=-80\lambda$, $R_2=-60\lambda$.

In the previous cases, all the projecting directions of the incident beam are along $+x$ direction. However, in this case, an incident angle of $\varphi_i=15^\circ$ is taken, as shown in Figure 3.4. Therefore, the extended Phase Matching method of section 3.3.2 should be implemented. For simplicity, the reflected field is calculated at a field cut at $(y=0, z=300\lambda)$. Other parameters can be found in the caption of Figure 3.17.

It can be observed that, by using the extended Phase Matching method, only a -0.56 dB field amplitude deviation is introduced within a ± 50λ range. Therefore, the extended Phase Matching method is accurate for analysing Gaussian beam reflection of a curved surface.

3.6 Summary

The treatment of Gaussian beam reflection by using the PO, GO and the Phase Matching methods are introduced in this chapter. The extended Phase Matching method has been verified to be a more accurate analysis method than the GO in 2D-DGBA for examining reflection of a general, elliptical, astigmatic Gaussian beam incidence from an arbitrary projection onto a curved surface. Only a ± 2.5 dB field amplitude deviation can be observed within ± 50λ range when the incident angle $\theta_i<30^\circ$ and $\varphi_i<15^\circ$, in

comparison with tens of dB field amplitude deviation of GO in 2D-DGBA. Also, the result can be described in the form of a general, elliptic, astigmatic, Gaussian beam.

References

[1] G. C. Zogbi, "Reflection and diffraction of general astigmatic Gaussian beam from curved surfaces and edges [D]", Ph.D. dissertation, The Ohio State University, Columbus, OH, USA, Jun. 1994.

[2] G.L.James, Geometrical Theory of Diffraction for Electromagnetic Waves, Chapter 4, ThirdEdition Revised, Peregrinus, London, 1986.

[3] C. Rieckmann, "SOFTWARE USER'S MANUAL FOR THE DIFFRACTED GAUSSIAN BEAM ANALYSIS (DGBA) TOOL FOR A SINGLE REFLECTOR" [R], Queen Mary and Westfield College, 1999.

[4] C. Rieckmann, "UPDATE OF THE SOFTWARE USER'S MANUAL FOR THE DIFFRACTED GAUSSIAN BEAM ANALYSIS (DGBA) TOOL" [R], Queen Mary College, University of London, 2007

[5] C. Rieckmann, M. R. Rayner, C. G. Parini, D. H.Martin and R.S.Donnan, "Novel modular approach based on Gaussian beam diffraction for analyzing quasi-optical multi-reflector antennas", IEE Proc.-Microw. Antennas Propag., 149, No. 3, June 2002.

[6] Keller, Joseph B. "Geometrical theory of diffraction." JOSA 52.2 (1962): 116-130.

[7] James G L. Geometrical theory of diffraction for electromagnetic waves[M]. IET, 1986.

[8] Bowman J J, Senior T B, Uslenghi P L. Electromagnetic and acoustic scattering by simple shapes[R]. MICHIGAN UNIV ANN ARBOR RADIATION LAB, 1970.

[9] Ufimtsev P Y. Fundamentals of the physical theory of diffraction[M]. John Wiley & Sons, 2007

[10] Deschamps G A. Ray techniques in electromagnetics[J]. Proceedings of the IEEE, 1972, 60(9): 1022-1035.

Chapter 4 2D Gaussian Beam Diffraction on a Half-Plane

4.1 Overview

This chapter presents two kinds of method for analysing Gaussian beam diffraction on a half screen in two-dimensional space. The first is canonical Gaussian beam boundary diffraction wave (BDW) theory applied to a Kirchhoff half-screen [1], and the other is Gaussian beam summation (GBS) in half plane diffraction [2].

4.2 Boundary diffraction wave theory in 2D-DGBA

4.2.1 Principles of BDW theory in 2D-DGBA

In 2D-DGBA, diffraction by reflectors is calculated using the asymptotic solution of a canonical problem of a Gaussian beam, with a circular spot, normally-incident upon an opaque Kirchhoff half-screen. This is based on the boundary diffraction wave (BDW) theory [1].

Figure 4.1 illustrates the geometry of the problem. It is assumed that the incident Gaussian beam propagates along the z-axis. The scalar field of the incident Gaussian beam is given by equation (2.8). Rewritten in Cartesian coordinates

$$U_i(x,y,z)=\frac{q(0)}{q(z)}\exp(jk_0\varphi(x,y,z)) \ , \tag{4.1}$$

where， $\phi(x,y,z)=z+\dfrac{x^2+y^2}{2q(z)}$ and $q(z)=z+z_0-\pi\dfrac{w_0^2}{\lambda}$.

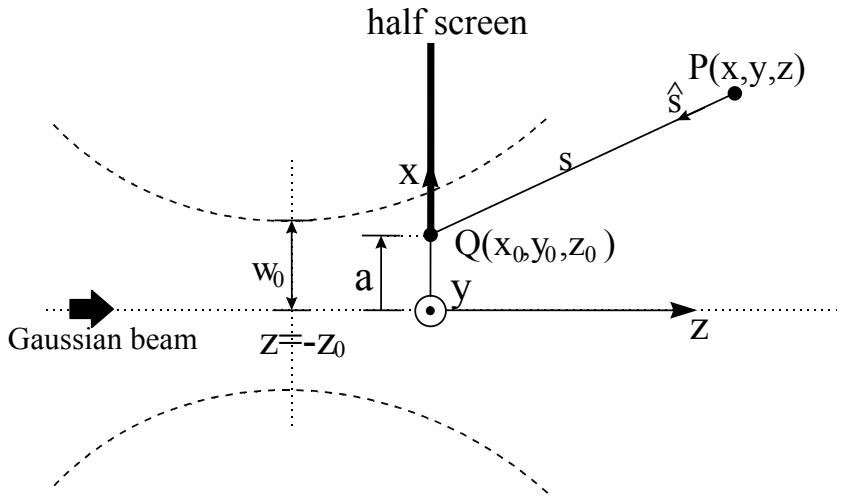

Figure 4.1 Geometry of boundary diffraction wave (forward-scattering region). An incident Gaussian beam with beam waist w_0 at $z=-z_0$ normally impinges upon a half-screen $(x>a, z=0)$. The Gaussian beam is propagating along the z-axis. $Q(x_0,y_0,z_0)$ is a source-point of boundary-diffraction located on the boundary of the half-screen and $P(x,y,z)$ represents the observation point. [1]

The incident beam waist is located at $z=-z_0$. $Q(x_0,y_0,z_0)$ is a source-point of boundary-diffraction located on the boundary Γ of the half-screen. The total diffracted field $U_k(P)$ in the space $z>0$ at observation point $P(x,y,z)$ is given by

$$U_K(P)=U_B(P)+\sum_i F_i(P)\,, \tag{4.2}$$

where the second term $\sum_i F_i(P)$ is the contribution from the singularities of a potential $\vec{W}(P,Q)$ in the aperture plane $x<a$, $z=0$. It is generally interpreted as a Geometrical Optics wave. The first term $U_B(P)$ is the boundary diffraction wave, which is given by

$$U_B(P)=\int_\Gamma \vec{W}(P,Q)d\vec{l}=\int_\Gamma U_i(Q)\frac{\exp(jk_0 s)}{4\pi s}\frac{\hat{s}\times\nabla_Q\phi}{1+\hat{s}\cdot\nabla_Q\phi}d\vec{l}\,, \tag{4.3}$$

where $\vec{l}$ is the unit vector tangential to the boundary Γ of the half-screen traced counter-clockwise when viewed from the observation point P. $\hat{s}$ is the unit vector pointing from P to the source point Q and s is the distance between the two points. ∇_Q is the gradient operator taken with respect to the coordinates of Q.

In the paraxial region $(x-x_0)^2+(y-y_0)^2 << (z-z_0)^2$, the total diffracted field can be written as a superposition of the GO incident field and a diffracted field in terms of complementary error functions, given by

$$U_K(P)=\begin{cases} U_i(P)-\dfrac{q(0)}{2q(z)}\operatorname{erfc}(j\left[jk_0(d(y_s)-d(y_p^1))\right]^{\frac{1}{2}}) \\ \cdot\exp(-jk_0(d(y_s)-d(y_p^1)-s(Q_d))U_i(Q_d) & x\le x_s \\ \dfrac{q(0)}{2q(z)}\operatorname{erfc}(-j\left[jk_0(d(y_s)-d(y_p^1))\right]^{\frac{1}{2}}) & x\ge x_s \\ \cdot\exp(-jk_0(d(y_s)-d(y_p^1)-s(Q_d))U_i(Q_d) \end{cases} . \quad (4.4)$$

y_s is a complex saddle-point and y_p^1 is a complex pole of the integral in equation (4.3). They are given by,

$$y_s=\frac{q(0)}{q(z)}y \quad \text{and} \quad (4.5)$$

$$y_p^1=y_s-j\left(a-\frac{q(0)}{q(z)}x\right) . \quad (4.6)$$

The source-point of diffraction is characterised by the complex coordinate $Q_d=(a,y_s,0)$. x_s marks the shadow boundary of the GO field.

After further simplification, equation (4.4) can be written in a more compact form.

$$U_k(P)=U_i(P)\cdot\begin{cases} 1-\dfrac{1}{2}erfc(j[jk_0(d(y_s)-d(y_p^1))]^{\frac{1}{2}}), & x\le x_s \\ \dfrac{1}{2}erfc(j[jk_0(d(y_s)-d(y_p^1))]^{\frac{1}{2}}), & x\ge x_s \end{cases} . \quad (4.7)$$

The method of DGBA focuses on how the BDW solution can be adopted in the context of a single reflector analysis [2, 3]. The formulation cannot be used directly because: (1) compared with the forward region, the backward scattering regions ($z<0$) in the diffracted field are more important when analysing multi-reflector system; and (2), the direction of propagation of the incident beam is not perpendicular to the edge of the half-screen. Figure 4.2 illustrates an equivalent geometry to describe the diffracted field

in the backward-scattering region for oblique incidence. In Figure 4.2, there are three coordinate systems: the half-screen-based coordinate system (x, y, z), the incident-beam coordinate system (x_i, y_i, z_i), and the reflected-beam coordinate system (x_r, y_r, z_r).

For the backward-scattering region, the reflected wave in the backward-scattering region is characterised by an image beam at the opposite side of the half-screen. The image beam is of the same magnitude but opposite in sign to the incident beam. Meanwhile the original coordinate system (x, y, z) has to be transformed to $(-x, y, -z)$. The equivalent half screen must then be complementary to the true half-screen to generate a shadow region in the lower half-space $(x < 0)$. The offset distance a turns into $-a$.

For oblique incidence, we assume an incidence angle notated as ϕ_0. The observation point is described in the half-screen-based cylindrical (ρ, ϕ, y) coordinate system. The transmitted and reflected beams propagate in the $(\pi + \phi_0)$ and $(\pi - \varphi_0)$ directions, respectively. The relationships of the half-screen-based cylindrical (ρ, ϕ, y) coordinate system and the incident/reflected-beam coordinate systems, are given by

$$\begin{pmatrix} z_i \\ x_i \end{pmatrix} = \rho \begin{pmatrix} \cos(\phi - (\pi + \phi_0)) \\ \sin(\phi - (\pi + \phi_0)) \end{pmatrix} + \begin{pmatrix} z_e \cos\phi \\ 0 \end{pmatrix} \text{ and} \tag{4.8}$$

$$\begin{pmatrix} z_r \\ x_r \end{pmatrix} = \rho \begin{pmatrix} \cos(\phi - (\pi - \phi_0)) \\ \sin(\phi - (\pi - \phi_0)) \end{pmatrix} + \begin{pmatrix} z_e \cos\phi_0 \\ 0 \end{pmatrix}. \tag{4.9}$$

Since the boundary diffraction field is obtained as a line integral along the edge and is independent of the normal facing of the half-screen, the equations of the canonical problem above can be applied in terms of the reflected-beam coordinate system. The offset distance a from the edge is related to the axial position z_e of the edge in the half-screen-based coordinate system and is given by $a = z_e \sin\phi_0$.

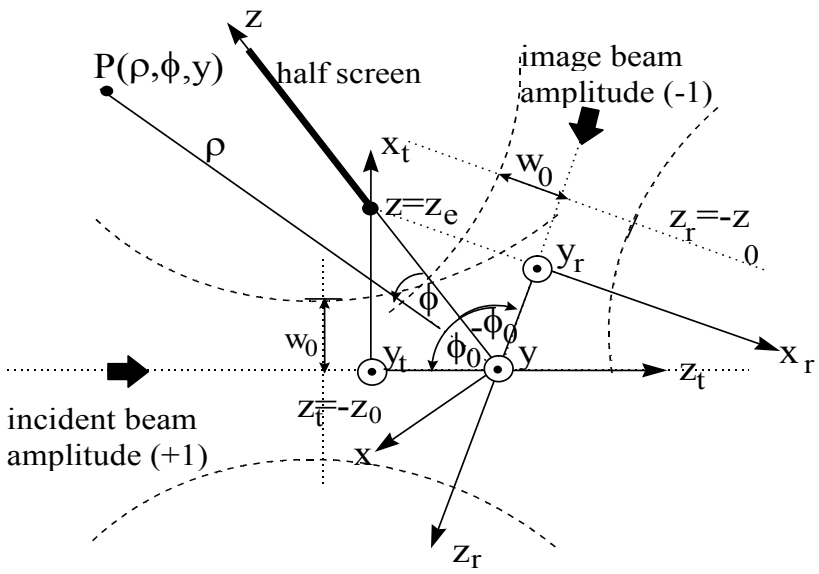

Figure 4.2 Equivalent geometry for determining the diffracted field in the backward-scattering region at oblique incidence. An incident Gaussian beam with beam waist w_0 at $z_t = -z_0$ obliquely impinges upon a half-screen $(z > z_e, x = 0)$. The incident Gaussian beam is propagating along the z_t-axis with reflected beam along z_r-axis. Three coordinate systems are constructed: the transmitted beam related coordinate system (x_t, y_t, z_t), the reflected beam related coordinate system (x_r, y_r, z_r), and the half-screen based coordinate system (x, y, z). The incidence angle is ϕ_0 and the observation point is described in the half-screen-based cylindrical (ρ, ϕ, y) coordinate system. The diffracted field in the backward-scattering region is characterised by an image beam with same magnitude but opposite in sign to the incident beam at the opposite side of the half-screen. [4]

4.2.2 Limitations and approximations of the BDW method in 2D-DGBA

4.2.2.1 Circular incident beams limitation

In 2D-DGBA, both reflection and diffraction methods can only deal with diffraction of stigmatic Gaussian beams with a circular spot. Rieckmann *et al* undertook a comparison of the canonical Kirchhoff half-screen BDW theory in comparison with PO for an incident elliptical Gaussian [3]. For normal incidence, the fields in the back-scatter region at a distance of 300λ are shown for various angles α characterising the principal directions. The elliptical Gaussian beam is assumed propagating in z-direction and is characterised by two principal directions of curvature $\hat{\xi}, \hat{\eta}$ in the transverse xy-plane

such that $\begin{pmatrix}\hat{\xi}\\ \hat{\eta}\end{pmatrix}=\begin{bmatrix}\cos(\alpha) & -\sin(\alpha)\\ \sin(\alpha) & \cos(\alpha)\end{bmatrix}\begin{pmatrix}\hat{x}\\ \hat{y}\end{pmatrix}$. The agreement is not brilliant and deviations of several dB are observed, as shown in Figure 4.3.

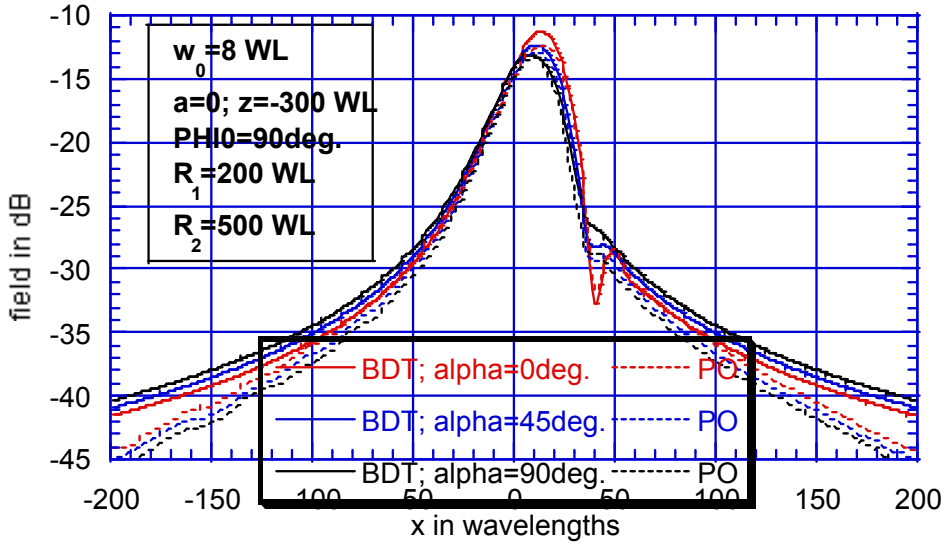

Figure 4.3 Simulated backscattered field with Boundary diffraction wave theory (BDT) in 2D-DGBA and PO for a normally incident elliptical Gaussian beam. The two principal radii of curvature at the diffracting edge are 200λ and 500λ, respectively. The beam half width is 8λ. The diffracted field is simulated at a distance of 300λ for various angles α characterising the principal directions. [4]

4.2.2.2 Circular emergent beams approximation

It is well-known that after reflection and scattering by a reflector, beams become astigmatic (elliptical). As mentioned in Chapter3, in 2D-DGBA, when dealing with reflection, elliptical reflected beams are used and the reflected field is given by (3.15) to be

$$E^r = E_0\sqrt{\frac{q_1^r q_2^r}{(z_r+q_1^r)(z_r+q_2^r)}}e^{-jk_z z}\cdot e^{\frac{j}{2k}\left[\frac{x_r^2}{z_r+q_1^r}+\frac{y_r^2}{z_r+q_2^r}\right]} \quad . \tag{4.10}$$

However, classic Kirchhoff half-screen boundary diffraction theory fails because the locations of the poles are not symmetric with respect to the stationary point. Therefore, although the two principal radii of the emergent beam R_1^r and R_2^r can be calculated in

2D-DGBA, when dealing with diffraction, the reflected elliptical beams are approximated by a circular beam with a complex beam parameter of λ

$$q = (\frac{1}{\sqrt{R_1^r R_2^r}} + j\frac{\lambda}{\pi w^2})^{-1} \ . \tag{4.11}$$

4.2.2.3 Normal polar incidence approximation

2D-DGBA uses Kirchhoff half-screen boundary-diffraction theory, which deals with the diffraction of a Gaussian beam normally incident upon a Kirchhoff half-screen. This means that it can only handle normal incidence (the angle $\theta_i = \frac{\pi}{2}$ and the incident beam is parallel to the xy-plane in Figure 4.4). Here, a Cartesian coordinate system (x, y, z) is used to describe the half plane ($z = 0, x > 0$).Spherical polar coordinates $(\rho_i, \theta_i, \varphi_i)$ are used to describe the incident beam.

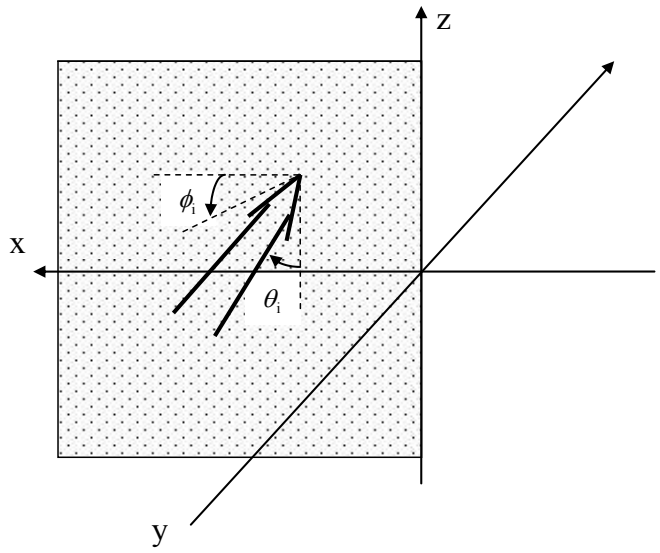

Figure 4.4 A Gaussian beam (the arrow in the figure) impinges on a half-plane $(y = 0, x \geq 0)$ in an arbitrary direction of (φ_i, θ_i). However, in 2D-DGBA, all the incident beams are approximated by the beams that normally impinge the half plane ($\theta_i = \pi / 2$).

The errors introduced by this approximation will be discussed in Chapter 5. The conclusion is that Kirchhoff half-screen BDT is not correct outside the paraxial region, and more than 50 dB field deviation can be observed with respect to PO.

4.2.2.4 Oblique azimuth angle incidence error

Figure 4.5 shows a comparison of 2D-DGBA with Physical Optics for various azimuth incident angles φ_i illustrated in Figure 4.4, where normal incidence of the polar angle is assumed ($\theta_i = \frac{\pi}{2}$). The incident beam impinges on the edge of the half plane. The field is calculated for a near-field cut with the coordinates ($y = 0; z = -300\lambda$). The beam-width w_0 has been chosen to be 8λ. Deviations are noted to be quite small for normal incidence and become progressively larger for more oblique azimuth angles of incidence. It is observed that at even only 10° off from normal incidence, errors appear in the main lobe.

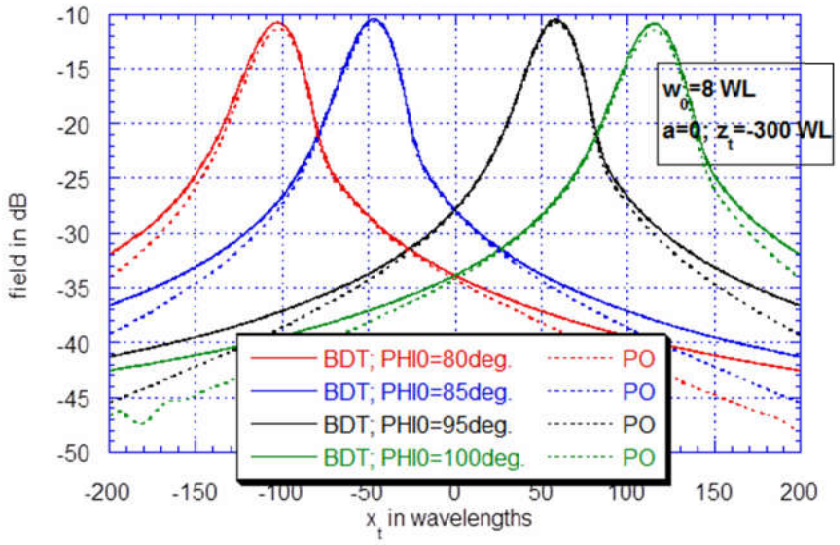

Figure 4.5 Simulated backscattered field with BDT in 2D-DGBA and PO for various azimuth angle φ_i of the incident beam, with polar angle normal incidence ($\theta_i = 90°$). The field are calculated for a nearfield cut with the coordinates ($y = 0; z = -300\lambda$), based on the modelled scenario of Fig. 4.1. The parameter a is chosen to be zero and the half beam width w_0 is 8λ. [3]

According to these limitations and approximations, canonical Kirchhoff half-screen BDW theory can only be considered as a "2.5D" diffraction theory.

4.3 Gaussian beam summation method in half plane diffraction

By using equation (4.7), the canonical Gaussian beam Kirchhoff half-screen boundary-diffraction method accounts for the diffraction field rather than for diffracted beams. In reference [2], a 2D GBS method is presented dealing with half-plane Gaussian beam diffraction. In this GBS method, the scattered field is expressed as a sum of diffracted beams in all directions emerging from the edge, as shown in Figure 4.6.

Consider now a perfectly conducting half-plane located along the x axis at $(x \geq 0)$. A Gaussian beam B_i illuminates the half plane at azimuth angle ϕ_0 relative to the x axis. σ_0 is the distance along the principal axis of the incident beam and between the beam waist of the incident Gaussian beam and the edge. η_0 is the distance in the direction transverse to the principle axis of the incident beam and between the centre of the beam waist and the edge. So the displacement of the incident Gaussian beam from the edge can be described by (σ_0, η_0) in the (σ_i, η_i) coordinate system, with the edge locating at the $(x = 0, y = 0)$. The observation point is $\mathbf{r} = (x, y) = (r, \phi)$ in the 2D coordinate system.

The total field is given by, for $\eta \leq 0$,

$$u(\mathbf{r}) = B_i(\mathbf{r}) + u_s(\mathbf{r}), \tag{4.12}$$

with

$$u_s(\mathbf{r}) = \frac{j}{4\pi} \sum_n \delta\alpha \Phi(\alpha_n) B(\mathbf{r}, \alpha_n). \tag{4.13}$$

For $\eta \geq 0$,

$$u(\mathbf{r}) = \begin{cases} B_i(\mathbf{r}) + B_r(\mathbf{r}) + \breve{u}_s(\mathbf{r}), & 0 \leq \phi \leq \pi \\ \breve{u}_s(\mathbf{r}), & \pi \leq \phi \leq 2\pi \end{cases}, \tag{4.14}$$

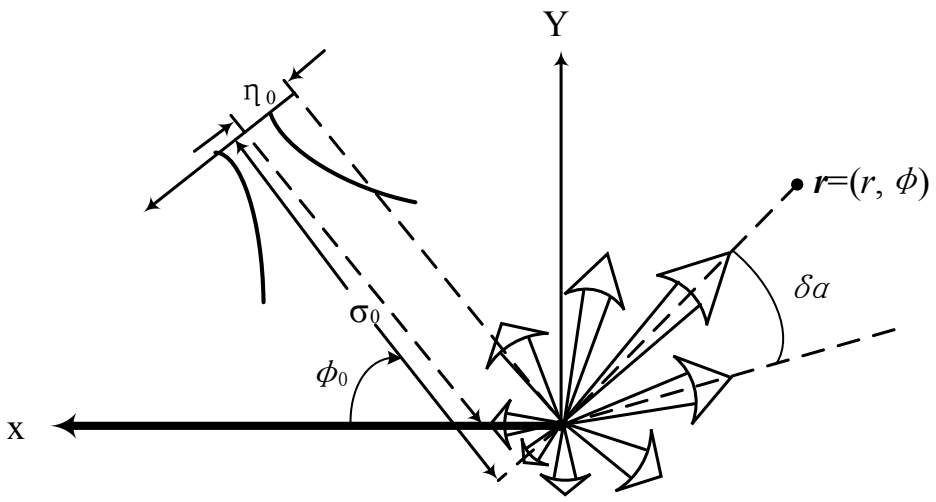

Figure 4.6 Geometry for determining the problem of 2D Gaussian beam summation method. A Gaussian beam impinges upon a half-plane at an angle φ_0. σ_0 is the distance of the edge from the beam waist, and η_0 is that from the beam axis which describes the incident beam displacement from the edge. The scattered field is described as a sum of Gaussian beam emerging from the edge in all directions with the spectral discretization $\delta\alpha$. The observation point is $\mathbf{r} = (r, \phi)$, [2].

in which

$$\breve{u}_s(\mathbf{r}) = \frac{j}{4\pi}\sum_n \delta\alpha \breve{\Phi}(\alpha_n) B_{2\mathrm{D}}(\mathbf{r}, \alpha_n) \ . \tag{4.15}$$

It can be seen that all the diffracted beams $B(\mathbf{r}, \alpha_n)$ emerge from the edge, and later it will be noted that each is in the form of a Gaussian beam

$$B_{2\mathrm{D}}(\mathbf{r}, \alpha) = \sqrt{\frac{-jZ_R}{\sigma - jZ_R}} e^{jk(\sigma + \frac{1}{2}\frac{\eta^2}{\sigma - jZ_R})}, \quad \sigma > 0 \tag{4.16}$$

with

$$Z_R = b_t = \frac{\pi w_0^2}{\lambda} \text{ and }, \tag{4.17}$$

$$(\sigma, \eta) = r(\cos(\alpha - \phi), \sin(\alpha - \phi)) . \tag{4.18}$$

Z_R is the Rayleigh range. As illustrated in Figure 4.6, a spectral distance between the two adjacent diffracted Gaussian beams is $\delta\alpha$.

Since (4.13) and (4.15) show two Gaussian beams with scatting matrices (each otherwise termed a "spectral function") Φ and $\breve{\Phi}$, this method can be referred to as a beam-to-beam GBS method.

The spectral functions Φ and $\breve{\Phi}$ in (4.13) and (4.15) are

$$\Phi(\alpha,\zeta)=\sqrt{\frac{jkq_0}{2}}B_i(0)\left\{-j\sqrt{\pi}e^{-s_{p\pm}^2}D_p erfc(is_{p\pm})+\bar{G}(0)\right\} \tag{4.19}$$

$$\breve{\Phi}(\alpha,\zeta)=\sqrt{\frac{jkq_0}{2}}B_i(0)\left\{j\sqrt{\pi}e^{-s_{p\pm}^2}D_{p\pm} erfc(-js_{p\pm})+\bar{G}(0)\right\} \tag{4.20}$$

where

$$\bar{G}(0)=\sqrt{\frac{2}{jkq_0}}\left\{D(\alpha-\alpha_s')+\frac{D_{p\pm}}{\alpha_s'-\alpha_{p\pm}'}\right\} \quad \text{and} \tag{4.21}$$

$$D(\alpha,\alpha')=\varepsilon\sec\frac{1}{2}(\alpha+\alpha')-\sec\frac{1}{2}(\alpha-\alpha') \ . \tag{4.22}$$

α_s' is the stationary phase point of the spectral expression of the incident Gaussian beam, with q_0=σ_0-z_R, which measures the complex radius of curvature of the incident beam. $\alpha_{p\pm}'$ are the poles of $D(\alpha,\alpha')$:

$$\alpha_s'=\phi_0-\eta_0/q_0 \quad \text{and} \tag{4.23}$$

$$\alpha_{p\pm}'=\begin{cases}\pi-\alpha & if \quad \alpha\in C_+\\ \alpha-\pi & if \quad \alpha\in C_-\end{cases}. \tag{4.24}$$

$s_{p\pm}$ is the distance between $\alpha_{p\pm}'$ and α_s', thus

$$s_{p\pm}\simeq\sqrt{\frac{1}{2}ikq_0}[(\alpha_{p\pm}'-\alpha_s')]. \tag{4.25}$$

$B_i(0)$ in (4.19), and (4.20) is the field of the incident beam at the edge and is given by

$$B_i(0)=A_i\sqrt{-jb_t/q_0}\,e^{jk(\sigma_0+\frac{\eta^2}{q_0})} \ . \tag{4.26}$$

Some typical examples of Φ patterns are given. In the first example, we assume the incident Gaussian beam as a stigmatic beam with $\delta_{11}=\delta_{22}=1$, $\delta_{12}=\delta_{21}=0$. The frequency is set to 100 GHz and the beam-waist of the incident beam is 8λ and located at $\sigma_0=100\lambda$. The incident Gaussian beam intersects the half plane at $(x_0=8\lambda, y_0=0)$ or $(\sigma_0=100\lambda, \eta_0=8\lambda)$. The patterns of $\breve{\Phi}$ in the scattering field produced by a normally incident beam are shown in Figure 4.7.

Figure 4.8 is the absolute value of $\breve{\Phi}$ in the second example. This example is like the first, but with the azimuth angle set at $\phi_0=\frac{\pi}{4}$. Also, the displacement of the incident Gaussian beam is $(\sigma_0=100\lambda, \eta_0=8\lambda)$.

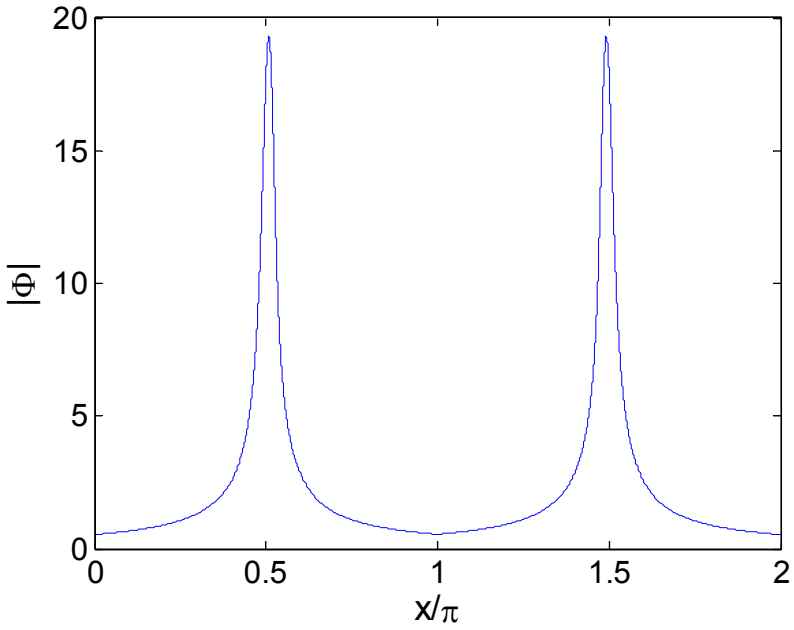

Figure 4.7 For $\alpha\in(0,2\pi)$, the result of spectral function $|\breve{\Phi}|$ with a stigmatic incident Gaussian beam ($\delta_{11}=\delta_{22}=1$, $\delta_{12}=\delta_{21}=0$, $w_0=8\lambda$) intersecting the half plane at $(\sigma_0=100\lambda, \eta_0=8\lambda)$ in the direction of $\phi_0=\pi/2$.

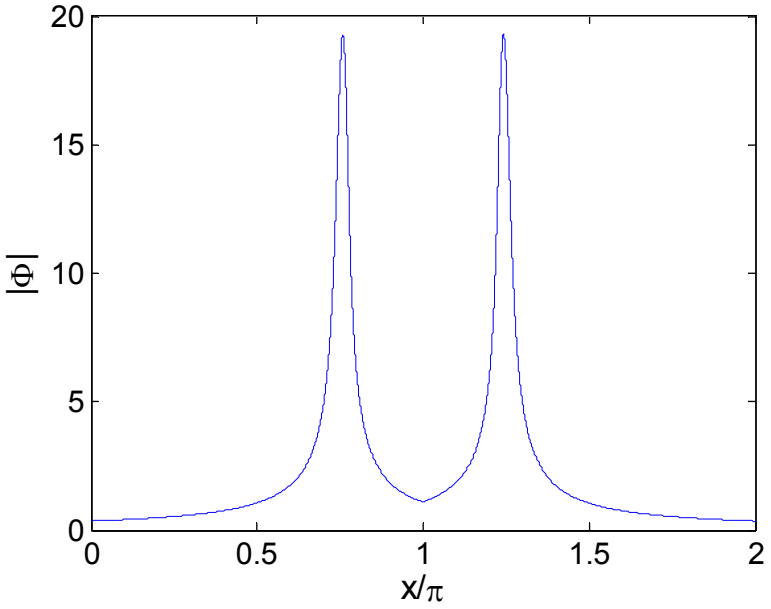

Figure 4.8 For $\alpha \in (0,2\pi)$, the result of spectral function $\left|\breve{\Phi}\right|$ with a stigmatic incident Gaussian beam ($\delta_{11}=\delta_{22}=1, \delta_{12}=\delta_{21}=0, w_0=8\lambda$) intersects the half plane at $(\sigma_0=100\lambda, \eta_0=8\lambda)$ in the direction of $\phi_0=\pi/4$.

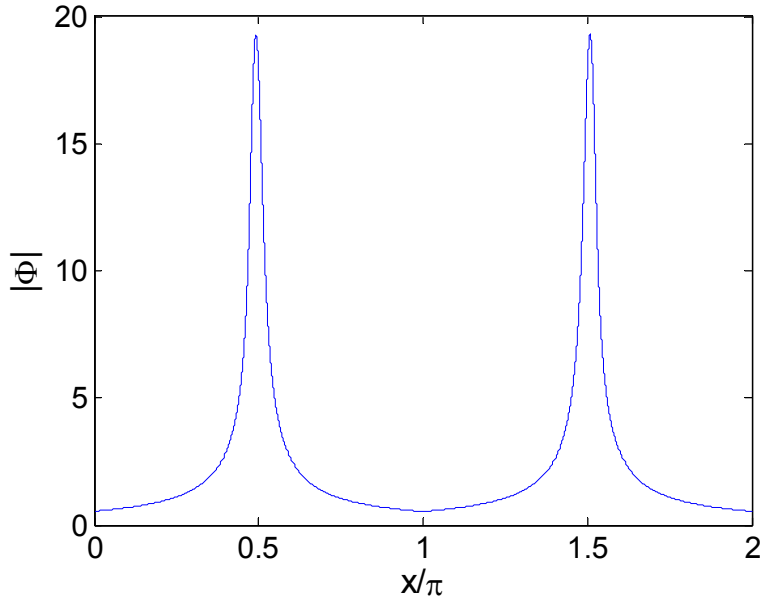

Figure 4.9 For $\alpha \in (0,2\pi)$, the result of spectral function $\left|\breve{\Phi}\right|$ with a stigmatic incident Gaussian beam ($\delta_{11}=\delta_{22}=1, \delta_{12}=\delta_{21}=0, w_0=8\lambda$) intersecting the half plane at $(\sigma_0=100\lambda, \eta_0=-8\lambda)$ in the direction of $\phi_0=\pi/2$.

The third example is for negative η_0 and Φ is chosen to replace $\breve{\Phi}$. All the parameters of the third example are the same as for the first, but for a displacement of incident Gaussian beam being $(\sigma_0 = 100\lambda, \eta_0 = -8\lambda)$. The result is shown in Figure 4.9.

It can be seen that the results in Figure 4.9 are quite similar with those in Figure 4.7. That is because both Φ in (4.19) and $\breve{\Phi}$ (4.20) are independent of η_0. Though similar, they are not exactly the same. To show the difference of Φ and $\breve{\Phi}$, results of the first and third case are compared. Figure 4.10 gives the results. The errors of 2D GBS by using Φ and $\breve{\Phi}$ are also discussed by Katsav *et al* [2]. The conclusion is that Φ is preferable when the incident beam passes near the half-plane and $\breve{\Phi}$ is suitable when it hits the half plane.

It should be noticed that the GBS method is limited to 2D, since the observation-point has to be in the same plane defined by the incident and emergent Gaussian beams.

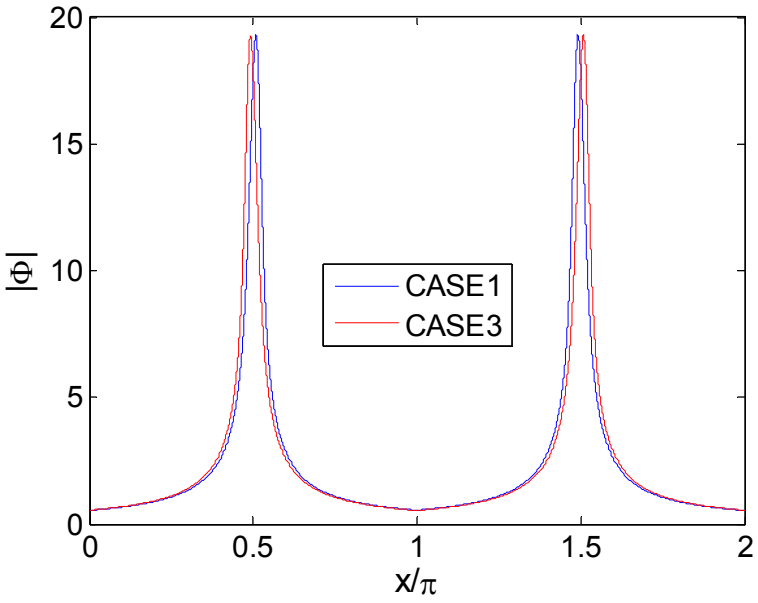

Figure 4.10 For $\alpha \in (0, 2\pi)$, the result of spectral function $|\breve{\Phi}|$ with a stigmatic incident Gaussian beam ($\delta_{11} = \delta_{22} = 1, \delta_{12} = \delta_{21} = 0$, $w_0 = 8\lambda$) intersecting the half plane in the direction of $\phi_0 = \pi/2$. The blue line represents the result with the intersection-point located at $(\sigma_0 = 100\lambda, \eta_0 = 8\lambda)$, and the black line is that with the intersection-point at $(\sigma_0 = 100\lambda, \eta_0 = -8\lambda)$.

4.4 Numerical verification

In this section, three numerical experiments are conducted to validate the 2D Gaussian beam summation method for half-plane diffraction in comparison with GRASP and Kirchhoff half-screen boundary-diffraction theory used in 2D-DGBA.

The geometry of the problem is illustrated in Figure 4.6. The frequency of all the incident beams is set to 100 GHz. In all these cases, the red line with data marked with 'o' is the field simulated by PO. The blue line with data marked with '+' is that simulated by 2D-BDT. The last is 2D-GBS and is the black dash curve. The scenarios used for analysis of PO are similar to those to come in Chapter 5.

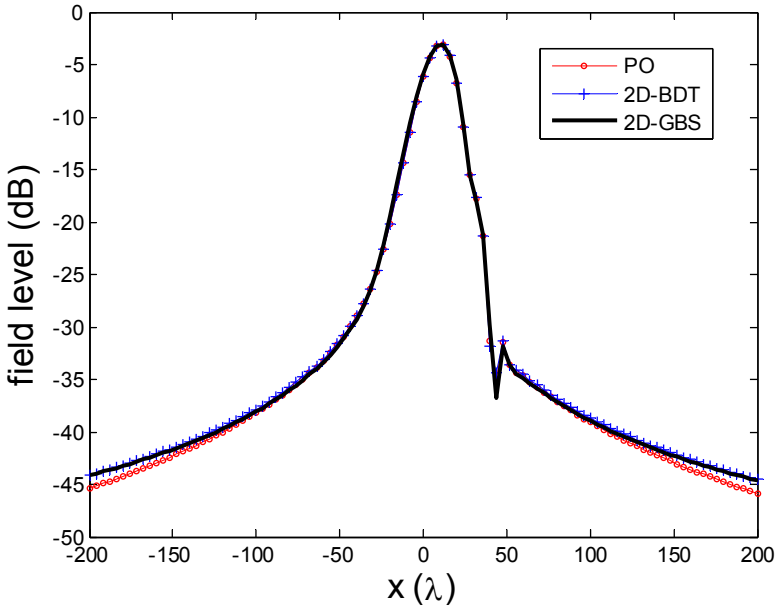

Figure 4.11 Comparison of the backward scattered field at $(y = 300\lambda)$ with physical optics and 2D Kirchhoff half-screen BDT with a stigmatic incident Gaussian beam ($w_0 = 8\lambda$) impinging on the half plane at $(\sigma_0 = 100\lambda, \eta_0 = 8\lambda)$ in the direction of $\phi_0 = \pi/2$.

In the first scenario, the simulation results of an incident Gaussian beam perpendicularly impinging on the half plane at $(x_0 = 8\lambda, y_0 = 0)$ in the direction of $\phi_0 = \pi/2$; i.e. the $-y$ direction is compared. The beam width w_0 (e^{-1}) has been chosen to be eight wavelengths wide and be located 100λ from the half-plane, i.e. $(\sigma_0 = 100\lambda, \eta_0 = 8\lambda)$. The backward field is of more importance when analysing a QoN or multi-reflector

system. So, the fields, presented in Figure 4.11, are calculated for a backward near field cut at $(y = 300\lambda)$.

In the second scenario, the same model is loaded as for the first but with $(\sigma_0 = 100\lambda, \eta_0 = -8\lambda)$. Corresponding to this negative η_0, Φ is used instead of $\breve{\Phi}$. Figure 4.12 shows the simulated result. We can see that no matter whether η_0 is positive or negative, both 2D-BDT and 2D-GBS yield similar accuracy.

The last scenario is about oblique incidence with $\phi_0 = \pi / 4$, and the displacement of the incident Gaussian beam is $(\sigma_0 = 100\lambda + w_0 \cos\phi_0, \eta_0 = w_0 \sin\phi_0)$. The calculated of the total diffracted field is a backward near field cut away from the half-plane along the principal optical axis of the reflected beam. It is shown in Figure 4.13 that the BDW method losses accuracy in the main lobe in comparison with 2D-DGBA but is still in good agreement with PO.

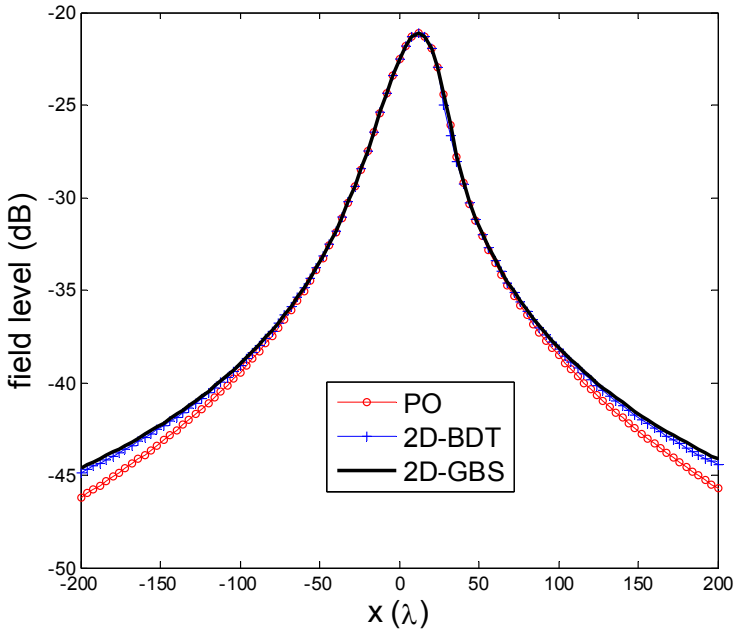

Figure 4.12 Comparison of the backward scattered field at $(y = 300\lambda)$ with physical optics and 2D Kirchhoff half-screen BDT with a stigmatic incident Gaussian beam ($w_0 = 8\lambda$) impinging on half plane out of the edge at $(\sigma_0 = 100\lambda, \eta_0 = -8\lambda)$ in the direction of $\phi_0 = \pi / 2$.

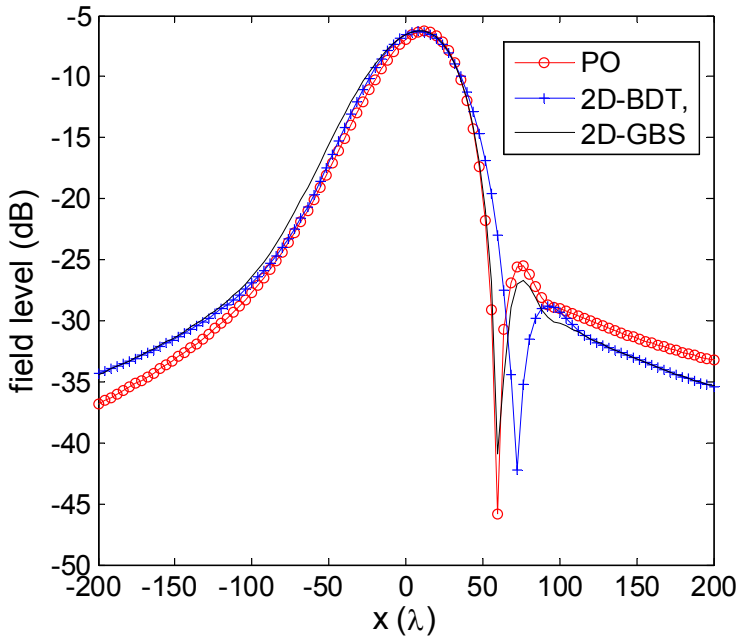

Figure 4.13 Comparison of the backward scattered field (600λ away from the half-plane along the principal optical axis of the reflected beam) with physical optics and 2D Kirchhoff half-screen BDT. The stigmatic oblique incident Gaussian beam ($w_0 = 8\lambda$) impinges on half plane at $(\sigma_0 = 100\lambda + w_0 \cos\phi_0, \eta_0 = w_0 \sin\phi_0)$ in the direction of $\phi_0 = \pi/4$.

Although in the $x-$ direction the results as predicted by using GBS, the half-plane diffraction starts to deviate from PO, but shows a better accuracy than BDW theory used in 2D-DGBA. Field deviation between 2D-GBS and PO holds at ±2.5 dB within a ±200 λ range in comparison with ±20 dB for BDT used in 2D-DGBA.

4.5 Summary

The principles of the canonical Gaussian beam Kirchhoff half-screen BDW method and 2D GBS were introduced. Due to limitations and approximations, especially concerning the normal polar incidence approximation, the BDW method can only be called a 2.5D diffraction method. Since the observation point has to be in the same plane as defined by the incident and emergent Gaussian beams. The GBS method is limited to 2D.

Simulation results of BDW and 2D GBS analysis were compared. For normal incidence, both were verified to be accurate in comparison with PO. However, for oblique

incidence, field deviation between 2D-GBS and PO holds at ±2.5 dB within a ±200 λ range in comparison with ±20 dB of BDT used in 2D-DGBA.

References

[1] T. Takenaka and O. Fukumitsu, "Asymptotic representation of the boundarydiffraction wave far a three-dimensional Gaussian beam incident upon a Kirchhoff halfscreen.", IEEE J. Opt. Soc. Am., vol. 72, no. 3, March 1982, pp. 331-336.

[2] Katsav M, Heyman E. "Gaussian Beam Summation Representation of a Two-Dimensional Gaussian Beam Diffraction by a Half Plane[J]". Antennas & Propagation IEEE Transactions on, 2007, 55(8):2247-2257.

[3] C. Rieckmann, M. R. Rayner, C. G. Parini, D. H.Martin and R.S.Donnan, "Novel modular approach based on Gaussian beam diffraction for analyzing quasi-optical multi-reflector antennas", IEE Proc.-Microw. Antennas Propag., 149, No. 3, June 2002.

[4] C. Rieckmann, "SOFTWARE USER'S MANUAL FOR THE DIFFRACTED GAUSSIAN BEAM ANALYSIS (DGBA) TOOL FOR A SINGLE REFLECTOR" [R], Queen Mary and Westfield College, 1999.

[5] C. Rieckmann, M. R. Rayner, C. G. Parini,"Diffracted Gaussian beam analysis of quasi-optical multi-reflector systems",IEE-ELECTRONICS LETTERS.,vol. 36, No.19, pp 1600-1601,2000.

Chapter 5 3D Gaussian Beam Diffraction on a Half-Plane

5.1 Overview

In 2D-DGBA, the Kirchhoff half-screen boundary-diffraction theory is used to deal with the diffraction of a Gaussian beam with a circular-spot, normally-incident upon a Kirchhoff half-screen. Essentially, this method is a 2.5-D analysis, as discussed in Chapter 4.

In 2009, Katsav and Heyman published a paper "Gaussian Beam Summation (GBS) Representation of Half Plane Diffraction: a Full 3D Formulation," [1]. In this paper, they showed a new method of half-plane diffraction to achieve 3D analysis. The 3D GBS half-plane diffraction analyses a general astigmatic GB impinging upon the half-plane at an arbitrary angle of incidence. The diffracted field is represented as a sum of diffracted GBs emerging from a discrete set of points and directions along the edge, making the calculation in a beam-to-beam (B2B) manner. When deriving the B2B scattering matrix, a phase-space beam expansion along the edge, and angular spectrum of beams around the edge, is utilised to deal with an edge-fixed lattice of expansion beams. The resultant GBS representation of the scattered field is obtained by adding up all the emergent beams.

This chapter covers the principles of 3D GBS half-plane diffraction analysis, which contains spectral representations of the scattered field, 3D GBS analysis and solution in the backward region. A numerical experiment is then conducted to compare the 3D analysis with PO and also the former BDT analysis used in 2D-DGBA.

5.2 Spectral representations of the scattered field

The scattered field described in cylindrical coordinates $\mathbf{r}=(\rho,\phi,\mathrm{z})$ is more conveniently cast as a triple integral spectrum function [2 – 4]; thus

$$u_s=(\frac{k}{2\pi})^2\int_{-\infty}^{\infty}d\zeta\int_{-\infty}^{\infty}d\xi\tilde{B}_i(\boldsymbol{\kappa})e^{ik\zeta z}\frac{i}{4\pi}\times\int_{C\pm}d\alpha D(\alpha,\alpha')e^{ik\varsigma\rho\cos(\alpha-\phi)}. \tag{5.1}$$

$\tilde{B}_i(\boldsymbol{\kappa})$ is the plane wave spectrum of the incident beam (see (2.60)), and the definitions of ξ and ζ are as shown in Chapter 2 for equation (2.41). In relation to the normalised spectral wavenumber $\gamma=\sqrt{1-\boldsymbol{\kappa}\cdot\boldsymbol{\kappa}}$ in the $-y$ direction, for this formulation it is, $\varsigma=\sqrt{1-\zeta^2}$ with $\mathrm{Im}\,\varsigma>0$ in the (x,y) plane, and $\rho=\sqrt{x^2+y^2}$. Here, the inner integral denotes the scattered field with α and α', respectively denoting the azimuthal direction of the emergent plane wave from the edge, and the direction of the incident plane wave. In addition, both directions are related by the spectral diffraction coefficient $D(\alpha,\alpha')$,

$$D(\alpha,\alpha')=\varepsilon\sec\frac{1}{2}(\alpha+\alpha')-\sec\frac{1}{2}(\alpha-\alpha'). \tag{5.2}$$

C_i is determined by $u_R(\mathbf{r})=B_i(\mathbf{r})+B_r(\mathbf{r})$ via $\breve{\Phi}$.

For a given α', the diffraction coefficient $D(\alpha,\alpha')$ has two poles in the α-plane

$$\alpha_{p\pm}=\pi\mp\alpha' \quad . \tag{5.3}$$

The α-integral contours $C_{\pm}$ are defined by

$$C_{\pm}=\begin{cases}\alpha \text{ goes from } i\infty \text{ to } \pi-i\infty, & \text{for } 0<\phi<\pi\\ \alpha \text{ goes from } \pi+i\infty \text{ to } 2\pi-i\infty, & \text{for } \pi<\phi<2\pi\end{cases}. \tag{5.4}$$

Meanwhile, C_+ passes above the pole α_{p+}, and C_- goes below the pole α_{p-}.

Here, Katsav *et al* used an alternative spectral representation of the scattered field rather than (5.1) [1]. This spectral representation along the z-axis is,

$$u_s(\mathbf{r}) = \frac{k}{2\pi}\int_{-\infty}^{\infty} d\zeta e^{ik\zeta z}\tilde{u}_s(\boldsymbol{\rho},\zeta) \tag{5.5}$$

where $\boldsymbol{\rho} = (x, y) = (\rho, \phi)$ describes a 2D coordinate frame perpendicular to the z axis. By replacing the order of the ξ and α integrations in (5.1), the transversal spectral representation is obtained,

$$\tilde{u}_s(\boldsymbol{\rho},\zeta) = \int_{c\pm} d\alpha \Phi(\alpha,\zeta) e^{ik\zeta\rho\cos(\alpha-\phi)} \tag{5.6}$$

with spectral function

$$\Phi(\alpha,\zeta) = \frac{ik}{8\pi^2}\int_{c_i} d\alpha' \gamma \tilde{B}_i(\alpha',\zeta) D(\alpha,\alpha') . \tag{5.7}$$

Here, it should be noticed that the element of integration in (5.7) is α'. Compared with $C_{\pm}$ in (5.1), the contour of integration C_i now extends from $\alpha' = i\infty$ to $\pi - i\infty$ and passes now above the poles of $D(\alpha,\alpha')$ in the α' plane. For a given α, the poles of $D(\alpha,\alpha')$ are easy to find and are given by,

$$\alpha'_{p\pm} = \begin{cases} \pi - \alpha & if \quad \alpha \in C_+ \\ \alpha - \pi & if \quad \alpha \in C_- \end{cases} . \tag{5.8}$$

The details to prove that (5.5) is equivalent to (5.1) can be found in ***Appendix-III.***

5.3 GB summation representation of a 3D diffraction

5.3.1. Total field representations in the forward-scattering region

If the centre of the incident beam does not intersect the half plane, generally, the total field is expressed by

$$u(\mathbf{r}) = B_i(\mathbf{r}) + u_s(\mathbf{r}) \tag{5.9}$$

where $B_i(\mathbf{r})$ is incident field assuming no reflecting half-plane, and the scattering field $u_s(\mathbf{r})$ is given by (5.5).

Note however, the formulation in (5.9) is exact and valid for all incident beams for any direction, regardless of the observation points located in front or behind the half-plane. Nevertheless, it is more efficient, with nearly no reflected beam produced; in other words, where nearly all beams pass the half-plane and propagate into the forward region $(y<0)$ with a slight destabilisation of the half plane. It happens when $x_i<0$ and in particular when $x_i \ll -w_i$, where w_i is the beam width of the incident beam.

When calculating the scattering field, determining the spectral function Φ is the first step. This function affects the diffracting beams' amplitudes and it is worth searching for an asymptotic approximation to the spectral function Φ in (5.7), rather than working with the former integration form.

Substituting the incident plane wave spectrum $\tilde{B}_i(\boldsymbol{\kappa})$ of (2.60) into (5.7), gives

$$\Phi(\alpha,\zeta)=\frac{-A_i}{4\pi\gamma_i\sqrt{\det\boldsymbol{\Gamma}_i}}\int_{C_i} d\alpha'\gamma e^{-ik\Psi(\alpha',\zeta)}D(\alpha',\alpha)\,. \tag{5.10}$$

Here Ψ is the spectral phase in (2.61). As with the pattern for the incident beam, this integral has a Gaussian localization about the spectral direction $(\alpha',\zeta)\simeq(\phi_i,\zeta_i)$. As noted earlier, α', here, is the azimuth direction of the incident plane wave, and ϕ_i is the azimuth angle of the incident beam.

5.3.2. Representation of spectral function Φ

The term Ψ in (5.10) is simplified by expanding Ψ in a Taylor series about ϕ_i and neglecting higher order terms; thus,

$$\Psi(\alpha',\zeta)\simeq\Psi_0(\zeta)+\Psi'_{\alpha'}(\zeta)\delta\alpha'+\frac{1}{2}\Psi''_{\alpha'\alpha'}\delta\alpha'^2\,. \tag{5.11}$$

$\delta\alpha'=\alpha'-\phi_i$, $\Psi_0(\zeta)=\Psi_0(\alpha',\zeta)\big|_{\alpha'=\phi_i}$ and $\Psi'_{\alpha'}(\zeta)=\partial_{\alpha'}\Psi(\alpha',\zeta)\big|_{\alpha'=\phi_i}$. Because the integrand is also localised in ζ, $\Psi'_{\alpha'}$ and $\Psi''_{\alpha'\alpha'}$ can be expanded in a Taylor series about $\zeta_i=\cos\theta_i$. Thus,

$$\begin{aligned}\Psi'_{\alpha'}(\zeta) &\simeq \Psi'_{0\alpha'} + \Psi''_{0\alpha'\zeta}\delta\zeta \\ &= \partial_{\alpha'}\Psi(\alpha',\zeta)\Big|_{\alpha'=\phi_i,\zeta=\zeta_i} + \partial_{\alpha'\zeta}\Psi(\alpha',\zeta)\Big|_{\alpha'=\phi_i,\zeta=\zeta_i}\delta\zeta\end{aligned} . \tag{5.12}$$

From (2.61), and using $\alpha' = \cos^{-1}(-\xi/\varsigma)$, $\gamma_i = \sin\theta_i \sin\varphi_i$ and $\varsigma = \sqrt{1-\zeta^2}$, $\varsigma_i = \sin\theta_i$, one has

$$\tilde{\eta}_i(\zeta) = \Psi'_{\alpha'}(\zeta) \simeq \gamma_i x_i - \Upsilon_i \delta\zeta \quad \text{and} \tag{5.13}$$

$$\tilde{q}_i = \Psi''_{\alpha'\alpha'} \simeq \gamma_i^2 \left[\bar{\mathbf{\Gamma}}_i^{-1}\right]_{11} - \xi_i x_i . \tag{5.14}$$

$\Upsilon_i = \varsigma_i^{-2}\gamma_i(x_i\zeta_i + \left[\bar{\mathbf{\Gamma}}_i^{-1}\right]_{11}\zeta_i\xi_i - \varsigma_i^2\left[\bar{\mathbf{\Gamma}}_i^{-1}\right]_{12})$.

The details of calculating $\tilde{\eta}_i$ and $\tilde{q}_i$ can be found in ***Appendix-IV.***

Substituting (5.13) and (5.14), for $\Psi(\alpha',\zeta)$ in (5.10) yields

$$\begin{aligned}\Psi(\alpha',\zeta) &\simeq \Psi_0(\zeta) + \Psi'_{\alpha'}(\zeta)\delta\alpha' + \frac{1}{2}\Psi''_{\alpha'\alpha'}\delta\alpha'^2 \\ &= \Psi_0(\alpha',\zeta)\Big|_{\alpha'=\phi_i} + \tilde{\eta}_i(\zeta)\delta\alpha' + \frac{1}{2}\tilde{q}_i\delta\alpha'^2 \\ &= \Psi_0(\zeta) + (\alpha'-\phi_i)\tilde{\eta}_i + \frac{1}{2}(\alpha'-\phi_i)^2\tilde{q}_i\end{aligned} . \tag{5.15}$$

Equation (5.10) then becomes

$$\begin{aligned}\Phi(\alpha,\zeta) = &\frac{-A_i}{4\pi\gamma_i\sqrt{\det\mathbf{\Gamma}_i}} e^{-ik\Psi_0(\zeta)} \\ &\times\int_{C_i} d\alpha' e^{-ik[\frac{1}{2}\tilde{q}_i(\alpha'-\phi_i)^2 + \tilde{\eta}_i(\alpha'-\phi_i)]} D(\alpha',\alpha)\end{aligned} . \tag{5.16}$$

This integral involves the pole of $D(\alpha,\alpha')$ and a complex saddle point

$$\alpha'_s = \phi_i - \tilde{\eta}_i/\tilde{q}_i . \tag{5.17}$$

In practice, the spectral direction α is near $\pi \mp \phi_i$ which are defined as the reflection and shadow boundaries.

The diffraction coefficient $D(\alpha,\alpha')$ of (5.10) is split into a pole and a regular term, with the method of Owen in reference [7]

$$D(\alpha',\alpha)=\frac{D_{p\pm}}{\alpha'-\alpha'_p}+\bar{D}(\alpha',\alpha)\ . \tag{5.18}$$

$$D_{p\pm}\equiv\lim_{\alpha'\to\alpha'_p}(\alpha'-\alpha'_p)D(\alpha',\alpha'_p)=\begin{cases}-2\varepsilon & for\quad \alpha'_{p+}\\ -2 & for\quad \alpha'_{p-}\end{cases}\ . \tag{5.19}$$

To simplify (5.16), the same procedure in [29, 30] is applied to find a uniform expression for $\Phi(\alpha,\zeta)$.

By introducing the standard transformation for the first order saddle point, the metric between $\alpha'_{p\pm}$ and α'_s is

$$s_{p\pm}\simeq\sqrt{\frac{1}{2}ik\tilde{q}_i}(\alpha'_{p\pm}-\alpha'_s)=\sqrt{\frac{1}{2}ik\tilde{q}_i}[\tilde{\eta}_i/\tilde{q}_i\mp(\alpha-\phi_{B\pm})] \tag{5.20}$$

where $\arg\{ik\tilde{q}_i\}\in(-(\pi/2),(\pi/2))$. Equation (5.16) then becomes,

$$\Phi(\alpha,\zeta)=\frac{i}{\pi}\sqrt{\frac{kq_i}{32\pi}}\tilde{B}_i^{edge}(\zeta)\int_{C_s}G(s)e^{-s_{p\pm}^2}ds \tag{5.21}$$

with

$$\tilde{B}_i^{edge}(\zeta)=\sqrt{\frac{k}{2\pi i\tilde{q}_i}}\gamma_i\tilde{B}_i(-\varsigma\cos\alpha'_s,\zeta) \tag{5.22}$$

where $\tilde{B}_i(\xi,\zeta)$ is given in (2.59). $\tilde{B}_i^{edge}(\zeta)$ is the spectral representation of the incident field at the edge denoted by tilde-bar. Substituting $\tilde{B}_i^{edge}(\zeta)$ into (5.5) and evaluating the integral for ζ one obtains the incident field $B_i^{edge}(z)$ along the edge.

Looking back to (5.21), here, $G(s)=D(\alpha',\alpha)\dfrac{d\alpha'}{ds}=\dfrac{D_{p\pm}}{s-s_{p\pm}}+\bar{G}(s)$, with C_S being the s -plane path of integration corresponding to C_i. Since $\bar{G}(s)$ is regular, its contribution can be evaluated by the saddle point approximation, hence the integral in (5.21) becomes

$$I = \int_{C_s} \frac{D_{p\pm}}{s - s_{p\pm}} e^{-s^2} ds + \pi \bar{G}(0) . \tag{5.23}$$

C_S passes above $s_{p\pm}$ since C_i passes above the poles of $D(\alpha, \alpha')$ in the α' plane. Letting $s = 0$, which leads to $\alpha = \alpha'_s$, one has

$$\bar{G}(0) = \sqrt{\frac{2}{i\pi k \tilde{q}_i}} \left\{ D(\alpha - \alpha'_s) + \frac{D_{p\pm}}{\alpha'_s - \alpha'_{p\pm}} \right\} . \tag{5.24}$$

The first term of I is evaluated by using the standard identity

$$\int_{C_s} \frac{D_{p\pm}}{s - s_{p\pm}} e^{-s^2} ds = \begin{cases} i\pi D_{p\pm} e^{-s_{p\pm}^2} erfc(-is_{p\pm}) & \text{for } \mathrm{Im} s_{p\pm} > 0 \\ -i\pi D_{p\pm} e^{-s_{p\pm}^2} erfc(is_{p\pm}) & \text{for } \mathrm{Im} s_{p\pm} < 0 \end{cases} . \tag{5.25}$$

Here

$$erfc(z) = \frac{2}{\sqrt{\pi}} \int_z^\infty dt e^{-t^2} \tag{5.26}$$

is the complementary error function. Because C_s passes above $s_{p\pm}$, if $\mathrm{Im} s_{p\pm} > 0$, the deformation of C_s onto the s-axis captures the pole which leads to the upper case of (5.25); otherwise, it does not capture the pole and the lower holds. From (5.24) and (5.25), (5.23) is evaluated by

$$\begin{aligned} I &= \begin{cases} -H(\mathrm{Im}\, s_{p\pm}) 2\pi i D_{p\pm} e^{-s_{p\pm}^2} + i D_{p\pm} e^{-s_{p\pm}^2} erfc(-is_{p\pm}) + \pi \bar{G}(0) & \text{for } \mathrm{Im} s_{p\pm} > 0 \\ -H(\mathrm{Im}\, s_{p\pm}) 2\pi i D_{p\pm} e^{-s_{p\pm}^2} - i D_{p\pm} e^{-s_{p\pm}^2} erfc(is_{p\pm}) + \pi \bar{G}(0) & \text{for } \mathrm{Im} s_{p\pm} < 0 \end{cases} \\ &= -i\pi D_{p\pm} e^{-s_{p\pm}^2} erfc(is_{p\pm}) + \pi \bar{G}(0) \end{aligned} . \tag{5.27}$$

Substituting (5.27) into (5.21), the final result is given by [1]

$$\Phi(\alpha, \zeta) = \sqrt{\frac{ik\tilde{q}_i}{32\pi}} \bar{B}_i^{edge}(\zeta) \left\{ e^{-s_{p\pm}^2} D_{p\pm} erfc(is_{p\pm}) - i\bar{G}(0) \right\} . \tag{5.28}$$

Figures 5.1 to 5.8 show typical examples of $\Phi(\alpha, \zeta)$ patterns. In this example, a circular incident Gaussian beam with $\delta_{11} = \delta_{22} = 1$, $\delta_{12} = \delta_{21} = 0$ and $q(0) = -500i$

intersects the half plane $y=0$ at $(x_i=2, z_i=0)$. For simplicity, the wave number is chosen such that $k=1$.

For $\alpha \in (0,\pi)$ and $(\theta_i, \pi+\varphi_i)=(\frac{\pi}{2}, \pi+\frac{\pi}{2})$, the patterns of $\Phi(\alpha,\zeta)$ in the scattering field produced by a normally incident beam are as shown in Figure 5.1, 2.

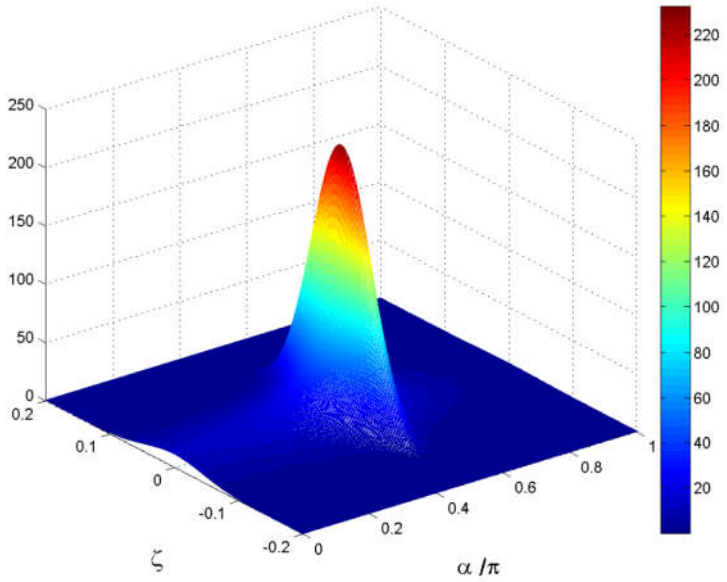

Figure 5.1 For $\alpha \in (0,\pi)$, the side view of the result of spectral function $\Phi(\alpha,\zeta)$ with a stigmatic incident Gaussian beam ($\delta_{11}=\delta_{22}=1$, $\delta_{12}=\delta_{21}=0$, $q(0)=-500i$) impinging upon the half plane at $(x_i=2, z_i=0)$ in the direction of $(\theta_i, \pi+\varphi_i)=(\pi/2, \pi+\pi/2)$.

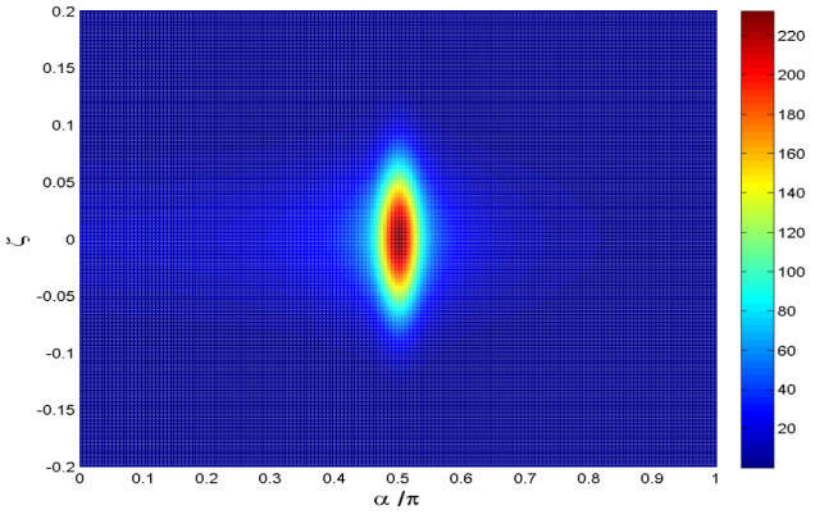

Figure 5.2 For $\alpha \in (0,\pi)$, the plan view of the result of spectral function $\Phi(\alpha,\zeta)$ with a stigmatic incident Gaussian beam ($\delta_{11}=\delta_{22}=1, \delta_{12}=\delta_{21}=0, q(0)=-500i$) impinging upon the half plane at $(x_i=2, z_i=0)$ in the direction of $(\theta_i, \pi+\varphi_i)=(\pi/2, \pi+\pi/2)$.

Following a similar process, the patterns of $\Phi(\alpha,\zeta)$ with $(\theta_i,\pi+\varphi_i)=(\frac{\pi}{2},\pi+\frac{\pi}{2})$ in the domain of $\alpha \in (\pi, 2\pi)$ are drawn in Figure 5.3, 4.

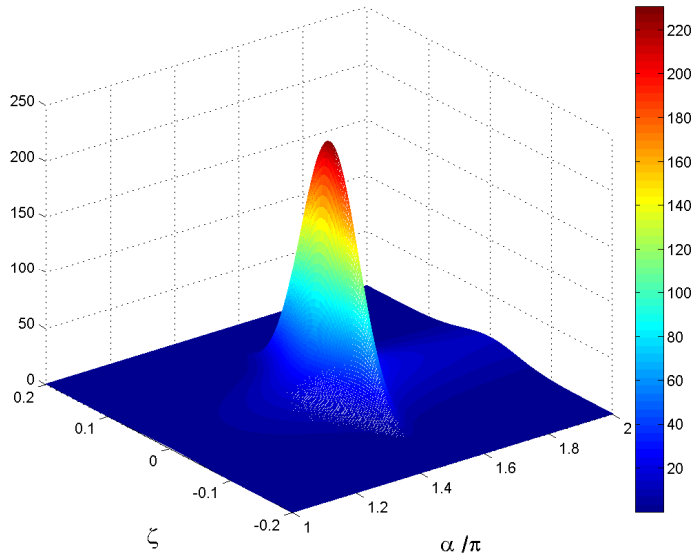

Figure 5.3 For $\alpha \in (\pi, 2\pi)$, the side view of the result of spectral function $\Phi(\alpha,\zeta)$ with a stigmatic incident Gaussian beam ($\delta_{11}=\delta_{22}=1$, $\delta_{12}=\delta_{21}=0$, $q(0)=-500i$) impinging upon the half plane at $(x_i=2, z_i=0)$ in the direction of $(\theta_i, \pi+\varphi_i)=(\pi/2, \pi+\pi/2)$.

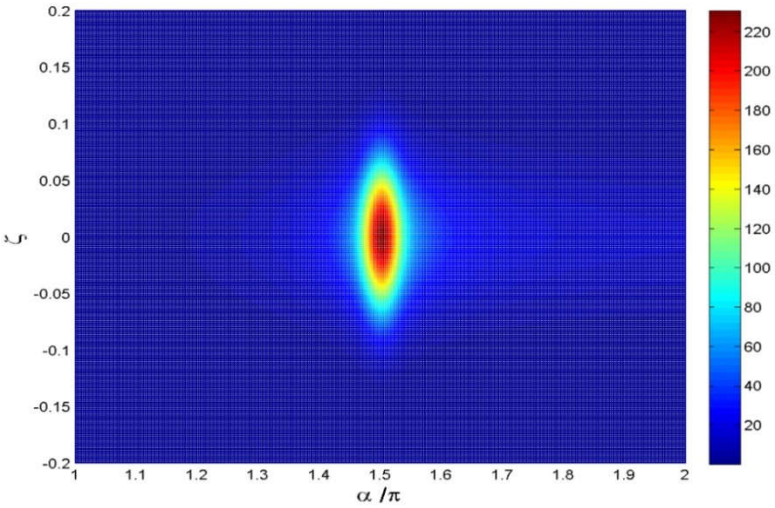

Figure 5.4 For $\alpha \in (\pi, 2\pi)$, the plan view of the result of spectral function $\Phi(\alpha, \zeta)$ with a stigmatic incident Gaussian beam ($\delta_{11} = \delta_{22} = 1$, $\delta_{12} = \delta_{21} = 0$, $q(0) = -500i$) impinging upon the half plane at $(x_i = 2, z_i = 0)$ in the direction of $(\theta_i, \pi + \varphi_i) = (\pi / 2, \pi + \pi / 2)$.

Finally, by combining the two results, the set of patterns for $\Phi(\alpha, \zeta)$ within $\alpha \in (0, 2\pi)$ are presented in Figure 5.5, 6.

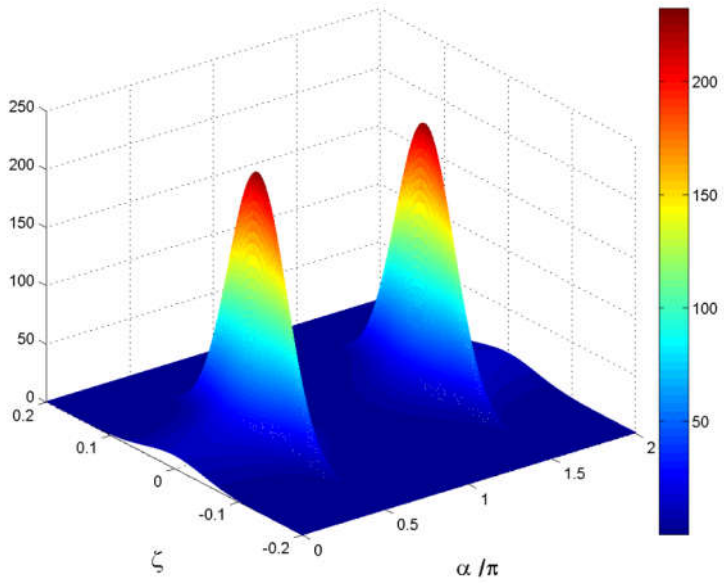

Figure 5.5 For $\alpha \in (0, 2\pi)$, the side view of the result of spectral function $\Phi(\alpha, \zeta)$ with a stigmatic incident Gaussian beam ($\delta_{11} = \delta_{22} = 1$, $\delta_{12} = \delta_{21} = 0$, $q(0) = -500i$) impinging upon the half plane at $(x_i = 2, z_i = 0)$ in the direction of $(\theta_i, \pi + \varphi_i) = (\pi / 2, \pi + \pi / 2)$.

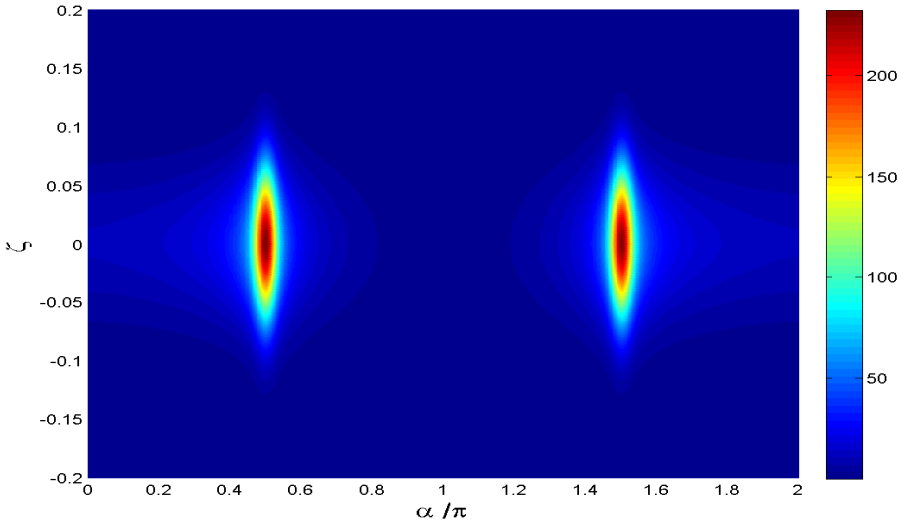

Figure 5.6 For $\alpha \in (0, 2\pi)$, the plan view of the result of spectral function $\Phi(\alpha, \zeta)$ with a stigmatic incident Gaussian beam ($\delta_{11} = \delta_{22} = 1$, $\delta_{12} = \delta_{21} = 0$, $q(0) = -500i$) impinging upon the half plane at $(x_i = 2, z_i = 0)$ in the direction of $(\theta_i, \pi + \varphi_i) = (\pi / 2, \pi + \pi / 2)$.

A more complicated scenario is a general elliptical beam with $\delta_{12} = \delta_{21} = 0$, $q(0) = -500i$ but with $\delta_{11} = 1 / q(0) = 4\delta_{22}$, impinging on the half plane at $(x_i = 2, z_i = 0)$. For simplicity, the wave number is chosen such that $k = 1$. This time, however, the incident spherical angle is $(\theta_i, \pi + \varphi_i) = (\frac{\pi}{4}, \pi + \frac{\pi}{3})$. Here, the combined patterns of $\Phi(\alpha, \zeta)$ are drawn directly, as illustrated in Figure 5.7, 8.

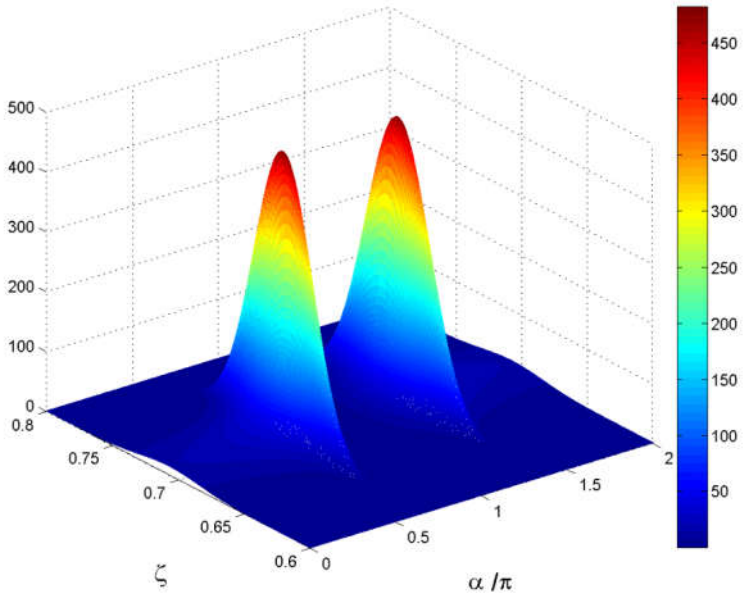

Figure 5.7 For $\alpha \in (0, 2\pi)$, the side view of the result of spectral function $\Phi(\alpha, \zeta)$ with an elliptical astigmatic incident Gaussian beam ($\delta_{12} = \delta_{21} = 0$, $\delta_{11} = 1/q(0) = 4\delta_{22}, q(0) = -500i$) impinging upon the half plane at $(x_i = 2, z_i = 0)$ in the direction of $(\theta_i, \pi + \varphi_i) = (\pi/4, \pi + \pi/3)$.

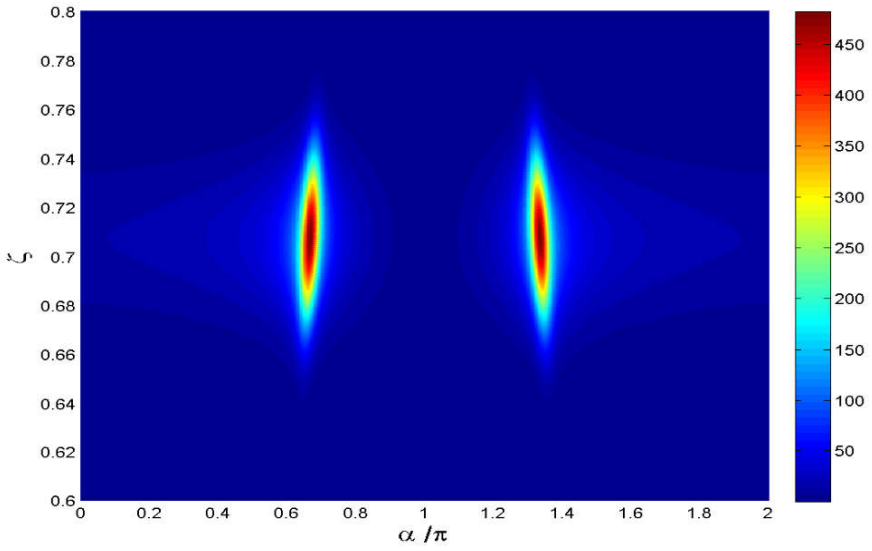

Figure 5.8 For $\alpha \in (0, 2\pi)$, the plan view of the result of spectral function $\Phi(\alpha, \zeta)$ with an elliptical astigmatic incident Gaussian beam ($\delta_{12} = \delta_{21} = 0$, $\delta_{11} = 1/q(0) = 4\delta_{22}, q(0) = -500i$) impinging upon the half plane at $(x_i = 2, z_i = 0)$ in the direction of $(\theta_i, \pi + \varphi_i) = (\pi/4, \pi + \pi/3)$.

From these patterns it can be seen that Φ governs the amplitudes of diffracting beams. The transmission pattern over the domain of $\alpha \in (0, 2\pi)$, and the reflection pattern over the domain of $\alpha \in (0, \pi)$, both seem symmetrical, since x_i is so small in comparison to the beam waist.

5.3.3. GBS representation

Using the result of the spectral function mentioned above, the scattering field can be calculated using (5.6) and (5.5). However, if the diffracted beams can be described in the form of Gaussian beams, this is to be preferred.

As mentioned in Chapter 1, there are two main methods of Gaussian beam summation: in one, an electric field is described as a discrete phase-space sum of beams that emerge from a set of points and directions in the source domain used for distributed (aperture) sources; whereas in the second, the field is expanded as an angular spectrum of beams that emerge from sources in all directions. In reference [1], a hybrid GBS scheme for radiation from a line source is introduced, which is suitable for a half-plane diffraction situation. In a word, this beam expansion method includes two different expansions:

A) A phase-space expansion along the edge;

B) And, an azimuth angular expansion in the plane perpendicular to the edge.

In section 4.3, the 2D azimuth angular expansion in the plane perpendicular to the edge had already been derived. This section will focus on obtaining the GBS expansion along the edge. Section 5.3.3.1 is about the windowed Fourier transform (WFT) expansion used in 3D GBS method, section 5.3.3.2 gives the corresponding expression of expansion coefficients, and last in section 5.3.3.3 the final form of 3D GBS with combined expansions are given.

5.3.3.1 Problem description and WFT Expansion

As shown in Figure 5.9, assume a line source distribution $I(\mathrm{z})$ along z-axis and set the 3D coordinate system to be as $\mathbf{r} = (x, y, z)$ [1].

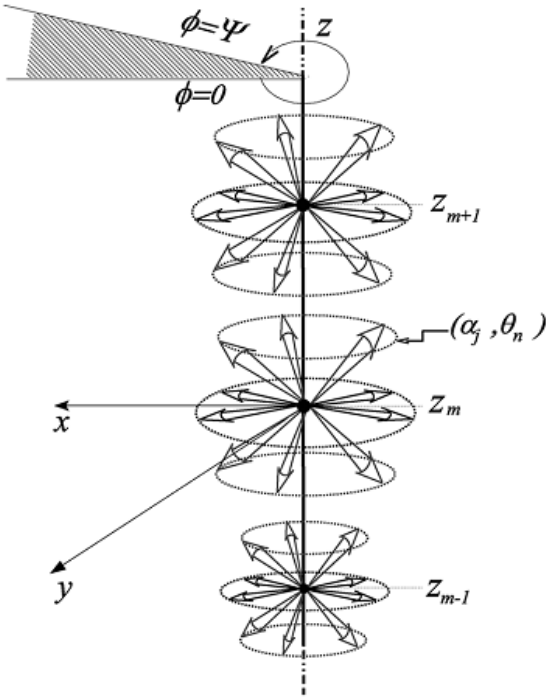

Figure 5.9 Physical configuration: A general Gaussian beam, marked by a heavy arrow, impinges on a half-plane (wedge angle $\Psi = 2\pi$ at direction (φ_i, θ_i). It intersects the $y = 0$ plane at an arbitrary point $X_i = (x_i, z_i)$, where x_i can be positive or negative. The beam expansion of the scattered field (dashed arrows) involves a phase-space beam expansion along the edge, and an azimuthal spectrum of beams around the edge. The beams emerge from the points z_m, m = 0, ±1, ... , along the edge with conical angle $\theta_n = \cos^{-1}\zeta_n$, n = 0, ±1, ... , and azimuthal angles α_j , j = 0, 1, ..., reprint from [1].

With the aid of Green's function, the field of this line source can be expressed as [8]

$$\begin{aligned} u(\mathbf{r}) &= \int_{-\infty}^{\infty} I(z')G(\mathbf{r},\mathbf{r}')dz' \\ &= \frac{k}{2\pi}\int_{-\infty}^{\infty} \tilde{I}(\zeta)\tilde{G}(\boldsymbol{\rho},\xi)e^{ik\zeta z}d\zeta \end{aligned} \tag{5.29}$$

where $G(\mathbf{r},\mathbf{r}')$ is the 3D Green's function, and

$$\tilde{I}(\zeta) = \int_{-\infty}^{\infty} I(z)e^{ik\zeta z}dz\,. \tag{5.30}$$

$\tilde{G}(\rho,\xi)=(-i/4)H_0^{(1)}(k\xi\rho)$ is the 2D Green's function. We now explore using a windowed Fourier transform (WFT) frame instead of the Fourier transform in (5.30). Assume a WFT frame set $\{\psi_{\boldsymbol{\mu}}(z)\}$ such that

$$\psi_{\boldsymbol{\mu}}(z)=\psi(z-z_m)e^{ik\zeta_n(z-z_m)} \tag{5.31}$$

where

$$(z_m,\zeta_n)=(m\bar{z},n\bar{\zeta}),\quad \boldsymbol{\mu}=(m,n)\in\mathbb{Z}^2 \tag{5.32}$$

with $(\bar{z},\bar{\zeta})$ being the unit cell dimensions. Specifically, $\bar{z}$ and $\bar{\zeta}$ are the spatial and spectral widths. These frame elements are localised in the (z,ζ) phase-space about lattice points (z_m,ζ_n). To make $\{\psi_{\boldsymbol{\mu}}(z)\}$ a frame, the lattice should be over-complete and satisfy $\bar{z}\bar{\zeta}<2\pi/k$. For simplicity, an over-complete parameter v is introduced and the former condition can be written as $k\bar{z}\bar{\zeta}<2\pi v,\ \ v<1$.

The beam formulation given below presents emergent beams, where each frame element $\psi_{\boldsymbol{\mu}}(z)$ constitutes a beam from the point z_m on the z-axis with polar angle $\theta_n=\cos^{-1}\zeta_n$. For UWB application, $v=k/\bar{k}$ is chosen with $\bar{k}$ being a reference frequency and in this case. The lattice points (z_m,ζ_n) are frequency independent. Obviously, to form an over-complete frame, the reference frequency should be chosen to satisfy $\bar{k}>k$, where v<1. For a Gaussian window, widely used in engineering fields, $\bar{k}>3k_{\max}$ is chosen, where $k_{\max}$ is greatest for all the relevant frequencies, and it implies that v<1/3.

The function $I(z)$ is expand by the WFT frame $\psi_{\boldsymbol{\mu}}(z)$, giving

$$I(z)=\sum_{\boldsymbol{\mu}}a_{\boldsymbol{\mu}}\psi_{\boldsymbol{\mu}}(z). \tag{5.33}$$

As mentioned above, although the choice of window function is arbitrary, for applications in wave theory, the Gaussian window function is preferred. Here, an iso-diffracting (ID) Gaussian window [9] is used and given by

$$\psi_{ID}(z,w)=e^{-kz^2/2b_z} \tag{5.34}$$

where, the parameter b_z controls the Gaussian width. This ID function is designed for frequency independence. Once the GB's propagation parameters, such as the complex radius of curvature, are calculated, the results can be used for all other frequencies. Theoretically, b_z can be chosen arbitrarily, yet the optimal choice is matching the phase-space lattice such that

$$b_z = \bar{z} / \bar{\zeta} = \bar{k}\bar{z}^2 / 2\pi . \tag{5.35}$$

Based on (5.35), b_z is related to the reference frequency $\bar{k}$ rather than k, so that it can be used for all the frequencies.

After having $\psi_{\mu}(z)$, it remains to find a suitable set of coefficients a_{μ} for (5.33). Yet it is not unique and can be found via searching algorithms. A good choice to calculate a_{μ} by a "dual frame" set $\varphi(z)$ similar to that used in 2D-DGBA. If v is sufficiently small, say v<1/3 as mentioned above, $\varphi(z)$ may be approximated by

$$\varphi(z) \cong \frac{v}{\|\psi\|^2}\psi(z) . \tag{5.36}$$

Therefore, the dual-window of ψ_{ID} is given by

$$\varphi_{\mathrm{ID}}(z) \cong v\sqrt{k / \pi b_z}\psi_{\mathrm{ID}}(z) . \tag{5.37}$$

Projecting $I(\mathrm{z})$ onto the dual-frame set $\varphi(z)$, the coefficient set is

$$\begin{aligned} a_{\mu}(\alpha) &= \left\langle I(z), \varphi_{\mu}(z) \right\rangle \\ &= \int_{-\infty}^{\infty} I(z)\varphi^*(z - z_m)e^{ik\zeta_n(z-z_n)}dz \end{aligned} \tag{5.38}$$

where $\langle , \rangle$ is the conventional L^2 inner product defined by $\langle f, g \rangle = \int f(z)g^*(z)dz$.

5.3.3.2 Expansion Coefficients Expression

Applying WFT expansion to (5.30), the expansion of the spectral function $\tilde{I}(\zeta)$ becomes

$$\tilde{I}(\zeta) = \sum_{\mu} a_{\mu}(\alpha)\tilde{\psi}_{\mu}(\zeta), \tag{5.39}$$

and from (5.31), $\tilde{\psi}_{\mu}(\zeta) = \tilde{\psi}(\zeta - \zeta_n)e^{-jk\zeta z_m}$ is the spectral counterpart of $\psi_{\mu}(z)$.

Substitute (5.38) into (5.29), results in

$$u(\mathbf{r}) = \sum_{\mu} a_{\mu}(\alpha)u_{\mu}(\mathbf{r}). \tag{5.40}$$

As mentioned above, the field $u(\mathbf{r})$ is expressed by summation of conical beam waves $u_{\mu}(\mathbf{r})$ that emerge from z_m on the z-axis with polar angle $\theta_n = \cos^{-1}\zeta_n$.

Returning now to the scattering field formulation in (5.5)-(5.7), the same WFT expansion steps are followed, and the expansion of Φ becomes

$$\Phi(\alpha,\zeta) = \sum_{\mu} a_{\mu}(\alpha)\tilde{\psi}_{\mu}(\zeta). \tag{5.41}$$

In contrast to (5.38), the expansion coefficients a_{μ} are calculated by the spectral counterpart of the inner product, namely

$$a_{\mu}(\alpha) = \frac{k}{2\pi}\left\langle \Phi(\alpha,\zeta), \tilde{\varphi}_{\mu}(\zeta) \right\rangle. \tag{5.42}$$

When using the spectral counterpart of ID windows $\tilde{\psi}_{ID}(\zeta) = \sqrt{2\pi bz/k}\,e^{-\frac{1}{2}kbz\zeta^2}$ and the spectral counterpart of dual ID windows obtained through Equation (5.36) $\tilde{\varphi}_{ID}(\zeta) = v\sqrt{2}e^{-\frac{1}{2}kb_z\zeta^2}$, the expansion coefficients can be finally re-written as

$$a_{\mu}(\alpha) = \frac{kv}{\sqrt{2\pi}}\int d\zeta \Phi(\alpha,\zeta)e^{-(1/2)kb_z(\zeta-\zeta_n)^2}e^{ikz_m\zeta}. \tag{5.43}$$

Corresponding to Figures 5.1-8, Figures 5.10-17 show the patterns of $a_{\mu}(\alpha)$. $b_z = 12000$, $v = 1/4$ are set and all other parameters then can be calculated by the foregoing expressions. The method for choosing the expansion parameters will be discussed in section 6.4.2.

First, the patterns of the expansion coefficients $a_{\mu}(\alpha)$ of a circular stigmatic beam are presented in Figure 5.10-13, which correspond to the case behind Figures 5.5-6.

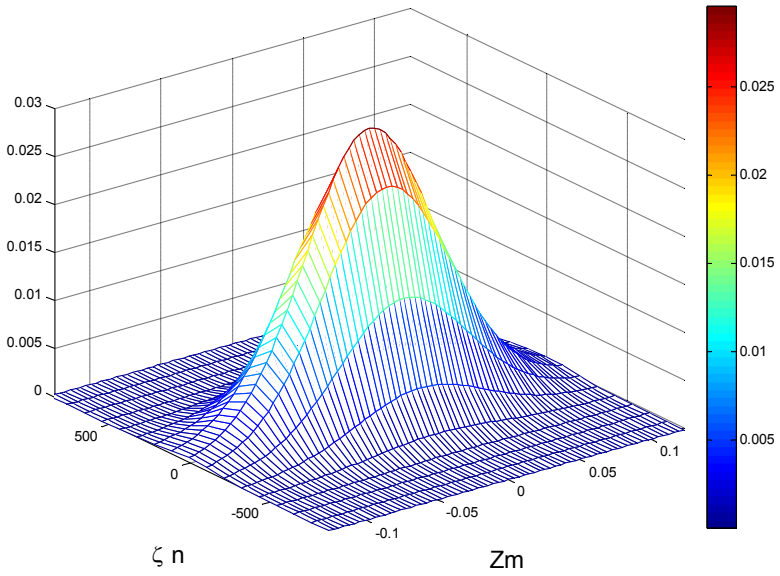

Figure 5.10 The side view of absolute value of $a_{\mu}(\alpha)$ in the (z_m, ζ_n) plane with $\alpha_i = \pi/2$, $b_z = 12000$ and . It is calculated for a stigmatic incident Gaussian beam ($\delta_{11} = \delta_{22} = 1$, $\delta_{12} = \delta_{21} = 0$, $q(0) = -500i$) impinging upon the half plane at $(x_i = 2, z_i = 0)$ in the direction of $(\theta_i, \pi + \varphi_i) = (\pi/2, \pi + \pi/2)$, corresponding to the case of Fig. 5.5 and Fig. 5.6.

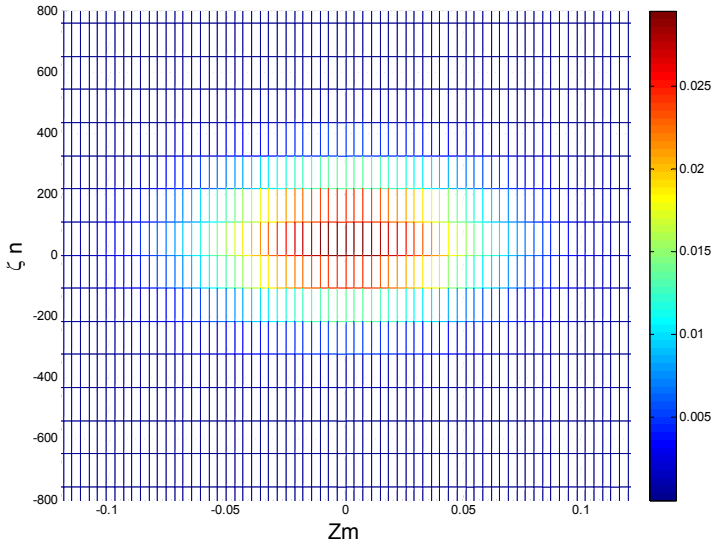

Figure 5.11 The plan view of absolute value of $a_{\mu}(\alpha)$ in the (z_m, ζ_n) plane with $\alpha_i = \pi/2$, $b_z = 12000$ and $v = 1/4$. It is calculated for a stigmatic incident Gaussian beam ($\delta_{11} = \delta_{22} = 1$, $\delta_{12} = \delta_{21} = 0$, $q(0) = -500i$) impinging upon the half plane at $(x_i = 2, z_i = 0)$ in the direction of $(\theta_i, \pi + \varphi_i) = (\pi/2, \pi + \pi/2)$, corresponding to the case of Fig. 5.5 and Fig. 5.6.

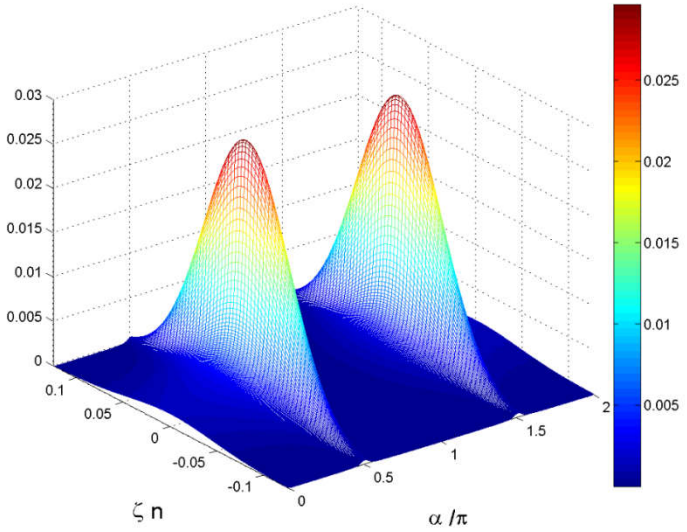

Figure 5.12 The side view of absolute value of $a_{\mu}(\alpha)$ in the (α_j, ζ_n) plane with $z_m = 0$, $b_z = 12000$ and $v = 1/4$. It is calculated for a stigmatic incident Gaussian beam ($\delta_{11} = \delta_{22} = 1$, $\delta_{12} = \delta_{21} = 0$, $q(0) = -500i$) impinging upon the half plane at $(x_i = 2, z_i = 0)$ in the direction of $(\theta_i, \pi + \varphi_i) = (\pi/2, \pi + \pi/2)$, corresponding to the case of Fig. 5.5 and Fig. 5.6.

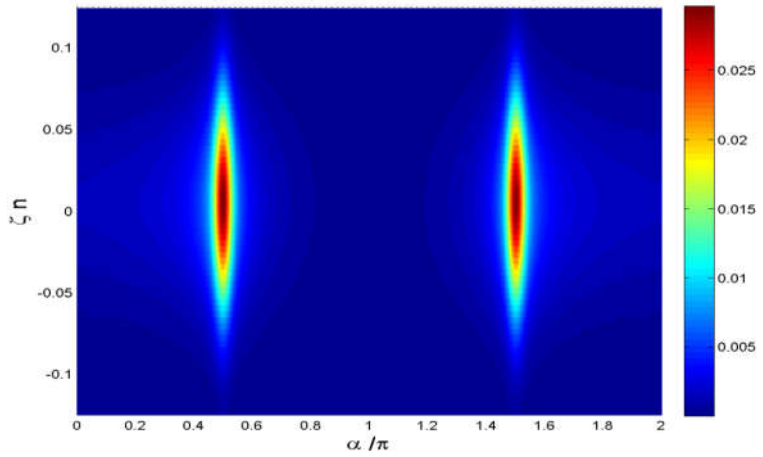

Figure 5.13 The plan view of absolute value of $a_{\mu}(\alpha)$ in the (α_j, ζ_n) plane with $z_m = 0$, $b_z = 12000$ and $v = 1/4$. It is calculated for a stigmatic incident Gaussian beam ($\delta_{11} = \delta_{22} = 1$, $\delta_{12} = \delta_{21} = 0$, $q(0) = -500i$) impinging upon the half plane at $(x_i = 2, z_i = 0)$ in the direction of $(\theta_i, \pi + \varphi_i) = (\pi/2, \pi + \pi/2)$, corresponding to the case of Fig. 5.5 and Fig. 5.6.

The patterns of expansion coefficients a_{μ} are now shown under the complicated general elliptical beam situation, which corresponds to the case of Figure 5.7 and Figure 5.8.

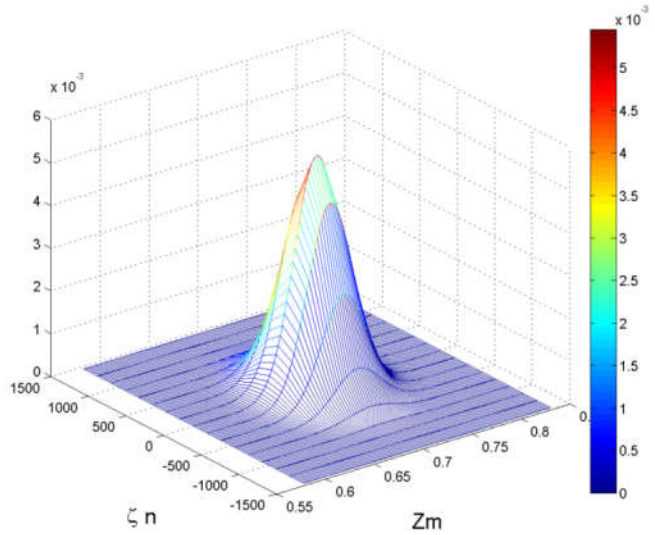

Figure 5.14 The side view of absolute value of $a_{\mu}(\alpha)$ in the (z_m, ζ_n) plane with $\alpha_j = 2\pi/3$, $b_z = 12000$, and $v = 1/4$. It is calculated for an elliptical astigmatic incident Gaussian beam ($\delta_{12} = \delta_{21} = 0$, $\delta_{11} = 1/q(0) = 4\delta_{22}$, $q(0) = -500i$) impinging upon the half plane at $(x_i = 2, z_i = 0)$ in the direction of $(\theta_i, \pi + \varphi_i) = (\pi/4, \pi + \pi/3)$, corresponding to the case of Fig. 5.7 and Fig. 5.8.

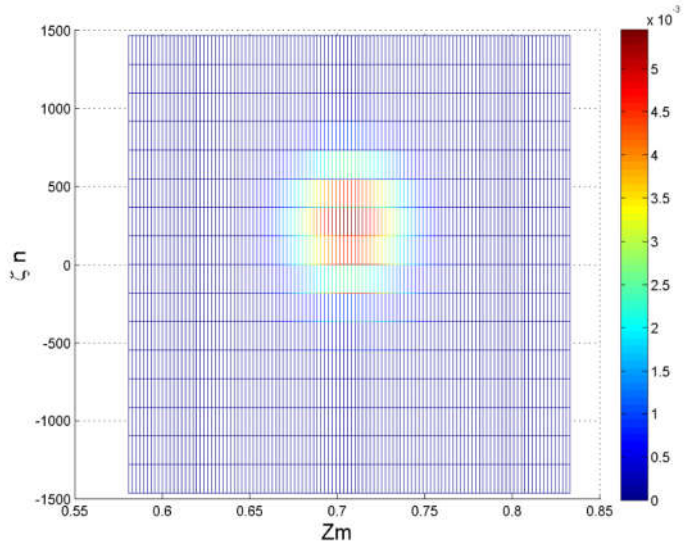

Figure 5.15 The plan view of absolute value of $a_{\mu}(\alpha)$ in the (z_m, ζ_n) plane with $\alpha_j = 2\pi/3$, $b_z = 12000$, and $v = 1/4$. It is calculated for an elliptical astigmatic incident Gaussian beam ($\delta_{12} = \delta_{21} = 0, \delta_{11} = 1/q(0) = 4\delta_{22}$, $q(0) = -500i$) impinging upon the half plane at $(x_i = 2, z_i = 0)$ in the direction of $(\theta_i, \pi + \varphi_i) = (\pi/4, \pi + \pi/3)$, corresponding to the case of Fig. 5.7 and Fig. 5.8.

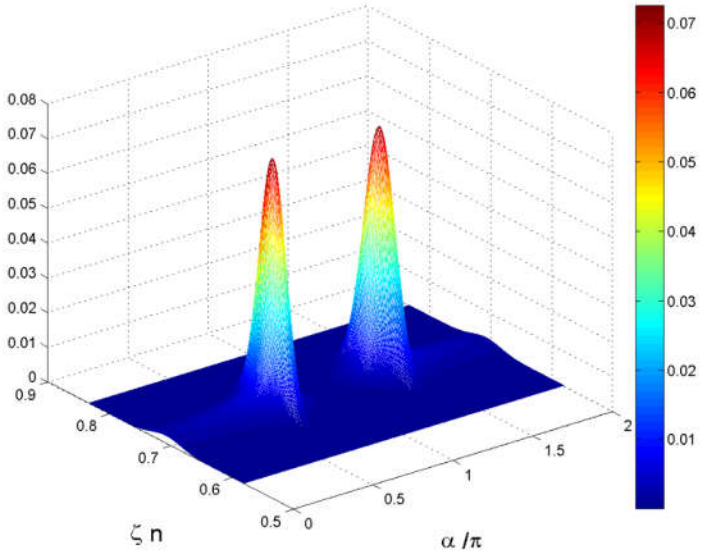

Figure 5.16 The side view of absolute value of $a_{\mu}(\alpha)$ in the (α_j, ζ_n) plane with $z_m = 0$, $b_z = 12000$, and $v = 1/4$. It is calculated for an elliptical astigmatic incident Gaussian beam ($\delta_{12} = \delta_{21} = 0, \delta_{11} = 1/q(0) = 4\delta_{22}$, $q(0) = -500i$) impinging upon the half plane at $(x_i = 2, z_i = 0)$ in the direction of $(\theta_i, \pi + \varphi_i) = (\pi/4, \pi + \pi/3)$, corresponding to the case of Fig. 5.7 and Fig. 5.8.

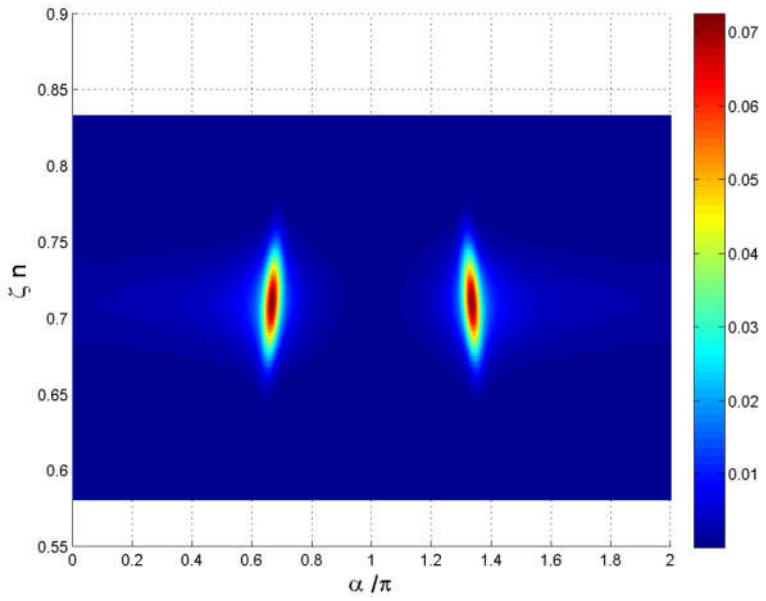

Figure 5.17 The plan view of absolute value of $a_{\boldsymbol{\mu}}(\alpha)$ in the (α_j, ζ_n) plane with $z_m = 0$, $b_z = 12000$, and $v = 1/4$. It is calculated for an elliptical astigmatic incident Gaussian beam ($\delta_{12} = \delta_{21} = 0, \delta_{11} = 1/q(0) = 4\delta_{22}$, $q(0) = -500i$) impinging upon the half plane at $(x_i = 2, z_i = 0)$ in the direction of $(\theta_i, \pi + \varphi_i) = (\pi/4, \pi + \pi/3)$, corresponding to the case of Fig. 5.7 and Fig. 5.8.

Table 5.1 Expressions and their spectral counterparts in WFT frame expansion

Expressions	spectral counterparts
$u_s(\mathbf{r}) = \dfrac{k}{2\pi}\int_{-\infty}^{\infty} d\zeta e^{ik\zeta z}\bar{u}_s(\boldsymbol{\rho},\zeta)$	$\tilde{u}_s(\boldsymbol{\rho},\zeta) = \int_{c\pm} d\alpha \Phi(\alpha,\zeta) e^{ik\zeta\rho\cos(\alpha-\phi)}$
$I(z) = \sum_{\boldsymbol{\mu}} a_{\boldsymbol{\mu}}\psi_{\boldsymbol{\mu}}(z)$	$\Phi(\alpha,\zeta) = \sum_{\boldsymbol{\mu}} a_{\boldsymbol{\mu}}(\alpha)\bar{\psi}_{\boldsymbol{\mu}}(\zeta)$
$\psi_{\boldsymbol{\mu}}(z) = \psi(z - z_m)e^{ik\zeta_n(z-z_m)}$	$\tilde{\psi}_{\boldsymbol{\mu}}(\zeta) = \bar{\psi}(\zeta - \zeta_n)e^{-ik\zeta z_m}$
$\psi_{\mathrm{ID}}(z) = e^{-kz^2/2b_z}$	$\tilde{\psi}_{\mathrm{ID}}(\zeta) = \sqrt{2\pi b_z / k}\, e^{-(1/2)kb_z\zeta^2}$
$\phi(z) \cong \dfrac{v}{\|\psi\|^2}\psi(z)$	$\tilde{\varphi}_{\boldsymbol{\mu}}(\zeta) = \bar{\varphi}(\zeta - \zeta_n)e^{-ik\zeta z_m}$
$\phi_{\mathrm{ID}}(z) \cong v\sqrt{k/\pi b_z}\,\psi_{\mathrm{ID}}(z)$	$\tilde{\varphi}_{\mathrm{ID}}(\zeta) = v\sqrt{2}e^{-(1/2)kb_z\zeta^2}$

In wave theory, frequency domain expressions are very helpful, and without exception also in this 3D diffraction theory. Table 5.1 summarises some of these expressions mentioned above in the time-domain and their spectral counterparts.

5.3.3.3 GBS Representation

Before going to a 3D GBS representation of the scattered field, it is worth dealing firstly with the 2D case. As mentioned in Chapter4, in Katsav et al. [6] give an azimuthal GBS representation based on an angular spectrum of 2D Gaussian beams. The clue to this representation is forming 2D beam propagators $\tilde{B}_{2D}$ emerging in all azimuthal α directions instead of plane the wave propagators $e^{ik\zeta\rho\cos(\alpha-\phi)}$ of (5.6). This 2D GBS representation has been shown earlier in (4.16) as

$$\tilde{u}_s(\mathbf{\rho},\zeta) \cong \sum_j \delta\alpha_j \Phi(\alpha_j,\zeta)\tilde{B}_{2\mathrm{D}}(\mathbf{\rho},\alpha,\zeta) \tag{5.44}$$

where $\delta\alpha$ is the discretization step and α_j are the discrete beam directions. $\tilde{B}_{2D}$ can be expressed as

$$\tilde{B}_{2\mathrm{D}}(\mathbf{\rho},\alpha,\zeta) = \sqrt{\frac{-ib_t}{\sigma_j - ib_t}}\, e^{ik\zeta(\sigma_j + \frac{1}{2}\frac{\eta_j^2}{\sigma_j - ib_t})} \tag{5.45}$$

where (σ_j,η_j) are the coordinates of the observation point $\mathbf{\rho}=(\rho,\varphi)$ along and transverse to the axis of the j^{th} beam. They are related to conventional cylindrical coordinates via $\rho(\cos(\varphi-\alpha_j),\sin(\varphi-\alpha_j))$, respectively. All the details can be found in reference [6].

The 3D configuration can be obtained by substituting (5.41) into (5.44). The spectral scattered field $\tilde{u}_s$ is then given by,

$$\tilde{u}_s(\mathbf{\rho},\zeta) = \sum_{\boldsymbol{\mu},j} \delta\alpha_j a_{\boldsymbol{\mu},j}\tilde{\psi}_{\boldsymbol{\mu}}(\zeta)\tilde{B}_{2D}(\mathbf{\rho},\alpha_j,\zeta) \tag{5.46}$$

where $a_{\boldsymbol{\mu},j} = a_{\boldsymbol{\mu}}(\alpha_j)$. Upon substituting (5.46) into (5.5), the final 3D GBS representation for the scattered field u_s is,

$$u_s(\boldsymbol{\rho},\zeta)=\sum_{\mathbf{u},j}\delta\alpha_j a_{\mathbf{u},j}B_{\mathbf{u},j}(\mathbf{r}) \quad \text{and} \tag{5.47}$$

$$B_{\boldsymbol{\mu},j}(\mathbf{r})=\frac{k}{2\pi}\int d\zeta e^{ik\zeta z}\tilde{\psi}_{\boldsymbol{\mu}}(\zeta)\tilde{B}_{2D}(\boldsymbol{\rho},\zeta,\alpha_j)\,. \tag{5.48}$$

This representation contains the expansions perpendicular to the z-axis and along the z-axis. The beam form $B_{\boldsymbol{\mu},j}$ identifies a beam field that emerges from z_m on the z-axis at polar angle $\theta_n=\cos^{-1}\zeta_n$ and azimuthal direction α_j.

Substitute $\tilde{\psi}_{ID}(\zeta)=\sqrt{2\pi b_z/k}e^{-\frac{1}{2}kb_z\zeta^2}$ and (5.45) into (5.48), one has

$$\begin{aligned}
B_{\boldsymbol{\mu},j}(\mathbf{r}) &= \frac{k}{2\pi}\int_{-\infty}^{\infty} d\zeta e^{ik\zeta(z-z_m)}\tilde{\psi}_{\boldsymbol{\mu}}(\zeta-\zeta_n)\tilde{B}_{2D}(\boldsymbol{\rho},\zeta-\zeta_n,\alpha_j)\\
&= \frac{k}{2\pi}\int_{-\infty}^{\infty} d\zeta e^{ik\zeta(z-z_m)}\sqrt{2\pi bz/k}e^{-\frac{1}{2}kb_z(\zeta-\zeta_n)^2}\sqrt{\frac{-ib_{tn}}{\sigma_j-ib_{tn}}}e^{ik\varsigma_n(\sigma_j+\frac{1}{2}\frac{\eta_j^2}{\sigma_j-ib_{tn}})}\\
&= \sqrt{\frac{kb_z}{2\pi}}\sqrt{\frac{-ib_{tn}}{\sigma_j-ib_{tn}}}\int_{-\infty}^{\infty} d\zeta e^{ik(z-z_m)-\frac{1}{2}kb_z(\zeta-\zeta_n)^2+ik\varsigma_n(\sigma_j+\frac{1}{2}\frac{\eta_j^2}{\sigma_j-ib_t})}\\
&= \sqrt{\frac{kb_z}{2\pi}}\sqrt{\frac{-ib_t}{\sigma_j-ib_t}}\int_{-\infty}^{\infty} d\zeta e^{ik(\frac{1}{2}ib_z(\zeta-\zeta n)^2+\zeta(z-zm)+\xi S_j)}
\end{aligned}, \tag{5.49}$$

where $S_j=\sigma_j+\frac{1}{2}\frac{\eta_j^2}{\sigma_j-ib_{tn}}$.

Because the spectrum is localized near ζ_n, it is approximated that $\xi=\sqrt{1-\zeta^2}\simeq\xi_n-\frac{\delta\zeta\zeta_n}{\xi_n}-\frac{\delta\zeta^2}{2\xi_n^3}$ with $\delta\zeta=\zeta-\zeta_n$ and $\delta\xi=\sqrt{1-\zeta_n^2}$. The phase of (5.49) can be rewritten as

$$\Psi_B\simeq\xi_n S_j+\dot{z}\zeta_n+(\dot{z}-\zeta_n\xi_n^{-1}S_j)\delta\zeta-\frac{1}{2}(S_j\xi_n^{-3}-ib_z)\delta\zeta^2,\ \text{with}\ \dot{z}=z-z_m \tag{5.50}$$

This phase has a stationary point

$$\delta\zeta_s=(\dot{z}-\zeta_n\xi_n^{-1}S_j)/(S_j\xi_n^{-3}-ib_z)\,. \tag{5.51}$$

Using saddle point evaluation, the integral (5.51) becomes

$$B_{\boldsymbol{\mu},j}(\mathbf{r}) \simeq \sqrt{\frac{-ib_z}{S_j\xi_n^{-3} - ib_z}} \sqrt{\frac{-ib_{tn}}{\sigma_j - ib_{tn}}} e^{ik\Psi_{Bs}}, \tag{5.52}$$

where $\Psi_{Bs} = \Psi_B(\delta\zeta_s) \simeq \xi_n S_j + \dot{z}\zeta_n + \frac{1}{2}\frac{(\dot{z} - \zeta_n\xi_n^{-1}S_j)^2}{S_j\xi_n^{-3} - ib_z}$.

Here (σ, η_1, η_2) are the coordinates of position vector $\mathbf{r}$. It can be then relaxed that $(\sigma = \xi_n\sigma_j, \eta_1 = \zeta_n\sigma_j - \xi_n\dot{z}, \eta_2 = \eta_j)$. With some degree for precision, replacing σ_j / ξ_n with σ and omitting negligible-quantity terms, enables Ψ_{Bs} be simplified to

$$\Psi_{Bs} = \sigma + \frac{1}{2}\frac{\eta_1}{\sigma - ib_z\xi_n^2} + \frac{1}{2}\frac{\eta_2}{\sigma - ib_{tn}/\xi_n}. \tag{5.53}$$

The amplitude term, can be approximated as $S_j\xi_n^{-3} \approx \sigma_j\xi_n^{-3} \approx \sigma\xi_n^{-2}$. And the field of (5.52) then becomes

$$B_{\mathbf{u},j}(\mathbf{r}) = \sqrt{\frac{-iF_1}{\sigma - iF_1}\frac{-iF_2}{\sigma - iF_2}} e^{ik[\sigma + \frac{1}{2}\frac{\eta_1^2}{\sigma - iF_1} + \frac{1}{2}\frac{\eta_2^2}{\sigma - iF_2}]}, \tag{5.54}$$

where $F_1 = b_z\varsigma_n^2$ and $F_2 = b_t / \varsigma_n$ with $\varsigma_n = \sqrt{1 - \zeta_n^2} = \sin\theta_n$. This expression has a similar form to the astigmatic Gaussian beam of (2.36) with $\boldsymbol{\Gamma}_0 = \begin{pmatrix} i / b_z\varsigma_n^2 & 0 \\ 0 & i\varsigma_n / b_t \end{pmatrix}$. Compared with (2.36), the expression of (5.54) shows an astigmatic GB with principal axes in the (η_1, η_2) directions, and waist at $\sigma = 0$. Here, (F_1, F_2) are the respective collimation lengths. For certain applications it may be preferable to choose b_t via $b_t = \varsigma_n^3 b_z$.

5.4 Field representations in the backward-scattering region

It is worth discussing the field in the backward region. When $x_i > 0$, the field is usually described in a reflection form and the total field written as

$$u(\mathbf{r}) = u_R(\mathbf{r}) + \breve{u}_s(\mathbf{r}). \tag{5.55}$$

For $y > 0, u_R(\mathbf{r}) = B_i(\mathbf{r}) + B_r(\mathbf{r})$, while for $y < 0$, there is no reflection field. Here $B_r(\mathbf{r})$ is the reflected beam field assuming an infinite reflecting plane at $y = 0$. The only difference here is that the spectral function Φ in (5.7) is replaced by $\breve{\Phi}$. Suedan [10] gives the relationship between the two spectral functions

$$\Phi(\alpha, \zeta) = \frac{k\gamma_i}{4\pi} \tilde{B}_i(\alpha'_{p\pm}, \zeta) D_{p\pm} + \breve{\Phi}(\alpha, \zeta), \tag{5.56}$$

where $\tilde{B}_i(\alpha'_{p\pm}, \zeta)$ is the value of $\tilde{B}_i$ at the pole of $\alpha'_{p\pm}$. The contour of integration C_i in (5.7) that passes above the poles $\alpha'_{p\pm}$ of $D(\alpha, \alpha')$ is replaced by $\breve{C}_i$ passing below and the expression of $D_{p\pm}$ is given by (5.19).

The term $\frac{k\gamma_i}{4\pi} \tilde{B}_i(\alpha'_{p\pm}, \zeta) D_{p\pm}$ in (5.56) describes the beam optics field. When $y > 0$, it yields the reflected field $B_r(\mathbf{r})$, whereas, for $y < 0$, it yields $-B_i(\mathbf{r})$ to cancel the incident beam field.

As shown in section 5.2.1, both field expressions in (5.9) and (5.55) are exact and are valid for all x_i. However, this formulation is preferable for $x_i > 0$ when it consists of a dominant BO reflection and a weak diffracted field $\breve{u}_s$.

Substituting (5.28) into (5.56) and using the identity $erfc(z) = 2 - erfc(-z)$, the expression of $\breve{\Phi}(\alpha, \zeta)$ is given by

$$\breve{\Phi}(\alpha, \zeta) = \sqrt{\frac{ik\tilde{q}_i}{32\pi}} \bar{B}_i^{edge}(\zeta) \left\{ -e^{-s_{p\pm}^2} D_{p\pm} erfc(-is_{p\pm}) - i\bar{G}(0) \right\}. \tag{5.57}$$

Referring to other formulas of 3D GBS representation in the backward-scattering region, all have similar forms forward except is used $\breve{\Phi}(\alpha, \zeta)$ instead of $\Phi(\alpha, \zeta)$.

An example similar to that in reference [1] by Katsav *et al* is shown. It considers an incident stigmatic Gaussian beam impinging on the half-plane with incident spherical

angles $(\theta_i, \pi+\varphi_i) = (\frac{\pi}{3}, \pi+\frac{\pi}{4})$. Additionally we assume $k=1$, $q(0)=-500i$ and the intersection point to be $(x_i, z_i) = (2,0)$. The output field is shown in the (z,ϕ) plane at a distance $\rho = 3500$ from the edge. The collimation length is chosen to be $b_t = 7500$, since $b_z = b_t / \sin^3\theta_i \approx 12000$. With an *over-completeness* parameter $v = 1/4$, the lattice $(\bar{z}, \bar{\zeta}) = (137.3, 0.0114)$ is calculated via (5.35).

The pattern of spectral function $\breve{\Phi}(\alpha,\zeta)$ for the problem parameters defined above is depicted in Figure 5.18.

The cross-section cuts of the expansion coefficients $\breve{a}_{\mu}(\alpha)$ in the 3D index domain are shown in Figure 5.19, 20. Figure 5.19 is in the (z_m, ζ_n) plane at $a_j = 0.75\pi$, and Figure 5.20 is in the (α_j, ζ_n) plane at $z_m = 0$.

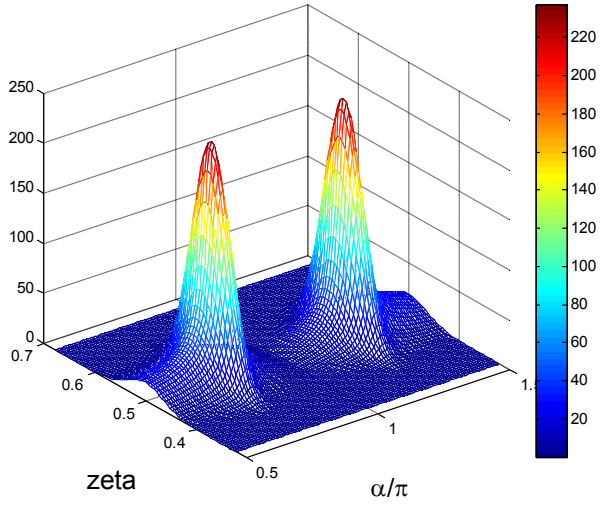

Figure 5.18 The side view of spectral function $\breve{\Phi}(\alpha,\zeta)$ with a stigmatic incident Gaussian beam ($\delta_{12}=\delta_{21}=0$, $\delta_{11}=\delta_{22}=1$, $q(0)=-500i$) impinging upon the half plane at $(x_i=2, z_i=0)$ in the direction of $(\theta_i, \pi+\varphi_i) = (\pi/3, \pi+\pi/4)$ with $k=1$.

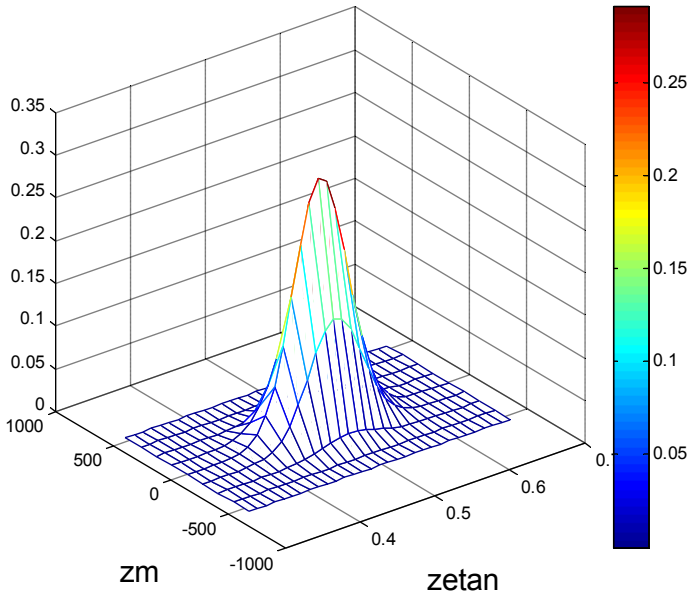

Figure 5.19 The side view of absolute value of $\breve{a}_{\mu}(\alpha)$ in the (z_m, ζ_n) plane with $a_j = 3\pi/4$. It is calculated for a stigmatic incident Gaussian beam ($\delta_{12} = \delta_{21} = 0$, $\delta_{11} = \delta_{22} = 1$, $q(0) = -500i$) impinging upon the half plane at $(x_i = 2, z_i = 0)$ in the direction of $(\theta_i, \pi + \varphi_i) = (\pi/3, \pi + \pi/4)$ with $k = 1$.

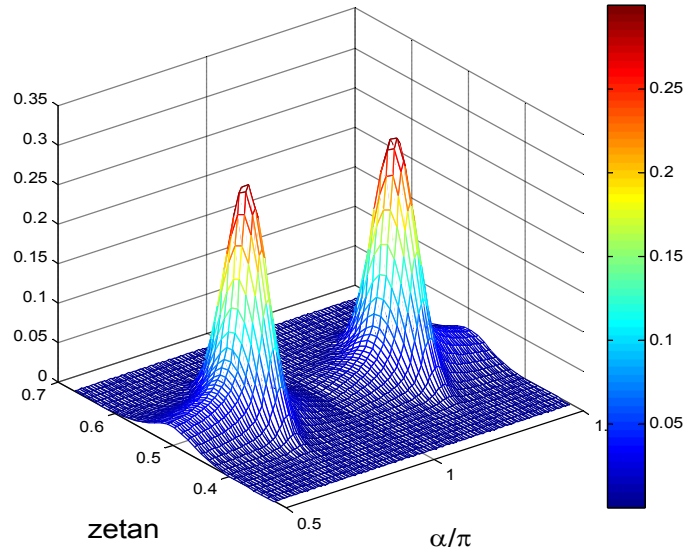

Figure 5.20 The side view of absolute value of $\breve{a}_{\mu}(\alpha)$ in the (α_j, ζ_n) plane with $z_m = 0$. It is calculated for a stigmatic incident Gaussian beam ($\delta_{12} = \delta_{21} = 0$, $\delta_{11} = \delta_{22} = 1$, $q(0) = -500i$) impinging upon the half plane at $(x_i = 2, z_i = 0)$ in the direction of $(\theta_i, \pi + \varphi_i) = (\pi/3, \pi + \pi/4)$ with $k = 1$.

Finally, Figure 5.21, 22 depict the total field with the observation distance set at $\rho = 3500$.

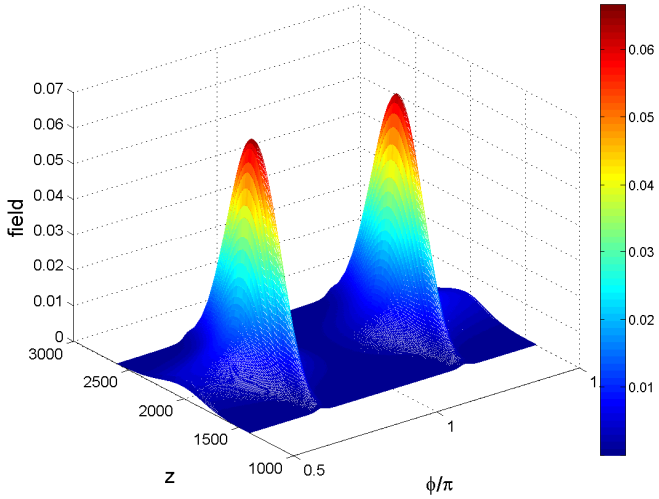

Figure 5.21 The side view of absolute value of the field u with $\rho = 3500$. It is the total field for a stigmatic incident Gaussian beam ($\delta_{12} = \delta_{21} = 0$, $\delta_{11} = \delta_{22} = 1$, $q(0) = -500i$) impinging upon the half plane at $(x_i = 2, z_i = 0)$ in the direction of $(\theta_i, \pi + \varphi_i) = (\pi/3, \pi + \pi/4)$ with $k = 1$.

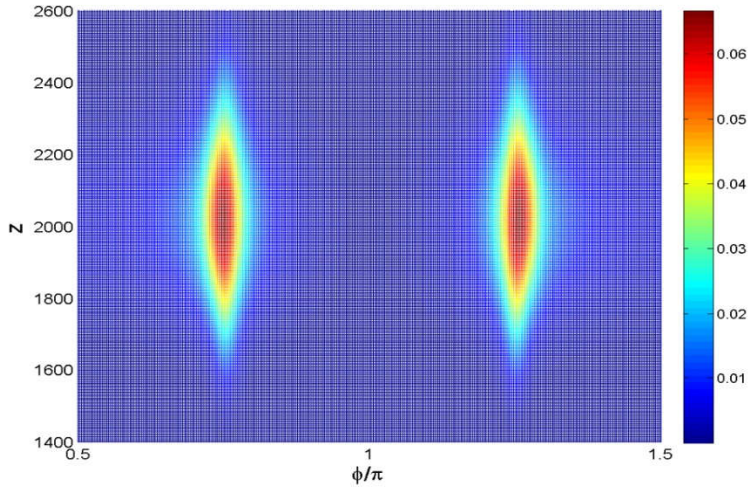

Figure 5.22 The plan view of absolute value of total field u with $\rho = 3500$. It is the total field for a stigmatic incident Gaussian beam ($\delta_{12} = \delta_{21} = 0$, $\delta_{11} = \delta_{22} = 1$, $q(0) = -500i$) impinging upon the half plane at $(x_i = 2, z_i = 0)$ in the direction of $(\theta_i, \pi + \varphi_i) = (\pi/3, \pi + \pi/4)$ with $k = 1$.

All the patterns show the same results of Katsav [1].

5.5 Numerical verification

In this section, several numerical experiments are conducted to validate the above 3D Gaussian beam summation method for half-plane diffraction by comparison with GRASP and the Kirchhoff half-screen Boundary-diffraction theory used in 2D-DGBA.

As shown in Figure 5.23, the diffraction of a Gaussian beam by a perfectly conducting half-plane in 3D space is considered. The half-plane is in the $y=0$ plane with $x \geq 0$. The edge-axis coincides with the z-axis. φ_i and θ_i are respectively also used to express the azimuth and polar angles of the incident beam. The frequency of all the incident beams is set at 100 GHz.

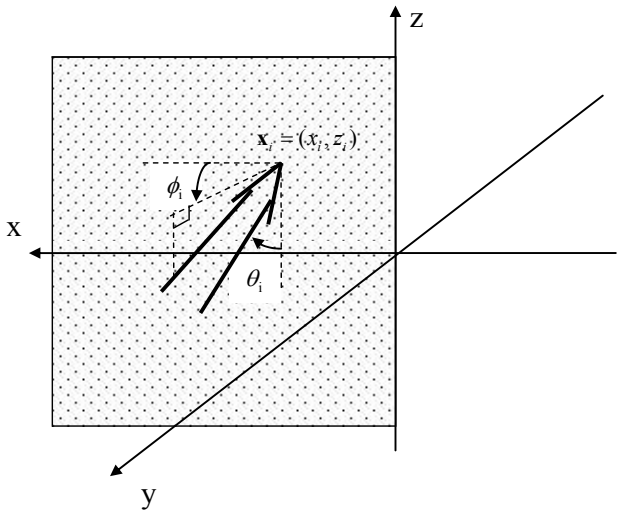

Figure 5.23 The basic model of 3D half plane diffraction. A Gaussian beam (the arrow in the figure) impinges on a half plane $(y=0, x \geq 0)$, in the direction of (φ_i, θ_i).

In the first scenario, assuming a circular incident Gaussian beam, perpendicularly impinging on the half-plane at $\mathbf{X}_i = (w_0, 0)$ in the direction of $(\varphi_i = \pi + \pi/2, \theta_i = \pi/2)$, i.e. the $-z$ direction; the simulation results of 3D GBS, BDT and PO are compared. The beam width w_0 has been chosen to be eight wavelengths wide and located 100λ away from the half-plane. The fields are calculated for a backward near-field cut at the co-ordinates $(y=0, z=300\lambda)$.

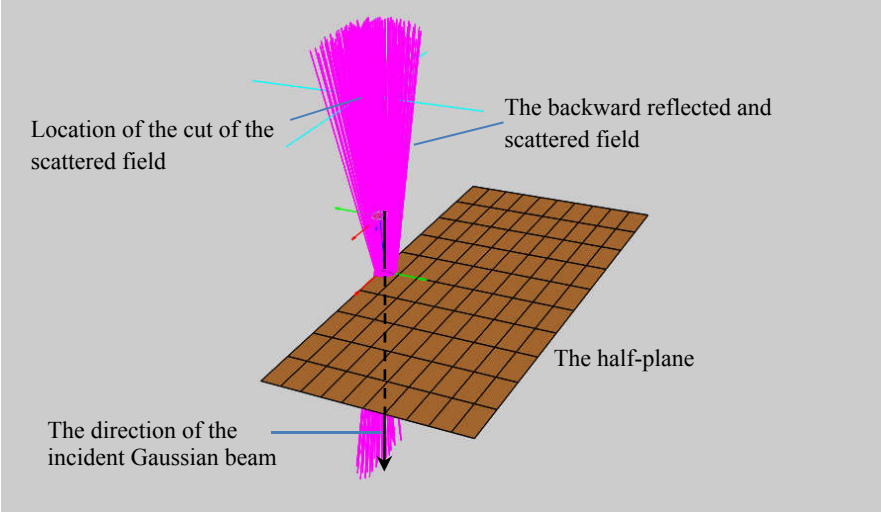

Figure 5.24 The first scenario modelled in GRASP where a circular Gaussian beam ($w_0 = 8\lambda$) impinges on the half plane at $\mathbf{X}_i = (w_0, 0)$ in the direction of $(\varphi_i = \pi + \pi/2, \theta_i = \pi/2)$.

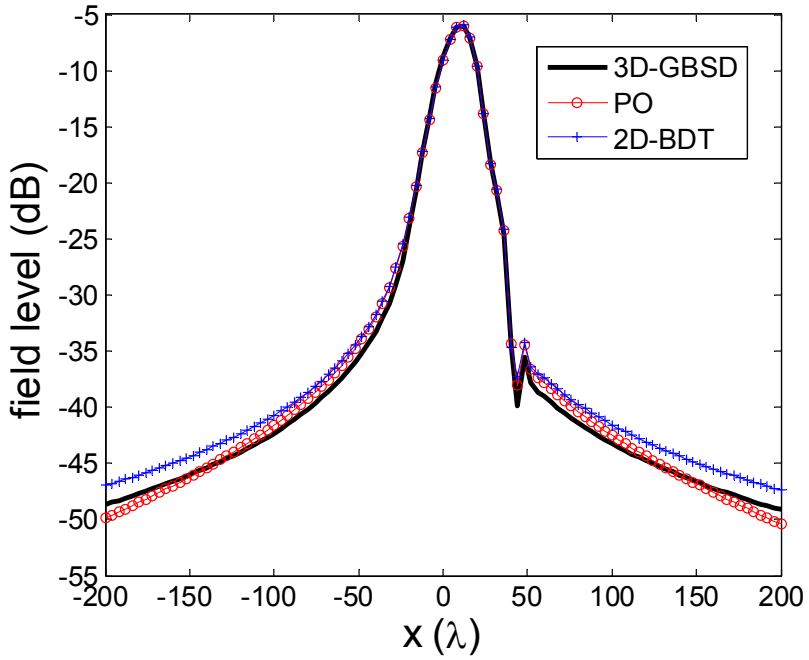

Figure 5.25 Comparison of the backward scattered field with PO and Kirchhoff half-screen BDT with the parameters $w_0 = 8\lambda$, $\mathbf{X}_i = (w_0, 0)$ and $(\varphi_i = \pi + \pi/2, \theta_i = \pi/2)$, based on the modelled scenario of Fig. 5.24.

The model for simulation in GRASP is present in Figure 5.24. In it, the pink rays are launched from a source point coincident with the centre of the beam waist.

Figure 5.25 plots the simulated results. It is seen that the 3D GBS diffraction theory is very accurate near the beam axis. In some areas, the results start to deviate from physical optics and Kirchhoff half-screen BDT; but even there the deviation is not more than a decibel or two.

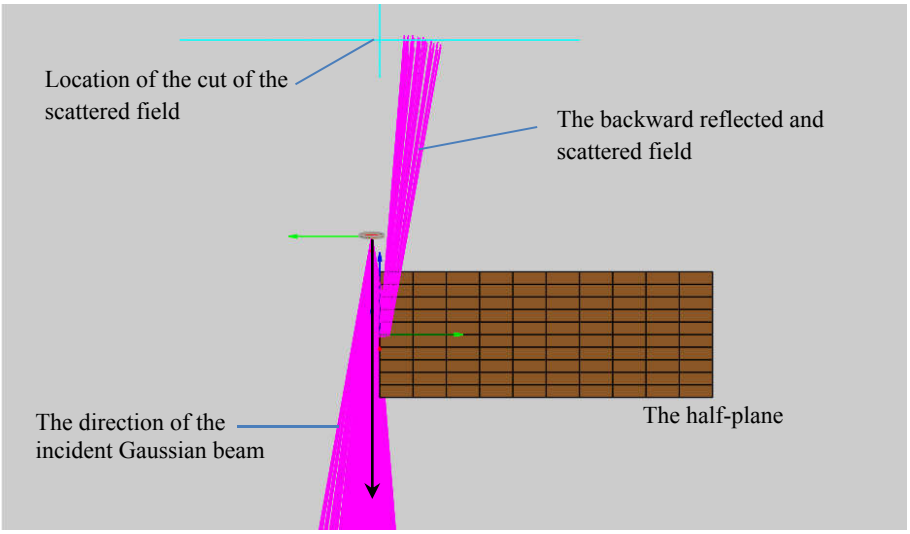

Figure 5.26 The model built in GRASP for the second case with a circular Gaussian beam ($w_0 = 8\lambda$) impinges on the half plane at $\mathbf{X}_i = (-w_0, 0)$ in the direction of $(\varphi_i = \pi + \pi/2, \theta_i = \pi/2)$.

In the second scenario, the same model as for the first is employed but with $\mathbf{X}_i = (-w_0, 0)$. Figure 5.26 again presents the GRASP model and Figure 5.27 the simulated results. Note again, the results of 3D GBS diffraction theory are very accurate near the beam axis, better in fact than for Kirchhoff half-screen BDT. Outside the paraxial region, the results start to deviate from physical optics, but even there the deviation is not more than a decibel or two.

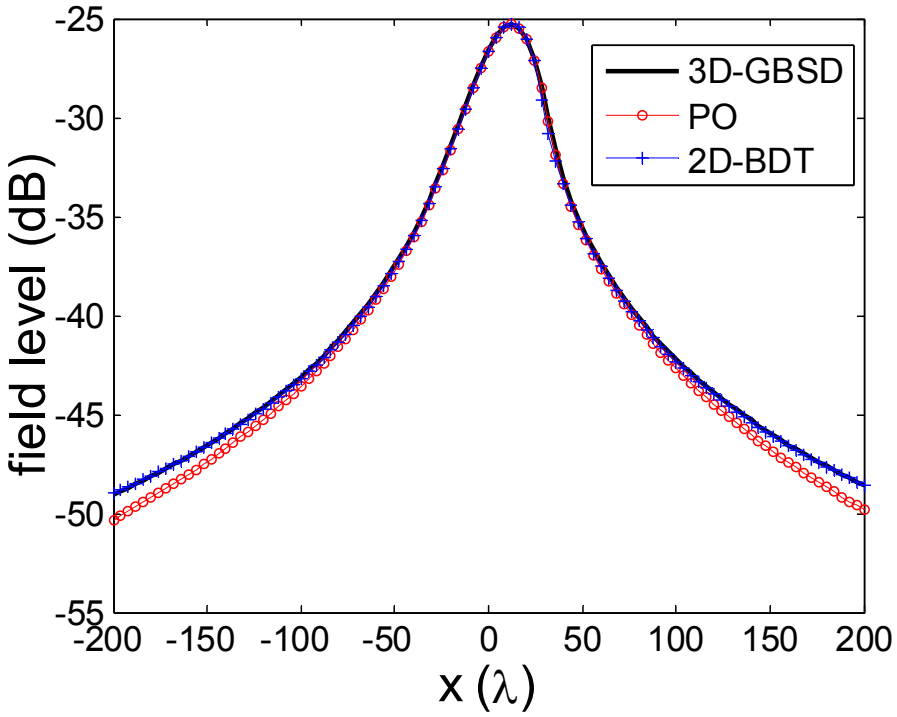

Figure 5.27 Comparison of the backward scattered field with PO and Kirchhoff half-screen BDT with the parameters $w_0 = 8\lambda$, $\mathbf{X}_i = (-w_0, 0)$ and $(\varphi_i = \pi + \pi/2, \theta_i = \pi/2)$, based on the modelled scenario of Fig. 5.26.

In the third scenario, the simulation results are compared of a circular incident Gaussian beam obliquely impinging on the half-plane at $\mathbf{X}_i = (w_0, 0)$ in the direction $(\varphi_i = \pi + \pi/4, \theta_i = \pi/2)$. The beam width w_0 is still 8λ wide and located 100λ from the half-plane along the principal optical axis of the beam. In order to have a better display of the differences, the fields are calculated for a backward near field cut 600λ away from the half-plane along the principal optical axis. The simulation model built in GRASP is shown in Figure 5.28. Figure 5.29 shows the associated simulated results. As mentioned at the beginning of this chapter, by using 2D-DGBA, there will be some deviations even near the centre for reflected beams when beam incidence grows to be progressively more oblique in azimuth angle. Contrariwise, it shows that the 3D GBS diffraction theory is very accurate near the beam axis, even when the azimuth angle φ_i off from $\pi/2$. The 3D GBS half-plane diffraction method shows its advantage of accuracy when dealing with oblique azimuth angles of incidence.

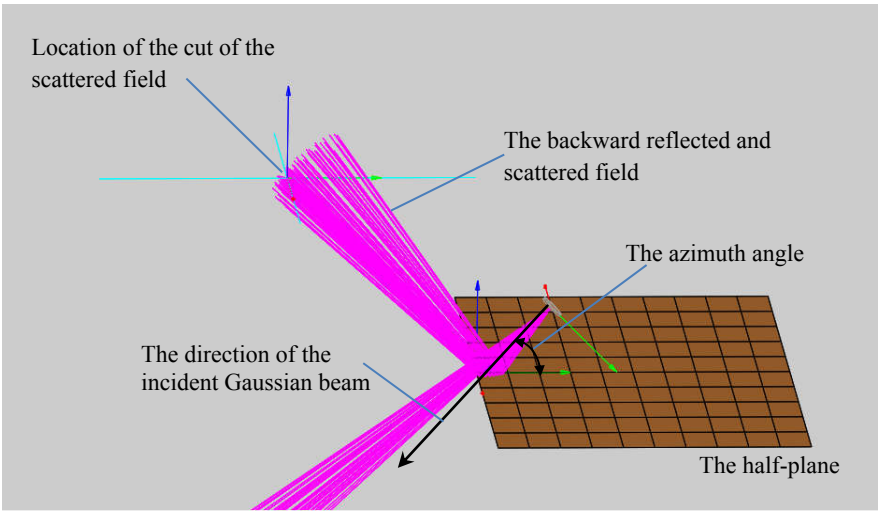

Figure 5.28 The model built in GRASP for the third case with a circular Gaussian beam ($w_0 = 8\lambda$) impinges on the half plane at $\mathbf{X}_i = (w_0, 0)$ in the direction of $(\varphi_i = \pi + \pi/4, \theta_i = \pi/2)$.

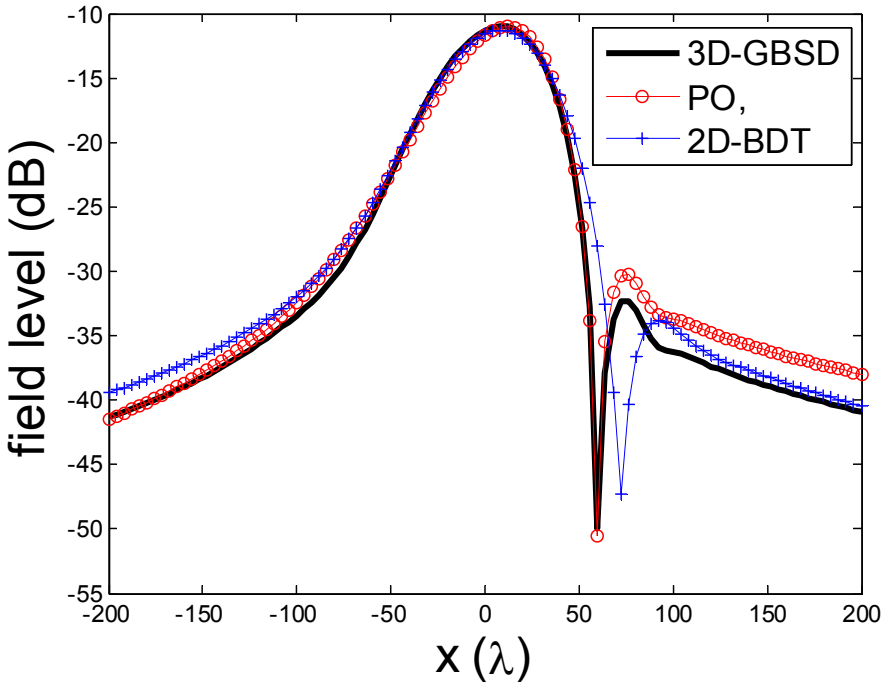

Figure 5.29 Comparison of the backward scattered field with PO and Kirchhoff half-screen BDT with the parameters $w_0 = 8\lambda$, $\mathbf{X}_i = (w_0, 0)$ and $(\varphi_i = \pi + \pi/4, \theta_i = \pi/2)$, based on the model in Fig. 5.28.

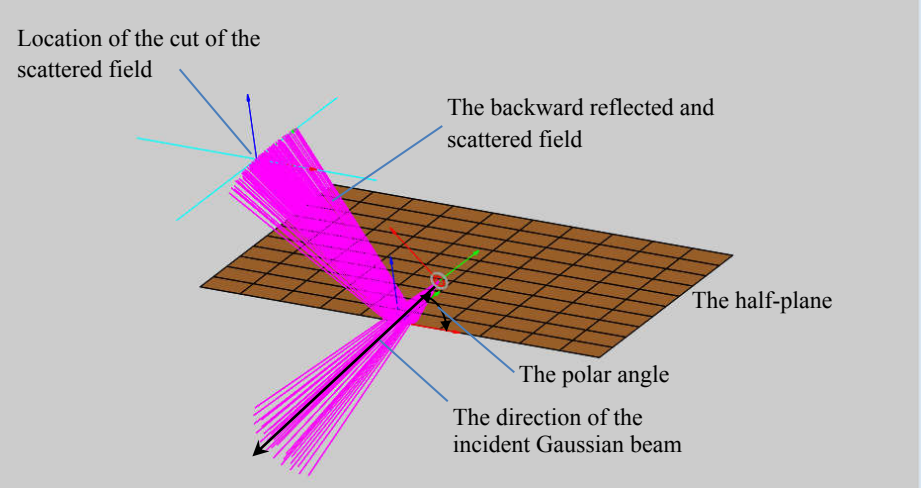

Figure 5.30 The model built in GRASP for the fourth case with a circular Gaussian beam ($w_0 = 8\lambda$) impinges on the half plane at $\mathbf{X}_i = (w_0, 0)$ in the direction of $(\varphi_i = \pi + \pi/2, \theta_i = \pi/4)$.

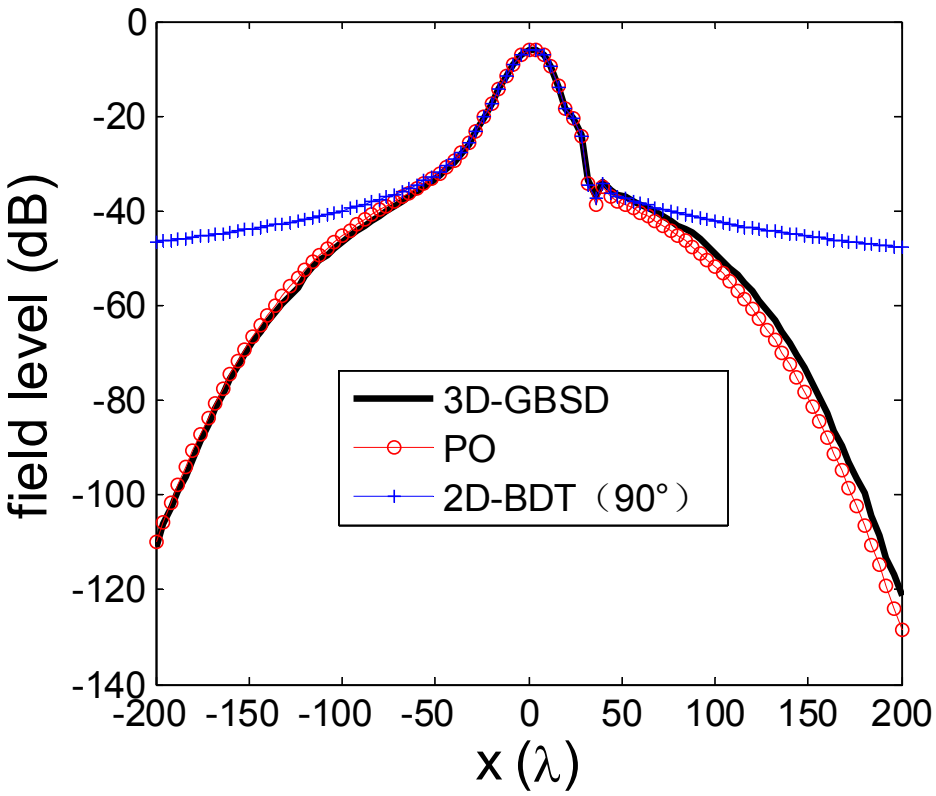

Figure 5.31 Comparison of the backward scattered field with PO and Kirchhoff half-screen BDT with the parameters $w_0 = 8\lambda$, $\mathbf{X}_i = (w_0, 0)$ and $(\varphi_i = \pi + \pi/2, \theta_i = \pi/4)$.

The fourth scenario is just like the third but in the direction $(\varphi_i = \pi + \pi/2, \theta_i = \pi/4)$. The model in GRASP is shown in Figure 5.30. BDT of 2D-DGBA fails in this case, and in practice, normal incidences $(\varphi_i = \pi + \pi/2, \theta_i = \pi/2)$ are applied to replace the polar angles of oblique incidence.

Figure 5.31 presents comparative plots of the simulation results. 3D GBS diffraction theory is seen to be significantly accurate. Meanwhile, Kirchhoff half-screen BDT is incorrect outside the paraxial region, and more than 50 dB field deviation is observed. It is one of the main reasons to incorporate the 3D GBS half-plane diffraction method to DGBA.

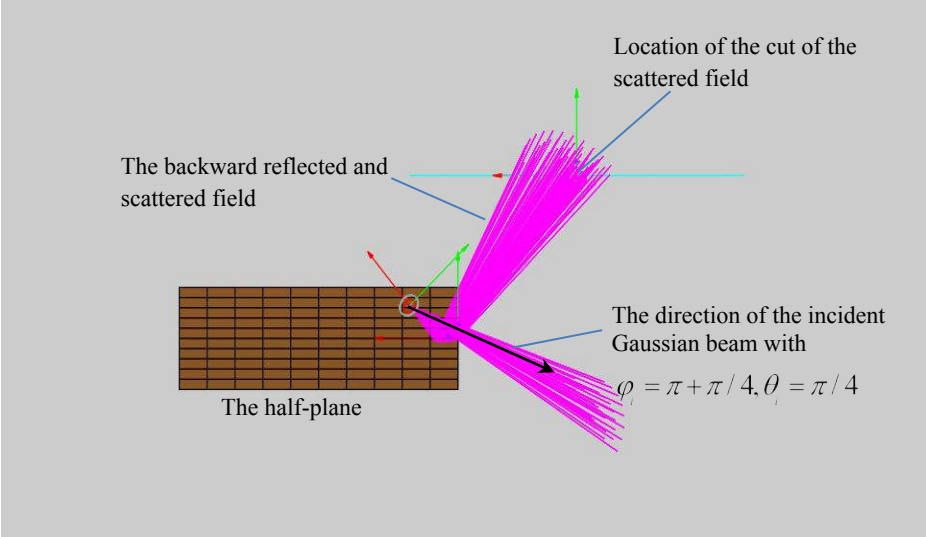

Figure 5.32 The model built in GRASP for the fifth case with a circular Gaussian beam ($w_0 = 8\lambda$) impinges on the half plane at $\mathbf{X}_i = (w_0, 0)$ in the direction of $(\varphi_i = \pi + \pi/4, \theta_i = \pi/4)$.

The fifth scenario considers an even more oblique incidence. The direction of the incident beam is $(\varphi_i = \pi + \pi/4, \theta_i = \pi/4)$; neither azimuth nor polar angle is normal. All other parameters are as for the fourth scenario. The GRASP model is shown in Figure 5.32, and the simulation results coming from it in Figure 5.33. Note in this low field region, a ± 5.0 dB field deviation can be observed within ± 25λ of BDT in comparison of ± 1.0 dB for the 3D GBS method. Again, the results prove that the 3D GBS half-plane diffraction method is accurate for arbitrary orientations of incident, which is superior to the BDT method of 2D-DGBA.

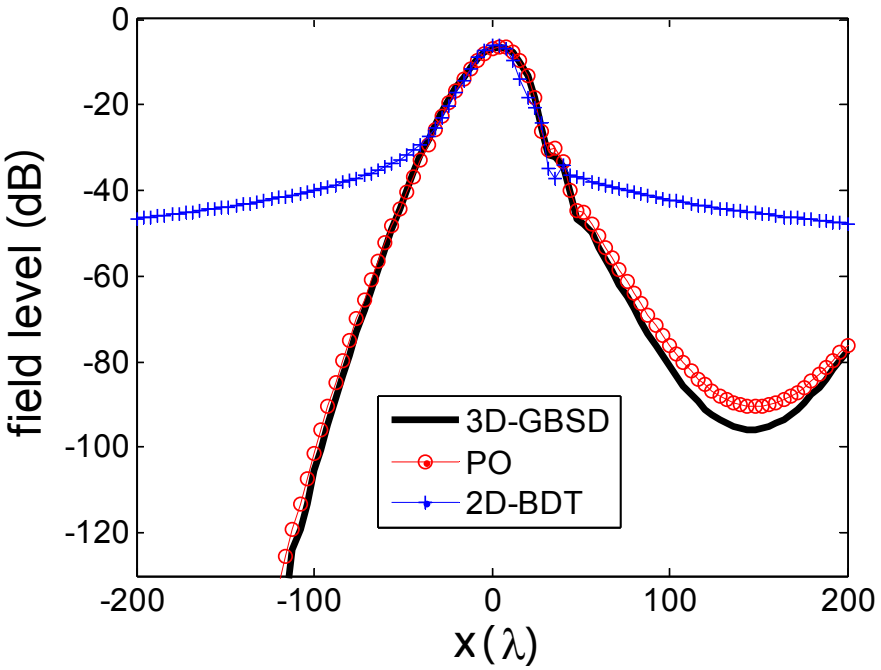

Figure 5.33 Comparison of the backward scattered field with PO and Kirchhoff half-screen BDT with the parameters $w_0 = 8\lambda$, $\mathbf{X}_i = (w_0, 0)$ and $(\varphi_i = \pi + \pi/4, \theta_i = \pi/4)$, for the scenario modelled in Fig. 5.32

The last scenario considers an incident elliptical Gaussian beam with $\delta_{11} = 4\delta_{22}, \delta_{22} = 1$ impinging upon the half-plane at $\mathbf{X}_i = (w_0, 0)$ in the direction $(\varphi_i = \pi + \pi/2, \theta_i = \pi/2)$. The beam has width 8λ and the fields are calculated at a backward near-field cut-plane with the co-ordinates $(y = 0, z = 300\lambda)$. The result of 3D GBS half-plane diffraction analysis is shown in Figure 5.34.

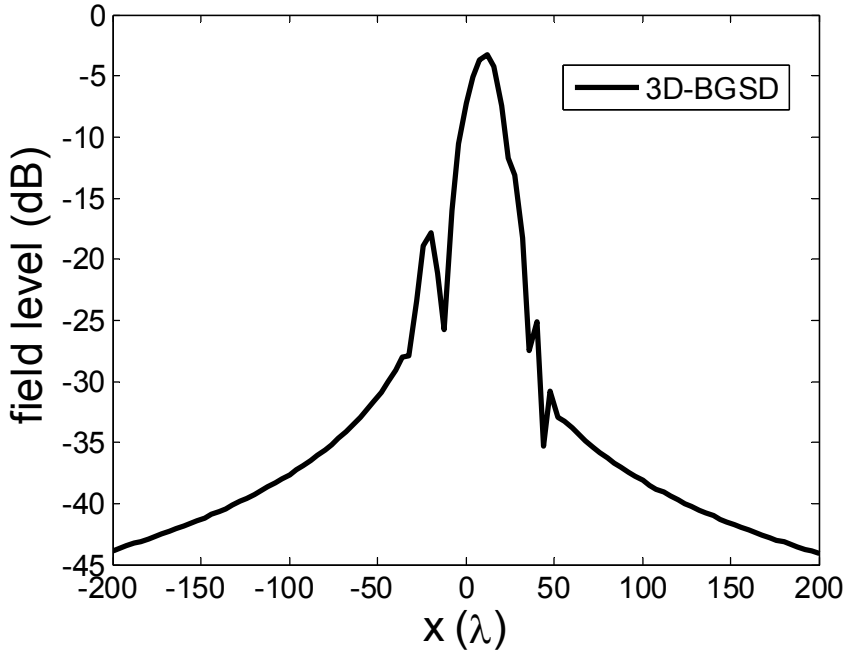

Figure 5.34 3D GBS simulation analysis result of the backward scattered field of an elliptical, normally-incident GB with waist parameters $\delta_{11} = 4\delta_{22}, \delta_{22} = 1$ from a half plane. The intersection point is $\mathbf{X}_i = (w_0, 0)$.

5.6 Summary

The principles of the 3D GBS half-plane diffraction method have been derived. This method has the capability of analysing a general, astigmatic, GB impinging on a half-plane at an arbitrary angle of incidence. The diffracted field is represented as a sum of diffracted Gaussian beams emerging from a discrete set of points and directions along the edge, making the method one of beam-to-beam (B2B) analysis. By comparison with PO, 3D GBS shows its advantage of accuracy in comparison with BDT analysis as used in 2D-DGBA.

References

[1] Katsav M, Heyman E. Gaussian beams summation representation of half plane diffraction: A full 3-D formulation [J]. Antennas and Propagation, IEEE Transactions on, 2009, 57(4): 1081-1094.

[2] J. Bowman, T. Senior, and P. Uslenghi, Electromagnetic and Acoustic Scattering by Simple Shapes. Amsterdam: North-Holland, 1969.

[3] L. Felsen and N. Marcuvitz, Radiation and Scattering of Waves. Englewood Cliffs, NJ: Prentice-Hall, 1973.

[4] P. Clemmow, "The Plane Wave Spectrum Representation of Electromagnetic Fields." New York: IEEE Press, 1996.

[5] N. Bleistein, "Uniform asymptotic expansions of integrals with stationary point near algebric singularity," Comm. Pure Applied Mathem., vol. XIX, pp. 353-370, 1966.

[6] M. Katsav and E. Heyman, "Beam summation analysis of half plane diffraction," IEEE Trans. Antennas Propag., vol. 55, pp. 2247-2257, 2007.

[7] M. Katsav and E. Heyman, "Phase space beam summation analysis of half plane diffraction," IEEE Trans. Antennas Propag., vol. 55, pp. 1535-1545, 2007.

[8] M. Katsav and E. Heyman, "A beam summation representation for 3D radiation from a line source distribution," IEEE Trans. Antennas Propag., vol. 56, pp. 601-605, 2008.

[9] T. Heilpern, V. Timchenko, and E. Heyman, "Beam summation algorithm for wave radiation and guidance in stratified media," J. Acoust.Soc. Am., vol. 121, pp. 1856-1864, 2007.

[10] G. Suedan and E. Jull, "Beam Diffraction by a half-plane and wedges: Uniform and asymptotic solutions," J. Electromagnetic Waves Applicat., vol. 3, pp. 17-26, 1989.

Chapter 6 Implementation of a Modular 3D Gaussian Beam Diffraction Approach

6.1 Overview

A 3D Gaussian Beam (GB) diffraction approach for reflector antenna analysis is presented. This method expands the input beam/field from the feed or prior FSS into a set of elementary Gaussian beams by using a windowed Fourier transform (WFT). These Gaussian beams propagate to the next reflector. Reflected beams are treated in an extended Phase Matching manner as outlined in chapter 3. Diffracted beams are treated with the 3D Gaussian beam diffraction method of chapter 5. Diffraction is now considered of a general, astigmatic, Gaussian beam, impinging arbitrarily close to an edge of arbitrary orientation. The diffracted field will be seen to be expressed as a sum of diffracted Gaussian beams emerging from a discrete set of points and directions along the edge axis. The output field is a superposition of all reflected and diffracted Gaussian beams propagating to the next reflector, making the method highly modular and suitable for analysis of large, multi-element, quasi-optical systems.

6.2 Applying the Gaussian beam expansion method

In 3D-DGBA, as in 2D-DGBA, the Windowed Fourier Transform (WFT) [1-4] is applied as in the Gaussian beam expansion method. With this method the field on an input plane, produced by the previous feed, FSS, or reflector, is defined by Gaussian elementary beam modes. Let

$A_{mn\mu\nu} = \iint f(x,y)\exp(-j\Omega_0(nx+vy))\tilde{w}(x-mL_0)\tilde{w}(y-\mu L_0)dxdy$ with dual frame function $\tilde{w}$, be the expansion coefficients over a plane, and $B_{nm\mu\nu}(x,y,z)$ denote the beam mode. The field $f(x,y,z)$ is represented as an expansion such that

$$\begin{aligned} f(x,y,z) &= \sum_{m,n,\mu,\nu} A_{mn\mu\nu} w_{2D}(x-mL_0, y-\mu L_0)\exp(j(n\Omega_0 x + v\Omega_0 y)) \\ &= \sum_{m,n,\mu,\nu} [A_{mn\mu\nu}\exp(j(mn+\mu\nu)\Omega_0 L_0)]\, B_{nm\mu\nu}(x,y,z) \end{aligned}, \tag{6.1}$$

with a Gaussian shaped window function

$$w_{2D}(x,y) = w(x)w(y) = \frac{\sqrt{2}}{L}\exp(\frac{-\pi(x^2+y^2)}{L^2}). \tag{6.2}$$

Integers m and μ are indices of spatial-shift at an interval of L_0; and, n and v denote the spectral shift at an interval of Ω_0. L is the supporting width of the windowing function that is related to the Gaussian beam waist.

Two important parameters: over-sampling rate and zoom-factor are defined by

$$q = \frac{2\pi}{\Omega_0 L_0} \text{ and} \tag{6.3}$$

$$C = L / L_0 \quad . \tag{6.4}$$

They both significantly affect the shape of the dual frame function, and the over-sampling rate q has be to chosen larger than one. ($q > 1$)

Asymptotically, one has

$$B_{mn\mu\nu}(\rho_t, z_t) \cong \frac{\sqrt{2}}{L}\frac{q_{nv}(0)}{q_{nv}(z_t)}\exp(jk_0(z_t + \frac{\rho_t^2}{2q_{nv}(z_t)})), \tag{6.5}$$

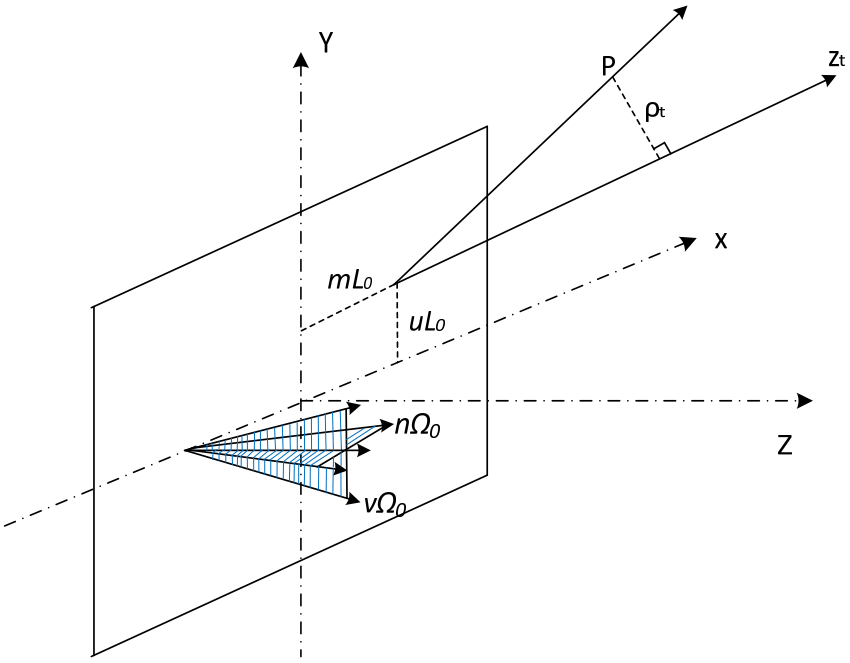

Figure 6.1 Interpretation of Gaussian beam expansion used in DGBA. An electromagnetic field on the aperture plane $z=0$ is expanded into a set of elementary Gaussian beams with Windowed Fourier Transform (WFT) method, with m and μ are indices of spatial-shift at an interval of L_0; and, n and v denote the spectral shift at an interval of Ω_0. Each of the expanded Gaussian beam are propagate along the direction of $\hat{z}_t$, and P is denoted as an observation point.

The transformed coordinates ρ_t and z_t are linked with the global co-ordinates (x, y, z). The spectral components of the wave-vector are obtained via transformations

$$\begin{aligned} z_t &= \left[n\Omega_0(x - mL_0) + v\Omega_0(y - \mu L_0) + \sqrt{k_0^2 - (n\Omega_0)^2 - (v\Omega_0)^2}\; z \right] \Big/ k_0 \\ \rho_t^2 &= (x - mL_0)^2 + (y - \mu L_0)^2 + z^2 - z_t^2 \end{aligned}, \qquad (6.6)$$

where $k_0 = 2\pi/\lambda$. z_t is the projection of the vector pointing from the source point $(mL_0, \mu L_0, 0)$ to the observation point $P(x, y, z)$ in the direction $\hat{z}_t = \frac{1}{k_0}(n\Omega_0, vK_0, \sqrt{k_0^2 - (n\Omega_0)^2 - (v\Omega_0)^2})$ of the wave-vector. All the information about the local radius of curvature $R(z_t)$ and the local spot size $w(z_t)$, of the beam at each axial position z_t, are absorbed by the complex beam parameter $q_{nv}(z_t)$, given as

$$q_{nv}(z_t)=\left(\frac{1}{R(z_t)}+j\frac{\lambda}{\pi w^2(z_t)}\right)^{-1}=z_t-j\frac{L^2}{\lambda}\left(1-\left(\frac{n\Omega_0}{k_0}\right)^2-\left(\frac{\Omega_0}{k_0}\right)^2\right). \tag{6.7}$$

It is noted that the asymptotic expression in terms of a complex beam is accurate only to within the range of the paraxial approximation. Figure 6.1 illustrates this interpretation of the expansion in terms of Gaussian beam modes and one of these expanded Gaussian beams propagates in the direction of $\hat{z}_t$.

A comparison is made between the field of the expanded Gaussian beam and that of the original. A schematic diagram of this is illustrated in Figure 6.2. Here a Gaussian beam is propagating along $+z$ with a 0.005 m beam waist, and the centre of the waist is located at $(x=0, y=0, z=0)$. This Gaussian beam is expanded into constituent Gaussian beams in the plane $(x, y, z=0.05m)$ and then each of these propagates independently to the plane $(x, y, z=0.1m)$. In Figure 6.2, for example, only several constituent beams propagating along $z+$ are shown. In fact, there are 664 such beams and each propagating along different directions. Now, an original Gaussian beam, propagating to the plane $(x, y, z=0.1m)$ directly, without using an expansion process, is traced for comparison, the working frequency being 54 GHz.

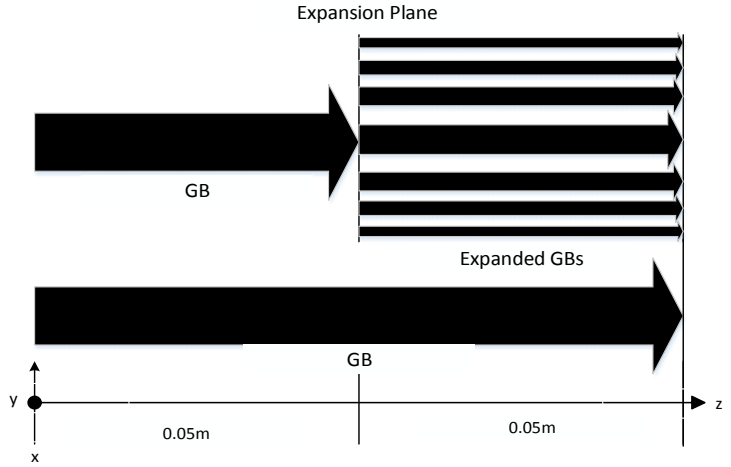

Figure 6.2 Schematic diagram of comparison between the fields with and without expansion. In the lower part of the figure, a Gaussian beam (GB) propagates along $z+$ from beam waist plane z=0 to plane z=0.1. In the upper part, the field produced by the same GB on z=0.05 plane is expanded by Windowed Fourier Transform (WFT) method. The expanded sub GBs also propagates to the z=0.1 plane.

Figure 6.3 shows the result. The blue trace in the figure is the field produced by the original Gaussian beam without expansion and the "+" trace the field produced by constituent Gaussian beams. The agreement is within 0.3 dB. In this case, we set the over-sampling rate to be $q = 2$ and the zoom factor to be $c = \sqrt{q}$.

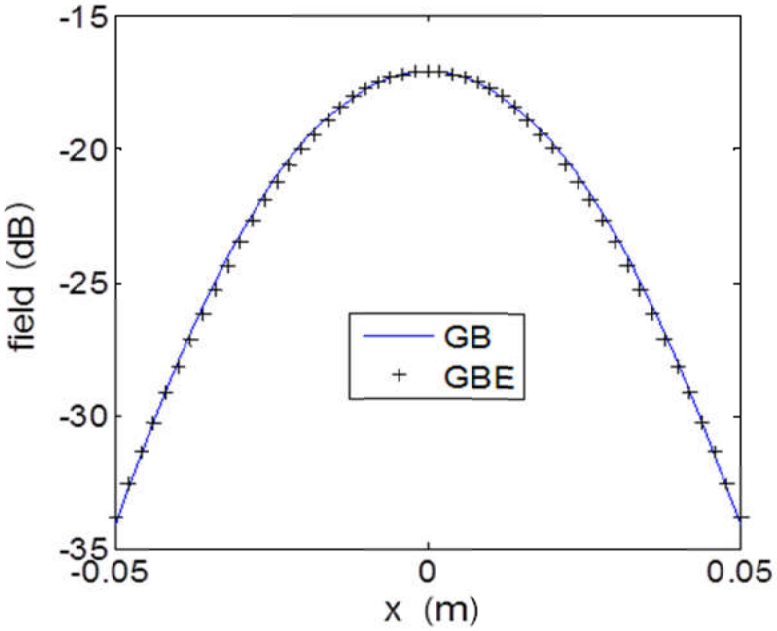

Figure 6.3 Comparison of field descriptions in terms of 1) constituent Gaussian beams and 2) with the original Gaussian Beam field expression (blue-line).

6.3 Incorporating the phase matching reflection method

Reflection analysis is fundamental to DGBA, especially for multi-reflector analysis. There are two reasons for this.

Firstly, assuming a normal incident Gaussian beam impinges on a half-plane with the intersection-point marked by P; if the distance a between P and the edge of the half-plane is $2w$, from (2.14), 99.97% of the power is found to remain within two beam widths. As illustrated in Figure 6.4, the conclusion is that only about 0.006% of the beam power leaks past the half-plane. If the distance is widened to $a = 3.5w$, nearly all of the beam power is intercepted. In practice, for safety, 3D-DGBA uses $a \geq 3.5w$ to distinguish reflection from diffraction.

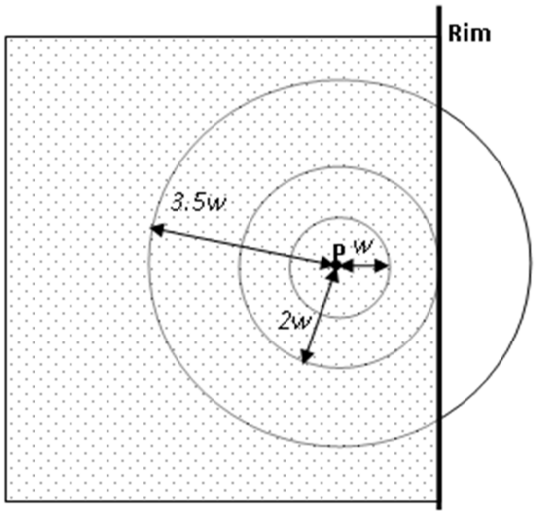

Figure 6.4 Schematic diagram: A normally incident Gaussian beam impinges on a half-plane with an intersection-point P. Only about 0.006% of the beam power is out of the rim when P is $2w$ away from the edge.

Secondly, when studying diffraction, it is natural to calculate the total diffraction field in the backward region by adding the scattered field to the reflected field, as considered in equations (4.12) and (5.55). The accuracy of reflection analysis significantly affects performance of DGBA.

In chapter 3, Phase Matching analysis is verified to be a better choice when dealing with elliptical, astigmatic incident, Gaussian beams. While in DGBA, the input beam field is expanded into a set of elementary circular Gaussian beams, the elliptical GB is the general case. Furthermore, in (3.24), the reflected beam has a more general form, which is easy to incorporate into the 3D diffraction method.

In 2D DGBA, the incident beam and the observation points are both described in a global (x, y, z) co-ordinate system, different from the local surface co-ordinate system $(\hat{\xi}, \hat{\eta}, \hat{n})$. It is difficult to apply the conclusion of the general case in section 3.3.1 directly. Therefore, in practice, the extended solution is applied, as given in section 3.3.2.

A comparison of Phase Matching analysis, PO reflection and GO reflection analyses for analysing an ellipsoidal reflector is given in this section. Figure 6.5 illustrates the geometry of the problem. The incident beam is chosen to propagate along +z with a beam waist of $w_0 = 5mm$. The centre of the waist is located at the origin of the global

coordinate system. The centre of the expansion plane is at $(x=0, y=0, z=0.01m)$ on the z-axis. The optical centre of the ellipsoidal reflector beam is set at $(x=0, y=0, z=0.74m)$ with an angle of incidence of 30°. The calculated reflected field is 0.2 m far away from the optical centre of the reflector.

The model of an ellipsoidal reflector is illustrated in Figure 6.6 with F1 and F2 noted as two focal points. The main axis of the incident beam is along the direction of F1-B and the main axis of the emergent beam is in the direction B-F2. The key parameters of the reflector are shown in Table 6.1.

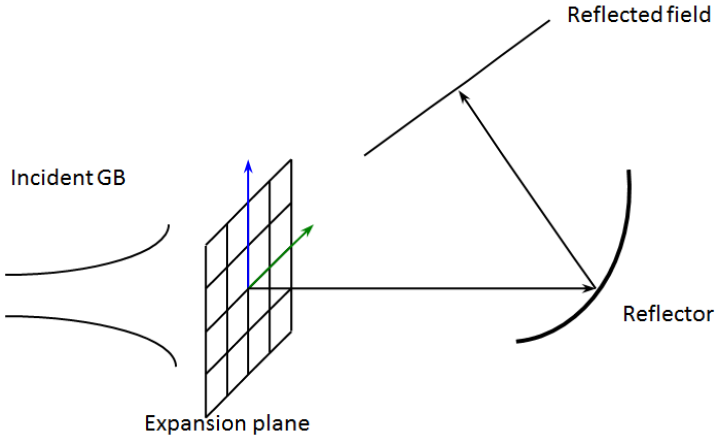

Figure 6.5 Geometry of the reflection on an ellipsoidal reflector. A Gaussian beam (GB) is first expanded on the expansion plane, and the produced sub GBs hit a reflector. The reflected field is calculated.

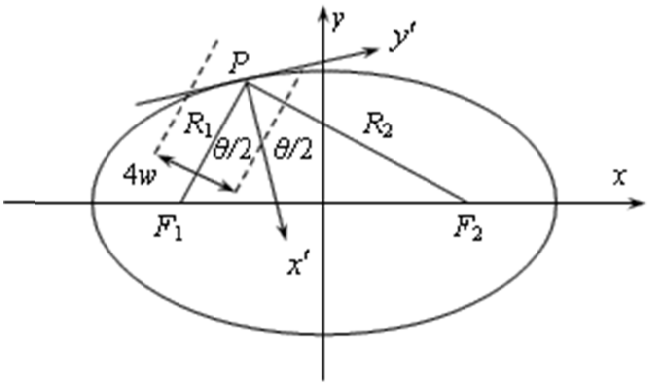

Figure 6.6 Geometry of single reflector taken as the portion of the surface from an ellipsoid centred at point P having distance R_1 and R_2 to the foci of the ellipse at F_1 and F_2 respectively. w is the beam width of the incident Gaussian beam and $4w$ is the diameter of the cylinder used to cut the surface.

Table 6.1 Parameters of the ellipsoidal reflector

Parameters	Value
Focal length（mm）	77.55
Major half axis（ mm）	209.3
Distance between F1 and B（ mm）	77.1
Distance between F2 and B（ mm）	341.5
Diameter of the reflector（ mm）:	107.3
Angle between incident and emergent beam θ（deg）	60

Figure 6.7 and Figure 6.8 illustrate the simulated reflected fields using GO analysis, Phase Matching analysis and an approximated PO analysis. Figure 6.7 shows the reflected field on the offset plane, and Figure 6.8 the field on the symmetric plane. Phase Matching analysis agrees well with GO, because each of them is essentially a GO method. Obviously, the agreement is poor in comparison with PO. They are consistent in the centre of the field, but deviations appear at low field levels.

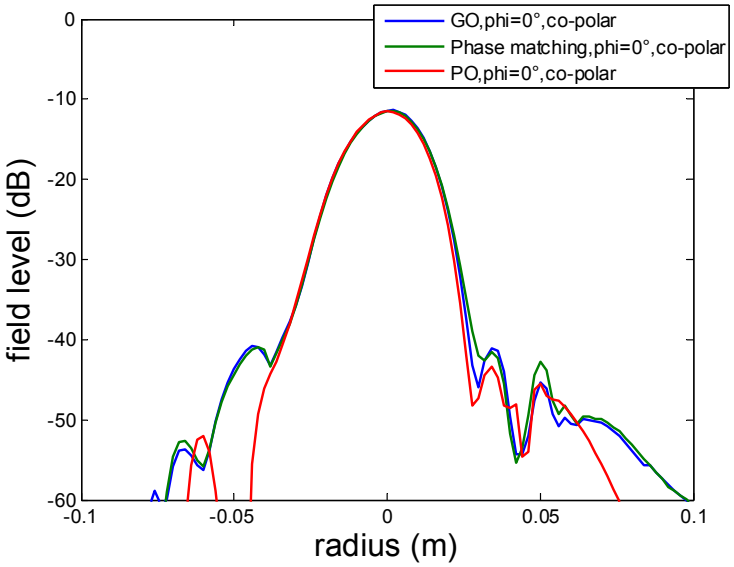

Figure 6.7 Reflected field 0.2m behind the ellipsoidal reflector (co-polar, offside plane), based on the modelled scenario of Fig. 6.5.

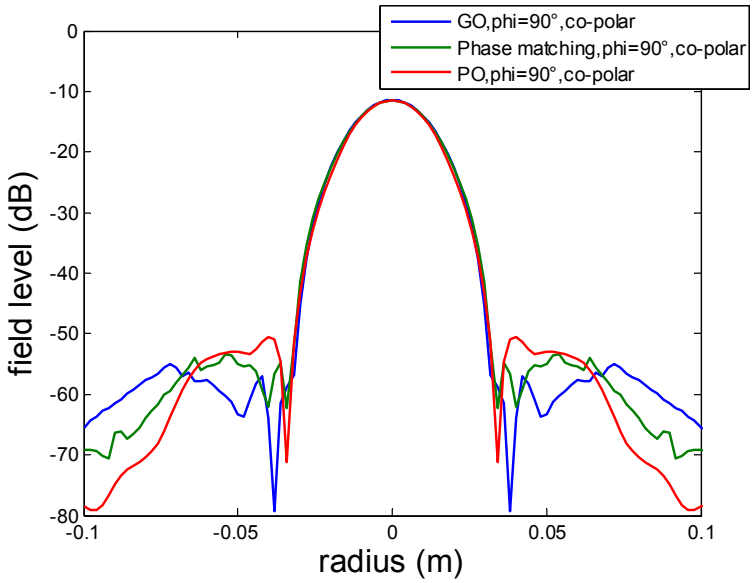

Figure 6.8 Reflected field 0.2m behind the ellipsoidal reflector (co-polar, symmetric plane), based on the modelled scenario of Fig. 6.5.

6.4 Incorporating 3D GBS diffraction analysis

Diffraction analysis is the most difficult calculation when undertaking analysis of a reflector antenna. By the Gaussian beam expansion method, the incident beam or field is expanded into many constituent Gaussian elemental beams. If the expanded elemental Gaussians impinge on the reflector with the point of intersection within $2w$ of the edge, the reflection method loses accuracy and diffraction analysis should be applied. When the spot sizes of the elemental GBs on the reflector are much less than that of the reflector, we use half-plane diffraction to approximate diffraction from a curved surface. In order to build 3D analysis software, the 3D GBS method of half-plane diffraction is incorporated into the 3D DGBA.

6.4.1 Models adaptation

In chapter 5, the details of the 3D GBS diffraction method were presented. According to the results of Chapter 5, this method is more accurate than classic Kirchhoff half-screen diffraction analysis in 2D DGBA. Also, the diffracted Gaussian beams, rather than only the diffracted field, can be directly obtained.

According to equation (5.5), it is critical to determine whether the intersection point P is located on the surface of the reflector or not, which in turn determines whether the reflected field should be added to the diffracted field, or not.

Figure 6.9 through to 6.12 show the relationship between the yet to be introduced parameters of A, $ZOFFS$, besides the position and azimuth direction of the incident GB. Assuming point R is on the rim of the reflector/half-plane, and the edge of the reflector/half-plane is along the vector perpendicular to the page of this paper, $\vec{z}_e$ denotes a vector from rim R to the intersection point P, which is equivalent to the vector $\overrightarrow{PR'}$. R' are the symmetric points of R with respect to point P along the line x_s. The local coordinate system $(\hat{x}_s, \hat{y}, \hat{n}_s)$ and reflected beam related coordinate system $(\hat{x}_r, \hat{y}, \hat{z}_r)$ are also illustrated in the Figures 6.9 - 12, with the y-direction being the same in both. The parameters A and ZOFFS are given by,

$$A = \vec{z}_e \cdot \hat{x}_r \quad \text{and} \tag{6.8}$$

$$ZOFFS = \vec{z}_e \cdot \hat{z}_r \,. \tag{6.9}$$

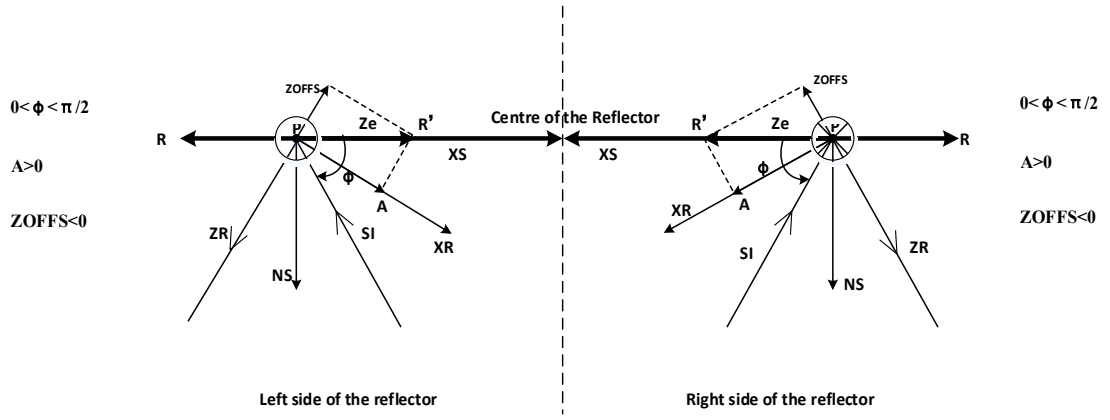

Figure 6.9 Two incident Gaussian beams with the same incident angle $(\pi/2-\varphi)$ impinge on the left and right side of a reflector/half-plane at intersection-points P. R denote the nearest points on the rim of the reflector. The local coordinate system $(\hat{x}_s,\hat{y},\hat{n}_s)$ and reflected beam related coordinate system $(\hat{x}_r,\hat{y},\hat{z}_r)$ with are constructed with $\hat{s}_i$ is the propagating direction of the incident beam, and $\hat{z}_r$, that of the reflected beam. R' are the symmetric points of R with respect to point P along the line x_s, and $\vec{z}_e$ denotes a vector from rim R to the intersection point P. A and $ZOFFS$ are the projected lengths of $\vec{z}_e$ on the $\hat{x}_r$ and the $\hat{z}_r$. The conclusion is when $A>0$ and $ZOFFS<0$, the intersection point P is on the surface of the reflector/half-plane with azimuth angle $0<\varphi_i<\pi/2$.

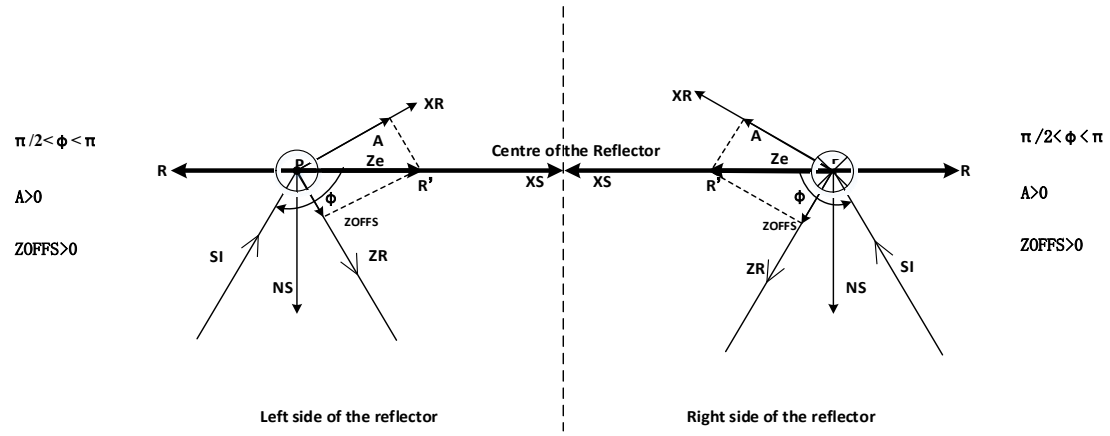

Figure 6.10 When $A>0$ and $ZOFFS>0$, the intersection-point P is on the surface of the reflector/half plane with azimuth angle $\pi/2<\varphi_i<\pi$. All other annotations are as for Fig. 6.9.

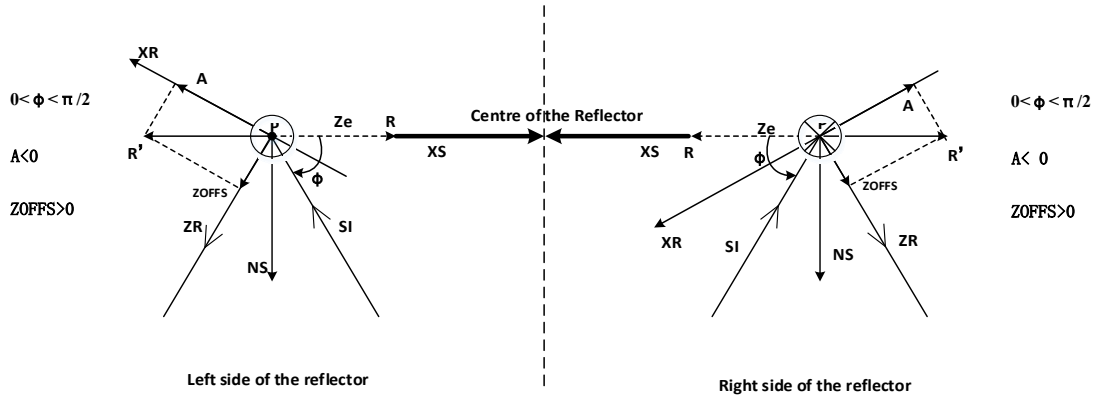

Figure 6.11 When $A<0$ and $ZOFFS>0$, the intersection-point P is out of the surface of the reflector/half plane with azimuth angle $0<\varphi_i<\pi/2$. All other annotations are as for Fig. 6.9.

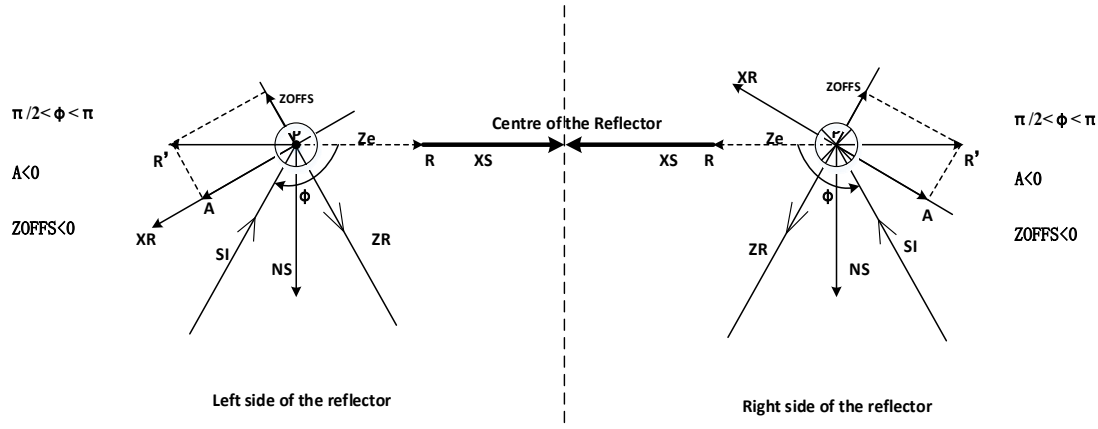

Figure 6.12 When $A<0$ and $ZOFFS<0$, the intersection-point P is out of the surface of the reflector/half plane with azimuth angle $\pi/2<\varphi_i<\pi$. All other annotations are as for Fig. 6.9.

It can be seen that, when $A>0$, the intersection point P is located on the reflector/half-plane. When $A<0$, it is off the reflector/half-plane. If $A\cdot ZOFFS<0$, the azimuth angle will be in the domain $0\le\varphi_i\le\pi/2$; if $A\cdot ZOFFS>0$, the domain is $\pi/2\le\varphi_i\le\pi$.

In calculating the diffracted field, an edge coordinate system should be built to suit 3D GBS analysis. The geometry of the problem is illustrated in Figure 6.13. The origin of the edge coordinate system $(x_s=0, n_s=0, z_s=0)$ is located at the edge of the half-plane. The intersection point of the incident beam, and the half-plane P lie on the plane (x_s, z_s) and also on the x_s axis. $\hat{n}_s$ and $\hat{z}_s$ are respectively the normals of the half plane and the

rim-tangential vector. $\hat{x}_s$, $\hat{n}_s$ and $\hat{z}_s$ construct a right-handed coordinate system. All the observation points Q in the original global coordinate system (x, y, z) are transformed to this edge coordinate system by

$$\begin{bmatrix} Q_{xs} \\ Q_{ns} \\ Q_{zs} \end{bmatrix} = (Q - P) \cdot \begin{bmatrix} x_{sx} & x_{sy} & x_{sz} \\ n_{sx} & n_{sy} & n_{sz} \\ z_{sx} & z_{sy} & z_{sz} \end{bmatrix} \begin{bmatrix} x \\ y \\ z \end{bmatrix}. \tag{6.10}$$

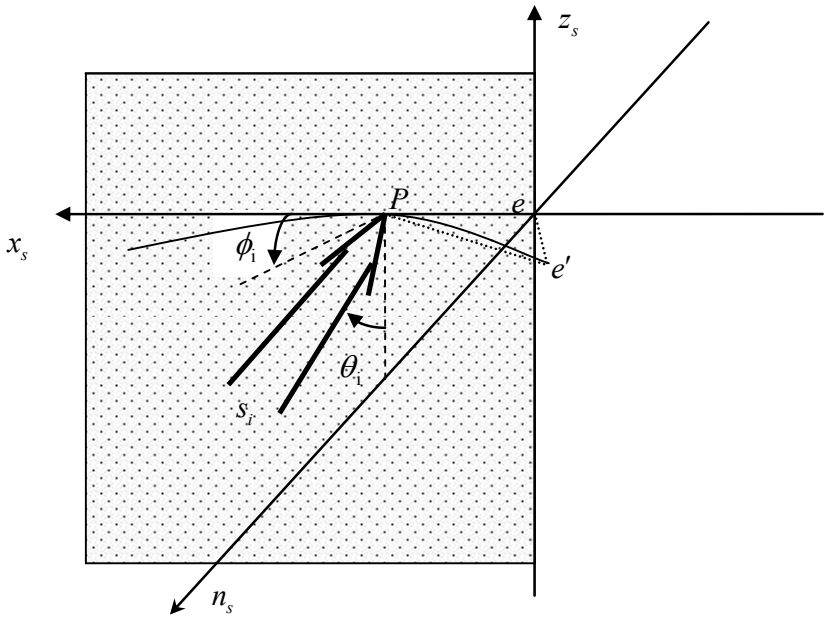

Figure 6.13 Geometry of a Gaussian beam imping on a reflector in the direction of $\hat{s}_i$ with an incident spherical angle (φ_i, θ_i). The intersection point is P, and the closest point on the rim of the reflector to P is denoted as e'. $\hat{n}_s$ is along the normal direction of the surface of the reflector at intersection point P, and a local coordinate system $(\hat{x}_s, \hat{n}_s, \hat{z}_s)$ is constructed with $\hat{z}_s$ tangent to the rim. The distance between P and e' is $z_{e'}$ Point e is denoted as the projected point of e' on vector $\hat{x}_s$.

The next step is to find the incident polar angle and azimuth angle of each elemental Gaussian beam. By describing the direction of incident of a beam as $\hat{s}_i$ in the global coordinate system (x, y, z), it is easy to calculate the polar angle θ_i as

$$\theta_i = \cos^{-1}(\hat{s}_i \cdot \hat{z}_s). \tag{6.11}$$

Defining the normal direction of the plane (x_s, s_i) as $\hat{t}_s$ such that

$$\hat{t}_s = \hat{s}_i \times \hat{z}_s, \tag{6.12}$$

the projection direction $\hat{p}_s$ of incident beam on the plane (x_s, n_s) is

$$\hat{p}_s = \hat{t}_s \times \hat{z}_s. \tag{6.13}$$

The azimuth angle φ_i is given by

$$\varphi_i = \cos^{-1}(\hat{p}_s \cdot -\hat{x}_s). \tag{6.14}$$

Also, because the reflector has a curved surface, generally the nearest point e' on the rim may not be in the $\hat{x}_s$ direction, as shown in Figure 6.13. This may affect the accuracy of the analysis. It is therefore rewritten to be

$$\left|\overrightarrow{Pe}\right| = \overrightarrow{Pe'} \cdot \hat{x}_s \ . \tag{6.15}$$

In practice, four new subroutines are coded into 2D-DGBA for full 3D analysis. The first subroutine is SUBOUTBEAMS coded for calculating the output Gaussian beams that emerge from z_m on the z-axis at polar angle $\theta_n = \cos^{-1}\zeta_n$ and azimuth direction α_j with expansion coefficients $a_{\boldsymbol{\mu}}$. The second subroutine DIFFR3D, is coded to replace the former DIFFER subroutine and to calculate the diffraction field. The third subroutine NEWGBDIF0, and forth NEWGBDIFF, are used for evaluating the contribution of the reflected and diffracted beams to the desired grid points (or all grid points of the output plane for analysing near field for the next reflector or, for calculating the far field.

6.4.2 Selection of parameters

Values of parameters significantly affect the efficiency and accuracy of 3D GBS diffraction analysis. Key parameters of the subroutine SUBOUTBEAMS are chosen according to the following principles [5]:

1) Over-completeness v

The Over-completeness parameter is defined by $v = k / \bar{k}$. For accuracy, v<1/3 and in practice v=1/4 is chosen.

2) Discretisation $\delta\alpha$

The Discretisation parameter $\delta\alpha$ is used to define the emergent directions of diffracted Gaussian beams. It is chosen to be $\delta\alpha$=$0.5\theta_{Di}$=$0.5/\sqrt{k\varsigma_i b_i}$.

3) b_t of emergent Gaussian beam

b_t is chosen to be $5000/(k\varsigma_i b_i)$ to make emergent Gaussian beams well collimated.

4) b_z of WFT-frame expansion

b_z is calculated by $b_z = b_t / \sin\theta_i$.

5) Spatial width of the WTF frame $\bar{z}$

$\bar{z}$ is the spatial width of the WTF frame given by $\bar{z}$=$\sqrt{b_z v\lambda}$.

6) Spectral width of WTF frame $\bar{\zeta}$

$\bar{\zeta}$ is the spectral width of the WTF frame and is calculated by $\bar{\zeta}=\dfrac{\bar{z}}{b_z}$.

6.4.3 Methods of accelerating analysis

When calculating the diffraction field, all of the emergent diffracted Gaussian beams need to be superposed, which makes 3D GBS analysis time consuming. Under the constraint of not suffering loss in accuracy, improvement in the performance and efficiency of 3D-DGBA requires using as few emergent diffracted beams as possible. 3D-DGBA analysis is accelerated through judicious setting of the following parameters:

1) The range of ζ

The largest domain of ζ is $-1 \le \zeta \le 1$. However, it will be time consuming to span the whole domain in every case, especially when the energy of each elemental Gaussian beam is considered. In practice, we set this domain to 4 times *sin ()*, the asymptotic beam growth angle θ_0

$$\theta_0 = \lim_{z>>z_c}[\tan^{-1}(\frac{w}{z})] = \tan^{-1}(\frac{\lambda}{\pi w_0}). \tag{6.16}$$

Therefore,

$$\begin{cases} -1 < \zeta \le \zeta_i + 2\sin\theta_0, & if\ \ \zeta_i - 2\theta_0 \le \text{-}1 \\ \zeta_i - 2\sin\theta_0 \le \zeta < 1, & esleif\ \ \zeta_i + 2\theta_0 \ge 1 \\ \zeta_i - 2\sin\theta_0 \le \zeta \le \zeta_i + 2\sin\theta_0, & elseif \end{cases}. \tag{6.17}$$

Typically, by applying this constraint, more than 30% of the diffracted Gaussian beams can be removed from consideration.

2) The domain of α

According to Katsav *et al* [5], $\pi - \varphi_i - 3\theta_{Di} \le \alpha \le \pi - \varphi_i + 3\theta_{Di}$ is used for the backward space region and $\pi + \varphi_i - 3\theta_{Di} \le \alpha \le \pi + \varphi_i + 3\theta_{Di}$ for the forward. However, from Figures 5.6 and 5.13, it can be seen that the images of Φ and $a_{\mathbf{u}}$ cover nearly the whole domain 0 to 2π. In practice therefore, we focus on the backward region and choose the α to be $0 \le \alpha \le \pi$. Comparing then the range of $0 \le \alpha \le 2\pi$, 50% reduction is noted in the number of diffracted Gaussian beams required.

3) The range of z_m

z_m represents space-sampling points on the edge with m = 0, ±1, ±2... the distance between two adjacent points giving a span, z_m. It is found that when calculating the diffracted field of many incident Gaussian beams, the number of sampling points can be chosen to be very small. In practice, when analysing hundreds of expanded incident Gaussian beams, a few points is sufficient in most cases; choosing m = 0, ±1 is adequate. A significant amount of computing time can be saved by using the above combination of optimisations.

The typical acceleration in analysis is by a factor of three. This is outlined in Table 6.2, which compares time savings between employing and not employing the optimum parameter value selection.

Figure 6.14 and Figure 6.15 plot the associated analysis to Table 6.2. The use of optimum parameter settings increases efficiency of analysis by a factor of 20.

Table 6.2 Efficiency of 3D DGBA with and without speeding up methods

	The No. of incident GBs	Observed points	The No. of emergent GBs	Computing time
Without optimisation	350	402	113724	15464s
With optimisation	350	402	4212	713s

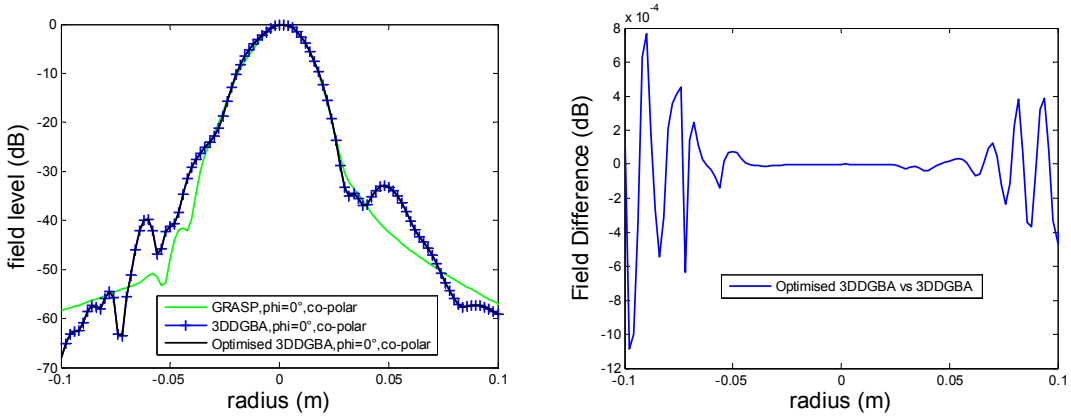

Figure 6.14 Near field difference between optimised and without optimised 3D-DGBA on the offset plane (co-polar). Parameters of without optimised 3D-DGBA: $-1 \le \zeta \le 1, 0 \le \alpha \le 2\pi$ **and m = 0, ±1, ..., ±8. Parameters of optimised 3D-DGBA:** $\max(-1, \zeta_i - 2\sin\theta_0) \le \zeta \le \min(1, \zeta_i + 2\sin\theta_0)$, $0 \le \alpha \le \pi$ **and m = 0, ±1.**

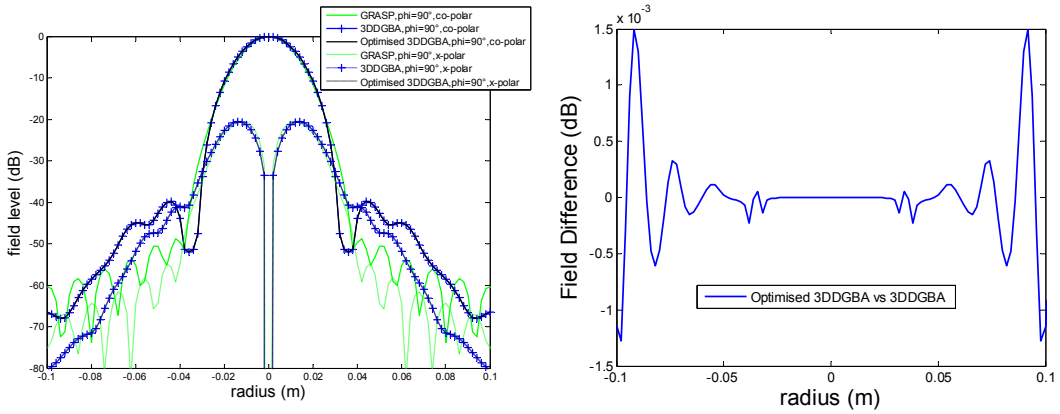

Figure 6.15 Near field difference between optimised and without optimised 3D-DGBA on the symmetric plane (co-polar and cross-polar). Parameters of without optimised 3D-DGBA: $-1 \le \zeta \le 1$, $0 \le \alpha \le 2\pi$ **and m = 0, ±1, ..., ±8. Parameters of optimised 3D-DGBA:** $\max(-1, \zeta_i - 2\sin\theta_0) \le \zeta \le \min(1, \zeta_i + 2\sin\theta_0)$, $0 \le \alpha \le \pi$ **and m = 0, ±1.**

6.5 Modularity

An analysis cycle of the improved DGBA approaches for multi-reflector analysis is illustrated in Figure 6.16. It consists of six steps:

1) The incident field on an input plane could be either the near field of a feed or the field from a previous FSS/reflector. 3D-DGBA applies a WFT on the input field to produce elementary Gaussian beams.
2) These Gaussian beams propagate to the next QO component, by the field expressions of Gaussian beam propagation.
3) Those Gaussian beams subsequently reflected are treated by Phase Matching analysis and so reflected Gaussian beams are produced.
4) Those beams that meet the reflector at less than 3.5 beam widths away from the rim, suffering significant diffraction. The 3D GBS diffraction analysis is then applied, producing a set of diffracted GBs.
5) Modularity

   5.1) The reflected and diffracted beams propagate to the next reflector. These beams can be handled with the same processes of (2), (3) and (4), making the method highly modular.

   5.2) Or, the reflected and scattered fields are superposed in the output plane. These beams fields can be then handled with the same processes of (1), (2) (3) and (4); again, modular analysis is enabled
6) Alternatively, all beams are superposed on an output plane for calculating the near field for an FSS or the far field when dealing with the final reflector in a train of mirrors.

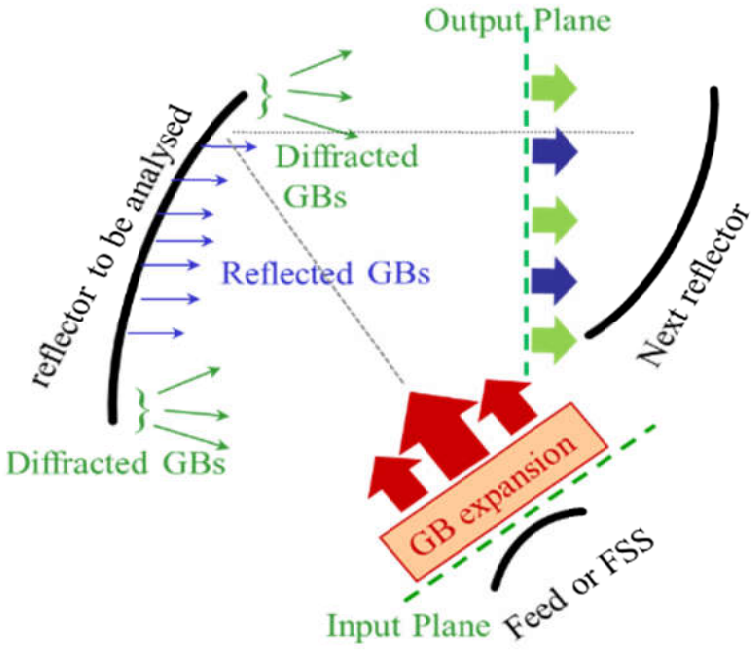

Figure 6.16 Illustration of a single step of the 3D-DGBA in a multi-reflector analysis: 3D-DGBA applies a WFT on the input field to produce elementary Gaussian beams. Those Gaussian beams subsequently reflected are treated by Phase Matching analysis and so reflected Gaussian beams are produced. Those beams that meet the reflector at less than 3.5 beam widths away from the rim are analysed 3D GBS, producing a set of scattered GBs. The reflected and scattered fields are superposed in the output plane. By repeating these steps, the cascaded reflectors can be analysed, which make 3D-DGBA highly modularised.

In step (5), only (5.2) is realised, meaning the field in the output plane is always calculated and then expanded into its elemental Gaussian beams propagating to the next reflector or other QoN device. However, as mentioned in section 6.1, this expansion method is not strictly accurate and may cause errors. In future, it is worth searching for an efficient way to use the reflected and scattered Gaussian beam more directly.

6.6 Flow chart of 3D-DGBA

The relationship of files in 3D-DGBA is presented in Figure 6.17. It is similar to that for 2D-DGBA. The program "conic.f90" is used for generating grids of conic reflectors. The input file is " conic.in " and two output files "refl.out" and "normals.out" which contain the coordinates of the grid points and the surface normals at the grid-points, respectively. "dual_frame.txt" describes the dual frame functions for the Gaussian beam

expansion. “gaubeam.in” gives the input parameters for the single reflector analysis. The output file “GBE.in” storages the coefficients of the result of Gaussian beam expansion used for analysing the far field or preparing the input field for the next reflector. Another Output file “field.txt” gives the result of simulated near or far fields. “gaubeam.f90” is the main program of 3D-DGBA. All reflection and diffraction analysis are handled in the file of gaubeam.f90.

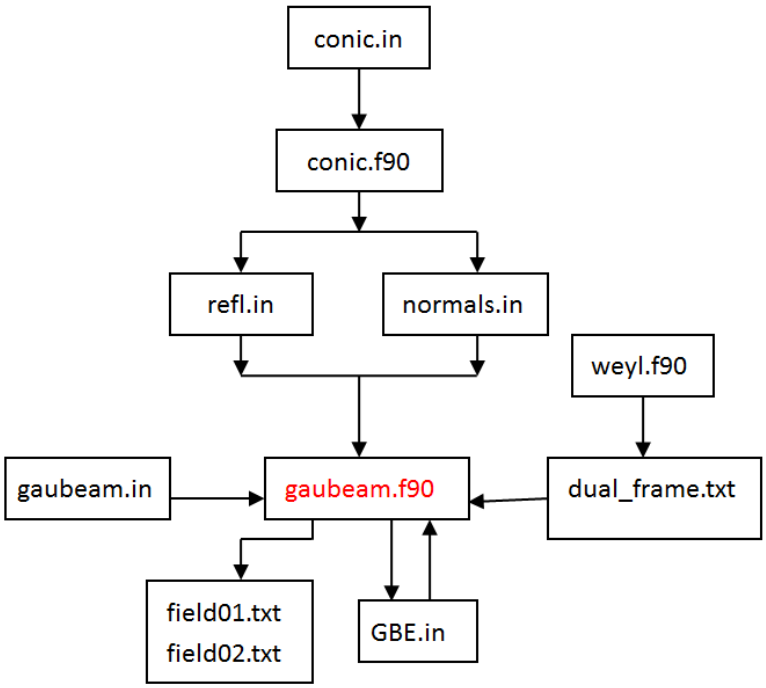

Figure 6.17 Files relationship in 3D-DGBA. The arrows represent the input and output files to the three “f90” programs. “gaubeam.f90” is the main program of 3D-DGBA.

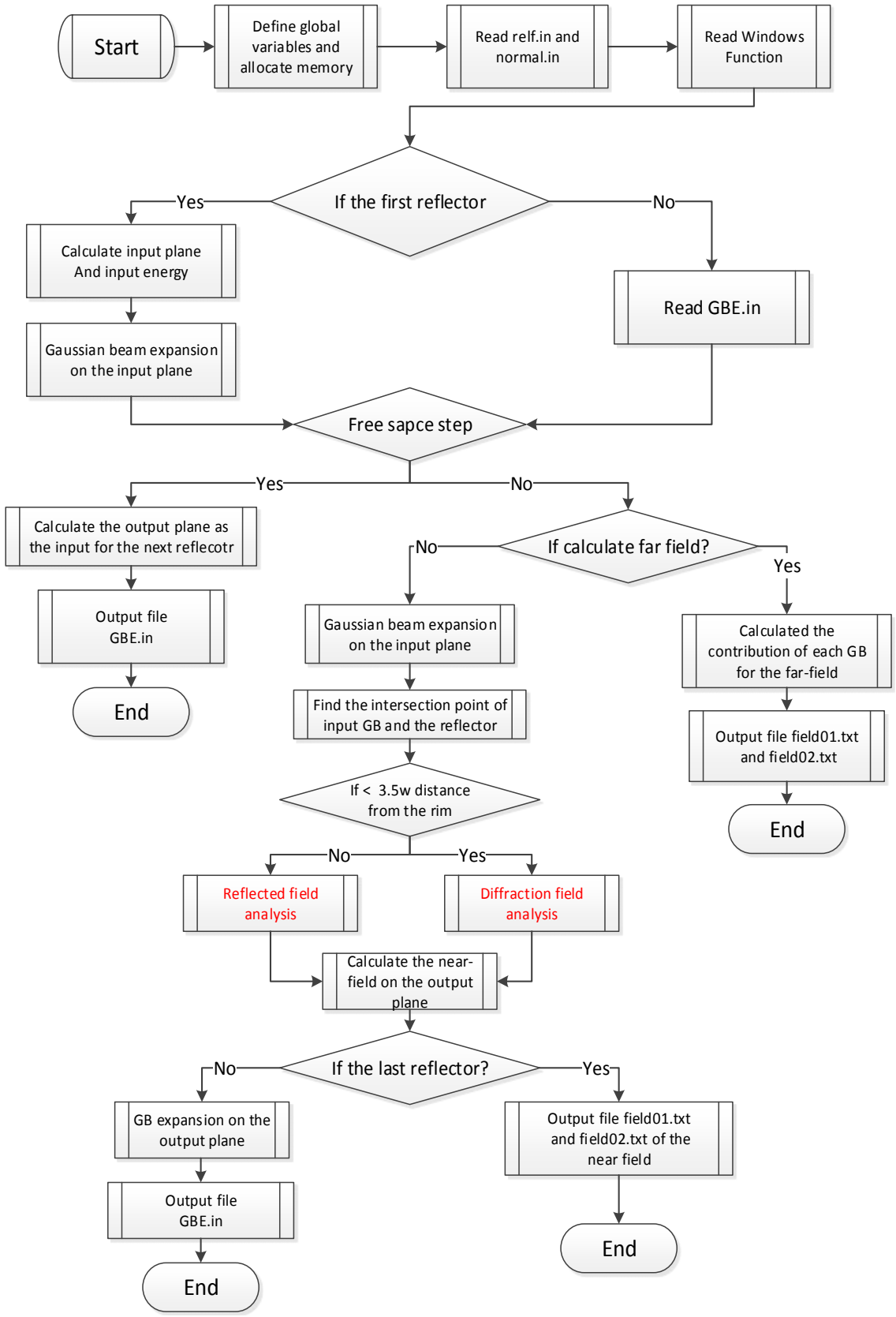

Figure 6.18 Flow chart of 3D-DGBA. Reflected beam analysis and diffracted beam analysis are two of the most important nodes.

The flow chart of gaubeam.f90 FORTRAN functions in 3D-DGBA is shown in Figure 6.18. Computational processes and parameter selection decisions are illustrated in the flow chart. Reflected and diffraction field analysis are the two key actions.

6.7 Summary

A three dimensional Gaussian Beam diffraction analysis called 3D-DGBA was developed. It is based on the original 2D-DGBA. Extended Phase Matching reflection analysis and optimized 3D GBS diffraction analysis are incorporated to replace the original GO reflection analysis and Kirchhoff half-screen boundary diffraction wave (BDW) theory. Modelling and key parameters selection issues are discussed with regard to reduce operational complexity. Specifically, three methods for accelerating computation are applied to significantly increase computing efficiency. It is again emphasised that 3D-DGBA is inherently a flexible analysis by virtue of its modularity.

References

[1] I. Daubechies, “The wavelet transform, time-frequency localisation and signal analysis”, IEEE Trans. Information Theory, vol. 36, no. 5, Sept. 1990, pp. 961-1005.

[2] P.D. Einziger, S. Raz, and M. Shapira, “Gabor representation and aperture theory”, IEEE J. Opt. Soc. Am., vol. 3, no. 4, April 1986, pp. 508-521.

[3] D. Lugara and C. Letrou, “Alternative to Gabor’s representation of plane aperture
radiation”, IEE Electron. Lett., vol. 34, no. 24, Nov. 1998, pp. 2286-2287.

[4] C. Rieckmann, M. R. Rayner, C. G. Parini, D. H.Martin and R.S.Donnan, “Novel modular approach based on Gaussian beam diffraction for analyzing quasi-optical multi-reflector antennas”, IEE Proc.-Microw. Antennas Propag., 149, No. 3, June 2002.

[5] Katsav M, Heyman E. “Gaussian beams summation representation of half plane diffraction: A full 3-D formulation [J].” Antennas and Propagation, IEEE Transactions on, 2009, 57(4): 1081-1094.

[6] Liang Xu, Xiaodong Chen, Xiaoming Liu, and Zejian Lu, " A Comparison of the Results of Two Types of Gaussian Beam Half-screen Diffraction Theories", 7th Europe/UK-China Workshop on Millimeter Waves 2nd-4th September 2014 Chengdu China.

Chapter 7 Experimental Verification of 3D-DGBA Analysis

7.1 Overview

In this chapter, a specific design procedure of a dual-path QoN is presented. Two different kinds of systems were developed at Queen Mary University of London, and Beijing University of Posts and Telecommunications (BUPT) [1-3]. 3D-DGBA is utilised to analyse one of these QoNs and is compared to GRASP and 2D-DGBA analyses. The measured results verify the accuracy of 3D-DGBA.

7.2 System requirement and QoN configuration

Figure 7.1 shows a schematic configuration of the two-path QoN. The photograph in Figure 7.2 shows the corresponding physical QoN, contained in an area of 364 x 417 mm^2. The QoN was designed to feed an offset reflector system that required an input beam width of 20˚ at −8.68 dB. The two paths are the atmospheric sounding frequencies at 54 GHz (oxygen lines) and 89 GHz (atmospheric windows). M1-54, M1-89 and M2 are three ellipsoidal reflectors used to condition the Gaussian beams from the feed horns. H-54 and H-89 are two corrugated horns at 54 GHz and 89 GHz respectively, which are used as sources to generate output beams. Each horn includes a transition from rectangular to circular waveguide. Component D is the low-pass dichroic filter. The transmission (blue lines) and reflection (red lines) paths of the QO beams are shown in Figure 7.2 below.

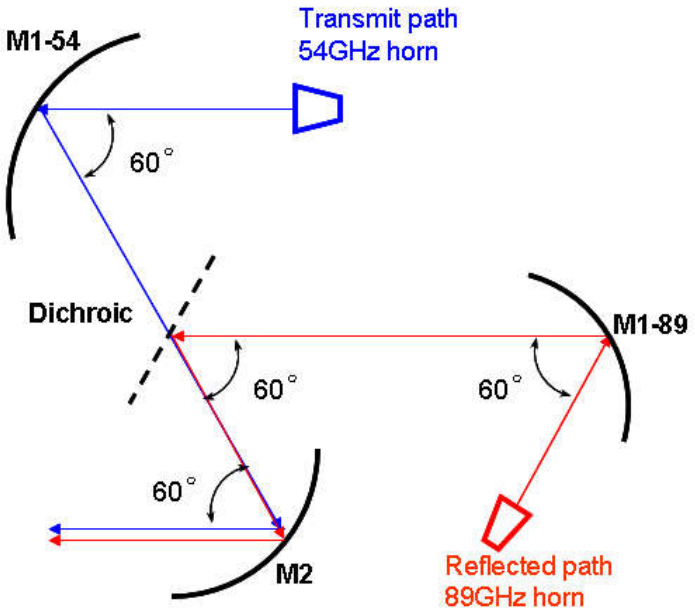

Figure 7.1 Layout of the dual-path Quasi-Optical Network. The 54 GHz (blue lines) is the transmission path; the 89 GHz (red lines) is the reflection path. H-54 and H-89 are the corrugated horns for 54 GHz path and 89 GHz path respectively; M1-54 and M1-89 are the first ellipsoidal mirrors for 54 GHz path 89 GHz path respectively; M2 is the second ellipsoidal mirror for both paths; D stands for the dichroic.

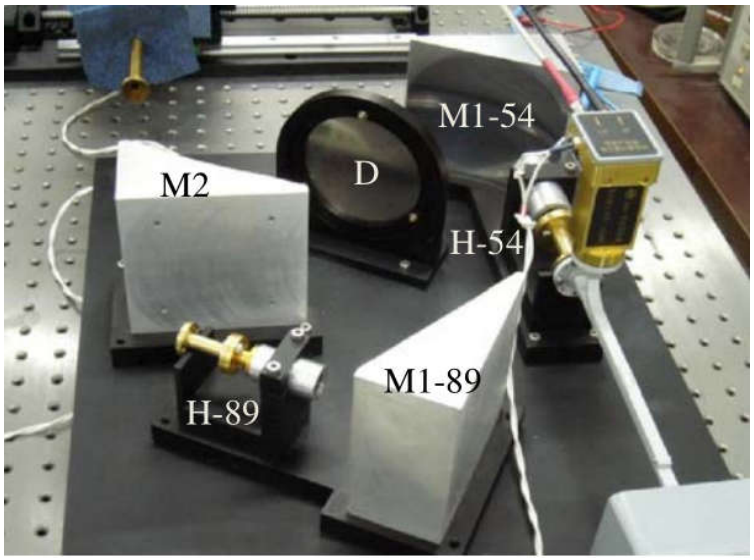

Figure 7.2 Fabricated Quasi-Optical Network according to the schematic of Figure 7.1. Annotation is as for Fig. 7.1.

7.3 Ellipsoidal reflectors design

Goldsmith gives a design procedure of a Quasi-optical network, as illustrated in Figure 7.3 [4]. It is seen as a general guideline for QoN design.

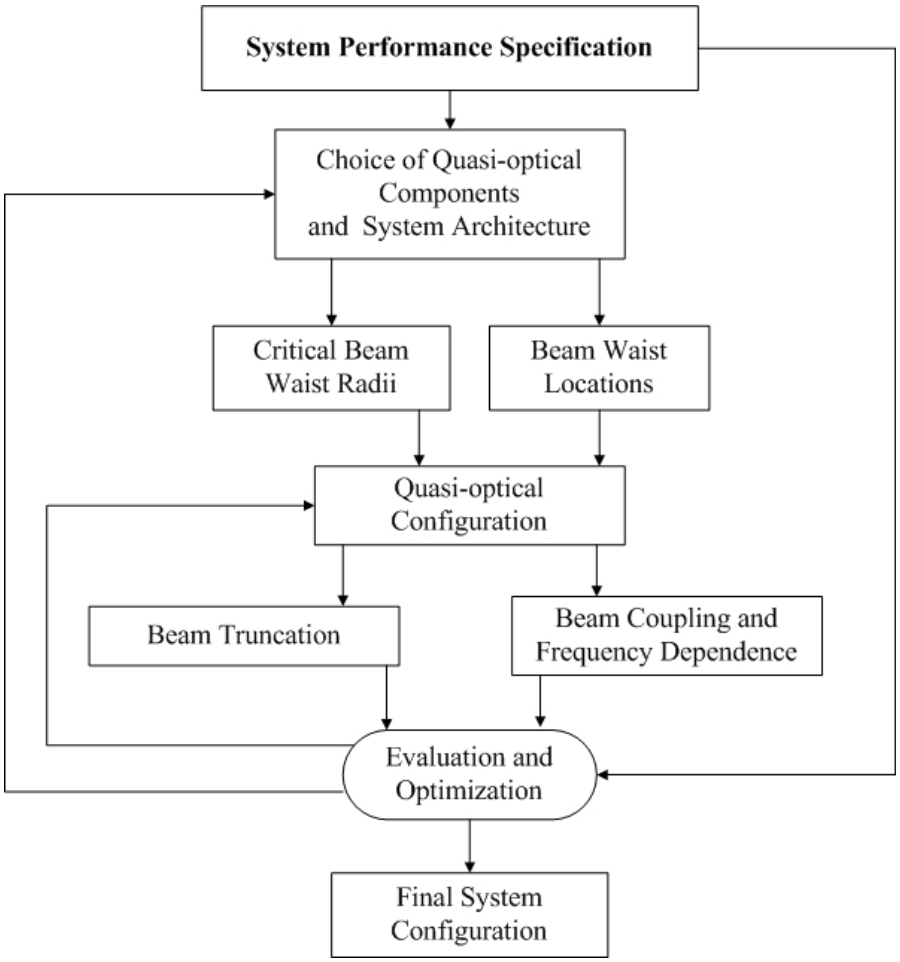

Figure 7.3 Quasi-optical network design procedure, reprint from [4]

A more specific design procedure for multi-reflector QoNs will be shown. It has three parts: i) design of ellipsoidal reflectors; ii) single-path design and, iii) dual-path system design: each will be introduced in subsequent sections.

As discussed in Chapter 2, Gaussian beam width diffractively spreads as the beam propagates and hence requires refocusing or re-collimating. The procedure of re-collimation/refocusing a Gaussian beam to another beam waist is called Gaussian beam transformation; the operation to perform this is given by the $ABCD$ law of GO.

In the geometry of paraxial theory, the $ABCD$ law is:

$$R_e = \frac{AR_i + B}{CR_i + D}. \tag{7.1}$$

R_i and R_e are respectively the radius of curvature of the incident and emergent beams; A, B, C, D are the geometrical optical system elements. The extension of this ray transformation leads to the four elements A, B, C, D operating on the complex radius of curvature similar to (7.1), giving:

$$q_{out} = \frac{Aq_{in} + B}{Cq_{in} + D}. \tag{7.2}$$

An ellipsoidal reflector operating in the paraxial limit is approximated fairly close to the action of an ideal lens in that it essentially gives a quadratic phase-increment to a signal. The $ABCD$ matrix for an ellipsoidal mirror as given by [4]:

$$M_{ellipsoid} = \begin{bmatrix} 1 & 0 \\ -\left(\frac{1}{R_1} + \frac{1}{R_2}\right) & 1 \end{bmatrix}. \tag{7.3}$$

The equivalent focal length for the ellipsoidal mirror is:

$$f_{ellipsoid} = \frac{R_1 + R_2}{R_1 R_2}. \tag{7.4}$$

R_1 and R_2 are the distances from the centre of a section from the boundary of an ellipsoid to the foci of the ellipsoid, as illustrated in Figure 7.4. It should be noticed that, for an ellipsoid, a very useful condition occurs when $R_i = R_1$ and $R_e = R_2$.

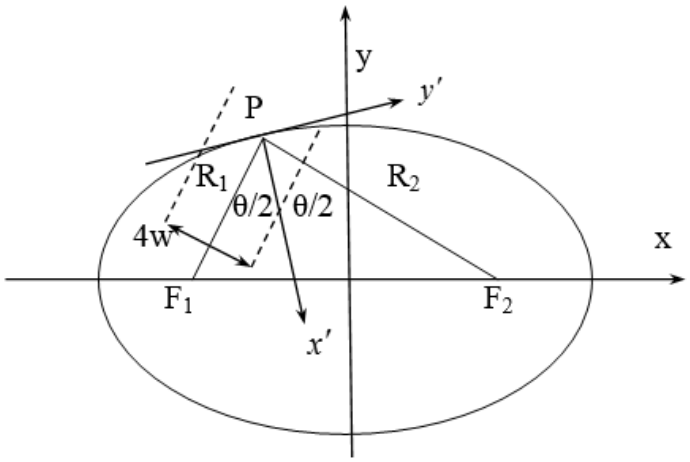

Figure 7.4 Geometry of single reflector taken as the portion of the surface from an ellipsoid centred at point P having distance R1 and R2 to the foci of the ellipse at F1 and F2respectively. The angle between incident and emergent beam is θ. w is the beam width of the incident Gaussian beam and 4w will be the diameter of the cylinder used to cut the surface.

The transformation procedure is illustrated in Figure 7.5, so the $ABCD$ matrix is:

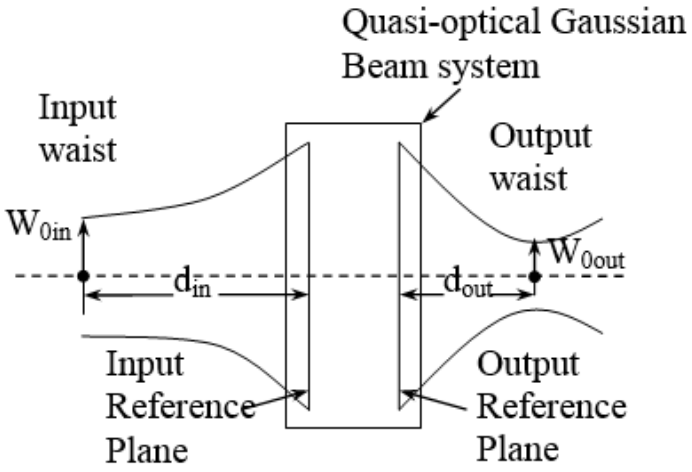

Figure 7.5 Gaussian beam transformation by a quasi-optical system. The input Gaussian beam waist is w_{0in} at a distance d_{in} from the input reference plane and the output waist is w_{0out} at a distance d_{out} from the output reference plane. [4]

$$M = \begin{bmatrix} 1 & d_{out} \\ 0 & 1 \end{bmatrix} \cdot \begin{bmatrix} 1 & 0 \\ -\frac{1}{f} & 1 \end{bmatrix} \cdot \begin{bmatrix} 1 & d_{in} \\ 0 & 1 \end{bmatrix}$$
$$= \begin{bmatrix} 1-\frac{d_{out}}{f} & d_{in} + d_{out}\left(1-\frac{d_{in}}{f}\right) \\ -\frac{1}{f} & 1-\frac{d_{in}}{f} \end{bmatrix} . \quad (7.5)$$

Taking (7.2) and (7.5) together, one has

$$R_1 = R_{in} = d_{in} + \frac{z_c^2}{d_{in}} , \quad (7.6)$$

$$R_2 = \frac{f \cdot R_1}{R_1 - f} , \quad (7.7)$$

$$d_{out} = f + f \cdot \frac{d_{in}/f - 1}{(d_{in}/f - 1)^2 + z_c^2/f^2} \text{ and} \quad (7.8)$$

$$w_{0out} = \frac{w_{0in}}{\left[(d_{in}/f - 1)^2 + z_c^2/f^2\right]^{0.5}} . \quad (7.9)$$

with confocal distance $z_c = \frac{\pi w_{0in}^2}{\lambda}$.

The system magnification is defined to be:

$$M = \frac{w_{0out}}{w_{0in}} = \frac{1}{\left[(d_{in}/f - 1)^2 + z_c^2/f^2\right]^{0.5}} . \quad (7.10)$$

Rearranging Equation (7.10), the focal length *f* can be written in terms of M.

For $M = 1$:

$$f = z_c \frac{1 + (d_{in}/z_c)^2}{2 d_{in}/z_c} . \quad (7.11)$$

For $M \neq 1$:

$$f = z_c\left(\frac{d_{in}}{Nz_c}\right)\left[1\pm\left(1-N\left[1+\left(\frac{d_{in}}{z_c}\right)^{-2}\right]\right)^{0.5}\right]. \tag{7.12}$$

where $N = 1 - M^{-2}$.

The equation of the ellipsoid in Cartesian coordinates is:

$$\frac{x^2+y^2}{b^2}+\frac{z^2}{a^2}=1. \tag{7.13}$$

$a = \frac{R_1+R_2}{2}$; eccentricity $e = \frac{(R_1^2+R_2^2-2R_1R_2\cos\theta)^{0.5}}{R_1+R_2}$; $c = e\cdot a$ and $b^2 = a^2 - c^2$. θ is the angle subtended by the incident and reflected rays and is equal to twice the incident angle, θ_i. Usually, it is a known parameter or one selected by the designer. Taking the former equations together, an ellipsoid can be created.

It is found that although w_{0in} and w_{0out} may be known a priori, the input distance d_{in} should still be carefully chosen. For $M \le 1$, there is no limitation for d_{in}/z_c. However, for $M > 1$, there is a minimum value for d_{in}/z_c, as shown in Figure 7.6 For a particular frequency and an input beam waist, z_c is a constant, which means d_{in} should be chosen large enough for the magnification [4].

After the ellipsoid is determined, the next step is to abstract the desired mirror-section from it. It becomes a trade-off between minimal-size and power-handling capability. The energy spilling over from the reflector is defined by the related radius r_e,

$$T_e(r_e) = \exp\left[\frac{-2r_e^{\,2}}{w^2}\right], \tag{7.14}$$

where $w = w_0\left[1+(\frac{\lambda z}{\pi w_0^2})^2\right]^{0.5}$.

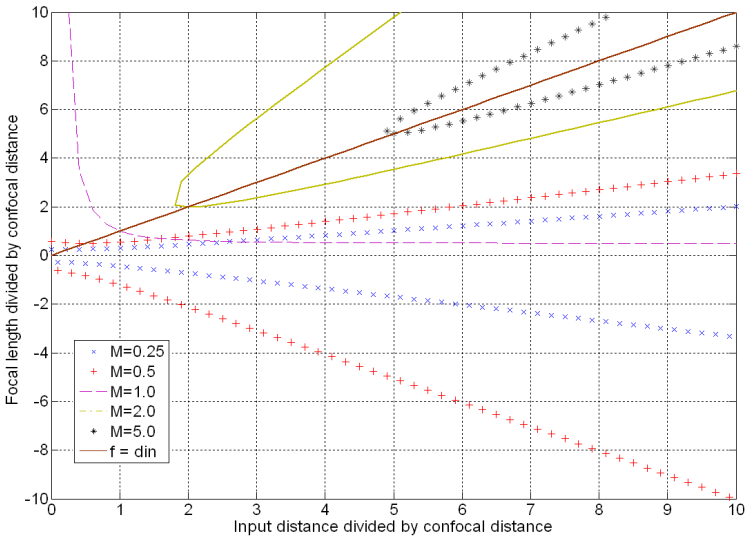

Figure 7.6 Focal length required for modal matching in terms of confocal distance. With a specific value of system magnification M=0.25, 0.5, 1.0, 2.0 and 5.0, the relationship between the input distance d_{in} and the focal length f is shown. For $M>1$, there is a minimum value for d_{in}/z_c, which means the input distance has to be chosen large enough for a specific system magnification $M>1$, [4].

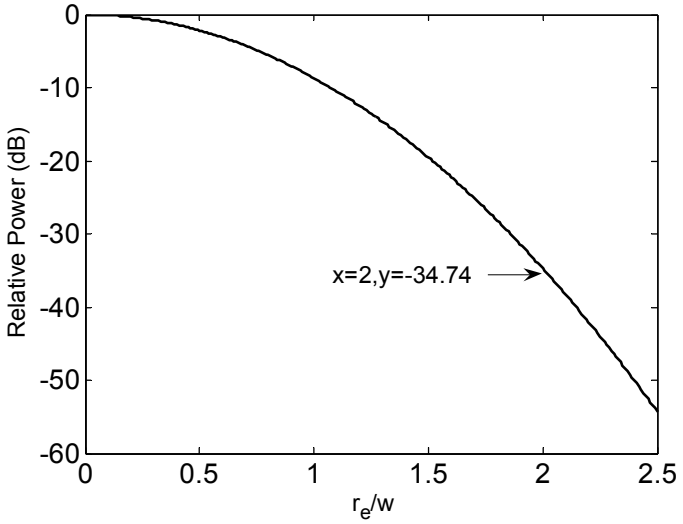

Figure 7.7 Fundamental Mode Gaussian beam and edge taper. If the reflector radius $r_e=2w$, the corresponding $T_e=-34.74dB$ and about 99.97% of the input power is intercepted.

For instance, $r_e=2w$, or a reflector aperture diameter $D_{aper}=4w$ means that 99.97% ($T_e=-34.74dB$) of the power is intercepted, as depicted in Figure 7.7. This would represent a good set of choices in parameter setting.

The last step is to find an appropriate angle θ. Define the fraction of power in the reflected beam in the fundamental Gaussian beam mode as [4]

$$K = 1 - \frac{w_p^2 \tan\theta_i}{8f^2} \tag{7.15}$$

where w_p is the beam width at the point of intersection P in Figure 7.2. A helpful conclusion is that when $D_{aper} = 4w$, to make $K \geq 99\%$, the incident angle θ_i needs to satisfy the following condition

for $f / D_{aper} \geq 1.0$

$$\theta_i \leq 45^\circ \tag{7.16}$$

and for $1.0 \geq f / D_{aper} \geq 0.5$

$$\theta_i \leq 30^\circ . \tag{7.17}$$

It is easy to show that it gives another restrictive condition on the input distance d_{in}. For a given θ_i, to make $K \geq 99\%$,

$$d_{in} \leq \frac{\pi w_0^2}{\lambda} \sqrt{\frac{0.08}{\tan\theta_i w_0^2} - 1} \ . \tag{7.18}$$

Other kinds of mirror, such as a hyperboloid or spherical mirror, can also be derived by following the same procedure. Taking one reflector design as a model, it becomes very easy to design a multi-reflector network.

7.4 Single path design

Generally speaking, there exist several reflectors in a single beam path. Following is the procedure for single reflector design:

1) calculate the output beam waist w_{0out} according to the system requirements;

2) find the input beam waist w_{0in} which is always determined by the matching feed

source;

3) using w_{0in} and w_{0out} to find the system magnification M and a proper input distance d_{in}; d_{in} is the first free parameter chosen by the designer to meet the space requirements of the whole system, but it should be under the condition as illustrated in Figure 7.3 and should also follow the constraint of equation (7.18).

4) calculate the focal distance using (7.11) or (7.12);

5) define the ellipsoid by using (7.6), (7.7) and (7.13);

6) calculate the size of the section D_{aper}.

7) finally, the second free parameter, the incident angle θ_i, is chosen in the domain given by (7.16) or (7.17).

Usually the main (or the last) reflector is defined first to meet system specifications, and then sub-reflectors can be designed by following the same procedures. It should be noted that the input beam waist of the main reflector is the output beam waist of the sub-reflector. It can be referred to as the intermediate beam waist $w_{0\mathrm{int}er}$. $w_{0\mathrm{int}er}$ is another free parameter, like θ_i and d_{in}. Therefore, the designer should choose a proper input beam waist first for the main reflector.

In order to deal with two reflectors in one optical path as depicted in Figure 7.8, assuming M1 to be the first reflector and M2 the second, to achieve the best matching condition, the output beam waist of M1 should be at the same position and of the same size as the input beam waist of M2, denoted here as the intermediate beam waist $w_{0\mathrm{int}er}$, which is another free parameter.

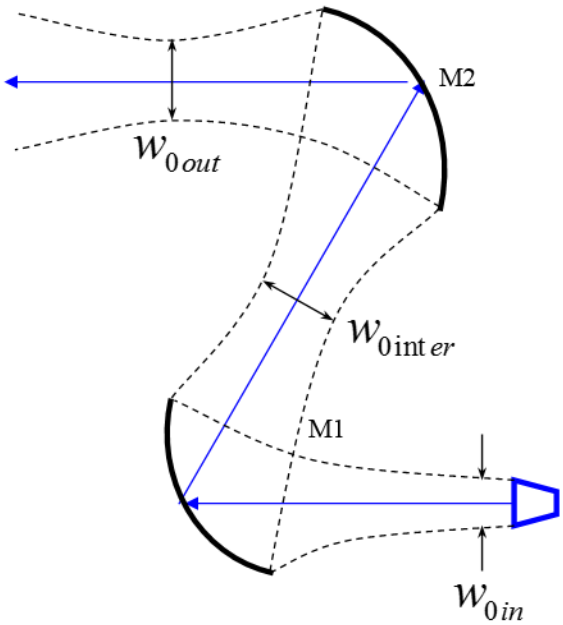

Figure 7.8 Illustration of transmission path: an afocal phase-error cancellation mirror train separated by the sum of mirror focal distances. M1 and M2 are reflector mirrors in sequence. w_{0in} is the beam waist of incident Gaussian beam produced by a horn. w_{0inter} is the beam waist between the two reflectors and w_{0out} is the beam output beam waist of M2.

7.5 Dual path QoN design

A dual-path system consists of a transmission and reflection path. In this situation, one of the two can be chosen and designed. However, the first will strongly affect the second. The size and location of the intermediate beam waist w_{0inter} and the location of the dichroic should be considered in the design of the second path. In order to reduce the size of the QON, neither intermediate beam waists of the two optical paths should coincide with the dichroic. However, to make spill over negligible, the radius of the dichroic is larger than the beam radius at the dichroic by a factor of two. A similar conclusion can be found in Foster *et al* [5], who undertook an experimental investigation into the effects of the position of the dichroic. The feeds used in our project are corrugated horns. Since the beam waist w_{0in} has been determined, the feed can be readily designed by following some routines given by Goldsmith [4]. A dichroic plate plays an important role in QONs, functioning to separate the incoming signal into different channels, or combining signals from several channels into co-propagating, coaxial beams [4]. In such a QON, the dichroic plate was designed as a low-pass filter.

It bears noting that, in the literature, by low and high pass, means passing, respectively, the low and high frequency content of a signal spectrum. Working as a frequency filter, the performance of the dichroic is critical. Losses in the dichroic for the transmitted and reflected bands must be minimised. An acceptable insertion loss is to be no more than 0.5 dB. Bandwidth is another particularly critical feature for transmission. A multi-layer dichroic offers an increased bandwidth, but the manufacturing cost will be increased too. Therefore, a trade-off between bandwidth and manufacturing cost holds.

The dichroic plate in the QoN was fabricated by etching [2]. Figure 7.9 shows a photo of the manufactured dichroic. It has a diameter of 100 mm and is embedded into a circular metal frame. Plastic rings are used to separate the two FSS layers. The two layers were separated by six plastic rings, and the thickness of each plate ring is 0.2 mm. The separation of the two layers is1.2 mm.

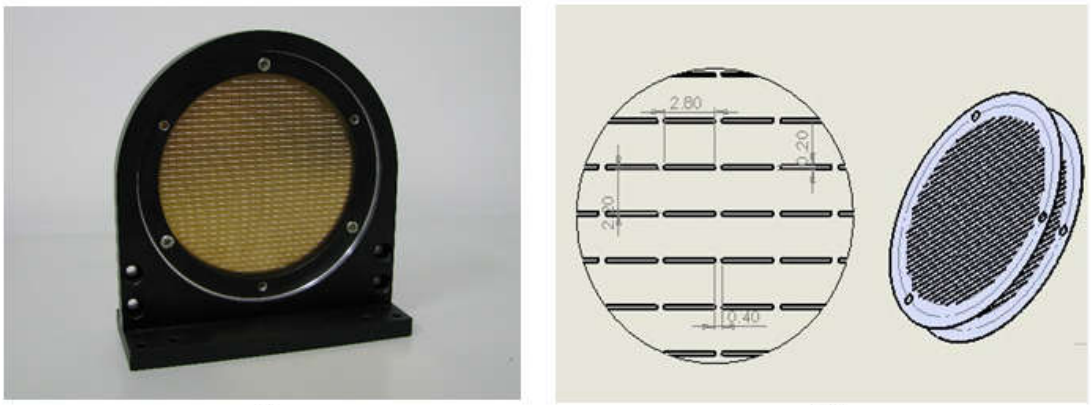

(a) (b)

Figure 7.9 The dichroic with rectangular slots and square lattice, (a) Photograph and (b) diagram. The dichroic is a round metal plate (100 mm in diameter) perforated with rectangular shaped holes: being 2.8 mm × 0.2 mm, and the separations between holes being 0.4 mm in horizontal and 2.2 mm in vertical. The thickness of the each plate is 0.2 mm. The separation of the two layers is 1.2 mm.

Figure 7.10 shows a comparison between measured (dotted curves) and simulated (solid curves) transmission and reflection coefficients of the dichroic over a span of frequencies. The measured and simulated results agree throughout the entire frequency domain. At 54 GHz, the simulated insertion loss is only -0.1 dB, compared to -1.0 dB by measurement. At 89 GHz, the simulated transmission is very low, down to -36 dB, in contrast with -30 dB from measurement.

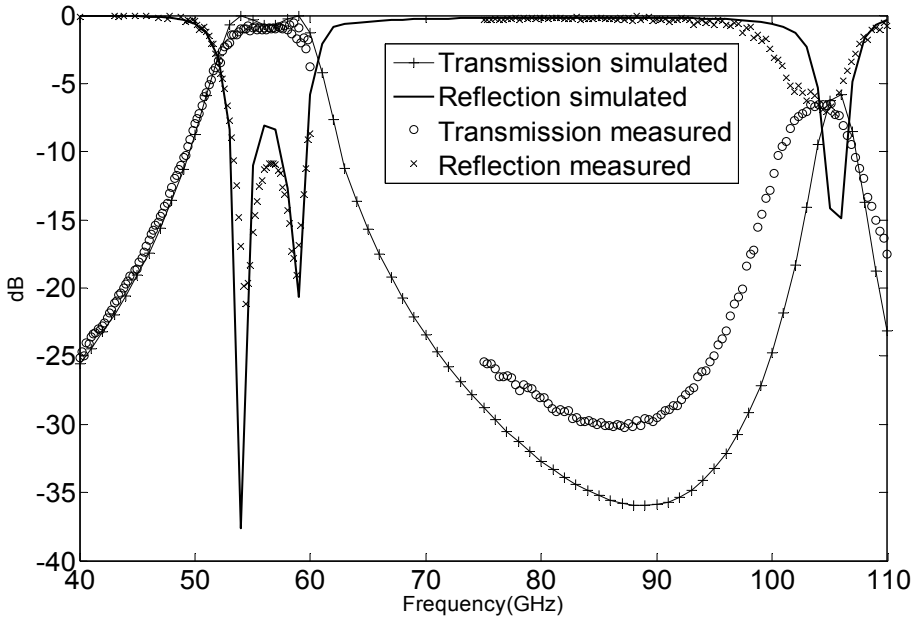

Figure 7.10 A comparison between measured (dotted curves) and simulated (solid curves) transmission and reflection coefficients of the dichroic over a range of frequencies.

7.6 Another dual path QoN

With the same reflectors as illustrated above, another dual path system was constructed. In this system, the transmitted and reflected paths are interchanged, as illustrated in Figure 7.11 [3]. This QO system is a prototype of an airborne remote sensing system, consisting of 54 and 89 GHz channels. The desired bandwidth is 2 GHz for both.

To accomplish this objective, another kind of dichroic i.e. a perforated FSS is studied and fabricated to function as a high-pass filter. It has a circular unit cell repeated on an equilateral triangular lattice. This makes it quite different to former resonate slot-array that reflected 54 GHz and transmitted 89 GHz waves. In this design, the diameter of the circular unit hole is 2.16 mm, the distance between the centres of two neighbouring unit circular holes is 2.46 mm. The depth of the hole is 2.25 mm. A photograph of the fabricated FSS is shown in Figure 7.12. The measurement was carried out by comparing the transmitted power, picked up by a raster scanning probe with and without the dichroic plate in place. The measured results are shown in Figure 7.13, in contrast with the simulation results.

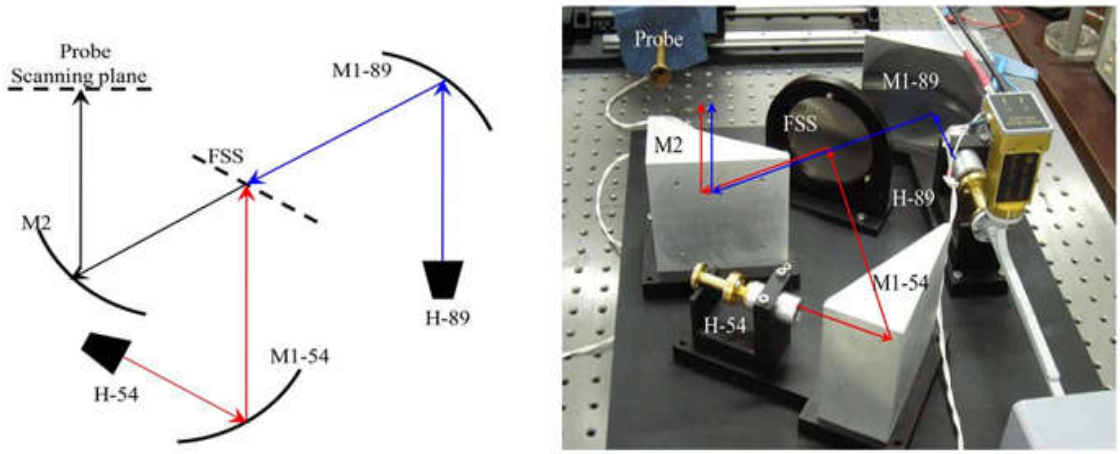

(a) **(b)**

Figure 7.11 Dual channel QO system: (a) Diagram and (b) photograph.M1–54 stands for the first mirror of 54 GHz channel; M1–89 stands for the first mirror of 89 GHz channel; M2 stands for the second mirror; H-54 stands for the horn of 54 GHz channel; H-89 stands for the horn of 89 GHz channel. The diagram is not to the scale.

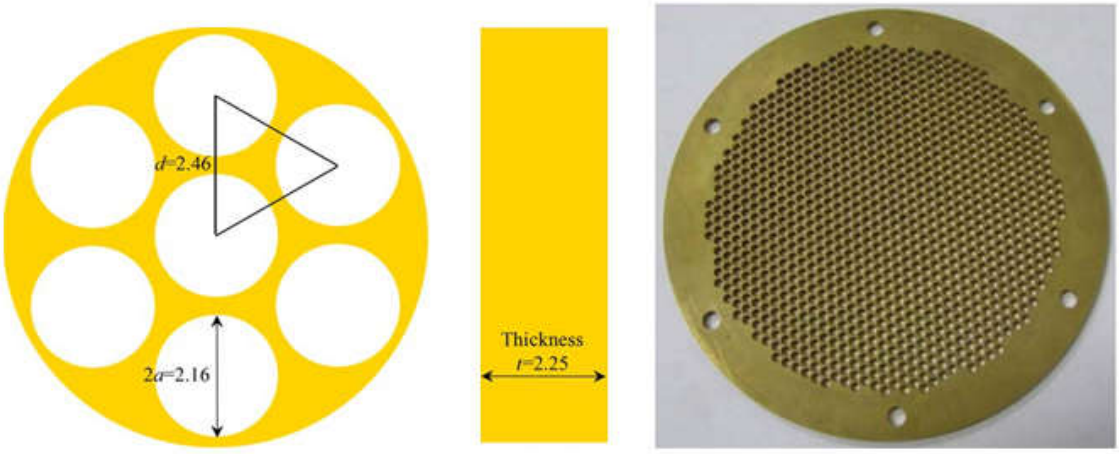

(a) (b)

Figure 7.12 Dual Perforated plate of circular unit cell and equal lateral lattice: (a) Diagram and (b) photograph. The diameter of the unit circular hole is 2.16 mm, the distance between the centres of two neighbouring unit circular hole is 2.46 mm. The thickness is 2.25 mm.

It is shown that the reflection coefficients in the stop band (53–55 GHz) are better than -0.15 dB, while the transmission in this frequency range is below -25 dB, indicating good reflection performance. In the pass band (88–89 GHz), the transmission coefficients are better than -0.25 dB, and the reflection is below -13 dB, showing that the insertion loss in the pass band meets the requirements.

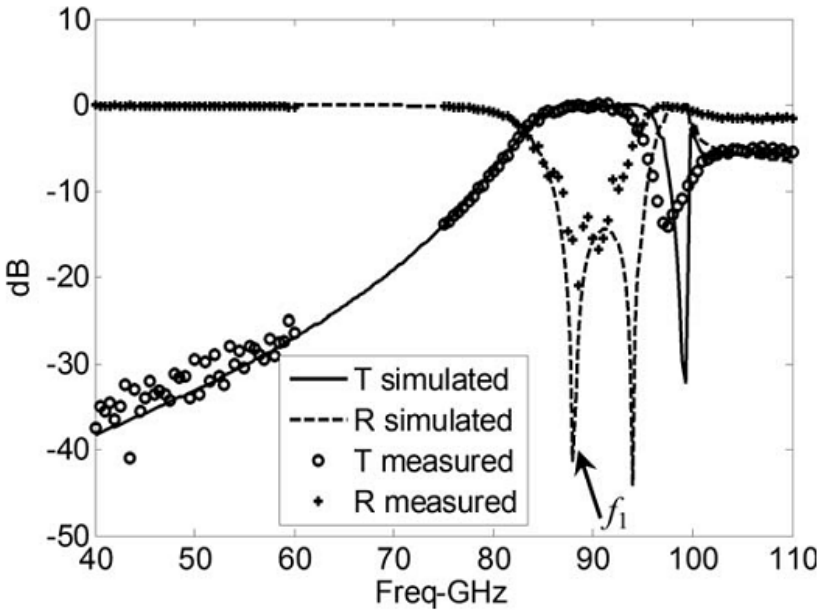

Figure 7.13 Comparison of the measured and simulated results of the perforated plate. T denotes the transmission coefficient; R, the reflection coefficient; f1 is the first resonant frequency point. Simulation results are produced by the periodic method of moments.

7.7 Simulation and experimental verification

To verify 3D-DGBA, measurement of the previously mentioned dual path QoN with low-pass dichroic has been conducted. The parameters of the three ellipsoidal reflectors are given in Table 7.1.

Table 7.1 Parameters of the ellipsoidal reflectors (mm)

	d_{in}	w_{in}	f	R_1	R_2	d_{out}	w_{out}
M1-54	70	5.148	70	73.21	1597.2	70	24.05
M1-89	65	3.17	65	66.39	3105.06	65	21.84
M2-54	136.37	24.05	136.37	920.3	160.09	136.37	10.029
M2-89	368.99	21.10	136.37	920.3	160.09	152.27	6.085

Both the 54 GHz and 89 GHz paths are measured at their centre frequencies. Two corrugated horns at 54 GHz and 89 GHz are fabricated to generate output beams. Key parameters of the two horns are given in Table 7.2.

Table 7.2 Parameters of the horns

Parameters	54GHz horn	89GHz horn
Bandwidth (GHz)	51~57	85~93
Beam Waist (mm)	5.00	3.10
Horn Aperture Radius (mm)	8.0	5.0
Horn Slant Length（mm）	61.1	34.7
Return Loss（dB）	<-27	<-27
Side Lobe（dB）	<-25	<-25
Cross Polarization（dB）	<-25	<-25

Measurements were carried out as follows: for the 54 GHz path, the dichroic was first removed in order to get a reference; while for the 89 GHz path, the dichroic was replaced by a metallic plate to produce total reflection. Measurements were then carried out with the dichroic in place. A step-positioner was employed to control the probe antenna to pick up the signals over a scanning plane. The far-fields are then computed from the measured near fields.

Figure 7.14 and Figure 7.15 present the near field of M1-54, the first reflector in 54GHz path. The scanned and simulated plane is 199.8 mm from the optical centre of M1-54. Only co-polar field experimental measurements are made. However, both co-polar and cross-polar simulated results are given.

It can be seen that in the centre of both offset and symmetric fields, all PO, 2D-DGBA and 3D-DGBA analyses present near identical assessment and agree well with the experimental result. Against these, GRASP analysis is set as the reference. In both cuts, only a ±1.25 dB field deviation can be observed within a ±0.03 m range. However, 3D-DGBA demonstrated its advantage when analysing off from the centre. It presents a similar trend to PO. Field deviation holds at ±20 dB within a ±0.2 m range in comparison with ±40 dB for 2D-DGBA. 3D-DGBA has an excellent symmetric distribution when simulating the symmetric-plane. Both co- and cross-polar simulated fields are in good agreement with the measured results.

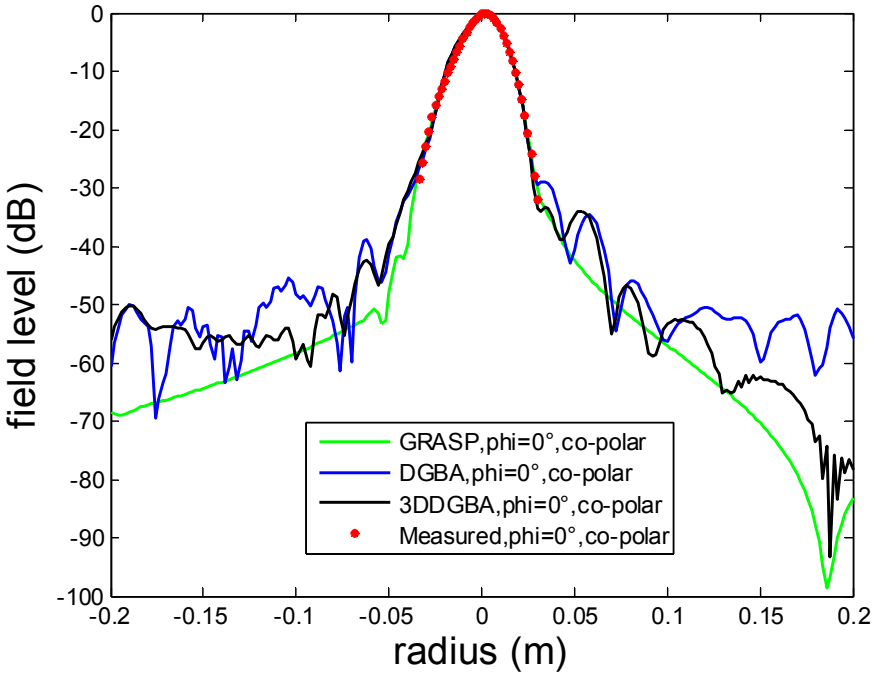

Figure 7.14 The near field distribution of 54GHz M1 in offset plane ($\varphi = 0^\circ$). The scan plane is 199.8 mm (~ 36λ) from the optical centre of reflector M1-54.

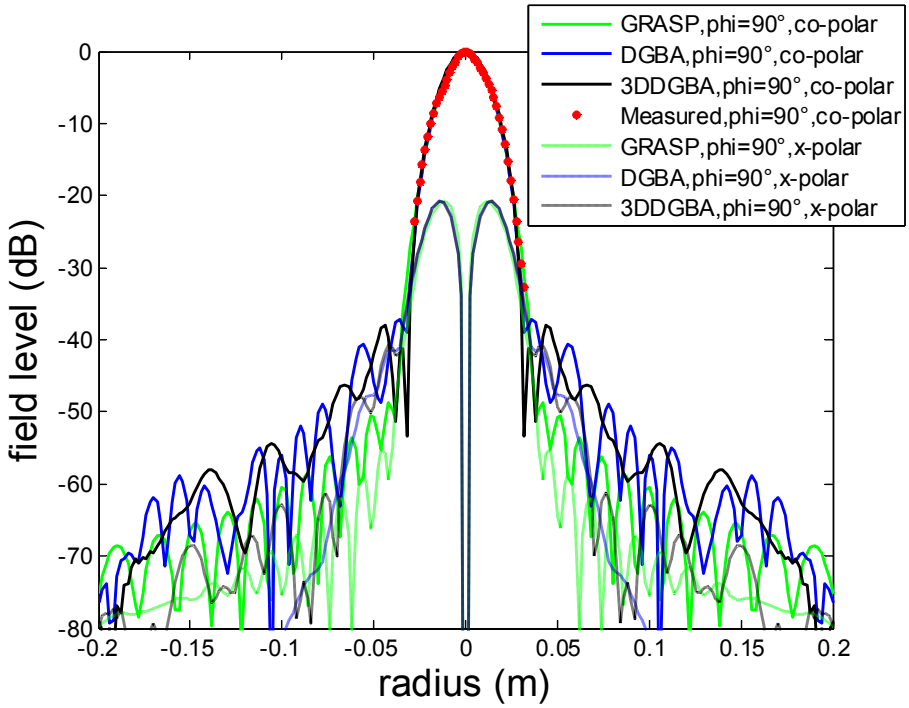

Figure 7.15 The near field distribution of 54GHz M1 in the symmetric plane ($\varphi = 90^\circ$). The scan plane is 199.8 mm (~ 36λ) from the optical centre of reflector M1-54.

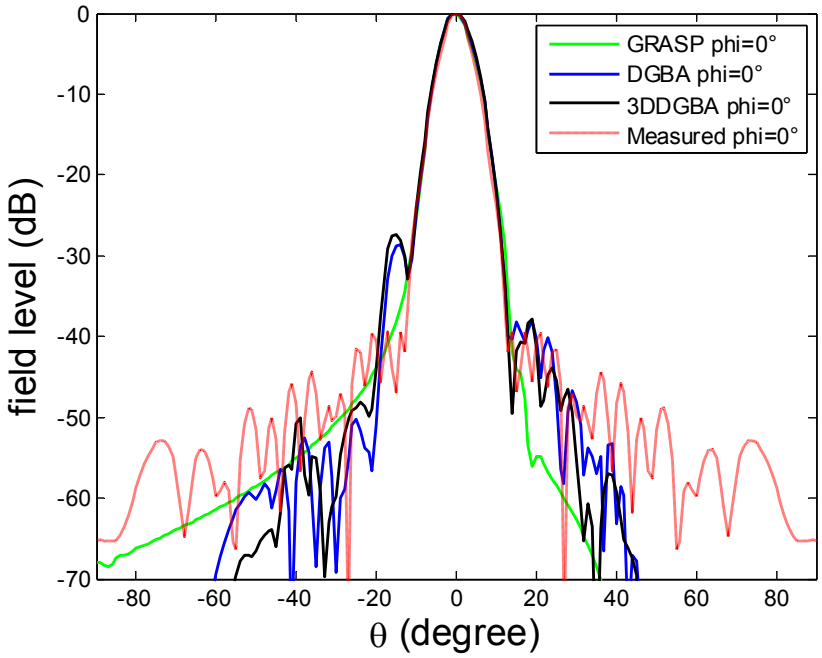

Figure 7.16 The far field distribution of 54 GHz M1 in the offset plane ($\varphi = 0^{\circ}$).

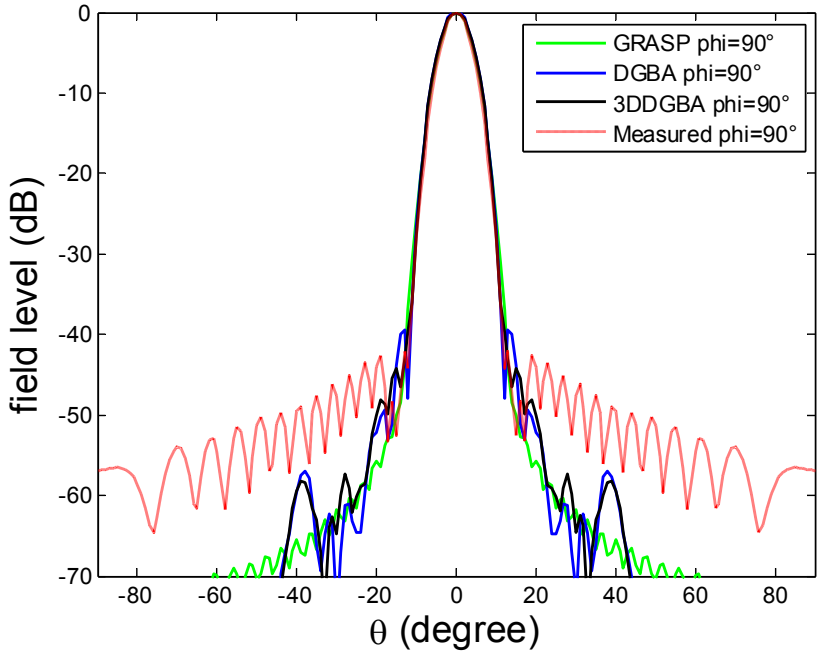

Figure 7.17 The far field distribution of 54GHz M1 in symmetric plane ($\varphi = 90^{\circ}$).

Figure 7.16 and Figure 7.17 show the far field of M1-54. All three simulation-methods are of similar accuracy when analysing the main beam of the far field in both offset and symmetric planes. Only a ±1.5 dB field deviation can be observed within ±10 degree. 3D-DGBA gives an even better pattern for the symmetric plane in that it is closer to PO.

However, in the offset plane (φ=0°), both 2D and 3D DGBA indicate a side lobe at about , which is not seen in GRASP and measured results. Its origin remains unclear. $\theta = -15°$

Figure 7.18 and Figure 7.19 present the offset plane near fields of the mirror M2 for the 54 GHz path with and without the dichroic in place, respectively. Figure 7.20 and Figure 7.21 present the same fields but in symmetric plane. Comparisons of simulated results between GRASP, 2D-DGBA and 3D-DGBA are given in these figures. Since there was no suitable tool for interfacing PMM with GRASP, GRASP is not used for simulation in the case of dichroic set in place.

Where appropriate, however, GRASP analysis is set as the reference. Analysis by both 3D-DGBA and 2D-DGBA deteriorates in the offset plane where a ±3 dB field deviation appeared within a ±0.03 m range. Fortunately, in the symmetric plane, only a ±0.75 dB field deviation occurred in the same range for 3D-DGBA. The deviation of 2D-DGBA is ±2.5 dB.

Also, compared with 2D-DGBA, 3D-DGBA analysis is closer to PO in the offset plane, particularly in the –x direction.

When analysing the system in the presence of the dichroic, both 2D and 3D DGBA show a more symmetric distribution than the measured results. The presence of the dichroic does not change the distribution greatly. This is due to the fact that simulation is based on an ideal model while the fabricated system will suffer from distortion produced by fabrication and positional errors. The near field beam is narrowed and distorted slightly with the presence of the filter. With the filter in place, the beam width at the −8.68 dB level is 7±0.25 mm, approximately 1.4λ less than that without the dichroic (beam width 52 ± 0.25 mm). The distortion introduced by the finite size of the dichroic and its insertion loss. However, the agreement between simulation and measurement for both cases (without and with dichroic), is still at an acceptable level.

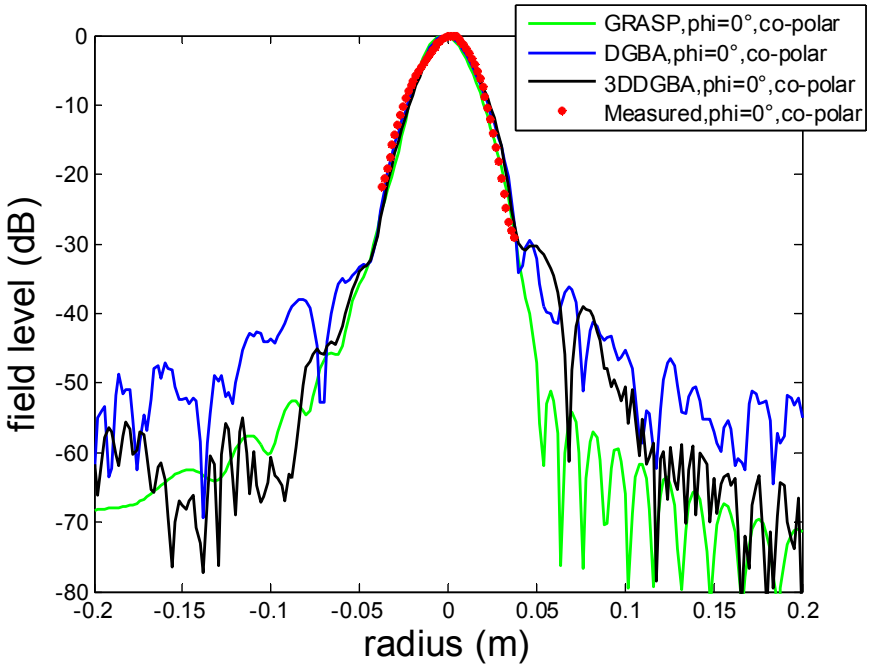

Figure 7.18 The near field distribution of M2 at 54 GHz in offset plane ($\varphi = 0^\circ$) without the dichroic present. The scan plane is 184.8 mm (~ 33λ) from the optical centre of reflector M2.

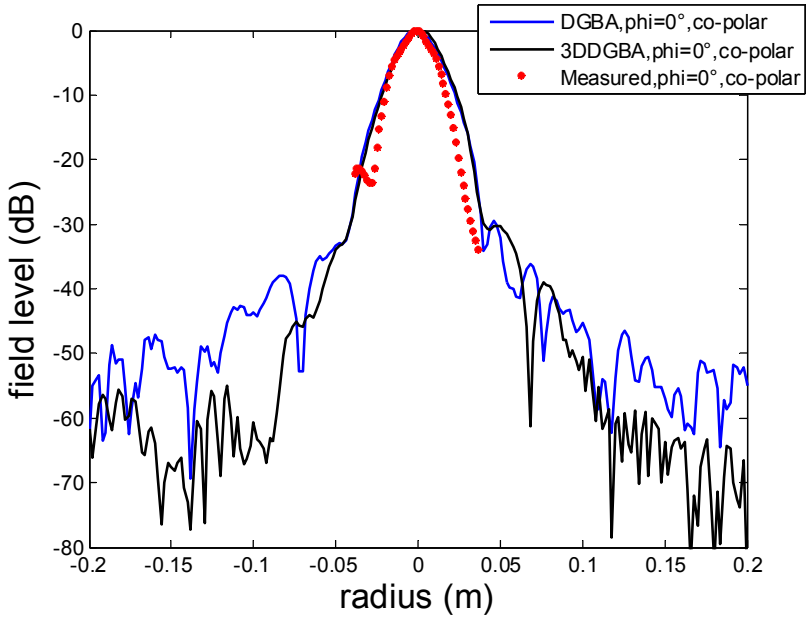

Figure 7.19 The near field distribution of M2 at 54 GHz in symmetric plane ($\varphi = 90^\circ$) with the dichroic in place. The scan plane is 184.8 mm (~ 33λ) from the optical centre of reflector M2.

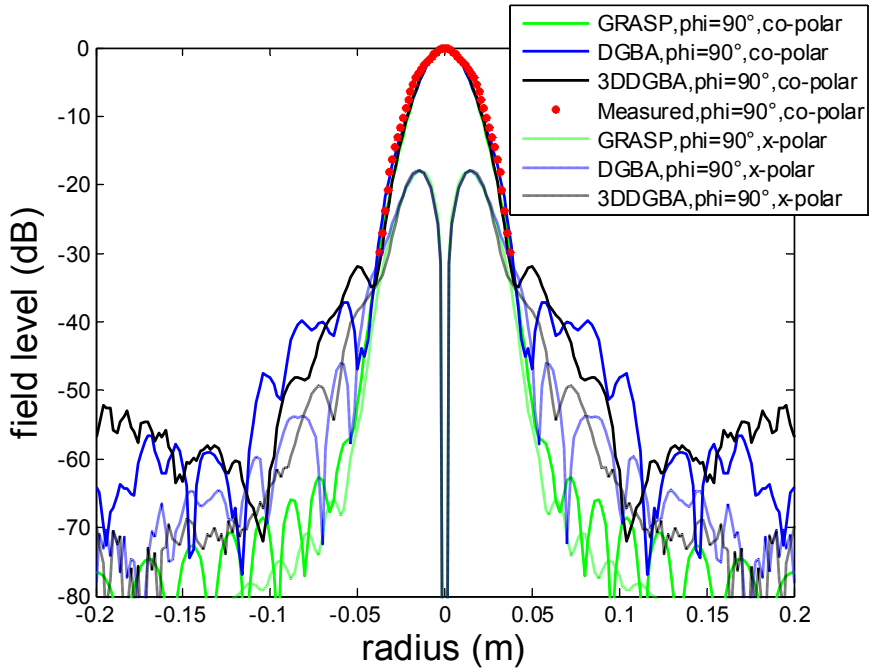

Figure 7.20 The near field distribution of M2 at 54GHz in offset plane ($\varphi = 0^{\circ}$) without the dichroic. The scan plane is 184.8 mm (~ 33λ) from the optical centre of reflector M2.

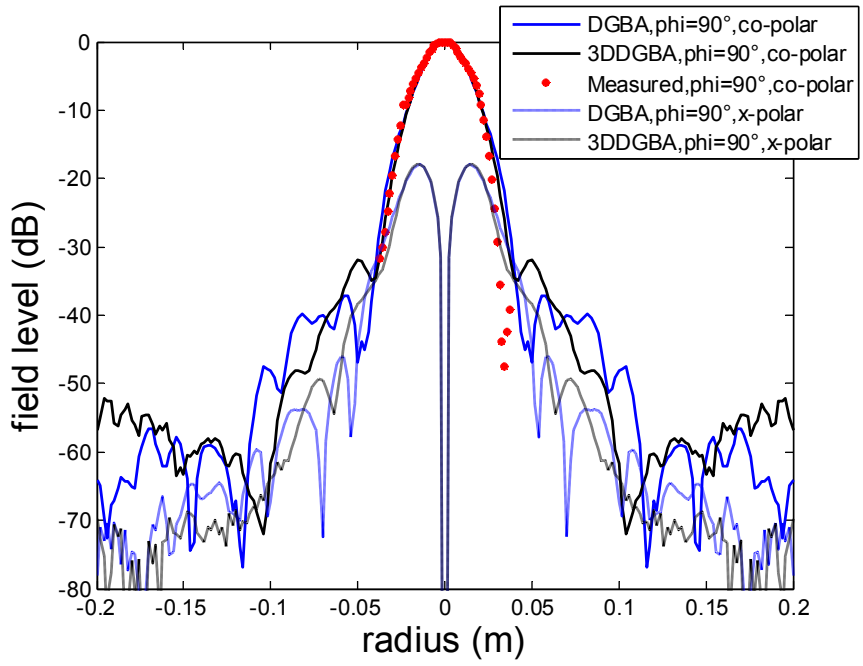

Figure 7.21 The near field distribution of M2 at 54 GHz in symmetric plane ($\varphi = 90^{\circ}$) with the dichroic in place. The scan plane is 184.8 mm (~ 33λ) from the optical centre of reflector M2.

Figure 7.22 to Figure 7.27 are the corresponding computed far fields. It is found that 3D-DGBA is also valid when analysing multi-reflectors in a single–path system. From

the field difference (Figure 7.23), it can be observed that the deviation between GRASP and 3D-DGBA in the offset-plane within 10˚ stays in the range of (-0.2 dB, 1.3 dB), similar to that of 2D-DGBA (-0.1 dB, 1.7 dB). In the symmetric plane, the field difference stays at (-0.4 dB, 0.2 dB) between 3D-DGBA and GRASP. The difference is (0dB, 0.9 dB) between 2D-DGBA and GRASP. The results of 3D-DGBA are closer to that of PO.

Simulation with dichroic present shows almost identical results as for its absence. Measurement shows the presence of the dichroic does not affect the main beams greatly. The main beam show reasonable agreement, while the side lobes have different deviations. However, the signal levels of side lobes without and with the filter present are low, below −40 dB for most cases. The level of the first side lobe seems to increase (<4 dB) when the dichroic is added, but the signal level is below −25 dB, which meets one of our specifications, the other one being a 20° beam width at the −8.68 dB signal level. This observation shows that the distortion by the dichroic is acceptable.

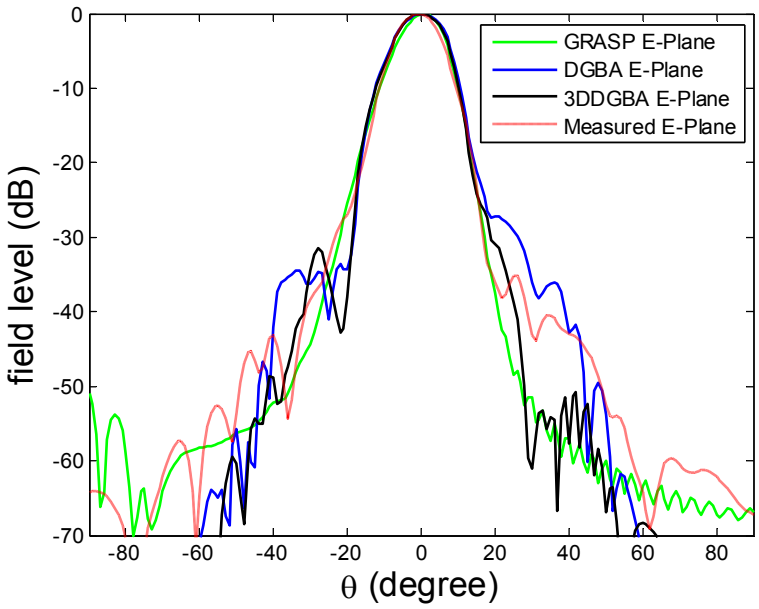

Figure 7.22 The far field distribution of 54 GHz M2 in the offset plane ($\varphi = 0^{\circ}$) without the dichroic.

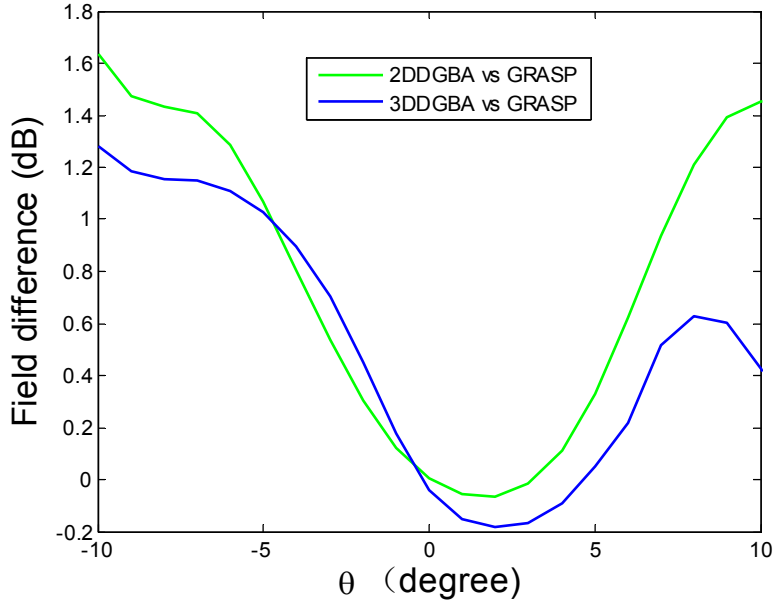

Figure 7.23 Field difference of far field distributions of 54 GHz M2 in the offset plane ($\varphi = 0^\circ$) without the dichroic. GRASP analysis provides the baseline reference standard.

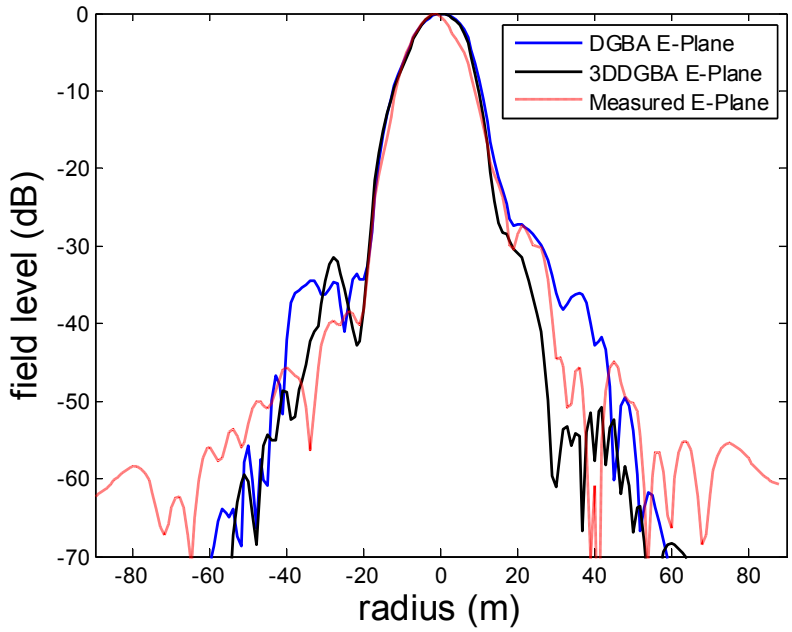

Figure 7.24 The far field distribution of 54 GHz M2 in the offset plane ($\varphi = 0^\circ$) with the dichroic in place.

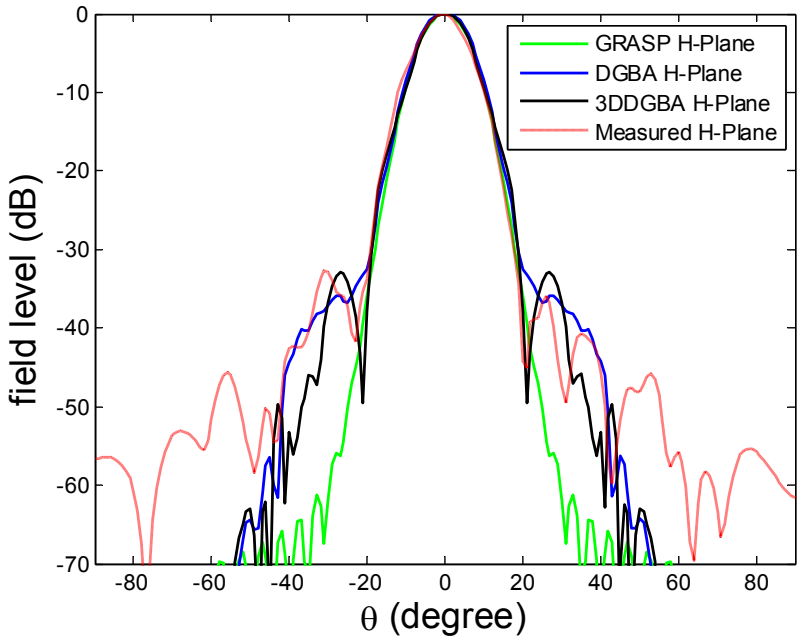

Figure 7.25 The far field distribution of 54 GHz M2 in the symmetric plane ($\varphi = 90^{\circ}$) without the dichroic.

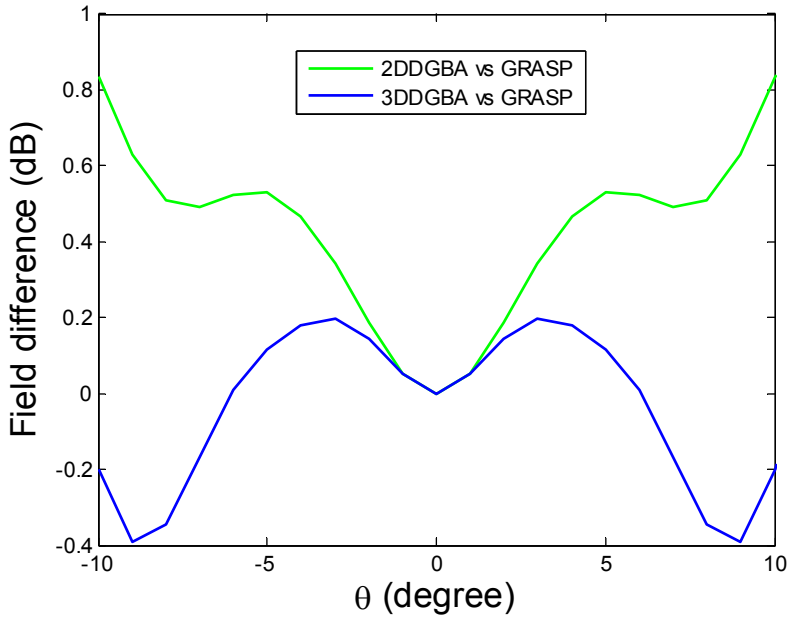

Figure 7.26 Field difference of far field distributions of 54 GHz M2 in the symmetric plane ($\varphi = 90^{\circ}$) without the dichroic. GRASP analysis provides the baseline reference standard.

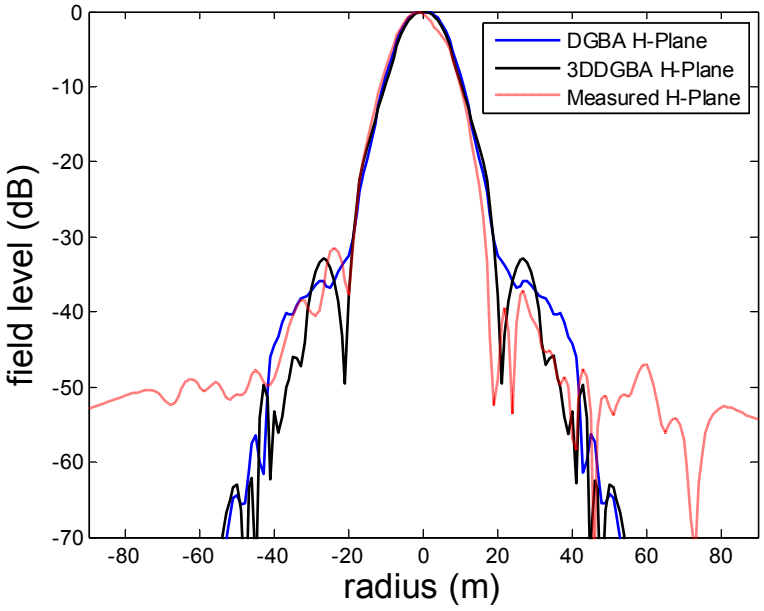

Figure 7.27 The far field distribution of 54 GHz M2 in the symmetric plane ($\varphi = 90^{\circ}$) with the dichroic in place.

Figure 7.28 through to Figure 7.41 are the corresponding results for the 89 GHz path. Similar performance conclusions can be drawn as for the 54 GHz path.

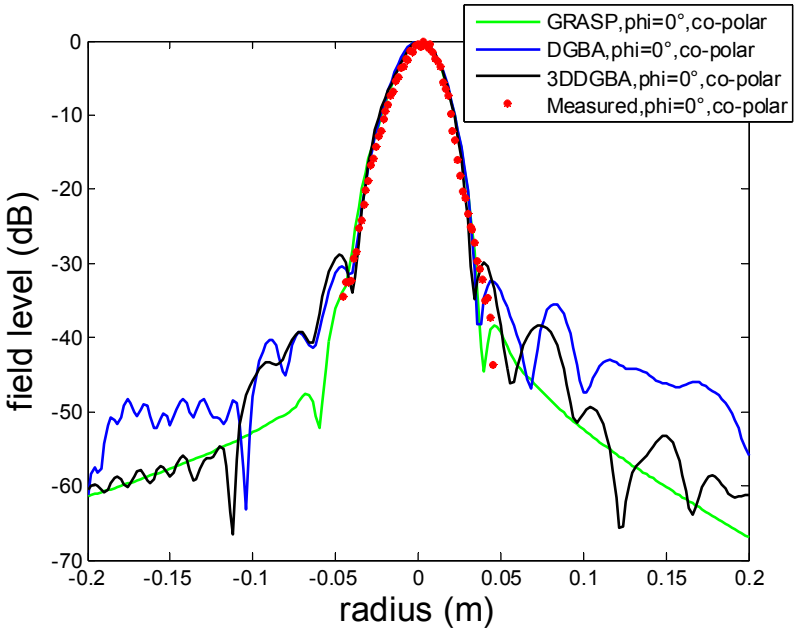

Figure 7.28 The near field distribution of 89 GHz M1 in the offset plane (φ=0°). The scan plane is 330 mm (~ 98λ), from the optical centre of reflector M1-89.

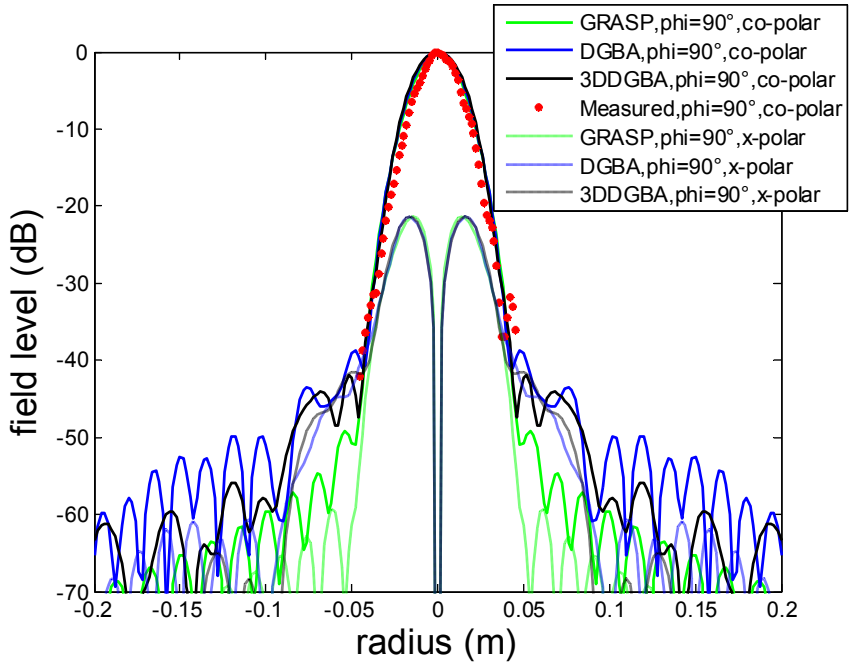

Figure 7.29 The near field distribution of 89 GHz M1 in the symmetric plane (φ=90°). The scan plane is 330 mm (~ 98λ) from the optical centre of reflector M1-89.

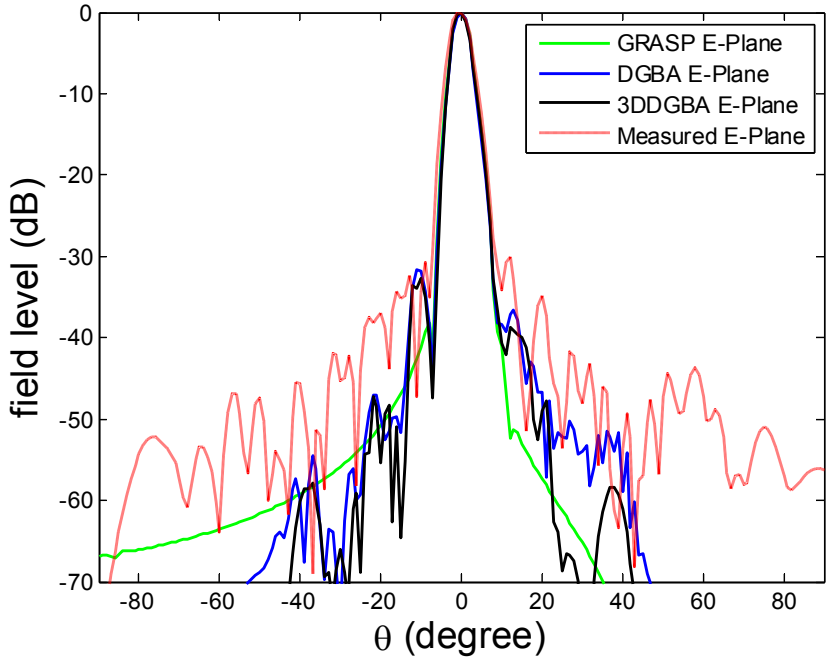

Figure 7.30 The far field distribution of 89 GHz M1 in the offset plane (φ=0°)

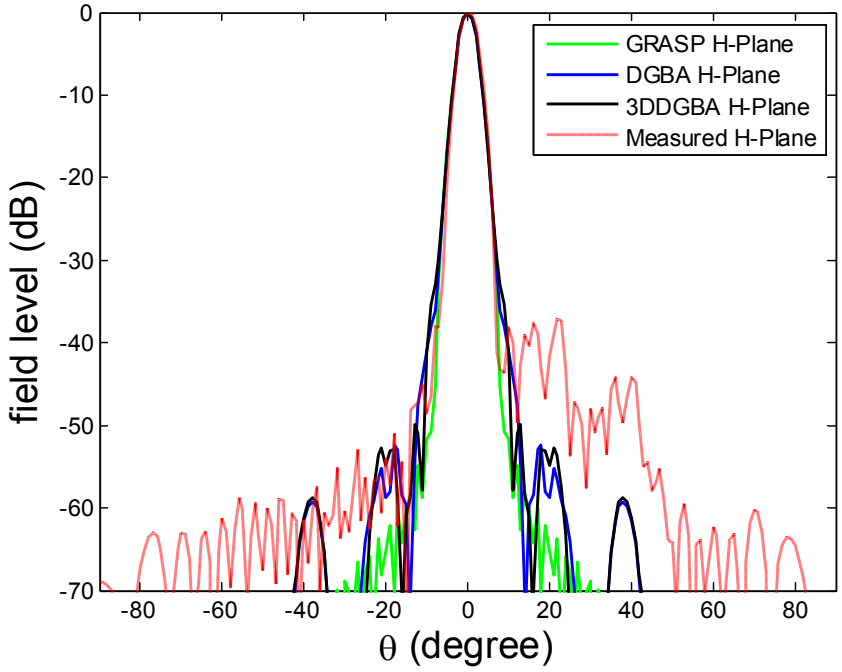

Figure 7.31 The far field distribution of 89 GHz M1 in the symmetric plane (φ=90°).

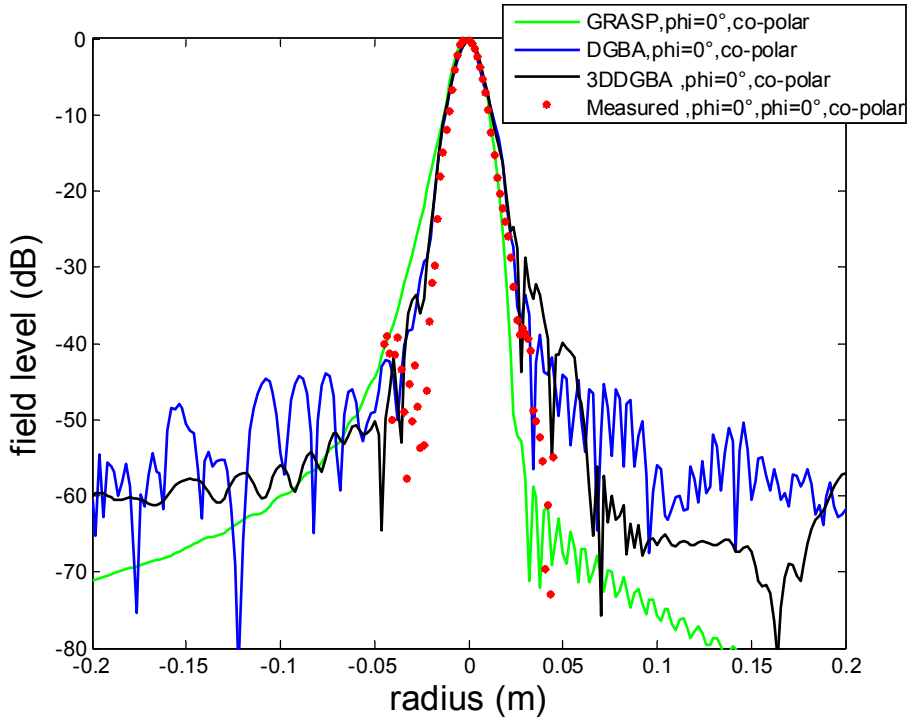

Figure 7.32 The near field distribution of M2 at 89 GHz in the offset plane (φ=0°) without the dichroic present. The scan plane is 170 mm (~ 50λ) from the optical centre of reflector M2-89.

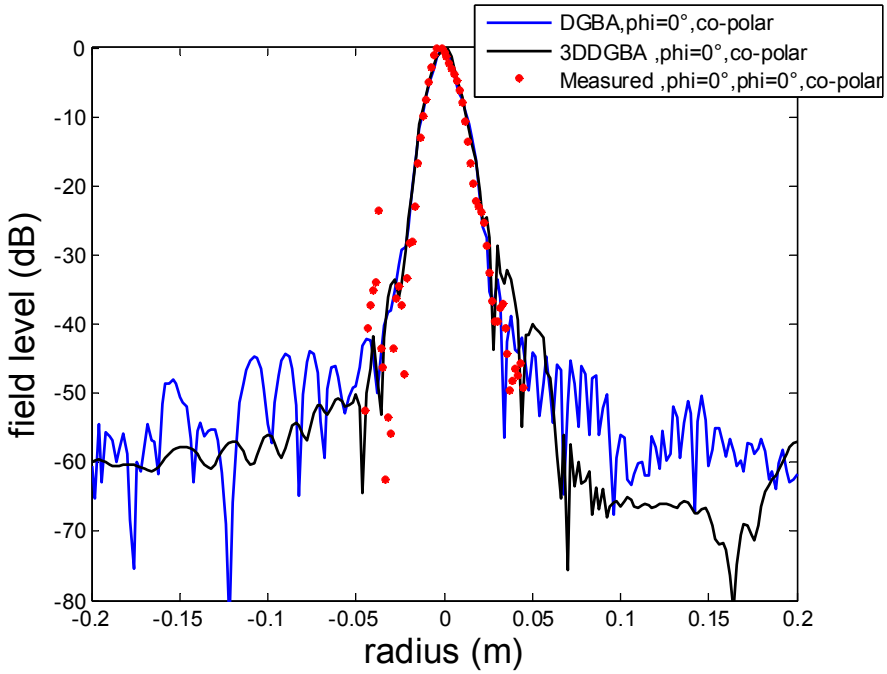

Figure 7.33 The near field distribution of M2 at 89 GHz in the offset plane (φ=0°) with the dichroic in place. The scan plane is 170 mm (~ 50λ) from the optical centre of reflector M2-89.

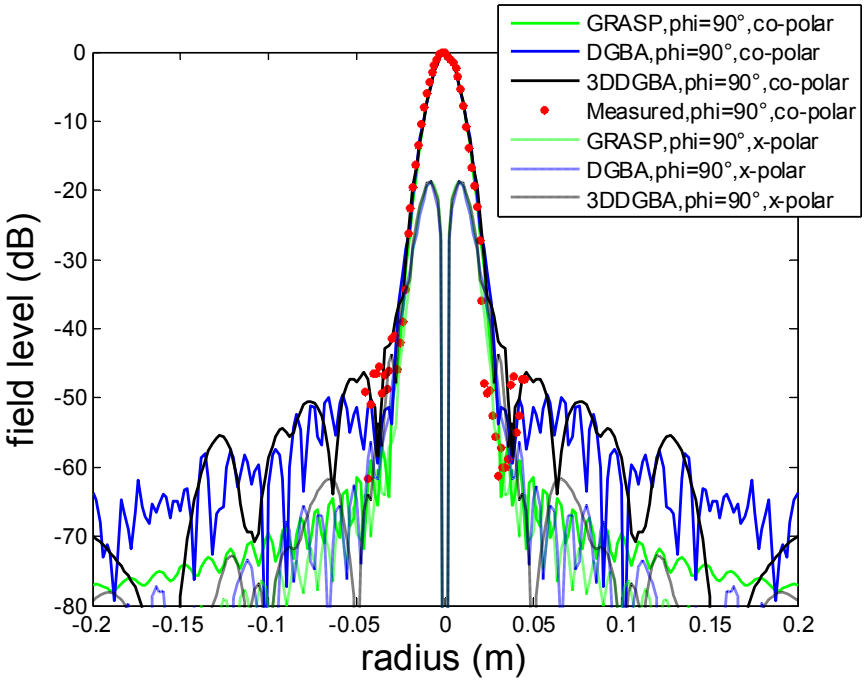

Figure 7.34 The near field distribution of M2 at 89 GHz in the symmetric plane (φ=90°) without the dichroic present. The scan plane is 170 mm (~ 50λ) from the optical centre of reflector M2.

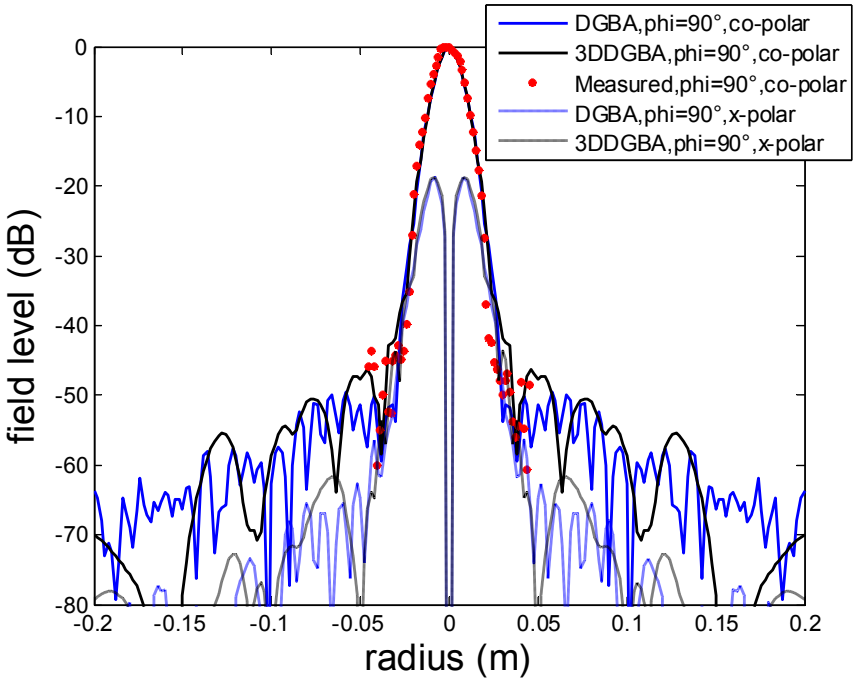

Figure 7.35 The near field distribution of M2 at 89 GHz in the symmetric plane (φ=90°) with the dichroic in place. The scan plane is 170 mm (~ 50λ) from the optical centre of reflector M2.

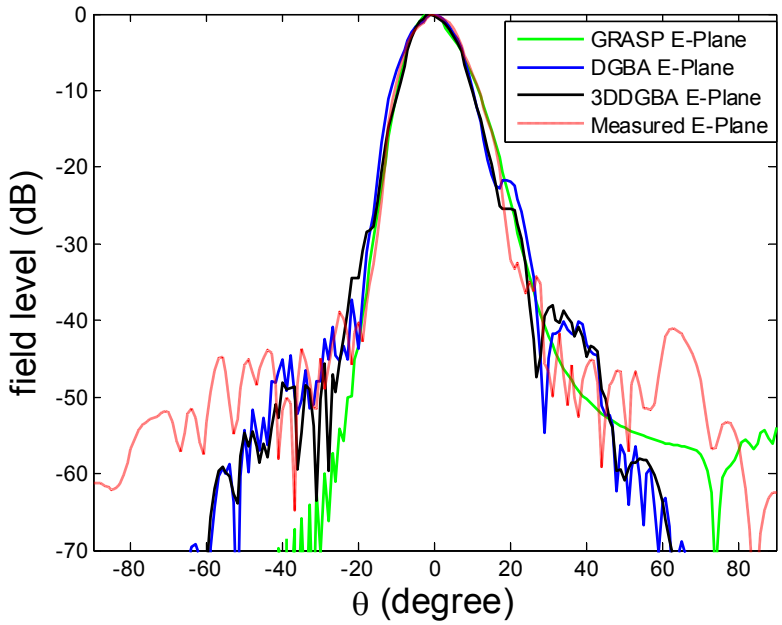

Figure 7.36 The far field distribution of 89 GHz M2 in the offset plane (φ=0°) without the dichroic

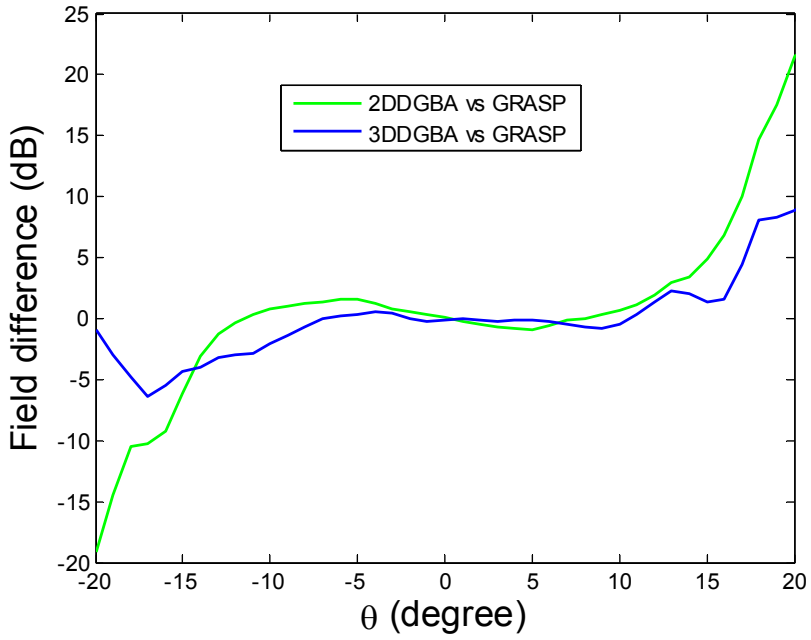

Figure 7.37 Field difference of far fields distribution of 89 GHz M2 in the offset plane (φ=0°) without the dichroic. GRASP analysis provides the baseline reference standard.

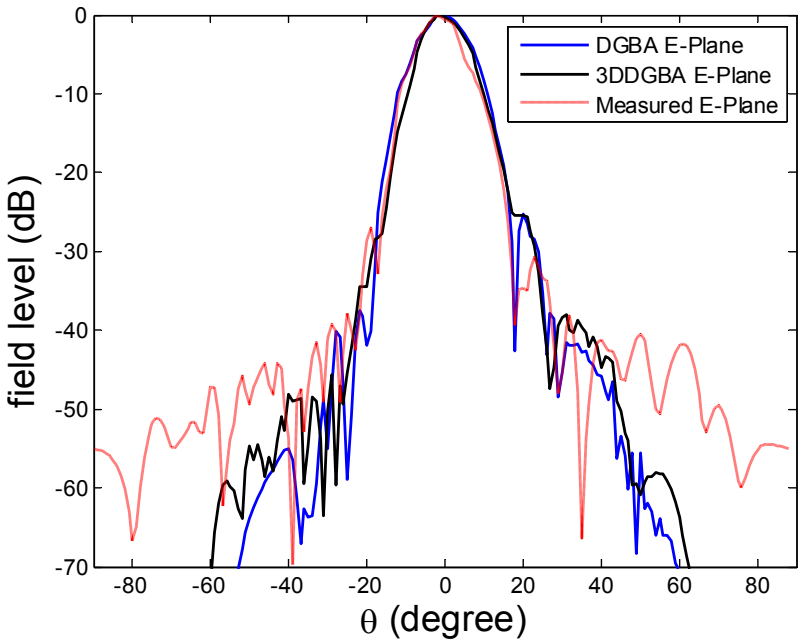

Figure 7.38 The far field distribution of 89 GHz M2 in the offset plane (φ=0°) with the dichroic in place.

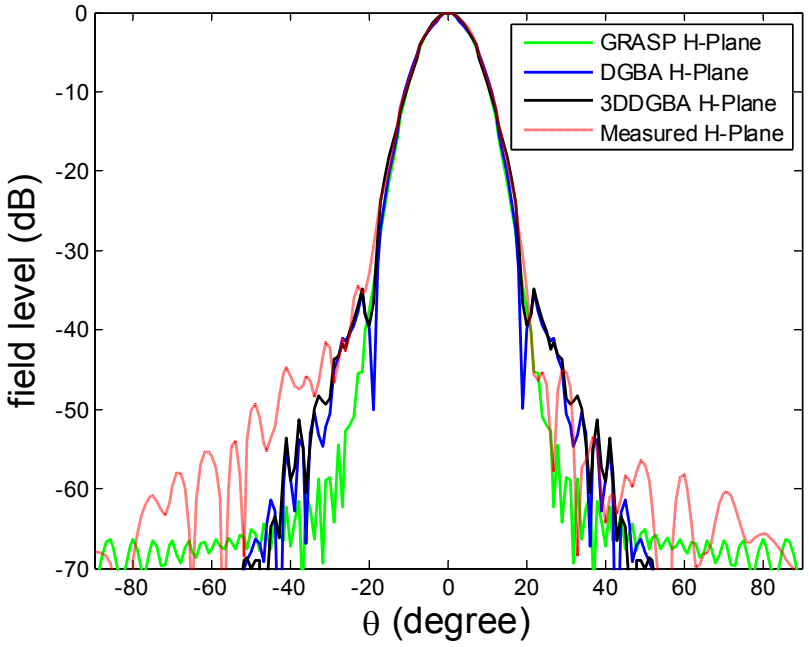

Figure 7.39 The far field distribution of 89 GHz M2 in the symmetric plane (φ=90°) without the dichroic.

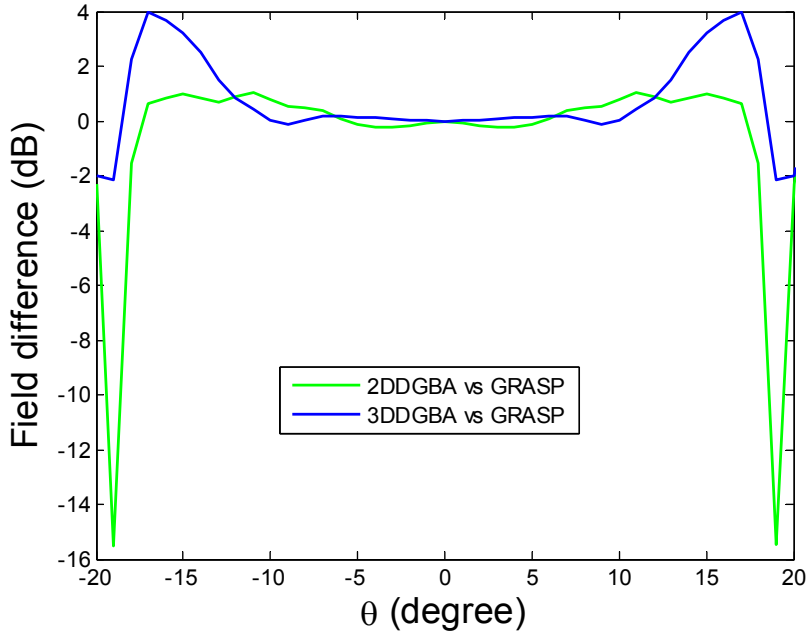

Figure 7.40 Field difference of far fields distribution of 89 GHz M2 in the symmetric plane (φ=90°) without the dichroic. GRASP analysis serves as the standard for reference.

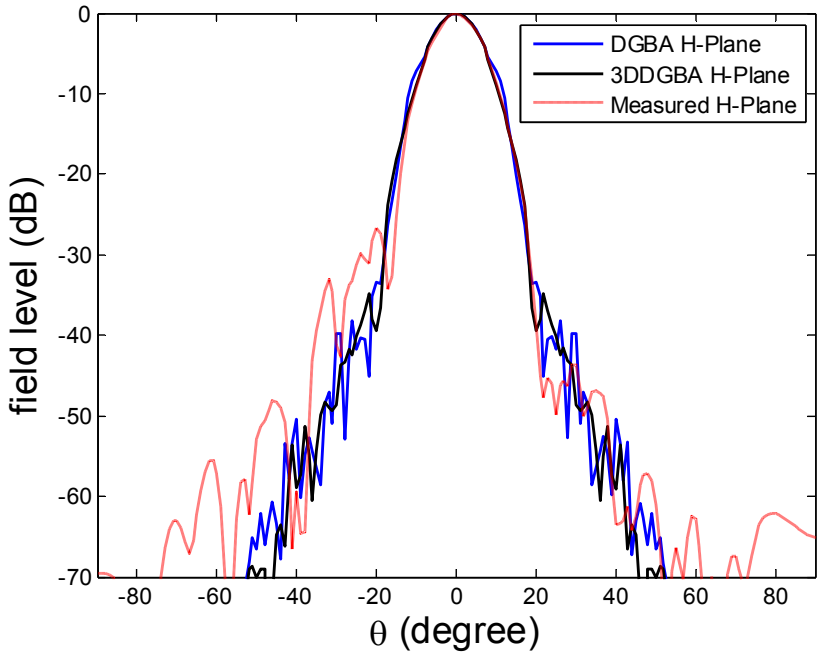

Figure 7.41 The far field distribution of 89 GHz M2 in the symmetric plane (φ=90˚) with the dichroic in place.

In 89GHz path, from the field difference (7.37), it can be observed that the deviation between GRASP and 3D-DGBA in the offset-plane within 20˚ stays in the range of ±8.0 dB in comparison with ±23.0 dB of 2D-DGBA. In the symmetric plane, the field difference within 20˚ stays in the range of ±4.0 dB between 3D-DGBA and GRASP in comparison with ±16.0 dB of 2D-DGBA.

7.8 Summary

A specific design procedure of multi-path, multi-reflector, QoNs is presented. Two different configurations of a dual-path QoN are demonstrated. The first uses a low-pass, resonant slot-array dichroic, with rectangular slots repeated on a square lattice; the second employs a high-pass perforated FSS with a circular unit cell repeated on a triangular lattice. 3D-DGBA is used for analysing the low-pass QoN. It is verified in comparison with the simulation results of GRASP as well as 2D-DGBA, and experimental measurement. Although deviation still exists in comparison with GRASP, it is obvious that 3D-DGBA is more accurate than 2D-DGBA.

References

[1] J. Yu, S. Liu, **L. Xu**, X. Liu, et al, "An Integrated Quasi-optical Analysis Method and Its Experimental Verification", Journal of Infrared, Millimeter and Terahertz Wave, Vol.31, No.2, pp. 181-195, Feb. 2010.

[2] J. Yu, S. Liu, **L. Xu**, H. Su, X. Liu, et al, "Study of A Two-Layer Dichroic for Quasi-OpticalNetwork", Microwave and Optical Technology Letters, Vol. 52, No. 4, April 2010.

[3] Liu X, **Xu L**, Yu J, et al. "Frequency selective surfaces design for a dual‐channel quasi‐optical system." Microwave and Optical Technology Letters, 2014, 56(10): 2365-2369.

[4] P.F.Goldsmith, "Quasioptical Systems: Gaussian Beam Quasioptical Propagation and Applications," IEEE Press, 1998

[5] P. F. Foster, P. A. R. Rde, R. S. Donnan, J. Dupuy, and J. McNiff, "Measurements on a quasi-optical testbench", International Journal of Infrared and Millimeter Waves, 28 (7), 521–529 (2005).

[6] C. Rieckmann, M. R. Rayner, and C. G. Parini, "Diffracted Gaussian beam analysis of quasi-opticalmulti-reflector systems," IEE-Electronics Letters 36 (19), 1600–1601 (2000).

[7] M. Katsav and E. Heyman, "A beam summation representation for 3D radiation from a line source distribution," IEEE Trans. Antennas Propag., vol. 56, pp. 601-605, 2008.

Chapter 8 Summary and Future Work

8.1 Conclusions

In this thesis, a 3D Diffraction Gaussian Beam Analysis (3D-DGBA) approach to the analysis of multi-reflector antennas has been developed. This new approach is based on the 2D diffracted Gaussian beam analysis (2D-DGBA) method developed at Queen Mary University of London. In 3D-DGBA, extended Phase Matching reflection analysis and 3D GBS diffraction analysis have been investigated and incorporated into 2D-DGBA, making the resulting 3D-DGBA capable of analysing general astigmatic incident GBs from arbitrary orientations. Also, it is a highly modular method suitable for analysis of electrically-large, multi-element, quasi-optical systems.

A specific design procedure of multi-path, multi-reflector QoNs is presented and two different configurations of dual-path QoNs have been built and presented with two kinds of FSS. By analysing one of these QoNs, the 3D-DGBA is verified in comparison with the simulation results of GRASP as well as the original 2D-DGBA, and finally with the experimental measurement. It is demonstrated that 3D-DGBA is more accurate than original 2D- DGBA.

It has been demonstrated that extended Phase Matching analysis and GO present the same accuracy when dealing with stigmatic Gaussian beams. However, for general astigmatic Gaussian beams, extended Phase Matching analysis performs better and the near field deviation remains in a ±0.8 dB with small angles of incidence. It has been shown that Phase Matching analysis can be applied under the condition that the spot size widths of the incident beams are much smaller compared with the principal curvatures of the surface.

Kirchhoff half-screen boundary diffraction wave (BDW) theory, 2D GBS diffraction analysis and 3D GBS have been investigated. It has been demonstrated that 2D GBS analysis is a two dimensional method where observation points have to be in the same plane as defined by the incident and emergent Gaussian beams. Kirchhoff half-screen boundary diffraction wave (BDW) theory can be seen as a 2.5D method. 3D GBS has proved to be a full 3D method of analysis handling general astigmatic incident Gaussian Beam incidence onto the reflector at arbitrary incident angles. In comparison with PO, 3D GBS has been verified to be more accurate than Kirchhoff half-screen boundary diffraction analysis. In some cases, a ±5.0 dB field deviation can be observed within ±25λ of BDT in comparison of ±1.0 dB of 3D GBS analysis. In the range of low signal level, more than 50 dB field deviation is presented for BDT in comparison to 10 dB for 3D GBS analysis.

Methods to accelerate computation have been developed to increase the computational efficiency of 3D-DGBA. The principle has been to reduce the number of diffracted Gaussian beams while holding the required level of accuracy. With these optimization methods, the simulation efficiency of 3D-DGBA has been increased by a factor of 20.

8.2 Key contributions

The key original contributions to knowledge from this thesis include:

1) Development of a three dimensional diffraction Gaussian beam analysis (3D-DGBA) for characterising multi-reflector antennas. By simulating a dual-channel QoN, the performance of 3D-DGBA has been verified in comparison with PO evaluation from GRASP and experiment results.

2) Although deviation still exists in comparison with GRASP, it can be observed that 3D-DGBA is more accurate than 2D-DGBA. For example, in one of the simulated cases, the far-field deviation between 3D-DGBA and GRASP in the offset-plane within 20˚ stays in the range of ±8.0 dB in comparison with ±23.0 dB of 2D-DGBA. In the symmetric plane, the far field difference within 20˚ stays in the range of ±4.0 dB between 3D-DGBA and GRASP in comparison with ±16.0 dB of 2D-DGBA.

3) In 3D-DGBA, the 3D GBS diffraction model is seamlessly applied into practical scenarios. Optimization methods have been developed and the simulation efficiency has been increased by a factor of 20.

4) In 3D-DGBA, reflected and diffracted fields are both represented as Gaussian beams. By contrast, in 2D-DGBA, only the diffracted fields are calculated rather than the diffracted Gaussian beams.

5) 3D-DGBA has the capability of analysing general astigmatic Gaussian Beams incident on a reflector at arbitrary angles. By contrast, in 2D-DGBA, the simulated Gaussian beam should be a stigmatic Gaussian beam and all the oblique polar angles of the incident beams are approximated by polar angles of normal incidence.

6) Two kinds of dual-path QoNs with different configurations have been designed and developed. A low-pass resonate slot-array dichroic with rectangular slots repeated on a square lattice, and an FSS high-pass filter made from a circular-hole unit cell repeated on a triangular lattice, are studied and fabricated for the QoNs. Both of the QoNs meet their system performance specifications. Experiments were conducted to verify the accuracy of 3D-DGBA.

8.3 Future work

Though 3D-DGBA has been developed, there are still many issues to be addressed. Many areas deserve further study and the future work may include:

- Consideration that, while the reflected and diffracted fields are represented in the form of Gaussian beams, in the current version of 3D-DGBA, these Gaussian beams cannot be traced to directly analyse cascaded reflectors. Gaussian beam expansion is employed for an analysis of cascaded reflectors, but this may cause deviations and loss of efficiency. Therefore, it is worthwhile finding ways to utilise reflected and diffracted Gaussian beams directly.

- The accuracy of the current 3D-DGBA is not clear for electrically large antennas.

- Analysis of a real 3D QoN is also necessary to evaluate further the performance of 3D-DGBA.

List of collaboration and publications

Journal papers

[1] Liu X, **Xu L**, Yu J, et al. Frequency selective surfaces design for a dual‐channel quasi‐optical system. Microwave and Optical Technology Letters, 2014, 56(10): 2365-2369.
[2] J. Yu, S. Liu, **L. Xu**, X. Liu, et al, "An Integrated Quasi-optical Analysis Method and Its Experimental Verification", Journal of Infrared, Millimetre and Terahertz Wave, Vol.31, No. 2, pp. 181-195, Feb. 2010.
[3] J. Yu, S. Liu, **L. Xu**, H. Su, X. Liu, et al, "Study of A Two-Layer Dichroic for Quasi-Optical Network", Microwave and Optical Technology Letters, Vol. 52, No. 4, April 2010.
[4] J. Yu, X. Chen, J. Miao, S. Liu, **L. Xu**, X. Liu, et al, "Dual-path Quasi-optical System for Space Remote Sensing," Chinese Space Science and Technology, Vol. 30, No.4, pp. 58-63, Aug. 2010.

Conference papers

[1] **Liang Xu**, Xiadong Chen, Hui Feng, Hao Tu, D. Xiao, S.Wu, " A three dimensional Gaussian beam diffraction approach to analysis of reflector antennas", 2015 IEEE International Symposium on Antennas and Propagation,19-24 July 2015,Vancouver, BC, Canada.
[2] Cheng Yang, Junsheng Yu, Yuan Yao, Xiaoming Liu, **Liang Xu**, Xiadong Chen, " Corrugated matched horn with low side-lobes for high performance offset reflector system", 2015 IEEE International Symposium on Antennas and Propagation,19-24 July 2015,Vancouver, BC, Canada.
[3] **Liang Xu**, Xiaodong Chen, Xiaoming Liu, and Zejian Lu, " A Comparison of the Results of Two Types of Gaussian Beam Half-screen Diffraction Theories", 7th Europe/UK-China Workshop on Millimetre Waves 2nd-4th September 2014 Chengdu China.
[4] Chengliang Li; **Liang Xu**; Yuan Yao; Xiaodong Chen; Junsheng Yu, "Application of diffracted Gaussian beam analysis to design 3D configured quasi-optical systems", 2012 IEEE MTT-S International Microwave Workshop Series on Millimeter Wave Wireless Technology and Applications (IMWS 2012), p3pp., 2012
[5] Di Wu, Junsheng Yu, **Liang Xu**, et al , "Design of Quasi-optical System for Plasma Radiometer", 3rd China - Europe Workshop on Millimetre Waves and THz Technologies, 23rd-25th, Sept. 2010, Beijing, China.
[6] Junsheng Yu; Shaohua Liu; Qingang Wei; **Liang Xu**; et al, " A 3D design software for Quasi-optical systems based on integrated methods" Microwave Technology and Computational Electromagnetics, 2009. ICMTCE. International Conference on Digital Object Identifier: 10.1049/cp.2009.1346 Publication Year: 2009 , Page(s): 372 - 374 , IET Conference Publications
[7] Junsheng Yu; Yuan Mai; Shaohua Liu; Xiaoming Liu; Hairui Liu; Hansheng Su; Qinggang Wei; Xiaodong Chen; **Liang Xu**, "Design of tri-reflector Compact Antenna Test Range",Microwave Technology and Computational Electromagnetics,

2009. ICMTCE. International Conference on Digital Object Identifier: 10.1049/cp.2009.1281 Publication Year: 2009 , Page(s): 133 - 136 IET Conference Publications

[8] Xiaoming Liu, Hansheng Su, **Liang Xu**, et al "The Influence of Dichroic on the Performance of a Quasi-optical System," 2ndUK/Europe-China Workshop on Millimetre Waves and Terahertz Technologies, Rutherford Appleton Laboratory, 19th to 21st October 2009.

[9] Hansheng Su, Xiaoming Liu, **Liang Xu**, et al, "Experimental Assessment of Periodic Method of Moments Design Accuracy for Quasi Optical Networks," 2ndUK/Europe-China Workshop on Millimetre Waves and Terahertz Technologies, Rutherford Appleton Laboratory, 19th to 21st October 2009.

[10] **Liang Xu**, Wei Wang, Yufeng Wang, Xiaodong Chen, et al, "Ellipsoidal Reflector Design for Quasi-optical Network", Microwave and Millimetre-wave Symposium of China, Ningbo, Zhejiang, China, Oct. 18-21, 2008, pp. 559-563.

[11] Junsheng Yu; Shaohua Liu; **Liang Xu**, et al, "Design and measurement of dichroic plate for Quasi-Optical Network" 8th International Symposium on Antennas, Propagation and EM Theory, 2008. ISAPE DOI: 10.1109/ISAPE.2008.4735466 Publication Year: 2008 , Page(s): 1310 - 1313

[12] Xiaodong Chen, C.Rieckmann, R.Donnan，Junsheng Yu, Shaohua Liu, **Liang Xu**, et al, "Quasi-optical analysis and design technique (Invited paper)," China-UK/Europe Workshop on Millimetre Waves and Terahertz Technologies 20th-22 nd October, 2008, Chengdu, China.

[13] Junsheng Yu, Shaohua Liu, Liang Xu, et al, "Experimental Validation of a Dual-Channel Multi-Reflector Quasi-Optical System," China-UK/Europe Workshop on Millimetre Waves and Terahertz Technologies 20th-22 nd October, 2008, Chengdu, China.

Appendix I Approximated PO Reflection Method

In reference [1], an approximated PO reflection method dealing with reflection of an elliptical astigmatic Gaussian beam on a curved surface is given. The reflected magnetic field with a closed form is given in equation (3.8)

$$\bar{H}^r(x,y,z) = -\frac{jk}{2\pi}\frac{e^{-jkr}}{r}\sum_{n=0}^{3}\sum_{m=0}^{3}\bar{W}_{nm}I_{nm} \quad , \tag{A1.1}$$

where,

$$\begin{aligned}
\bar{W}_{00} &= -\hat{x}W_1\frac{z}{r} - \hat{y}W_2\frac{z}{r} + \hat{z}(W_1\frac{x}{r} + W_2\frac{y}{r}) \\
\bar{W}_{10} &= \hat{x}\frac{1}{R_1}(W_2\frac{y}{r} + W_3\frac{z}{r}) - \hat{y}\frac{W_2}{R_1}\frac{x}{r} - \hat{z}(\frac{W_3}{R_1}\frac{x}{r} + \frac{W_1}{r}) \\
\bar{W}_{01} &= -\hat{x}\frac{W_1}{R_1}\frac{y}{r} + \hat{y}\frac{1}{R_2}(W_3\frac{z}{r} + W_1\frac{x}{r}) - \hat{z}(\frac{W_3}{R_2}\frac{y}{r} + \frac{W_2}{r}) \\
\bar{W}_{20} &= -\hat{x}\frac{W_1}{2rR_1} + \hat{y}\frac{W_2}{2rR_1} + \hat{z}\frac{W_3}{rR_1} \\
\bar{W}_{02} &= \hat{x}\frac{W_1}{2rR_2} - \hat{y}\frac{W_2}{2rR_2} + \hat{z}\frac{W_3}{rR_2} \\
\bar{W}_{11} &= -\hat{x}\frac{W_2}{rR_1} - \hat{y}\frac{W_1}{rR_2} \\
\bar{W}_{12} &= \hat{x}\frac{W_3}{2rR_1R_2} \\
\bar{W}_{21} &= \hat{y}\frac{W_3}{2rR_1R_2} \\
\bar{W}_{30} &= \hat{x}\frac{W_3}{2rR_1^2} \\
\bar{W}_{03} &= \hat{y}\frac{W_3}{2rR_2^2}
\end{aligned} \quad , \tag{A1.2}$$

with,

$$\begin{aligned} W_1 &= H_1 p_{11} + H_2 p_{21} \\ W_2 &= H_1 p_{12} + H_2 p_{22} \\ W_3 &= -H_1 p_{13} - H_2 p_{23} \end{aligned} \quad . \tag{A1.3}$$

p_{ij} are defined by the transformation between the reflected beam coordinate system and the surface coordinate system, the same as in equation (3.27).

The term I_{nm} is given by

$$\begin{aligned} I_{00} &= \frac{\pi}{\sqrt{a_1 a_0 - c^2}} \exp\left(\frac{a_1 b_0^2 + a_0 b_1^2 - 2 b_1 b_0 c}{4[a_0 a_1 - c^2]}\right) \\ I_{10} &= \frac{a_1 b_0 - b_1 c}{2(a_0 a_1 - c^2)} I_{00} \\ I_{01} &= \frac{a_0 b_1 - b_0 c}{2(a_0 a_1 - c^2)} I_{00} \\ I_{20} &= \left[\frac{(a_1 b_0 - b_1 c)^2}{4(a_0 a_1 - c^2)^2} + \frac{a_1}{2(a_0 a_1 - c^2)}\right] I_{00} \\ I_{02} &= \left[\frac{(a_0 b_1 - b_0 c)^2}{4(a_0 a_1 - c^2)^2} + \frac{a_0}{2(a_0 a_1 - c^2)}\right] I_{00} \\ I_{11} &= \left[\frac{(a_1 b_0 - b_1 c)(a_0 b_1 - b_0 c)}{4(a_0 a_1 - c^2)^2} + \frac{c}{2(a_0 a_1 - c^2)}\right] I_{00} \\ I_{12} &= \left[\frac{(a_0 b_1 - b_0 c)^2 (a_1 b_0 - b_1 c)}{8(a_0 a_1 - c^2)^3} + \frac{a_0 (a_1 b_0 - 3 b_1 c) + 2 b_0 c^2)}{4(a_0 a_1 - c^2)^2}\right] I_{00} \\ I_{21} &= \left[\frac{(a_1 b_0 - b_1 c)^2 (a_0 b_1 - b_0 c)}{8(a_0 a_1 - c^2)^3} + \frac{a_1 (a_0 b_1 - 3 b_0 c) + 2 b_1 c^2)}{4(a_0 a_1 - c^2)^2}\right] I_{00} \\ I_{30} &= \left[\frac{(a_1 b_0 - b_1 c)^3}{8(a_0 a_1 - c^2)^3} + \frac{3 a_1 (a_1 b_0 - b_1 c)}{4(a_0 a_1 - c^2)^2}\right] I_{00} \\ I_{30} &= \left[\frac{(a_0 b_1 - b_0 c)^3}{8(a_0 a_1 - c^2)^3} + \frac{3 a_0 (a_0 b_1 - b_0 c)}{4(a_0 a_1 - c^2)^2}\right] I_{00} \end{aligned} \tag{A1.4}$$

with

$$
\begin{aligned}
a_0 &= \frac{jk}{2}\left\{\frac{1}{R_1}(\frac{z}{r}+p_{33})+\frac{1}{r}(1+\frac{x^2}{r^2})+p_{11}^2\Gamma_{11}^i+p_{11}^2\Gamma_{22}^i+2p_{11}p_{22}\Gamma_{12}^i\right\} \\
b_0 &= jk(\frac{x}{r}-p_{31}) \\
a_1 &= \frac{jk}{2}\left\{\frac{1}{R_2}(\frac{z}{r}+p_{33})+\frac{1}{r}(1+\frac{x^2}{r^2})+p_{12}^2\Gamma_{11}^i+p_{22}^2\Gamma_{22}^i+2p_{12}p_{22}\Gamma_{12}^i\right\} . \qquad \text{(A1.5)} \\
b_1 &= jk(\frac{y}{r}-c_{32}) \\
c &= \frac{jk}{2}\left\{p_{11}p_{12}\Gamma_{11}^i+p_{21}p_{22}\Gamma_{22}^i+(p_{11}p_{22}+p_{21}p_{12})\Gamma_{12}^i-\frac{xy}{r^3}\right\}
\end{aligned}
$$

References

[1] G. C. Zogbi, “Reflection and diffraction of general astigmatic Gaussian beam from curved surfaces and edges [D]”, Ph.D. dissertation, The Ohio State University, Columbus, OH, USA, Jun. 1994.

Appendix II Phase Matching Analysis Method in GO

By Deschamps [1], the curved surfaces or a wave front is represented by a second-order equation (bi-parabolic expansion)

$$z = -\frac{1}{2}\vec{x}^{t} \cdot Q \cdot \vec{x} \tag{A2.1}$$

where $\vec{x}$ is the transverse position vector represented by its components (x_1, x_2), and Q is a 2 by 2 symmetric matrix, called the curvature matrix of the surface.

More generally, when $\vec{x}$ is small, the phase at any point $\vec{r} = (\vec{x}, z)$ is $kS(\vec{r})$ with

$$S(\vec{r}) = z + \frac{1}{2}\vec{x}^{t} \cdot \Gamma \cdot \vec{x}\,. \tag{A2.2}$$

Fig.A2.1 illustrates a beam incident on a curved surface. The equation near Q_R may be written as

$$\vec{r}(\vec{t}) = \vec{t} - \frac{1}{2}(\vec{t}^{\,t} \cdot Q \cdot \vec{t})\hat{n} \tag{A2.3}$$

with

$$\vec{t} = t_1\vec{u}_1 + t_2\vec{u}_2 \tag{A2.4}$$

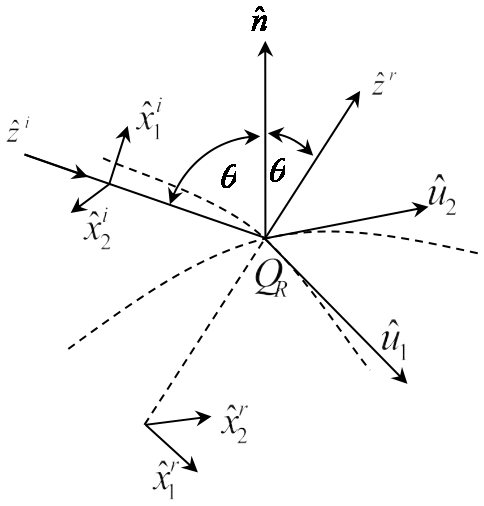

Figure A2.1: Geometry for the description of the wave front reflected from the curved surface. $(\hat{u}_1, \hat{u}_2, \hat{n})$ **is the surface coordinate at the intersection point** Q_R**, with** $\hat{u}_1$ **and** $\hat{u}_2$ **perpendicular to normal direction** $\hat{n}$ **.** $\hat{z}^i$ **and** $\hat{z}^r$ **are the propagation directions of the incident and reflected beams.** $\hat{n}$ **makes the angle** $\pi - \theta$ **with** $\hat{z}^i$**.**

The coordinates $(\vec{x}, z)$ of both incident and reflected beams can be written as

$$\vec{x} = \Theta \vec{t} + O\left(\vec{t}^{\,2}\right) \tag{A2.5}$$

$$z = \vec{v} \cdot \vec{t} - \frac{1}{2} \vec{t}^{\,t} \cdot \Gamma \cdot \vec{t} \cos(\pi - \theta) + O\left(\vec{t}^{\,3}\right) \tag{A2.6}$$

with

$$\Gamma = \begin{pmatrix} \dfrac{1}{R_1} & 0 \\ 0 & \dfrac{1}{R_2} \end{pmatrix} \tag{A2.7}$$

and Θ , the projection of the vector $\vec{t}$ onto the plane $z = 0$ is

$$\Theta = \begin{pmatrix} \hat{x}_1 \cdot \hat{u}_1 & \hat{x}_1 \cdot \hat{u}_2 \\ \hat{x}_2 \cdot \hat{u}_1 & \hat{x}_2 \cdot \hat{u}_2 \end{pmatrix}. \tag{A2.8}$$

$\vec{v}$ in (A2.6) is

$$\vec{v} = v_1\hat{u}_1 + v_2\hat{u}_2 = \left(\hat{z}\cdot\hat{u}_1\right)\hat{u}_1 + \left(\hat{z}\cdot\hat{u}_2\right)\hat{u}_2 . \tag{A2.9}$$

$S\left(\vec{r}\right)$ can therefore be rewritten as

$$\begin{aligned} S\left(\vec{r}\right) &= z + \frac{1}{2}\vec{x}\cdot\Gamma\vec{x} \\ &= \vec{v}\cdot\vec{t} - \frac{1}{2}\vec{t}\cdot Q\vec{t}\cos\left(\pi-\theta\right) + \frac{1}{2}\Theta\vec{t}\cdot\Gamma\Theta\vec{t} \\ &= \vec{v}\cdot\vec{t} + \frac{1}{2}\vec{t}\cdot\left[\Theta^T\Gamma\Theta - Q\cos\left(\pi-\theta\right)\right]\vec{t} \end{aligned} . \tag{A2.10}$$

Subscript *i* denotes incidence and *r* , reflection. By phase matching, the phase of incident beam is equal to the phase of reflected beam, thus

$$k_i S_i = k_r S_r . \tag{A2.11}$$

Substituting (A2.10) into (A2.11), one has

$$\begin{aligned} & k_i\vec{v}_i\cdot\vec{t}_i - \frac{1}{2}k_i\vec{t}_i\cdot\left[\Theta_i^T\Gamma_i\Theta_i + Q\cos(\pi-\theta_i)\right]\vec{t}_i \\ &= k_r\vec{v}_r\cdot\vec{t}_r - \frac{1}{2}k_r\vec{t}_r\cdot\left[\Theta_r^T\Gamma_r\Theta_r + Q\cos(\pi-\theta_r)\right]\vec{t}_r \end{aligned} . \tag{A2.12}$$

By matching the linear term and quadratic terms, (A2.12), yields

$$k_i\left[\Theta_i^T\Gamma_i\Theta_i + Q\cos(\pi-\theta_i)\right] = k_r\left[\Theta_r^T\Gamma_r\Theta_r - Q\cos(\pi-\theta_r)\right] \tag{A2.13}$$

Or

$$k_r\Theta_r^T\Gamma_r\Theta_r = k_i\Theta_i^T\Gamma_i\Theta_i - \left[k_i\cos\theta_i + k_r\cos\theta_r\right]Q . \tag{A2.14}$$

If $k_i = k_r, \theta_i = \theta_r$, (A2.14) can be reduced to

$$\Theta_r^T\Gamma_r\Theta_r = \Theta_i^T\Gamma_i\Theta_i - 2\cos\theta Q . \tag{A2.15}$$

By using Snell's law of reflection, we get

$$\hat{x}_{1,2}^r = \hat{x}_{1,2}^i - 2\left(\hat{n}\cdot\hat{x}_{1,2}^i\right)\hat{n} . \tag{A2.16}$$

But because,

$$\hat{u}_i \cdot \hat{x}_j^r = \hat{x}_j^i \cdot \hat{u}_i - 2\left(\hat{n} \cdot \hat{x}_j^i\right)\left(\hat{n} \cdot \hat{u}_i\right) = \hat{u}_i \cdot \hat{x}_j^i \tag{A2.17}$$

one has

$$\Theta_i = \Theta_r = \Theta\,. \tag{A2.18}$$

Finally, equation (3.25) is given where

$$\Gamma_r = \Gamma_i - 2\cos\theta_i \left(\Theta^T\right)^{-1} Q \Theta^{-1}\,. \tag{A2.19}$$

References

[1] Deschamps G A. Ray techniques in electromagnetics [J]. Proceedings of the IEEE, 1972, 60(9): 1022-1035.

Appendix III Details of Proof that Equation (5.5) is Equivalent to (5.1)

Proof:

Firstly, since $\xi = -\sin\theta\cos\varphi$， $\gamma = \sin\theta\sin\varphi$ and $\zeta = \cos\theta$， it may be shown that $\sqrt{1-\xi^2-\zeta^2} = \gamma$. The derivation of α' is therefore

$$\begin{aligned} d\alpha' &= d(\cos^{-1}(-\xi/\varsigma)) \\ &= \left(\frac{1}{-\sqrt{1-(-\frac{\xi}{\varsigma})^2}}\cdot(-\frac{1}{\varsigma})\right)d\xi \\ &= \left(\frac{1}{\sqrt{\frac{1-\xi^2-\zeta^2}{1-\zeta^2}}}\cdot\frac{1}{\sqrt{1-\zeta^2}}\right)d\xi \\ &= \frac{1}{\sqrt{1-\xi^2-\zeta^2}}d\xi \\ &= \frac{1}{\gamma}d\xi \end{aligned}.$$

Replacing ξ with α' ; the spectrum $\tilde{B}_i(\boldsymbol{\kappa})$ of incident beam can be rewritten as $\tilde{B}_i(\boldsymbol{\kappa}) = \tilde{B}_i((\xi,\zeta)^t) = \tilde{B}_i(-\varsigma\cos\alpha',\zeta)^t$ and denoted as $\tilde{B}_i(\alpha',\zeta)$. So, (5.7) is found to be

$$\Phi(\alpha,\zeta) = \frac{ik}{8\pi^2}\int_{c_i} d\alpha'\gamma\tilde{B}_i(\alpha',\zeta)D(\alpha,\alpha') = \frac{ik}{8\pi^2}\int_{-\infty}^{\infty} d\xi\tilde{B}_i(\boldsymbol{\kappa})D(\alpha,\alpha'). \qquad \text{(A3.1)}$$

Substitute (5.8) into (5.6), gives

$$\tilde{u}_s(\boldsymbol{\rho},\zeta) = \int_{c\pm} d\alpha\Phi(\alpha,\zeta)e^{ik\varsigma\rho\cos(\alpha-\phi)} = \frac{ik}{8\pi^2}\int_{-\infty}^{\infty} d\xi\tilde{B}_i(\boldsymbol{\kappa})\int_{c\pm} d\alpha D(\alpha,\alpha')e^{ik\varsigma\rho\cos(\alpha-\phi)}. \qquad \text{(A3.2)}$$

Finally, substituting (5.9) into (5.5) yields

$$u_s(\mathbf{r}) = \frac{k}{2\pi}\int_{-\infty}^{\infty} d\zeta e^{ik\zeta z}\tilde{u}_s(\boldsymbol{\rho},\zeta) = \frac{k}{2\pi}\int_{-\infty}^{\infty} d\zeta e^{ik\zeta z}\frac{ik}{8\pi^2}\int_{-\infty}^{\infty} d\xi \tilde{B}_i(\boldsymbol{\kappa})\int_{c\pm} d\alpha D(\alpha,\alpha')e^{ik\varsigma\rho\cos(\alpha-\phi)}$$
$$= (\frac{k}{2\pi})^2\int_{-\infty}^{\infty} d\zeta \int_{-\infty}^{\infty} d\xi \tilde{B}_i(\boldsymbol{\kappa})e^{ik\zeta z}\frac{i}{4\pi}\times\int_{c\pm} d\alpha D(\alpha,\alpha')e^{ik\varsigma\rho\cos(\alpha-\phi)} \quad .$$

Thus (5.5) is equivalent to (5.1).

End of Proof

Appendix IV Calculations of $\tilde{\eta}_i$ and $\tilde{q}_i$

In order to expand $\Psi'_{\alpha'}$, $\Psi''_{\alpha'\alpha'}$ in a Taylor's series about $\zeta_i = \cos\theta_i$, given as

$$\begin{aligned}\Psi'_{\alpha'}(\zeta) &\simeq \Psi'_{0\alpha'} + \Psi''_{0\alpha'\zeta}\delta\zeta \\ &= \partial_{\alpha'}\Psi(\alpha',\zeta)\Big|_{\alpha'=\phi_i,\zeta=\zeta_i} + \partial_{\alpha'\zeta}\Psi(\alpha',\zeta)\Big|_{\alpha'=\phi_i,\zeta=\zeta_i}\delta\zeta\end{aligned}$$

Note from (5.31) that because $\alpha' = \cos^{-1}(-\xi/\varsigma)$, $\gamma_i = \sin\theta_i \sin\varphi_i$, $\boldsymbol{\kappa} = (\xi,\zeta)^t$, $\varsigma = \sqrt{1-\zeta^2}$ and $\varsigma_i = \sin\theta_i$, one has

$$\begin{aligned}\partial_{\alpha'}\Psi(\alpha',\zeta)\Big|_{\alpha'=\phi_i,\zeta=\zeta_i} &= \left(\frac{1}{2}(\boldsymbol{\kappa}-\boldsymbol{\kappa}_i)^t\bar{\boldsymbol{\Gamma}}_i^{-1}(\boldsymbol{\kappa}-\boldsymbol{\kappa}_i) + \boldsymbol{\kappa}^t\mathbf{x}_i\right)'\Big|_{\alpha'=\phi_i,\boldsymbol{\kappa}=\boldsymbol{\kappa}_i} \\ &= (\boldsymbol{\kappa}_i{}^t\mathbf{x}_i)'\Big|_{\alpha'=\phi_i} \\ &= (\xi_i x_i + \zeta_i z_i)'\Big|_{\alpha'=\phi_i} \\ &= (-\cos\alpha'\cdot\varsigma_i x_i + \zeta_i z_i)\Big|_{\alpha'=\phi_i} \\ &= \sin\varphi_i \sin\theta_i x_i \\ &= \gamma_i x_i\end{aligned}$$

so,

$$
\begin{aligned}
&\partial_{\alpha'\zeta}\Psi(\alpha',\zeta)\Big|_{\alpha'=\phi_i,\zeta=\zeta_i} \\
&= \{(-\varsigma^2\sin\varphi_i\cos\varphi_i - \varsigma\xi_i\sin\varphi_i)[\bar{\boldsymbol{\Gamma}}_i^{-1}]_{11} \\
&\quad +(\varsigma\zeta\sin\varphi_i - \varsigma\zeta_i\sin\varphi_i)[\bar{\boldsymbol{\Gamma}}_i^{-1}]_{12} + \varsigma\sin\varphi_i x_i\}'\Big|_{\zeta=\zeta_i} \\
&= \{(-(\sqrt{1-\zeta^2})^2\sin\varphi_i\cos\varphi_i - (\sqrt{1-\zeta^2})\xi_i\sin\varphi_i)[\bar{\boldsymbol{\Gamma}}_i^{-1}]_{11} \\
&\quad +(\zeta\sqrt{1-\zeta^2}\sin\varphi_i - \sqrt{1-\zeta^2}\zeta_i\sin\varphi_i)[\bar{\boldsymbol{\Gamma}}_i^{-1}]_{12} + \sqrt{1-\zeta^2}\sin\varphi_i x_i\}'\Big|_{\zeta=\zeta_i} \\
&= \{-(1-\zeta^2)\sin\varphi_i\cos\varphi_i - \sqrt{1-\zeta^2}\xi_i\sin\varphi_i)[\bar{\boldsymbol{\Gamma}}_i^{-1}]_{11} \\
&\quad +(\zeta\sqrt{1-\zeta^2}\sin\varphi_i - \sqrt{1-\zeta^2}\zeta_i\sin\varphi_i)[\bar{\boldsymbol{\Gamma}}_i^{-1}]_{12} + \sqrt{1-\zeta^2}\sin\varphi_i x_i\}'\Big|_{\zeta=\zeta_i} \\
&= \{(2\zeta_i\sin\varphi_i\cos\varphi_i + \frac{\zeta_i}{\sqrt{1-\zeta_i^2}}\xi_i\sin\varphi_i)[\bar{\boldsymbol{\Gamma}}_i^{-1}]_{11} \\
&\quad +((\sqrt{1-\zeta_i^2} + \zeta\frac{-\zeta_i}{\sqrt{1-\zeta_i^2}})\sin\varphi_i - \frac{-\zeta_i}{\sqrt{1-\zeta_i^2}}\zeta_i\sin\varphi_i)[\bar{\boldsymbol{\Gamma}}_i^{-1}]_{12} + \frac{-\zeta_i}{\sqrt{1-\zeta_i^2}}\sin\varphi_i x_i\} \\
&= \{2\cos\theta_i\sin\varphi_i\cos\varphi_i - \frac{\cos\theta_i}{\sin\theta_i}\sin\theta_i\cos\varphi_i\sin\varphi_i)[\bar{\boldsymbol{\Gamma}}_i^{-1}]_{11} \\
&\quad +(\sqrt{1-\zeta_i^2}\sin\varphi_i - \frac{\zeta_i^2}{\sqrt{1-\zeta_i^2}}\sin\varphi_i + \frac{\zeta_i^2}{\sqrt{1-\zeta_i^2}}\sin\varphi_i)[\bar{\boldsymbol{\Gamma}}_i^{-1}]_{12} - \frac{\cos\theta_i}{\sin\theta_i}\sin\varphi_i x_i\} \\
&= (\cos\theta_i\sin\varphi_i\cos\varphi_i)[\bar{\boldsymbol{\Gamma}}_i^{-1}]_{11} + \sin\theta_i\sin\varphi_i[\bar{\boldsymbol{\Gamma}}_i^{-1}]_{12} - \frac{\cos\theta_i}{\sin\theta_i}\sin\varphi_i x_i \\
&= \frac{1}{\sin\theta_i\sin\theta_i}(-\xi_i\gamma_i\zeta_i)[\bar{\boldsymbol{\Gamma}}_i^{-1}]_{11} + \gamma_i[\bar{\boldsymbol{\Gamma}}_i^{-1}]_{12} + \frac{1}{\sin\theta_i\sin\theta_i}(-\sin\theta_i\sin\varphi_i\cos\theta_i x_i) \\
&= \varsigma_i^{-2}\gamma_i(-[\bar{\boldsymbol{\Gamma}}_i^{-1}]_{11}\xi_i\zeta_i + [\bar{\boldsymbol{\Gamma}}_i^{-1}]_{12}\varsigma_i^2 - \zeta_i x_i)
\end{aligned}
$$

and let $\Upsilon_i = \varsigma_i^{-2}\gamma_i(x_i\zeta_i + [\bar{\boldsymbol{\Gamma}}_i^{-1}]_{11}\zeta_i\xi_i - \varsigma_i^2[\bar{\boldsymbol{\Gamma}}_i^{-1}]_{12})$

$$
\begin{aligned}
\Psi'_{\alpha'}(\zeta) &\simeq \Psi'_{0\alpha'} + \Psi''_{0\alpha'\zeta}\delta\zeta \\
&= \partial_{\alpha'}\Psi(\alpha',\zeta)\Big|_{\alpha'=\phi_i,\zeta=\zeta_i} + \partial_{\alpha'\zeta}\Psi(\alpha',\zeta)\Big|_{\alpha'=\phi_i,\zeta=\zeta_i}\delta\zeta \\
&= \gamma_i x_i + \varsigma_i^{-2}\gamma_i(x_i\zeta_i + [\bar{\boldsymbol{\Gamma}}_i^{-1}]_{11}\zeta_i\xi_i - \varsigma_i^2[\bar{\boldsymbol{\Gamma}}_i^{-1}]_{12})\delta\zeta \\
&= \gamma_i x_i - \Upsilon_i\delta\zeta \\
&\equiv \tilde{\eta}_i
\end{aligned}
$$

So, $\tilde{\eta}_i = \gamma_i x_i - \Upsilon_i\delta\zeta$, where $\Upsilon_i = \varsigma_i^{-2}\gamma_i(x_i\zeta_i + [\bar{\boldsymbol{\Gamma}}_i^{-1}]_{11}\zeta_i\xi_i - \varsigma_i^2[\bar{\boldsymbol{\Gamma}}_i^{-1}]_{12})$.

Following a similar processes,

$$\partial_{\alpha'}\Psi(\alpha',\zeta)\big|_{\alpha'} = \{\frac{1}{2}(\boldsymbol{\kappa}-\boldsymbol{\kappa}_i)'\bar{\boldsymbol{\Gamma}}_i^{-1}(\boldsymbol{\kappa}-\boldsymbol{\kappa}_i)+\boldsymbol{\kappa}^t\mathbf{x}_i\}'\big|_{\alpha'}$$
$$= \{(-\varsigma^2\sin\alpha'\cos\alpha_i'-\varsigma\xi_i\sin\alpha')[\bar{\boldsymbol{\Gamma}}_i^{-1}]_{11}$$
$$+(\varsigma\zeta\sin\alpha'-\varsigma\zeta_i\sin\alpha')[\bar{\boldsymbol{\Gamma}}_i^{-1}]_{12}\}+\varsigma\sin\alpha' x_i$$

and expanding $\Psi''_{\alpha'\alpha'}$ as below,

$$\Psi''_{\alpha'\alpha'} \simeq \Psi''_{0\alpha'\alpha'}$$
$$= \{(-\varsigma^2\sin\alpha'\cos\alpha_i'-\varsigma\xi_i\sin\alpha')[\bar{\boldsymbol{\Gamma}}_i^{-1}]_{11}$$
$$+(\varsigma\zeta\sin\alpha'-\varsigma\zeta_i\sin\alpha')[\bar{\boldsymbol{\Gamma}}_i^{-1}]_{12}+\varsigma\sin\alpha' x_i\}'\Big|_{\alpha'=\phi_i,\zeta=\zeta_i}$$
$$= \{(-\varsigma_i^2(\sin\varphi_i\cdot(-\sin\varphi_i)+\cos\varphi_i\cdot\cos\varphi_i)-\varsigma_i\xi_i\cos\varphi_i)[\bar{\boldsymbol{\Gamma}}_i^{-1}]_{11}$$
$$+(\varsigma_i\zeta_i\cos\varphi_i-\varsigma_i\zeta_i\cos\varphi_i)[\bar{\boldsymbol{\Gamma}}_i^{-1}]_{12}+\varsigma_i\cos\varphi_i x_i\}$$
$$= (-\varsigma_i^2(\cos\varphi_i\cdot\cos\varphi_i-\sin\varphi_i\sin\varphi_i)-\varsigma_i\xi_i\cos\varphi_i)[\bar{\boldsymbol{\Gamma}}_i^{-1}]_{11}+\varsigma\cos\varphi_i x_i$$
$$= (-\sin\theta_i\sin\theta_i(\cos\varphi_i\cdot\cos\varphi_i-\sin\varphi_i\sin\varphi_i)+\sin\theta_i\sin\theta_i\cos\varphi_i\cos\varphi_i)[\bar{\boldsymbol{\Gamma}}_i^{-1}]_{11}$$
$$+\sin\theta_i\cos\varphi_i x_i$$
$$= \sin\theta_i\sin\theta_i\sin\varphi_i\sin\varphi_i[\bar{\boldsymbol{\Gamma}}_i^{-1}]_{11}+\sin\theta_i\cos\varphi_i x_i$$
$$= \gamma_i^2[\bar{\Gamma}_i^{-1}]_{11}-\xi_i x_i$$
$$\equiv \tilde{q}_i$$

The above may be summarised as

$$\tilde{\eta}_i(\zeta)=\Psi'_{\alpha'}(\zeta)\simeq\gamma_i x_i-\Upsilon_i\delta\zeta$$

$$\tilde{q}_i=\Psi''_{\alpha'\alpha'}\simeq\gamma_i^2[\bar{\Gamma}_i^{-1}]_{11}-\xi_i x_i$$

where $\Upsilon_i=\varsigma_i^{-2}\gamma_i(x_i\zeta_i+[\bar{\boldsymbol{\Gamma}}_i^{-1}]_{11}\zeta_i\xi_i-\varsigma_i^2[\bar{\boldsymbol{\Gamma}}_i^{-1}]_{12})$.